Boundary Layer Instabilities in High and Low Enthalpy Hypersonic Facilities using High Speed Schlieren



Suria Devi Subiah

Lady Margaret Hall

University of Oxford

A thesis submitted for the degree of

Doctor of Philosophy

Trinity 2022

This thesis is dedicated to my parents and the generations before me.
Thank you for sacrificing and enduring so that my path would be easier.

Acknowledgements

This was a fun section to write as my time at Oxford has been made so special by a number of people. Firstly, I would like to thank my supervisor, Prof. Matthew McGilvray. Thank you for always being willing to jump in and solve problems. Your ability to grasp complex concepts quickly and make decisions in stressful situations is something I admire. To Dr. Luke Doherty, thank you for teaching me so much and for your detailed appreciation for a good CAD drawing. Commissioning a hypersonic tunnel was extremely stressful but very cool and an experience not many people get to do so I am grateful that you were both there to guide me through this. Thank you to Chris Hambidge (whose passion for organisational storage exceeds even my own) for being the Dad of the group. Thank you also to Dr. Tobi Hermann, Dr. Laurent Le Page and the other Hyp postdocs for the many knowledgeable discussions and problem-solving sessions.

To the tunnel operators during my experiments, in particular Tristy and Maïlys who made my testing campaigns bearable even when things were stressful. Tristy, hearing your weekend adventures with your daughters were the highlight of my Mondays. To the T6 crew, particularly Alex and Joe, and to Eric and Raggy - thank you for always being willing to help out and for bringing such good vibes to the environment, it really made a difference. To the rest of the hypersonics group, thank you for all the memes, laughter and mutual venting.

To Dave, Harry, Duncan, James and the other excellent workshop technicians at the OTI for being so nice, always up for a chat and always willing to try and squeeze in last minute jobs on an already overloaded worksheet. To Anna, Alex, Kathryn and Alex M. for being fantastic at their jobs and making sure OTI runs smoothly. (Thank you Anna for always having pictures of Nala the Most Majestic Husky on hand).

To Chiara and Edo, thank you for being wonderful friends over the years. Chia - your resilience and determination has inspired me on so many occasions and I am so grateful for our coffee chats in the lab and dinners outside the lab. Your shared love of food and willingness to give me advice on Italian cooking has definitely made me

a happier person and better cook. To Priyanka, Tamara, Naomi and Hannah who are all amazing women in engineering I have been very fortunate to call my friends - words can't describe how important it has been to have you all as a support system during the years.

To Vani, Sofi and Charlie, my LMH family - there were many times when college felt like a shelter in a storm because of you and I absolutely loved it there. Vani, I am constantly in awe of your resilience, strength and openness in discussing uncomfortable topics most people would shy away from. Together with Mer our writing sessions made finishing up this thesis infinitely better. To my friends and family both in Oxford, in the US and South Africa, namely Beril, Ali, TK, Ness (whose deep love of British clotted cream made me appreciate it so much more), Blazenka, Kal, Jay, Karen and Rubes. Many of you have remained my friends through three continents of moving which is not easy (particularly when power cuts mean no video calls) but is very special to me.

To my partner, Jon. Your constant support, love and unfailing encouragement have meant the world to me over the years but especially in these last few months. At times when I had no confidence in myself, I always knew I could borrow some from you. You are a phenomenal human being (and I'm so happy you escaped the friendzone). Also thank you to the Connolly family for being wonderful people - I've loved the multiple Christmases per year with Luna (the World's Best Gift Unwrapping Dog) and look forward to many more.

Finally to my parents, who instilled in me a sense of purpose and determination and tirelessly worked their entire lives to provide me with all the skills I needed. Thank you for telling me how proud you are every chance you get and for being so adamant in your belief that there were no limits to what I could achieve - I ended up believing it too.

Abstract

This thesis presents results from the first experiments conducted in the Oxford T6 Stalker Tunnel in Reflected Shock Tunnel mode and observations on the boundary layer instabilities established over a cone model at Mach 7 and Mach 8 conditions characterised using high speed schlieren image processing techniques.

The Oxford T6 Stalker Tunnel was developed and commissioned in a new mode of operation, Reflected Shock Tunnel mode which was crucial to the establishment of boundary layer instabilities over a model. The process by which this was done is outlined, from an initial analytical model to a quasi one-dimensional facility simulation. Piston dynamics were modelled and characterised by blank-off experiments, followed by validation of the diaphragm properties with tests done in shock tube mode. Finally, reflected shock tunnel experiments at half and then full pressure were conducted. This was used iteratively to improve the test conditions, bringing them to within 1% of the required nozzle supply enthalpy and 2.6% of the required nozzle supply pressure. A nitrogen driver condition was developed to improve testing time and these conditions were used with both a Mach 7 and Mach 8 nozzle.

Traditional sensors were not reliable at the high frequencies of instabilities expected ($\sim$1 MHz) and would be damaged in the harsh flow environment. Thus, optical diagnostic techniques were explored as a means of extracting both quantitative and qualitative information from the flow. These techniques were developed based on high speed schlieren imaging and first applied to the Oxford High Density Tunnel, which is a cold flow facility for which pressure transducers could be used as a means of validating the developed techniques. Development of schlieren image processing techniques both for frequency and wavepacket convection speed detection as well as feature detection was undertaken. These methods were applied to experiments on a 7^o half-angle cone with a nose tip radius of 1.25 mm at Mach 7. Second mode instabilities were detected at a frequencies of 208-216 kHz with pressure transducers which allowed for validation of the image processing techniques. Nonlinear interactions were explored with the use of selected image processing techniques showing significant second harmonics in the flow. An investigation was conducted using three different high speed cameras and the effect of varying

camera parameters on the quality of the data extracted. Methods of extracting the frequencies of second mode instabilities using camera frame rates at much lower and much higher sampling rates than the expected frequency of the instabilities were developed and applied with varying levels of success.

Useful results were gained from these experiments, both as a review of the application of current schlieren processing methodologies, novel methodologies, and a comparison of different camera parameters which would inform future testing. Finally, both the commissioning work on the facility and the developed image processing techniques culminated in establishing and observing excellent first images of boundary layer instabilities in T6, namely high frequency second mode instabilities and non-modal instabilities at Mach 7 and Mach 8. Frame rates of 1-2 million frames per second allowed for capture of these instabilities. The extracted frequencies of these instabilities ranged from 0.8-1.4 MHz, at significantly higher frequencies than those observed in HDT. The methodologies allowed for the extraction of frequencies within 1-7% from the theoretical prediction. A blunt nose tip of 3.4 mm was used, allowing for the establishment of non-modal instabilities which could be visualised. These were fully characterised in terms of their convection speed and structure angle. These instabilities were swept along at just under the edge velocity (0.93-0.94U_e). Interesting results were obtained by tracking and identifying the structure angle variation in time, which clearly showed the instability collapsing from a maximum angle of 30^o to a more linear feature at approximately 8^o to the surface.
The results show significant progress in the development and study of hypersonic boundary layers in the T6 high enthalpy facility and allows for the extraction of accurate boundary layer information in harsh flow conditions without the use of traditional pressure sensors. This enables the UK to have the capability of high enthalpy testing for the study of hypersonic vehicle models and future boundary layer instability research at flight representative conditions.

Contents

List of Figures **x**

List of Tables **xx**

1 Introduction **1**
- 1.1 Research Aims and Contributions . . . 5
- 1.2 Thesis Structure . . . 6

2 Literature Review **8**
- 2.1 Introduction . . . 8
- 2.2 Flow over Hypersonic Vehicles . . . 10
- 2.3 Examining the Boundary Layer . . . 11
- 2.4 Second Mode Instability Results Using Different Measurement Techniques . . . 20
- 2.5 Transition Mechanisms on Blunt Geometries and Entropy Layer Effects 30
- 2.6 Summary . . . 34
- 2.7 Introduction . . . 36
- 2.8 Hypersonic Facilities at the University of Oxford . . . 39
- 2.9 Summary . . . 45

3 Experimental Setup **46**
- 3.1 Introduction . . . 46
- 3.2 HDT Model . . . 47
- 3.3 T6 Model . . . 48
- 3.4 T6 Pitot Rake . . . 51
- 3.5 Instrumentation . . . 53
- 3.6 Data Acquisition System . . . 55

4 Hypersonic Testing Facilities and Commissioning of the Oxford T6 Stalker Tunnel in Reflected Shock Tunnel Mode **56**
- 4.1 Introduction . . . 56
- 4.2 Condition Development Methodology . . . 58
- 4.3 First L1D Results . . . 65

4.4 Experimental Setup 73
4.5 Experimental Results and Adjusted L1D Model 77
4.6 Initial Reflected Shock Tunnel Tests 83
4.7 Use of nitrogen-argon driver gas mixtures for extended test time . . 90
4.8 Summary of T6 RST Mode Conditions Commissioned 93
4.9 Selection of Appropriate Test Time 95
4.10 Conclusion 96

5 Development of High-Speed Schlieren Image Processing Techniques 98
5.1 Introduction 99
5.2 The Morlet or Continuous Wavelet Transform 100
5.3 Image Pre-Processing 104
5.4 Frequency Detection Methods 107
5.5 Feature Detection Methods 113
5.6 Summary 121

6 Schlieren Image Processing Techniques in the Oxford High Density Tunnel 123
6.1 Introduction 123
6.2 Experimental Setup 124
6.3 Theoretical Prediction 129
6.4 Schlieren Frequency Detection Results Using Different Cameras . . 130
6.5 Schlieren Feature Detection Results Using Different Cameras 140
6.6 Parameter Comparison using Single Set of Data 145
6.7 Conclusion 159

7 Schlieren Image Processing Techniques in the Oxford T6 Stalker Tunnel 160
7.1 Introduction 161
7.2 Experimental Setup 162
7.3 Theoretical Prediction 168
7.4 Processing Methodology 169
7.5 Second Mode Instability Results 176
7.6 Non-Modal Instability Results 182
7.7 Conclusion 190

8 Conclusions and Further Work 193
8.1 Contributions 193
8.2 Future Work 199

References **201**

Appendices

A Cross-Correlation Results **215**

B Image Stitching Results **218**

C Wavelet Scalogram Results **221**

D Bispectral Analysis Results **227**

E SPOD Results **230**

F T6 and HDT Cone Model CAD **233**

G 90kg Piston Refurbishment CAD **256**

List of Figures

1.1 X-51A Waverider [7] 2
1.2 Laminar-turbulent boundary layer and the transition region, [8] . . 3

2.1 Major hypersonic vehicle types and associated phenomena [22] . . . 11
2.2 Depiction of the thin viscous boundary layer adjacent to the surface and the external inviscid flow, from [24] 12
2.3 Schematic showing mechanisms of transition (modified from [16]). References are: (Reshotko, 2001 [26, 27]), Schmid & Henningson, 2001 [28]), (Suder & O'Brien, 1988 [29]) 13
2.4 Visualisation in a water tunnel (top, [30]) and idealised sketch (middle, bottom, [31]) of transition over a flat plate in subsonic flow 14
2.5 Visualisation of the second mode instability waves from [32], originally adapted from [33] 16
2.6 Power spectral density results of hot-wire anemometer data from a cone at Mach 8 from Kimmel et al. [35] 17
2.7 Comparison of linear (top) and nonlinear (bottom) disturbance effects on second mode instabilities (from [38]) with the generalised inflection point (GIP) indicated by the dashed red line 18
2.8 Bicoherence spectra where peaks in the bicoherence value $b^2_{k,l}$ indicate the coupling of frequencies, at stations (a) 20, (b) 21, (c) 22 and (d) 36, from Kimmel et al. [35] 19
2.9 Comparison of amplification rates for a cone to Mack computations at M 8.5, from Kendall [39], ψ are values of oblique wave angle . . . 21
2.10 Energy spectrum at a fixed streamwise location for different Reynolds numbers, measured at the location of energy peak in the boundary layer [39] 22
2.11 Structure angles measured by Kimmel et al. [41] 22
2.12 Typical variation of velocity and temperature fluctuations at late stage second mode wave development normal to the surface of a sharp cone, in [34], adapted from [42] 24
2.13 Two types of schlieren systems (a) Toepler's lens-type schlieren system and (b) z-type schlieren system using twin parabolic mirrors [64] . . 25

2.14 Schematic of the cone model (top) and second mode instability wavepackets within the boundary layer (bottom) from Laurence et al. [68] 26
2.15 x-t diagram showing the normalised pixel intensities and development of instability waves (left) and energy spectral density as a function of normalised inverse wavelength for various heights in the boundary layer at $t = 54\mu s$ (right) [68] 27
2.16 Processed schlieren images over a cone with compression corner at Mach 6, unit Reynolds number of 4.94-5.31(10^6)/m, total specific enthalpy approximately 0.89 MJ/kg [70] 28
2.17 Average PSD at the unit Reynolds number 4.94-5.31(10^6) condition (top) for a frequency range of (a) 225-325 kHz and (b) 80-110 kHz. SPOD mode shapes (bottom) at (a) 289 kHz and (b) 90 kHz [70] . 29
2.18 Processed schlieren images over a cone with expansion corner at Mach 5.95, unit Reynolds number of 5.31(10^6)/m, total specific enthalpy approximately 0.89 MJ/kg [71]. Images are 10.7μs apart 30
2.19 Spatial distribution of second-mode fundamental PSD (top panel). SPOD mode shapes (bottom 4 panels) at 117 kHz, 204 kHz, 274 kHz and 344 kHz [71] 30
2.20 Schlieren image of a bow shock over a blunt cone, from experiments performed in the Oxford High Density tunnel on a 7^o cone at Mach 7 31
2.21 Schematic illustrating entropy swallowing distance (left) and swallowing distance parameter (right), from [12] (originally [17] and [74]) 32
2.22 Elongated structures extending beyond the boundary layer, visualised by Grossir et al. using LIF based schlieren on a 4.75 mm nose tip radius cone at Mach 11.7-11.9 [20] 34
2.23 Schematic of original T3 free piston shock tunnel, from [90] 38
2.24 Schematic of Oxford High Density Tunnel [102] 40
2.25 T6 facility mode comparison 42
2.26 CAD model of the Oxford T6 Stalker Tunnel in the RST configuration 43
2.27 Non-tailored (top) versus tailored (bottom) comparison, adapted from [105] 44
2.28 (a) Ratio of driver gas pressure to diaphragm rupture pressure versus non-dimensional time for an overdriven condition. (b) Typical piston trajectories [108], (1) Rebound Landing (2) Soft Landing (3) Direct Impact 45

3.1 Naming convention for cone model showing angle of attack α and azimuth Φ 47

3.2 Model in HDT 48
3.3 Labelled exploded view of T6 cone model 49
3.4 T6 cone in tunnel CAD with nozzle Mach number contours overlaid (nozzle simulations by T. Sopek) 50
3.5 Cone model in T6 50
3.6 Pitot probe schematic and distances from centreline (mm) 51
3.7 Image of pitot rake installed in T6, left ([111]), high speed image of pitot probes and bow shock formation during T6 test, right 52
3.8 PCB132A31, from [49] 54
3.9 Schematic with dimensions of inches and mm in brackets (top) and image of of Kulite XCS-062 sensor (bottom) from [113] 54
3.10 Image of UQ thin film gauge, from [114] 55

4.1 Flow features and numbering convention in reflected shock tube mode 59
4.2 Flowchart showing general methodology followed in condition development for RST mode 60
4.3 Numbering convention for Part I 60
4.4 Numbering convention and simplified geometry with orifice 62
4.5 Overtailored, tailored and undertailored cases 67
4.6 High RG alternate case, pressure at the diaphragm (MPa) 68
4.7 High RG alternate case, piston velocity (m/s) versus distance from the primary diaphragm (m) 68
4.8 High RG alternate case, pressure at the stagnation region (MPa) . . 69
4.9 (a) High RG alternate case, enthalpy at the stagnation region (MJ/kg) 69
4.10 Final condition, pressure at the diaphragm (MPa) 71
4.11 Final condition, piston velocity (m/s) versus distance from the primary diaphragm (m) 71
4.12 Final condition, pressure at the stagnation region (MPa) 72
4.13 Final condition, enthalpy at the stagnation region (MJ/kg) 72
4.14 Blanking plate setup 73
4.15 Blanking plate and buffers, post test (left) and detail of the blanking plate transducer mount (right), [92] 74
4.16 Schematic of shock timing station measurement locations and an example of the data selected to obtain the average shock speed . . . 74
4.17 90 kg steel piston, refurbished (left) and piston model in SolidWorks (right) 76
4.18 Example of unscored diaphragm (top) and scored diaphragm (bottom) before and after rupture 77
4.19 First adjusted model compared to T6 shot 66 and original model . . 79

4.20 Comparison of half blank off experimental results versus L1D model with first adjusted factors 79
4.21 Comparison of shot 66 and shot 67 80
4.22 Comparison of shot 68 adjusted reservoir gas pressure to required conditions 80
4.23 Shot 68 crush rods before (left) and after (right) 81
4.24 Full width at half maximum (left), experimental lag (centre), peak pressure comparison (right) 81
4.25 Comparison of shot 68 with final loss factors with close up to show experimental lag 82
4.26 Comparison of fitted Gaussian curves of all blank-off tests with their corresponding L1D models using the final loss factors 82
4.27 Shock speed achieved for Shot 85, compared to L1D and PITOT predictions 83
4.28 Nozzle supply pressure from RST shots 88 and 89 compared to predicted stagnation pressure with the approximate test time outlined 85
4.29 Incident shock speed (m/s) versus distance (m) for T6 in RST mode shots 88 and 89 compared to L1d prediction 86
4.30 Pitot pressure versus radial distance (m) from centreline of Pitot rake 87
4.31 Stagnation point heat flux for shot 88 (solid lines) and shot 89 (dotted lines) 87
4.32 Contour plot of Mach number for the Mach 7 nozzle and test section, indicating the core flow region and Pitot rake location 88
4.33 Pitot to stagnation pressure ratio (left) and Mach number (right) at nozzle exit 89
4.34 Static pressure profile (left) and temperature (right) at nozzle exit . 89
4.35 Stagnation pressure for forward and aft Pitot rake positions, Mach 8 nozzle and N2 driver condition D 91
4.36 Shock speed for forward and aft Pitot rake positions, Mach 8 nozzle and N2 driver condition D 92
4.37 Pitot to nozzle supply pressure indicating core flow diameter for forward and aft Pitot rake positions, Mach 8 nozzle and N2 driver condition D 93

5.1 Example of second mode instability wavepackets on the surface of a 7^o half angle cone in Mach 7 flow (flow is from left to right) circled, colour map applied for clarity 99
5.2 Example of a pure sinusoidal wave and it's cosine, or zero phase, function adapted from [155] 101

5.3 Example of a Gaussian envelope function with the width equal to the distance between half maximums (Δx), adapted from [155] . . . 102
5.4 Graphical representation of the product of a Gaussian function (top) and sinusoidal waves (middle), resulting in the final wavelet (bottom) with amplitude envelope superimposed [155] 102
5.5 The effect of varying the shape ratio k (left) and the effect of varying the dominant period X_0 (right), adapted from [155] 103
5.6 Flowchart summarising background image processing 104
5.7 A selected example frame, it's background image and the subtracted image 105
5.8 The background and mean subtracted images 105
5.9 The subtracted image, its rescaled and cropped image. The cropped region is highlighted by the red dashed line 106
5.10 The cropped image and image with continuous wavelet transform applied. Dimensions are the same as Fig. 5.9, y axis enlarged for clarity 106
5.11 Spatial calibration image with ruler at location of Kulite 4, 458 mm from a theoretically sharp nosetip for shot 1922. x and y axes are equal 107
5.12 Schlieren images using (left) and wavelet transform of images (right) for shot 1922. The location of PCB5 is shown by the red marker. Dimensions are the same as Fig. 5.9 108
5.13 Surface map of PSD (flattened view on the right) for heights above the wall for pixel intensity traces 108
5.14 Surface map of PSD (flattened view on the right) for heights above the wall for Morlet transformed images 109
5.15 Stitched wavepackets for shot 1932 109
5.16 Template image and wavepacket section (left). Identified wavepackets for a series of images (right). Dimensions are the same as Fig. 5.9 . 110
5.17 Subset of image frames and regions over which disparity was taken for shot 1922 (right) and shot 1936 (left) 112
5.18 Resulting image with lines indicating the gradient for shot 1922 . . 113
5.19 Example image, shot 1922 113
5.20 Pixel intensity across a row in regions I-III 114
5.21 Identification of turbulent spot 115
5.22 Example of a standard bispectrum [168] 116
5.23 Audio signal data example from Swami et al.[166] (left) and bispectrum (right) 117
5.24 Diagonal slice through bispectrum 117
5.25 Fluctuating pressure component (top) and mean pressure field (bottom) of a Mach 0.4 isothermal turbulent jet from LES [168] 120

5.26 SPOD eigenfunctions/modes of a turbulent jet LES data for representative frequencies of fD/U of 0.1 (top row), 0.6 (middle row), 1.5 (bottom row) [168] 120

6.1 Schematic of schlieren setup in HDT, optical path lengths and objects are not to scale 124
6.2 Images of the schlieren set up in HDT, source side on the left and detection side on the right 126
6.3 HDT facility Pitot to supply ratio as a function of supply pressures, dashed line indicates relationship used for Mach 7 nozzle, from [103] 127
6.4 Required fill pressure as a function of target supply pressure for each facility plateau, from [103] 128
6.5 Stagnation pressure and Mach number traces with test time indicated for shot 1922 129
6.6 Summary of methods used in analysis of high speed schlieren images 130
6.7 Histogram showing number of matched wavepackets at frequencies for frame rates of 30 kfps for shot 1928 (left) and 1932 (right) . . . 131
6.8 Histogram showing number of matched wavepackets at frequencies for frame rates of 870 kfps for shot 1922 (left) and 1936 (right) . 131
6.9 Frequencies for each cross-correlated frame in shot 1926 132
6.10 Percentage error from pressure sensor data for the cross-correlated results, both mean and modal values 133
6.11 Image stitching results for frame rates of 30 kfps for shot 1928 (left) and 1932 (right) 134
6.12 Image stitching results for frame rates of 870 kfps for shot 1922 (left) and 1936 (right) 135
6.13 Intensity probe schlieren results (normalised against the maximum pressure sensor values for each shot) compared to pressure fluctuation results 135
6.14 Semi-global matching disparity map indicating disparity values (left) for a subset of images and the averaged value of disparity over frames (right) for shot 1922 136
6.15 Semi-global matching disparity map indicating disparity values (left) and averaged value of disparity over frames (right) for shot 1936 . . 137
6.16 Convection speed percentage error difference from shot 1922 SGM method 138
6.17 Percentage error from pressure sensor data for intensity probe, image stitching methods, and cross correlation (modal values) 139
6.18 Indication of PCB axial locations and equivalent marker positions on a frame from shot 1922 140

6.19 Wavelet scalograms from pressure transducer data 141
6.20 Wavelet scalograms from schlieren images, shot 1922, at equivalent PCB locations, corresponding to the wall normal locations in Fig. 6.18 141
6.21 Bispectrum for shot 1922 from PCB data at sensor locations from theoretically sharp nose tip (left) and bispectrum for single PCB location at approximately 457 mm (right) 142
6.22 Bispectrum for shot 1922 from schlieren data at axial locations from theoretically sharp nose tip (left) and bispectrum for at a single PCB location at approximately 457 mm (right) 142
6.23 SPOD analysis for shot 1922 at 870kfps 143
6.24 Snapshot of original and de-resolved images in wall normal direction (axes are in pixels) 146
6.25 Snapshot of original and de-resolved images in axial direction (axes are in pixels) 147
6.26 Snapshot of original and de-resolved images in wall normal and axial direction (axes are in pixels) 148
6.27 Power spectral density comparison of de-resolved images in wall normal direction 149
6.28 Diagonal slice through the bispectrum for cases in the wall normal direction 149
6.29 Bispectrogram for cases in the wall normal direction 150
6.30 Power spectral density comparison of de-resolved images in the axial direction 151
6.31 Diagonal slice through the bispectrum for cases in the axial direction 151
6.32 Bispectrogram for cases in the axial direction 152
6.33 Power spectral density comparison of de-resolved images in the wall normal and axial directions 153
6.34 Diagonal slice through the bispectrum for cases in the wall normal and axial directions 153
6.35 Bispectrogram for cases in the wall normal and axial directions . . . 154
6.36 PSD comparison at different frame rates 155
6.37 PSD comparison at different number of frames 155
6.38 Diagonal slice through the bispectrum for different number of frames (zoomed in on the right) 156
6.39 Bispectrogram for cases for different number of frames 157

7.1 Schematic of schlieren setup in T6, optical path lengths and objects are not to scale 163
7.2 Test time analysis for T6s357 166
7.3 Test time analysis for T6s358 167

7.4 Test time analysis for T6s301 168
7.5 Series of images from shot T6s357, images have been processed by background subtraction. Time is referenced from the start of the test time for each condition 170
7.6 Series of images from shot T6s357, images have been processed by background and average image subtraction. Time is referenced from the start of the test time for each condition 171
7.7 Template image for cross correlation, shot T6s357 171
7.8 Matched wavepackets for a series of selected images, shot T6s357 . . 172
7.9 Template image for cross correlation, shot T6s301 172
7.10 Matched wavepackets for a series of selected images, shot T6s301 . . 173
7.11 Template image for cross correlation, shot T6s358 174
7.12 Matched wavepackets for a series of selected images, shot T6s358 . . 174
7.13 Images showing process of edge tracing. (a) Example pre-processed image (b) Edge detection applied and isolated region in red (c) Isolated region before edge refinement (d) Refined edge (e) Detected edge (f) Spline fit applied to detected edge 176
7.14 Cross correlated frequency results for each frame (left) and histogram (right) for shot T6s301 177
7.15 Stitched image of shot T6s301, first 20 frames in test time 177
7.16 PSD for stitched image, shot T6s301 178
7.17 Cross correlated frequency results for each frame (left) and histogram (right) for shot T6s357 179
7.18 Locations for convection speed calculation, shot T6s357 179
7.19 Time-location pixel intensity plots (left column) for shot T6s357 for selected rows at y = 0.67 mm (top), 0.50 mm (centre), 0.34 mm (bottom). Corresponding edge detection overlays and detected line for gradient calculation (right column) 180
7.20 Stitched image of shot T6s357, first 40 frames in test time 181
7.21 PSD for stitched image, shot T6s357 181
7.22 Image and regions for edge fit, t = 10μs (top). Edge and curve fit for each region (bottom) 183
7.23 Extracted edge overlaid on image (top) and plotted with angles (bottom) 184
7.24 Tracked edges over multiple frames (only every tenth frame is shown here for clarity but the analysis was applied to 50 frames) 185
7.25 Evolution of single instability structure angle over time at different heights above the surface. Dashed lines show linear fit 185
7.26 Locations for pixel intensity traces, shot T6s358 186

7.27 Power spectra from pixel intensity traces, shot T6s358 186
7.28 Scalogram based on pixel intensity traces 187
7.29 Regions of high scalogram intensity on images 187
7.30 Cross correlated velocity results for each frame (left) and histogram (right) for shot T6s358 188
7.31 Locations for convection speed calculation, shot T6s358 188
7.32 Time-location pixel intensity plots (left column) for shot T6s358 for selected rows at y = 1.85 mm (top), 1.34 mm (centre), 0.84 mm (bottom). Corresponding edge detection overlays and detected line for gradient calculation (right column) 189

A.1 Histogram showing number of matched wavepackets at frequencies for frame rates of 30 kfps for shots 1928 (left) and 1932 (right) . . 215
A.2 Histogram showing number of matched wavepackets at frequencies for frame rates of 100 kfps for shots 1926 (left) and 1930 (right) . . 216
A.3 Histogram showing number of matched wavepackets at frequencies for frame rates of 500 kfps for shots 1924 (left) and 1937 (right) . . 216
A.4 Histogram showing number of matched wavepackets at frequencies for frame rates of 540 kfps for shot 1931 216
A.5 Histogram showing number of matched wavepackets at frequencies for frame rates of 870 kfps for shots 1922 (left) and 1936 (right) . . 217

B.1 Image stitching results for frame rates of 30 kfps for shot 1928 (left) and 1932 (right) 218
B.2 Image stitching results for frame rates of 100 kfps for shot 1926 (left) and 1930 (right) 219
B.3 Image stitching results for frame rates of 500 kfps for shot 1924 (left) and 1937 (right) 219
B.4 Image stitching results for frame rates of 540 kfps for shot 1931 . . 219
B.5 Image stitching results for frame rates of 870 kfps for shot 1922 (left) and 1936 (right) 220

C.1 Locations of wavelet scalograms for shot 1922 222
C.2 Shot 1922 wavelet scalograms at locations downstream of a theoretically sharp nosetip and above the cone surface 222
C.3 Locations of wavelet scalograms for shot 1936 223
C.4 Shot 1936 wavelet scalograms at locations downstream of a theoretically sharp nosetip and above the cone surface 223
C.5 Locations of wavelet scalograms for shot 1931 224
C.6 Shot 1931 wavelet scalograms at locations downstream of a theoretically sharp nosetip and above the cone surface 224

C.7 Locations of wavelet scalograms for shot 1924 225
C.8 Shot 1924 wavelet scalograms at locations downstream of a theoretically sharp nosetip and above the cone surface 225
C.9 Locations of wavelet scalograms for shot 1937 226
C.10 Shot 1937 wavelet scalograms at locations downstream of a theoretically sharp nosetip and above the cone surface 226

D.1 Bispectrum for shot 1922 from PCB data at sensor locations from theoretically sharp nose tip 227
D.2 Bispectrum for shot 1922 at axial locations from theoretically sharp nose tip 228
D.3 Bispectrum for shot 1936 at axial locations from theoretically sharp nose tip 228
D.4 Bispectrum for shot 1931 at axial locations from theoretically sharp nose tip 228
D.5 Bispectrum for shot 1924 at axial locations from theoretically sharp nose tip 229
D.6 Bispectrum for shot 1937 at axial locations from theoretically sharp nose tip 229

E.1 SPOD analysis for shot 1922 at 870kfps 230
E.2 SPOD analysis for shot 1936 at 870kfps 231
E.3 SPOD analysis of shot 1931 at 540kfps 231
E.4 SPOD analysis for shot 1924 at 500kfps 232
E.5 SPOD analysis for shot 1937 at 500kfps 232

List of Tables

3.1 Sensors and location for HDT model 48
3.2 Nose tips for T6 cone 49
3.3 Sensors and locations from theoreically sharp nose tip for T6 models 51
3.4 Table showing Pitot probe setup 53

4.1 Initial conditions of interest 59
4.2 T6 tunnel dimensions 65
4.3 Initial and final input conditions 70
4.4 Table showing shock timing station distances from the primary diaphragm 75
4.5 Table showing stagnation probe setup 75
4.6 Description of blank-off shots and conditions 78
4.7 Summary of original and adjusted loss factors 81
4.8 Fill conditions from condition development 84
4.9 Modifications to nitrogen driver gas conditions 91
4.10 Nominal conditions commissioned in T6 RST mode 94

6.1 Camera and schlieren settings for each shot 126
6.2 Nominal Test Conditions for HDT Experiments 129
6.3 Cases and resolutions for de-sampling in height above surface 146
6.4 Cases and resolutions for de-sampling in axial direction 146
6.5 Cases and resolutions for de-sampling in both wall normal and axial directions 147
6.6 Cases and frame rates analysed 152
6.7 Cases and frames analysed 154

7.1 Camera settings for T6 163
7.2 Test conditions for T6 experiments 164
7.3 Summary of second mode instability frequency results for T6 experiments using different methods 181
7.4 Summary of non-modal instability convection speed to edge velocity ratio for T6s358 using different methods 189

Nomenclature

Symbols

A	Area (m^2)
Ar	Argon gas
a	Speed of sound (m/s)
b^2	Bicoherence value
$b_1 - b_5$	Piston dynamic parameters
$\tilde{\mathbf{C}}$	Two-point space-time correlation tensor
$\mathcal{C}$	Cross correlation
CO	Carbon monoxide gas
CO_2	Carbon dioxide gas
C_p	Specific heat at constant pressure (KJ/kgK)
c	Wave speed (m/s)
D	Compression tube diameter (m)
d	Shock tube diameter (m)
E	Energy (J)
F_s	Reconstructed sampling frequency (Hz)
f	Frequency (Hz)
fr	Frame Rate (frames per second)
f_{sf}	Friction seal factor
H	Enthalpy (J/kg)
He	Helium gas

Kn	Knudsen number
k	Shape ratio
L	Length (m)
l	Launcher loss factor
M	Mach number
m	Mass (kg)
N_2	Nitrogen gas
Pr	Prandtl number
p	Pressure (Pa)
R	Specific gas constant (J/kgK)
Re	Reynolds number
R_N	Nosetip radius (mm)
S	Entropy (J/K)
SF	Scaling factor
SP	Stagnation pressure/probe
$\hat{S}_{xyz}$	Bispectrum value
T	Temperature (K)
Tr	Trace
t	Time (s)
U	Velocity in a-direction (m/s)
V	Velocity in y-direction (m/s)
W	Weighting
w	Lag window function
X, x	Axial/horizontal distance (m)
Y, y	Normal/vertical distance (m)

α	Angle of Attack (degrees)
Γ	Cross-spectral density tensor
γ	Ratio of specific heats
δ	Boundary layer thickness (mm, unless otherwise specified)
θ	Structure angle (degrees)
κ	Non-dimensional piston velocity
Λ	Eigenvalues
λ	Wavelength (m)
λ_c	Compression ratio
μ	Dynamic viscosity (Pa.s)
Ξ	Expectation Operator
ξ	Non-dimensional piston displacement
ρ	Density (kg/m^3)
σ	Standard deviation
τ	Non-dimensional time
Φ	Azimuth Angle (degrees)
ϕ	Lens/mirror diameter
φ	Deterministic vector field
χ	Mass fraction
ω	Mean angular frequency (rad/s)

Superscripts/Subscripts

c	Characteristic
DG1	Initial condition of driver gas
e	Edge conditions
i	Chemical Species i

p	Condition of piston
RG1	Initial condition of reservoir gas
r	Condition at rupture
SW	Swallowing distance (m)
s	Shock conditions
tr	Transition
u	Unit
w	Wall
0	Stagnation conditions
∞	Freestream
†	Hermitian conjugation

Acronyms

AOTV	Aero-assisted Orbital Transfer Vehicle
ARV	Ascent and Re-entry Vehicle
CAD	Computer Aided Design
C	Camera
CV	Cruise Vehicle
CWT	Continuous Wavelet Transform
DHTG	Diamond Heat Transfer Gauge
DNS	Direct Numerical Simulations
FFT	Fast Fourier Transform
FLDI	Focused Laser Differential Interferometry
FOV	Field of view
FWHM	Full Width at Half Maximum
HDT	High Density Tunnel

HIFiRE Hypersonic International Flight Research Experimentation Program

IR Infrared

KE Knife Edge

LES Large Eddy Simulation

LICH Light Isentropic Compression Heating

LIF Laser Induced Fluorescence

LS Light Source

PEEK Polyether ether ketone

PM Parabolic Mirror

POD Proper Orthogonal Decomposition

PSD Power Spectral Density

RD Refractive disturbance

RST Reflected Shock Tunnel

RV Re-entry Vehicle

SGM Semi-Global Matching

SPOD Spectral Proper Orthogonal Decomposition

STS Shock timing station

TFG Thin Film Gauge

TSTO Two-Stage-to-Orbit System

1 Introduction

Contents

1.1 Research Aims and Contributions 5
1.2 Thesis Structure 6

The field of hypersonics is currently experiencing renewed global interest, with increased investment in hypersonics research pushing military and commercial technology to new frontiers. Hypersonics refers to the flight regime where fluid velocity is much higher than the speed of sound and coupled aerodynamic-thermodynamic effects become dominant, typically occurring above Mach 5 [1, 2]. Just recently, the US made hypersonics research and development a top priority by signing into effect the $770 billion National Defense Authorisation Act [3]. Funding for hypersonics research in the US alone increased by 740% between 2015 and 2020 as the US Department of Defence aims to fast-track production of the first hypersonic missile by 2022 [3]. In the UK, more than £2 billion has been allocated between 2022-2026 for the Ministry of Defence's Science & Technology Agenda which will invest in key elements such as the development of UK defence capabilities in space and hypersonics to equip the Armed Forces against future threats [4]. This new portfolio highlights the need for enhanced hypersonics research capability in the UK to enable the development of these vehicles and support the goals of making sustained

hypersonic flight possible. For commercial purposes, sustained hypersonic flight could get a plane from New York to London in 90 minutes, compared to three hours for the Concorde and six to seven hours for a regular passenger aircraft [5]. Just recently, United Airlines has committed to offering supersonic routes by 2029 [6]. Hermeus, a startup whose goal is to develop a hypersonic passenger aircraft, has started testing a hybrid turbojet-ramjet engine for this purpose in February 2020 [5].

Sustained hypersonic flight faces many challenges which must be solved first however. For one, hypersonic vehicles, such as the X-51A Waverider shown in Fig. 1.1, are extremely drag sensitive and are subject to very high heat loads. To understand this further, the boundary layer of a hypersonic vehicle must be well understood.

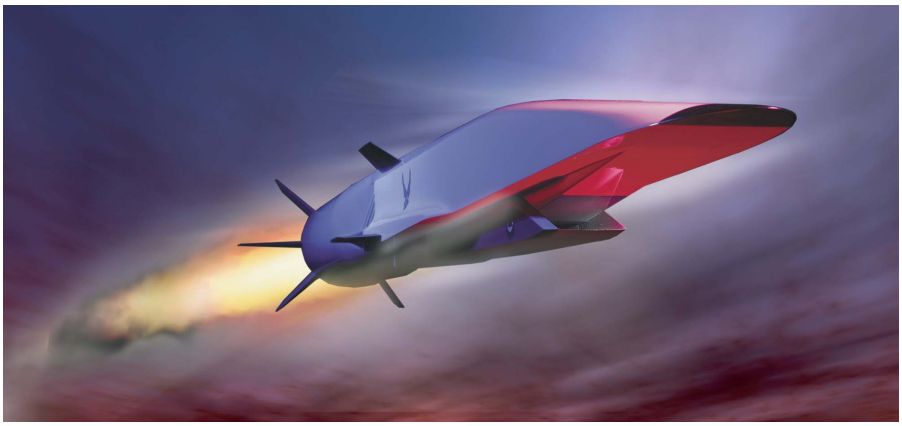


Figure 1.1: X-51A Waverider [7]

Within the boundary layer, two viscous flow regimes occur: laminar flow, in which the fluid elements have a smooth and ordered motion along a streamline, and turbulent flow, where the motion of the fluid is disordered and irregular [8]. Between these two regions there is a zone of transition. This is shown in Fig. 1.2.

The state of the boundary layer directly influences the rate of heat transfer to the vehicle surface and the skin friction. As the boundary layer transitions to turbulence, the drag increase can contribute to up to 50% of the total drag on the vehicle [9] and wall heat transfer can increase by an order of magnitude [10]. Thus, viscous effects such as boundary layer growth and laminar-turbulent transition become much more important to the survivability of the vehicle. A key goal is

therefore to understand the processes behind transition in order to inform design decision for future hypersonic vehicles.

Since the early experiments of Reynolds [11], transition has been thought to occur because of instabilities that develop in the laminar flow, amplify and break down. Vast investigations have followed in an attempt to gain an understanding of the complex nature of boundary layer instabilities but it still remains one of the greatest challenges in fluid dynamics [12].

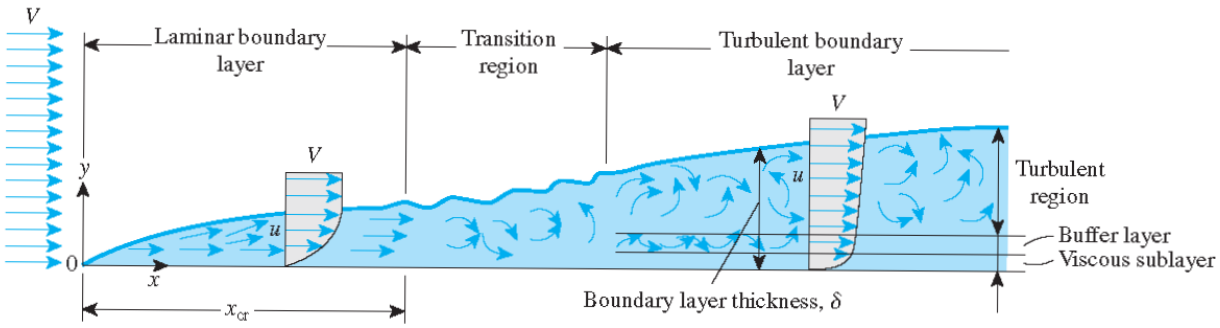


Figure 1.2: Laminar-turbulent boundary layer and the transition region, [8]

To understand laminar-turbulent boundary layer transition in hypersonic flows we need to examine the mechanisms by which this transition occurs which includes different types of instability processes. For the hypersonic flight regime this is geometry and orientation dependent, but for slender bodies at small angles of attack, instabilities called second or Mack mode instabilities dominate [13–17]. For blunter geometries non-modal instabilities have also emerged as a mechanism of interest [18–20]. The amplification and breakdown of these instabilities leads to turbulent transition and so their properties require investigation. While numerical simulations have advanced to this end, their transition models require detailed experimental databases. Direct Numerical Simulations (DNS) allow more insight into the physical phenomena, but proper initial excitation of the boundary layer remains challenging [12]. This is where the need for experimental research on hypersonic boundary layers and the use of ground test facilities becomes important. Ground tests also allow the use of non-intrusive measurement techniques to extract

information from the flow which is not always possible in a flight test. It is clear then that for the development of future hypersonic vehicles, an in-depth understanding of boundary layer transition is required, as well as established ground testing facilities able to generate such flows and validated measurement techniques suitable for these environments.

Testing facilities able to reproduce hypersonic flows are among a handful in the world but are crucial for the development of hypersonic vehicles. They exist as "cold" and "hot" flow facilities. Cold flow facilities are able to generate high Mach numbers but not velocities. Real gas effects are neglected as the temperature of the test gas is greatly reduced through expansion to just above liquefaction [21] so the test condition is of a low enthalpy. The primary advantage of cold facilities is their low noise environment ("quiet flow") and long test times. In contrast, hot flow facilities are able to recreate flight representative conditions like velocity and real gas effects as much higher temperature gas is expanded to obtain high enthalpy flows, at the cost of shorter test times and harsher or higher disturbance flow environments compared to flight conditions.

At Oxford University both a cold flow facility, the High Density Tunnel, has been developed and a hot flow facility, the T6 Stalker Tunnel, has been partially developed in recent years for hypersonics research. The T6 Stalker Tunnel is a multi-modal facility able to simulate flows in various flight regimes and has been previously commissioned in two different modes, however both have test time durations which are not long enough to allow the flow to establish over a representative vehicle model. For boundary layer research, the reflected shock tunnel mode is most applicable due to it's longer test times allowing for full boundary layer development. Prior to this work, this mode had not yet been commissioned but was necessary not only for the establishment of flight representative boundary layer research in this study, but also for providing the UK with the capability of having reliable test conditions relevant to hypersonic flight for future research and development.

Establishing the conditions for the formation of hypersonic boundary layer instabilities over a model in a hot flow facility is not without significant challenges, one of which is the noisy flow environment which has the potential to prevent the transition region from forming but rather forces the flow to directly transition from laminar to turbulent. Another difficulty is the harsh testing environment which can damage traditional pressure and heat transfer sensors. In addition to this, traditional pressure sensors are not reliable for characterising the high frequencies at which second mode instabilities would occur in these facilities, typically on the order of 1MHz or above. In terms of non-modal instabilities, pressure measurements only provide a small amount of useful information. Because of these constraints, and the difficulty in establishing conditions for boundary layers to form in hot flow facilities, little data exists both in capturing and characterising these high frequency instabilities in hot flow facilities. Non-intrusive measurement techniques and particularly the use of schlieren imaging has seen a re-emergence for extraction of quantitative information from the boundary layer as high-speed camera and laser technology has progressed. This study almost exclusively makes use of optical diagnostic techniques and develops novel processing methods in order to extract information from transitioning boundary layers in harsh flow environments.

1.1 Research Aims and Contributions

The major aims and original contributions that this work makes to the field are as follows:

1. **Develop a high enthalpy test capability in the UK for the study of hypersonic boundary layer transition**

   Previously, the Oxford T6 Tunnel did not have the capability to generate flows at hypersonic flight representative conditions which was required for the testing of a scaled vehicle model. The reflected shock tunnel mode of

operation was thus developed and commissioned over the course of this thesis by the author to enable this capability.

2. **Develop and validate experimental techniques to study hypersonic boundary layer transition mechanisms which could be applied at high frequencies**

   As a result of the high frequency nature of the instabilities expected, pressure transducers were not a reliable measurement technique. High speed schlieren image processing techniques were required to extract boundary layer instability information from the flowfield. This was first applied to experiments in the cold flow facility, the High Density Tunnel (HDT), in order to prove that the methodology worked in a less challenging environment where regular pressure transducers could be used as a means of validation. Methods to obtain nonlinear information and an investigation of the effect of varying camera parameters were explored.

3. **Explore boundary layer instabilities in a high enthalpy test environment**

   Very little experimental data exists on high frequency boundary layer instabilities in hot flow facilities on sharp and blunt nosed cone geometries. Both second mode instabilities which dominate transition for sharp nosed models and non-modal instabilities which dominate transition for blunt nosed models were established for the first time in this facility and characterised using novel image processing techniques.

1.2 Thesis Structure

The above contributions are explored in the remaining thesis chapters:

1. **Chapter 2** is divided into two parts. The first provides a review of boundary layer transition theory and explores the concepts behind mechanisms of transition. In particular, second mode instabilities are explored in detail along

with other studies using optical diagnostic techniques on which this work builds. Instability mechanisms occurring in blunt geometries are introduced and studies focusing on this are reviewed. The second part of the chapter reviews types of hypersonic facilities in use, the main facilities used for this research and concepts of reflected shock tunnel operation.

2. **Chapter 3** presents a description of the experimental models used in the HDT and T6 campaigns and their instrumentation.

3. **Chapter 4** details the process followed in commissioning the first tests in Reflected Shock Tunnel mode in T6, the analytical model developed for obtaining initial test conditions, the numerical facility model and the experiments undertaken to build up to the final developed conditions. Properties of the test conditions developed and their freestream characteristics are presented.

4. **Chapter 5** shows the development of various schlieren imaging processing techniques, some of which have been applied in other studies and others which are novel

5. **Chapter 6** analyses the data collected from HDT using three different high speed cameras and applies the developed techniques to extract properties of the second mode instability mechanisms present in the boundary layer. The results are compared to measurements from pressure transducers. Image parameters and their effect on the data quality are examined.

6. **Chapter 7** introduces the application of selected developed image processing techniques to the first boundary layer experiments conducted in T6, identifies second mode and non-modal instabilities occurring in the flow and characterises them with the use of these techniques.

7. **Chapter 8** concludes the thesis by summarising the key findings, discussing limitations of the study and suggesting improvements for the future. The implications of the results to future work are explored and avenues for further research are identified.

2
Literature Review

Contents

2.1 Introduction 8
2.2 Flow over Hypersonic Vehicles 10
2.3 Examining the Boundary Layer 11
2.3.1 Mechanisms of Transition 12
2.4 Second Mode Instability Results Using Different Measurement Techniques 20
2.4.1 Surface Mounted and Probe Measurements 20
2.4.2 Optical Diagnostic Techniques 23
2.5 Transition Mechanisms on Blunt Geometries and Entropy Layer Effects 30
2.6 Summary 34
2.7 Introduction 36
2.7.1 Types of Hypersonic Test Facilities 37
2.8 Hypersonic Facilities at the University of Oxford . . . 39
2.8.1 Oxford High Density Tunnel 39
2.8.2 Oxford T6 Stalker Tunnel 40
2.8.3 Tailoring and Tuning 43
2.9 Summary 45

2.1 Introduction

This literature review is divided into two main parts. The first provides a general overview of hypersonics before reviewing boundary layer transition theory,

hypersonic boundary layers and characteristics of some of their relevant associated instabilities, how they are measured traditionally and with optical diagnostics, and a brief review of the current work done specifically in the field of high speed schlieren for hypersonic boundary layers. This field has experienced renewed interest based on the advancements in high speed camera technology and the new application of image processing techniques. As outlined in this chapter, little data exists for instabilities in hot flow facilities due in part to the difficulty in establishing them and then in characterising them because traditional sensors are not suitable for reasons explained later.

In order for these instabilities to be established in T6, it was first necessary to develop and commission the Oxford T6 Stalker Tunnel in the reflected shock tunnel mode of operation which not only provided the test conditions for this boundary layer research, but also provided the capability for a host of future research to be undertaken in the tunnel using these commissioned conditions. Part two of the literature review thus provides an overview of hypersonic testing facilities, the two main facilities at Oxford which were used for these tests (the Oxford High Density "cold-flow" facility and the Oxford T6 Stalker Tunnel), particulars of the T6 Tunnel including it's different modes of operation and the principles of reflected shock tunnel commissioning.

Part I: Hypersonic Boundary Layer Transition

2.2 Flow over Hypersonic Vehicles

The term "hypersonics" was coined by a former doctoral student of Theodore von Kármán, Hsue-Shen Tsien to describe flow fields where the fluid velocity is much larger than the speed of sound [1]. It is generally understood to define the gas flow regime where coupled aerodynamic and thermodynamic effects become important and certain real gas phenomena are prevalent, typically above Mach 5.

Hypersonic vehicles place different importance on aerothermodynamic phenomena depending on their flight regime. Hirschel categorises hypersonic vehicles into four different types: winged re-entry vehicles, hypersonic cruise vehicles with airbreathing propulsion (ram propulsion up to Mach 7, scram propulsion up to Mach 12-14), ascent and re-entry vehicles (single-stage-to-orbit space transportation systems) and aero-assisted orbital transfer vehicles [22]. Aero-assisted vehicles are those that fly with aerodynamic lift in the atmosphere at altitudes and speeds approximately below 100km and 8 km/s [22]. These have different trajectories and are illustrated in Fig. 2.1.

Hypersonic cruise vehicles (CV) and ascent and re-entry vehicles (ARV) are drag sensitive, in contrast to aero-assisted re-entry vehicles. Typically, their lift and propulsion systems are also highly integrated. As the boundary layer transition affects the point of flow separation on control surfaces and hence control effectiveness, the stability of the vehicle, surface pressure fluctuations which may lead to structural fatigue and the performance of engines and their operability [12].

As heat fluxes increase, the use of more advanced thermal protection systems is

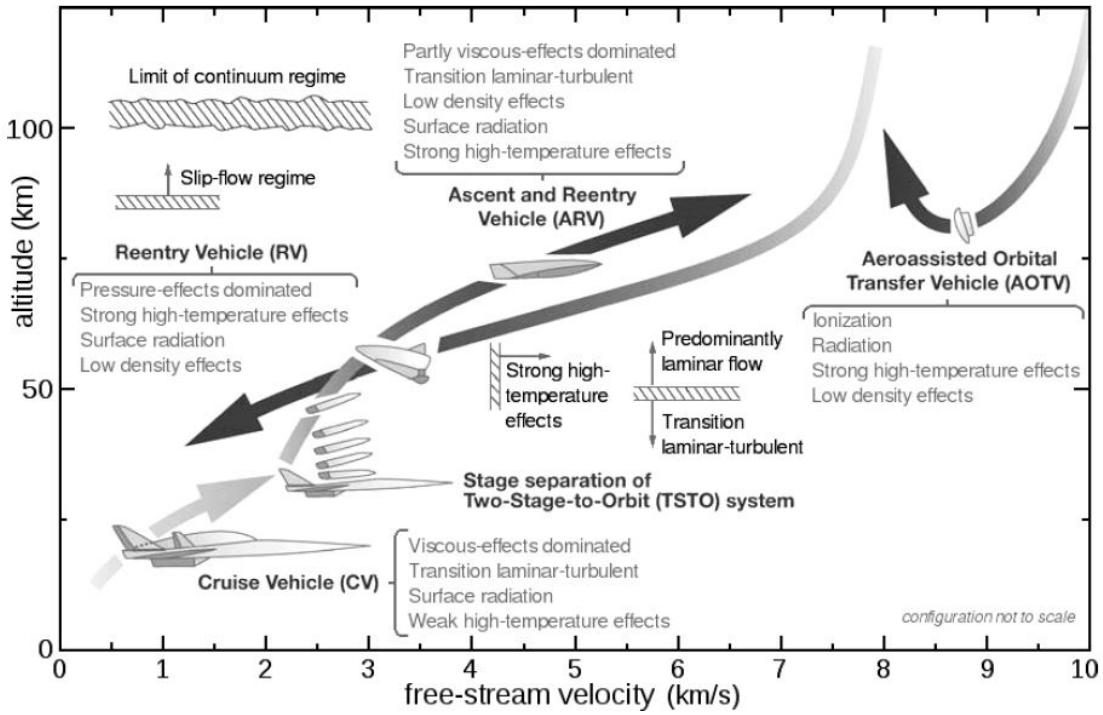


Figure 2.1: Major hypersonic vehicle types and associated phenomena [22]

required, which in turn requires a larger vehicle and more power, thus enhancing viscous effects and so on. This cycle highlights the need to understand fundamental boundary layer instability and transition phenomena in order to accurately predict the behaviour of the boundary layer as over-estimation due to the uncertainty in transition location can lead to oversized thermal protection systems which are costly and decrease the potential payload.

2.3 Examining the Boundary Layer

The concept of a boundary layer was first introduced by Ludwig Prandtl [23]. He theorised that the effect of friction was to cause the fluid adjacent to the surface of a solid body to adhere to the wall (in other words, a zero relative velocity between the fluid and the wall, the no-slip condition) and that frictional effects were experienced only in a thin region near the surface, the boundary layer ([24], from the original [23]). This concept revolutionised the field of fluid dynamics. In the flows associated with bodies in flight, the boundary layer is very thin compared to the size of the body and thus the flow can be examined as two parts, a thin boundary layer where

viscous effects dominate (shown in blue in Fig. 2.2), and an external inviscid flow. Within the boundary layer, there is a large velocity change over a very short distance normal to the surface. The large velocity gradient produces a large local shear stress according to Newton's shear stress law. As a result, the skin friction drag is not negligible. Along with this, in the boundary layer as the fluid slows down its kinetic energy is converted into internal energy, and the flow near the surface significantly increases in temperature. The consequences this has on heat transfer is particularly notable for hypersonic boundary layers, which will be examined in later sections.

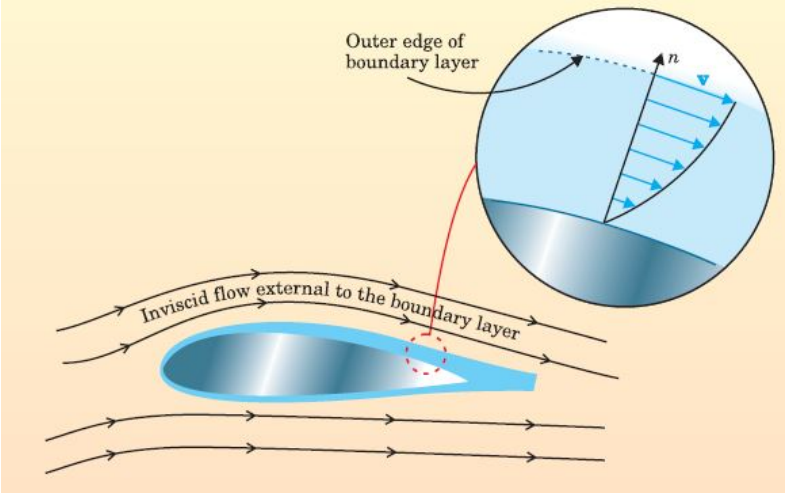


Figure 2.2: Depiction of the thin viscous boundary layer adjacent to the surface and the external inviscid flow, from [24]

2.3.1 Mechanisms of Transition

The development of a theory to describe instabilities forming in the boundary layer dates back to the 1930's with Tollmien and Schlichting [12]. Their approach was to decompose a laminar flow into a sum of the steady mean flow and unsteady small perturbation components. The Navier-Stokes equations could then be rewritten in terms of this decomposition. Terms which were small in magnitude, such as the product of perturbations, were neglected and thus Linear Stability Theory was formed. Perturbations were also assumed to propagate independently. This theory received very little attention until the seminal paper by Schubaer and Skramstad in 1947 [25] which experimentally showed the first evidence of the mathematically

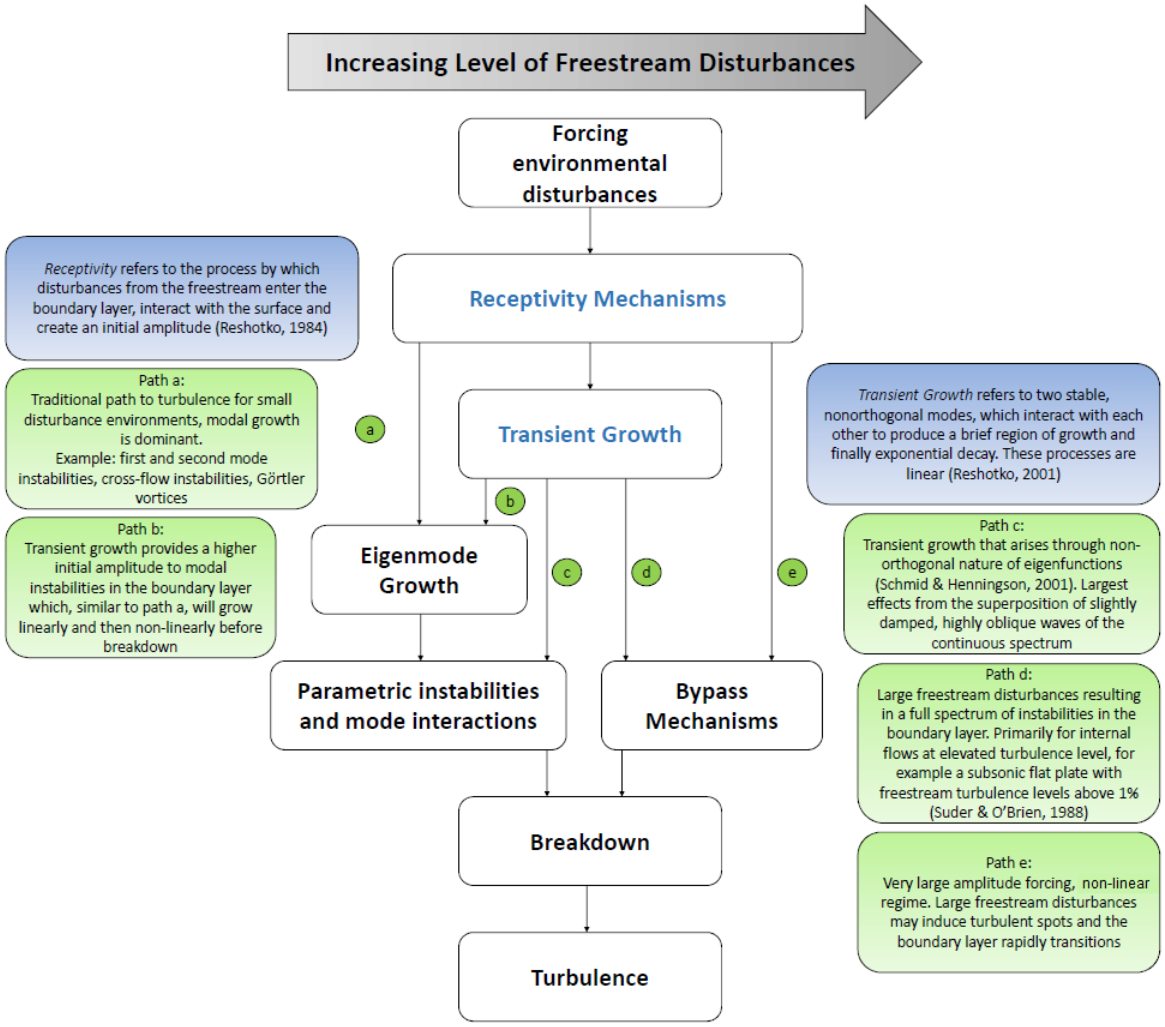
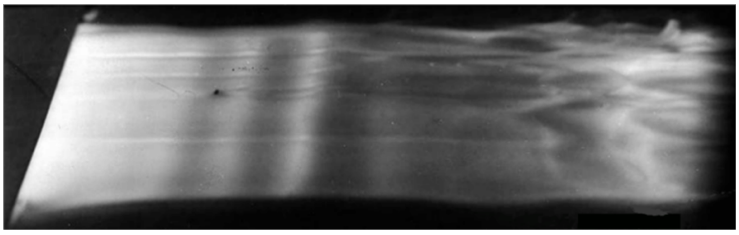


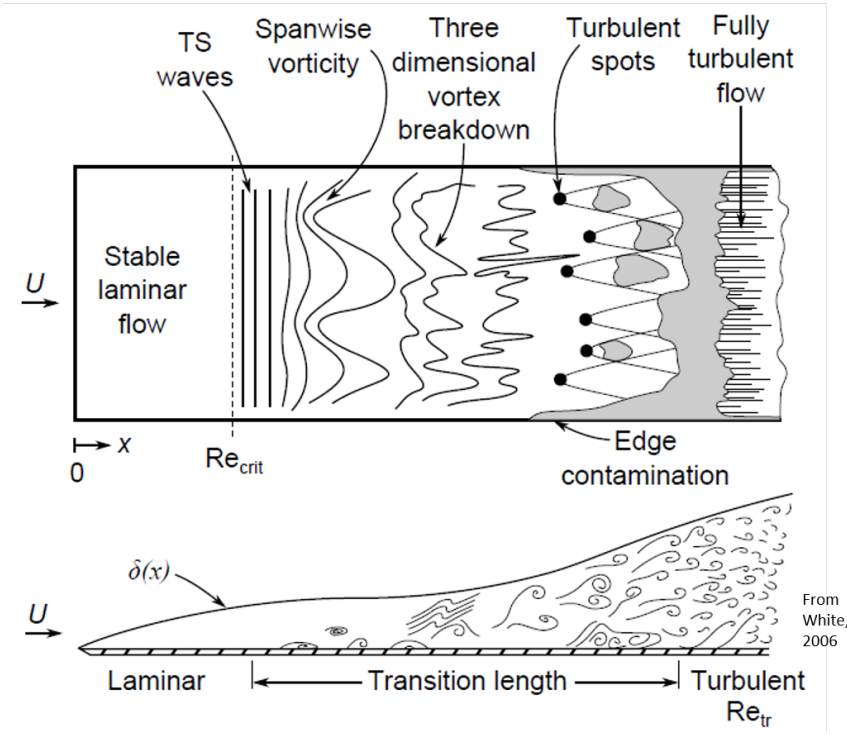
Figure 2.3: Schematic showing mechanisms of transition (modified from [16]). References are: (Reshotko, 2001 [26, 27]), Schmid & Henningson, 2001 [28]), (Suder & O'Brien, 1988 [29])

derived Tollmien-Schlichting waves. The observations were performed in a low freestream disturbance level environment and this allowed the previously held belief (that transition to turbulence occurred purely due to an existing level of noise in the freestream) to be successfully disproved. The method has been extended to compressible flows and is generally accepted as representative of the process provided it is linear. This introduced a new way of examining boundary layer transition, which depended highly on examining the various mechanisms by which transition can occur. A diagram which summarises the paths to transition is shown in Fig. 2.3, modified from the original in [16].

To elaborate on the process in Path a, which is the primary process of interest, we can examine the example of (subsonic) flow over a smooth, flat plate in a low freestream disturbance environment, shown for water flow and as an idealised sketch in Fig. 2.4. This flow exhibits a viscous instability referred to as first mode or Tollmien-Schlichting waves. Other examples where this mechanism of transition is dominant includes subsonic and moderate-supersonic flows over axisymmetric bodies at zero angle of attack and airfoils.



From Werlé, 1980



From White, 2006

Figure 2.4: Visualisation in a water tunnel (top, [30]) and idealised sketch (middle, bottom, [31]) of transition over a flat plate in subsonic flow

The laminar flow establishes from the leading edge of the plate and remains so until the transition location. Beyond this, small perturbations at a particular wavelength are exponentially amplified. These disturbances develop into

3-dimensional wave structures with eddies. Nonlinear interactions occur (secondary instabilities), and their growth is rapid, leading to turbulent spots. These spots coalesce, finally leading to a fully turbulent boundary layer. Within about 3-4 wavelengths of the fundamental Tollmien-Schlichting wave the laminar boundary layer rapidly breaks down [12].

Hypersonic Boundary Layer Transition

With respect to hypersonic boundary layers, new modes are introduced due to the increased complexity of high kinetic energies and enthalpies of the flow. While the basic paths to transition described in Fig. 2.3 are essentially the same for both low and high speed boundary layers, their specific features may be quite different [16]. Examining Path a, which is the excitation of unstable modes, amplification of these modes downstream, and nonlinear breakdown, we see some differences emerge in hypersonic flows when compared to subsonic and supersonic flow regimes. Besides the previously described first mode or Tollmien-Schlichting waves, there are second and higher modes coexisting in the boundary layer [14] [1].

Second Mode Instabilities

Various mechanisms of transition occur but generally for two-dimensional or axisymmetric bodies at zero degree angle of attack in a hypersonic flow the dominant mechanism of transition is the second or Mack [15] mode instability. Using linear stability analysis, Mack found that there exists a higher mode which is more dominant than the first mode instability for high Mach numbers. These are trapped acoustic waves which are reflected between the wall and the sonic line [16]. This is visualised in Fig. 2.5 [32, 33]. Compression waves are indicated by solid lines and expansion waves by dashed lines. The sonic line is the height at which the convective Mach number M_c equals 1, where M_c is:

$$M_c = \frac{c - u(y)}{a(y)} \tag{2.1}$$

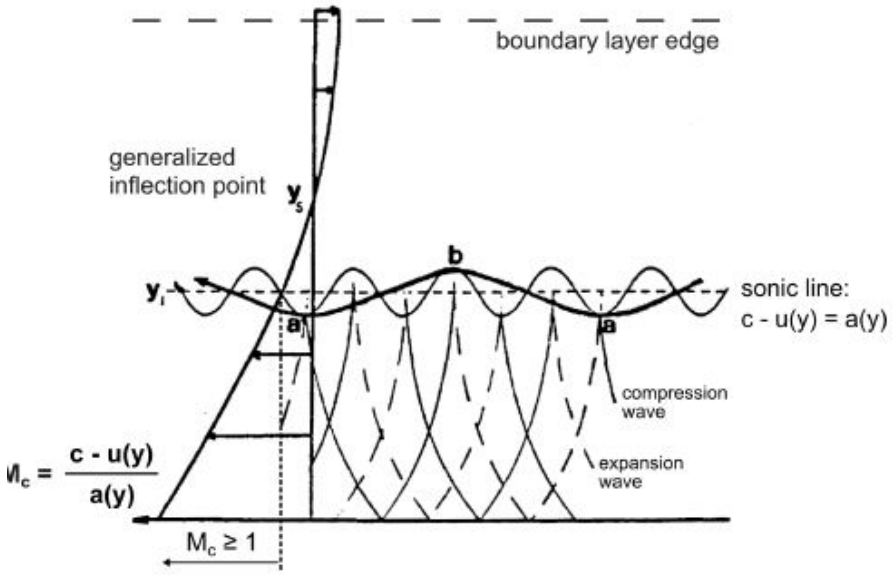


Figure 2.5: Visualisation of the second mode instability waves from [32], originally adapted from [33]

c is the second mode wave speed, u(y) is the velocity at distance y from the wall and a(y) is the speed of sound at that distance [34].

Nonlinear Effects

One of the first indications of nonlinear effects playing an important role in hypersonic boundary layer transition was a study done by Kimmel & Kendall [35], who also presented the first application of a bispectral analysis to this problem. Experiments were conducted on a 7^o half-angle, sharp cone at Mach 8 in AEDC Tunnel B and hot wire data was gathered at various points along the surface of the cone (a detailed description of the experimental set up can be found in Stetson et al.[17]).

The power spectral density results are shown in Fig. 2.6 with the energy peak at 80-120 kHz confidently attributed to the second mode based on Mack's calculations. However, Kimmel also found an unstable frequency band lying above the second mode frequency which was observed but not predicted by linear theory. This was approximately twice the frequency of the second mode. Another discrepancy that

[1]A note on the terminology used here, which follows that originally used by Mack. This is inconsistent with a proper mathematical analysis of normal modes but is commonly used for the interpretation and analysis of experimental data and so will be used here.

was found was that the measured amplification rates through the second mode frequency range were approximately 10-40% below the expectation. Mack [36] and Stetson [37] expressed the belief that nonlinear effects were the cause of unidentified high frequency band. Generally, the consequence of nonlinearity is the generation of harmonic components at frequencies related to the fundamental frequency.

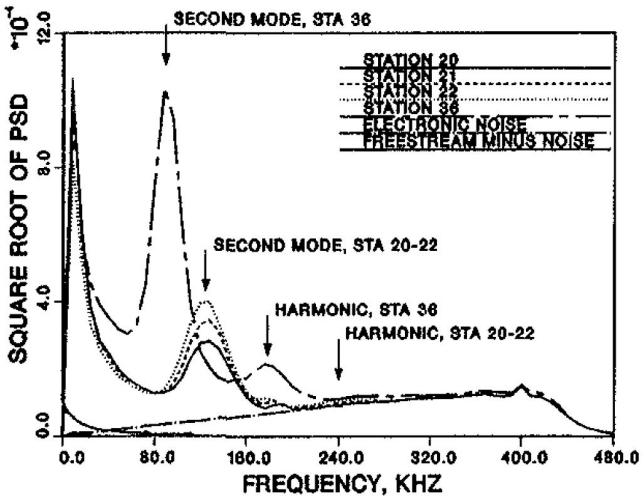


Figure 2.6: Power spectral density results of hot-wire anemometer data from a cone at Mach 8 from Kimmel et al. [35]

There are various approaches to identifying nonlinear effects in second mode instabilities, including some visual indicators from inspection of the waveforms, such as top-to-bottom asymmetry [35]. This is particularly evident in numerical simulations, such as those by Unnikrishnan and Gaitonde [38], which examined the nonlinear evolution of the second mode instabilities compared to the linear case shown in Fig. 2.7. The variations in the rope-shaped structures differ from linear to nonlinear. The nonlinear structures are asymmetric, with the negative variations being more dominant.

Another useful and direct approach first applied by Kimmel et al. [35] is the bicoherence, or bispectral analysis, which gives an indication of any harmonics of the fundamental second mode instability present in the signal. The method as applied in this thesis is described in detail in Section 5.5.2. The bicoherence spectra for each station along the cone is shown in Fig. 2.8. Stations correspond to one inch intervals along the model from station 10 (25.4 cm) to station 37 (95.09 cm).

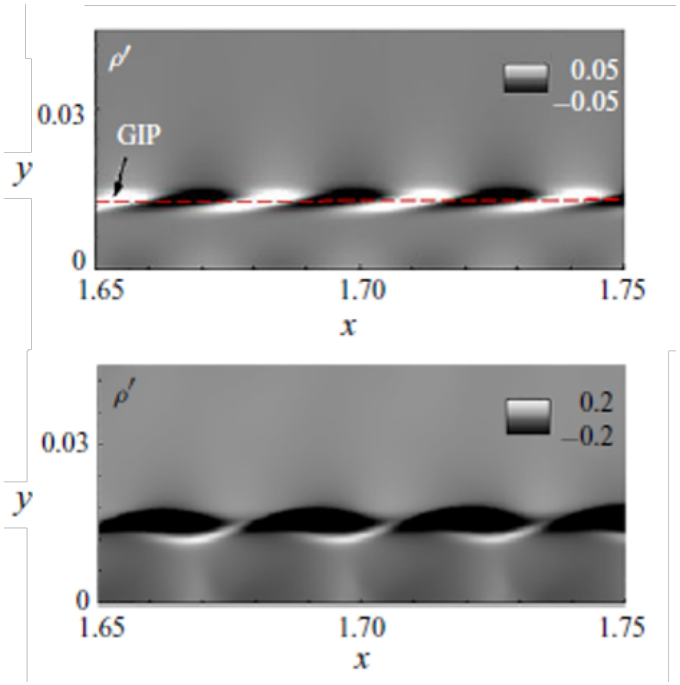


Figure 2.7: Comparison of linear (top) and nonlinear (bottom) disturbance effects on second mode instabilities (from [38]) with the generalised inflection point (GIP) indicated by the dashed red line

At station 20, there is no identifiable high frequency disturbance and the bicoherence is less than 0.1 everywhere. Further downstream, at station 21, a peak appears at 128 kHz and increases monotonically through to station 22. At station 36, the bicoherence at the second mode frequencies reaches a maximum. Four peaks are present. The peak at (88 kHz, 88 kHz) indicates a high level of phase coherence between the second mode and high frequency disturbance, meaning that the high frequency disturbance is a true harmonic of the second mode resulting from self-coupling. At roughly (88 kHz, 180 kHz) there is a broad peak which indicates coupling between the second mode and second harmonic, which contributes to a third harmonic at 268 kHz. Although no discernible peak is visible from the spectrum at 268 kHz, Stetson et al. [17] shows a positive amplification rate near this frequency which is suggestive of the presence of a third harmonic. Additionally, there is coupling between the low frequency component around 8 kHz and frequencies slightly above the second mode and its second harmonic. Some low-level nonlinear coupling is also apparent near 40 kHz - 60 kHz. At these frequencies, bicoherence

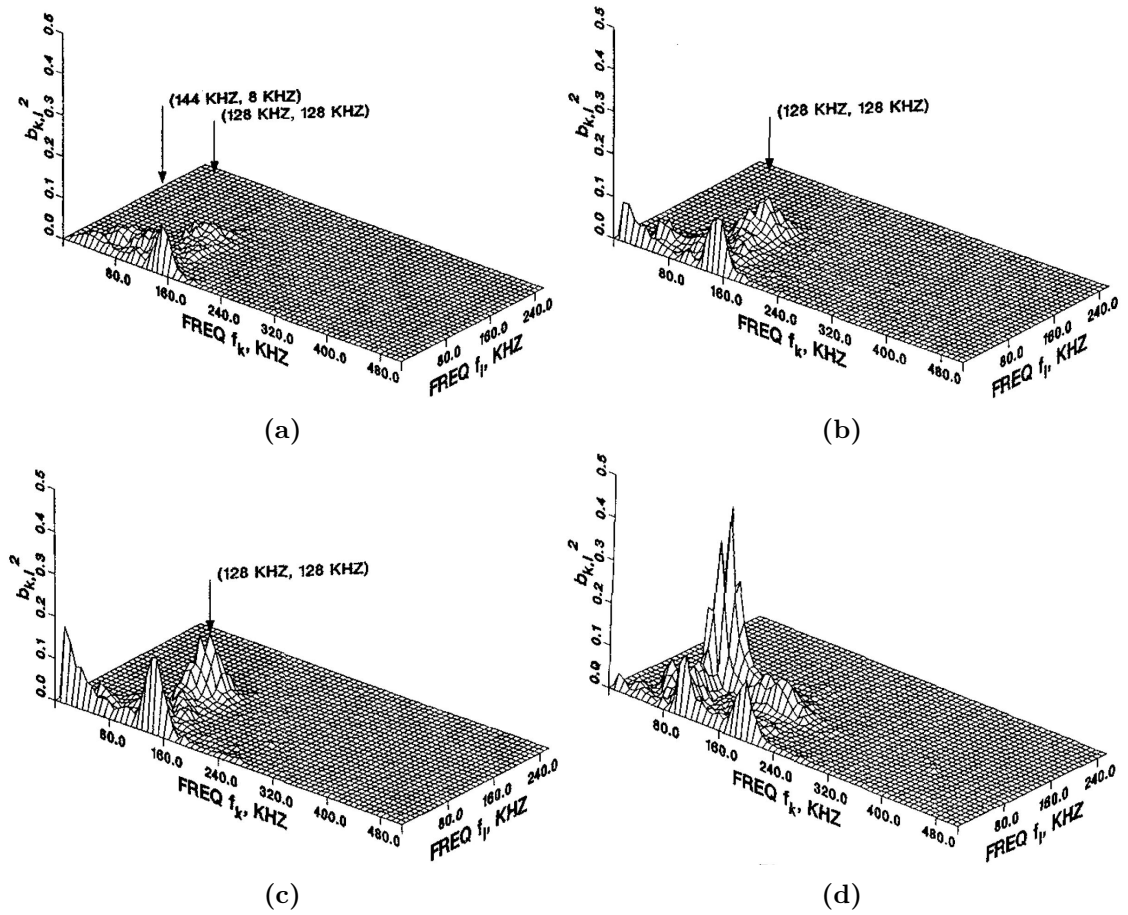


Figure 2.8: Bicoherence spectra where peaks in the bicoherence value $b^2_{k,l}$ indicate the coupling of frequencies, at stations (a) 20, (b) 21, (c) 22 and (d) 36, from Kimmel et al. [35]

could be interpreted as difference interactions, however this is unlikely since the low frequency components remain similar from station to station. It is more likely that these low frequency components modulate frequencies near the second mode and second harmonic and transfer energy to these sidebands [35]. The study by Kimmel et al. provided strong evidence that while linear theory is not invalid, it may have limited applicability to cases of hypersonic flows with high disturbance levels where nonlinear effects are notable.

2.4 Second Mode Instability Results Using Different Measurement Techniques

Various measurement techniques exist to characterise second mode instabilities. Among the more traditional methods are hot-wire anemometers, pressure transducers and heat flux gauges [34]. Recent results from studies using these techniques are summarised in Section 2.4.1. Numerical studies have also sought to simulate hypersonic boundary layers using Direct Numerical Simulations (DNS), such as the work by Unnikrishnan and Gaitonde [38] which was briefly mentioned previously. Finally, recent work using optical diagnostics techniques are presented in Section 2.4.2, with the majority of the section devoted to schlieren methods and results since this is the primary technique of interest. The experiments in this section are focused on a cone with a cold wall in hypersonic conditions where second mode instabilities are expected to be the dominant mode of transition.

2.4.1 Surface Mounted and Probe Measurements

One of the earliest experiments validating Mack's prediction of natural transition through second mode disturbances in a hypersonic cone boundary layer was performed by Kendall in 1975 [39] (first presented as a conference paper in 1974 [40]). Hot-wire anemometers were used to study the origin and growth of so-called "natural" fluctuations over a cone between Mach numbers of 1.6-8.5 and compared with computed amplification rates by Mack, Fig. 2.9. While amplification rates did not agree, the most amplified frequencies at an oblique wave angle of $\psi = 0$ (characteristic of the second mode waves) did, which indicated that the measured disturbances were indeed second mode instabilities.

Further studies using hot wire anemometers ([17, 41, 42], piezoelectric pressure (PCB) transducers and atomic layer thermopiles (ALTP's) ([43–45]) experimentally found further properties:

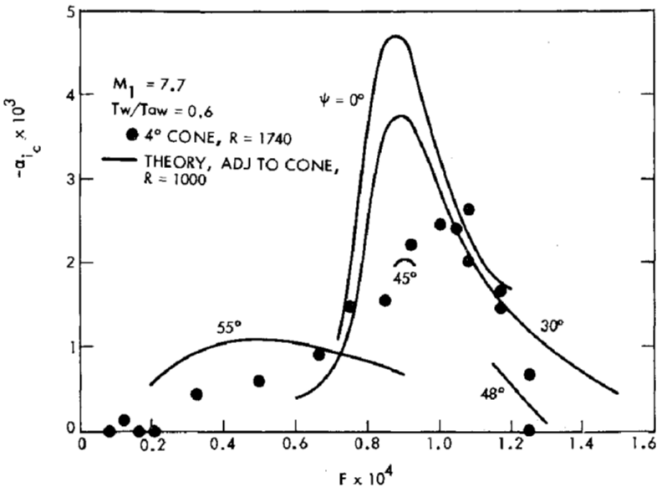


Figure 2.9: Comparison of amplification rates for a cone to Mack computations at M 8.5, from Kendall [39], ψ are values of oblique wave angle

1. The streamwise convection velocity of the disturbances was approximately $0.9U_e$ (U_e being the edge velocity), in some cases $0.8U_e$ [43, 46] and between 0.95-1.0U_e for [41]

2. The wavelengths were approximately 2δ, where δ is the thickness of the boundary layer defined by the location where the velocity reaches $0.99U_e$

3. The density fluctuations (through temperature measurements) are larger than the velocity fluctuations

Considering further results by Kendall Fig. 2.10, some additional observations can be made. For these test conditions, the expected fundamental second mode frequency range is around 70kHz, which is seen as the predominant peak. However, other peaks are observed at higher frequencies (∼140kHz) which are identified as the first harmonics of the fundamental frequency. These results were also observed in a quiet tunnel [47], eliminating the possibility of freestream disturbances causing higher harmonics. The harmonics are not predicted to be dominant by linear theory and thus imply non-linear interaction and growth. This is later seen in some numerical simulations and visualisation results. For lower Reynolds numbers in Fig. 2.10, the boundary layer is thicker and the frequency of the second mode waves is lower, which was dubbed “tuning” by Stetson and Kimmel [48]. Other

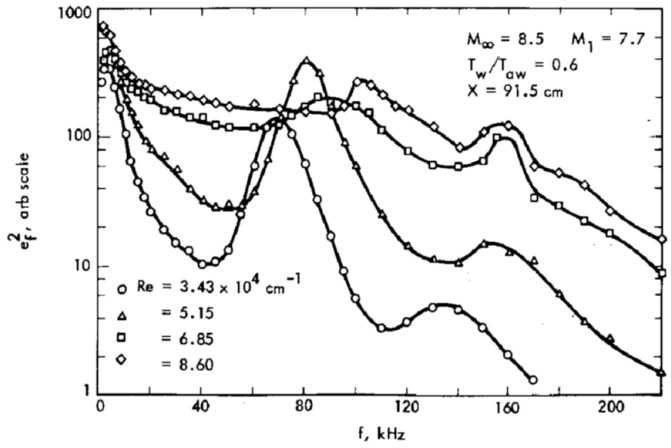


Figure 2.10: Energy spectrum at a fixed streamwise location for different Reynolds numbers, measured at the location of energy peak in the boundary layer [39]

interesting observations were made with these surface measurement and probe results. Kimmel et al. [41] used two hot-film probes to characterise the structure angle, θ, of second mode waves for a cone at Mach 6.8 and various Reynolds numbers, which gives an indication of how the second mode waves evolve into turbulent structures. The structure angle represents the inclination between the line of constant phase and the wall. The second mode structure angle is not constant

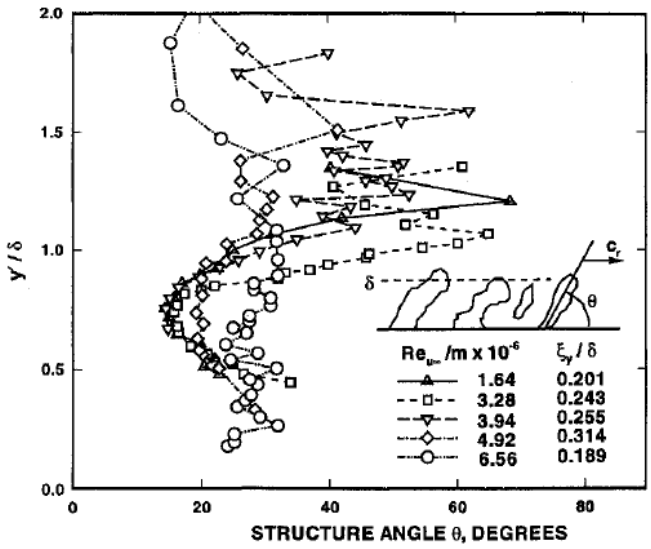


Figure 2.11: Structure angles measured by Kimmel et al. [41]

but increases toward the boundary layer edge (15^o at $\frac{y}{\delta} = 0.7$ to a maximum of 60^o close to the boundary layer).

2.4.2 Optical Diagnostic Techniques

In recent years optical diagnostic techniques have received attention due to their non-intrusive nature and ability to capture data above the surface. Most importantly for this study is the requirement to capture high frequency data ($\sim$ 1MHz) in the harsh testing environment of T6 where traditional sensors are not adequate for a number of reasons. First, they are susceptible to damage from particles following rupture of the diaphragm. The boundary layers are expected to be very thin, less than a millimetre, meaning that the corresponding second mode wavelengths will also be small. The sensing surface of a typical PCB132 sensor is around 3 mm [49] which may be wider than the second mode wavelength. Further, the frequency response of these sensors in the high frequency region (above 500 kHz) is not well understood as the manufacturer calibration for these frequencies has been limited since they were originally designed for shockwave time-of-arrival measurements [50]. Developments toward understanding the use of PCB's for high frequency boundary layer instability measurements have been made by Berridge [51] and more recently Wason [52].

Three main optical based techniques have been used to study second mode instabilities [34], schlieren, schlieren deflectometry and focused laser differential interferometry (FLDI). Included in this are modified schlieren techniques such as Regert and Grossir's [12, 53] development of LIF (Laser Induced Fluorescence) based schlieren in the VKI Longshot wind tunnel, which reduces interference fringes and speckles by using an intermediate flourescent material. Schlieren deflectometry makes use of photo detectors at the image plane instead of a camera (essentially behaving as an ultra-fast, two-pixel camera as in the arrangement of Laurence et al. [54]) and has been used for measurements in long-duration hypersonic tunnels by Vandercreek et al. [55] and Hofferth et al. [56], as well as by Laurence [54] in a harsher shock tunnel environment. Fluctuations in density gradient are recorded, as for a conventional schlieren setup, just with a much higher bandwidth.

Focused laser differential interferometry (FLDI) has been used most notably by Parziale, Shepherd and Hornung ([57–60]) in the T5 hypervelocity shock tunnel

at Caltech to obtain quantitative measurements of density disturbances, including amplification rates. FLDI detects differences in phase due to changes in density between two spatially separated focal regions [58].
Schlieren is primarily used in this thesis and will be discussed in depth in the sections which follow.

High Speed Schlieren for Second Mode Instabilities

Early measurements by Demetriades [61] indicate that the velocity variations within second mode waves are barely measurable, while density variations through fluctuations in temperature are about 25% (seen in Fig. 2.12). This makes schlieren and shadowgraph optical techniques particularly suitable as they are based on light refraction due to density gradients.

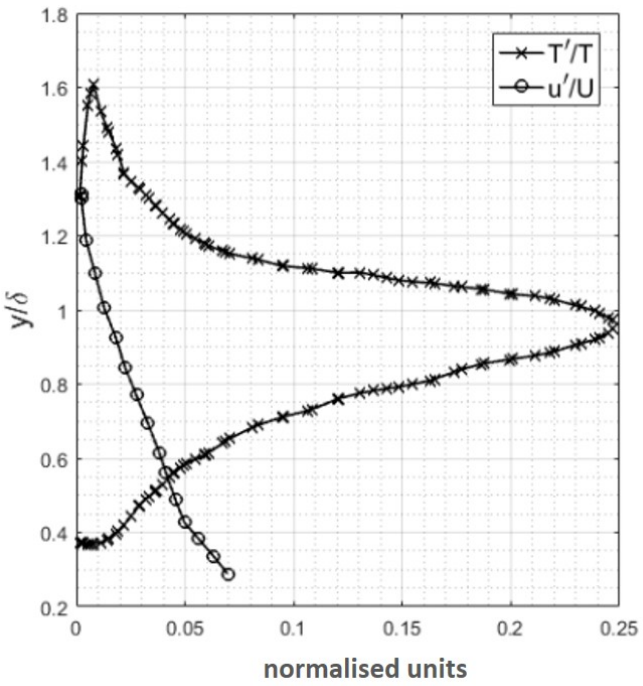


Figure 2.12: Typical variation of velocity and temperature fluctuations at late stage second mode wave development normal to the surface of a sharp cone, in [34], adapted from [42]

An overview of schlieren techniques is given here, for an in-depth review see for example Settles [62]. Fig. 2.13 (a) shows a classical schlieren setup first used by Toepler [63]. Light from a small source LS is collimated by lens L1 and focused by

lens L2, then the beam is captured by the camera C. A sharp knife-edge KE is put at the focus point. A refractive disturbance RD causes some light rays to be refracted upwards (dashed lines) which avoid the knife edge and proceed to the camera, while rays refracting downward (solid lines) are blocked. Thus the disturbance RD is captured as a gray-scale amplitude image. The lens diameter determines the field

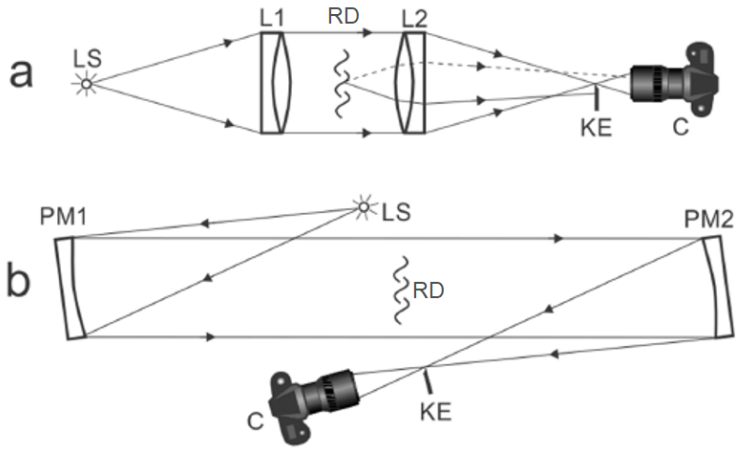


Figure 2.13: Two types of schlieren systems (a) Toepler's lens-type schlieren system and (b) z-type schlieren system using twin parabolic mirrors [64]

of view - for diameters greater than about 15 cm [64], parabolic telescope mirrors PM1 and PM2, ranging in diameter from a few cm to more than 1 m, are used to fold the optical path. This is the most common type of schlieren setup.

Results from High Speed Schlieren Visualisation

Using visualisation techniques have some distinct advantages over traditional measurements. They are non-intrusive and can be used in high enthalpy conditions where devices like hot wire anemometers could be damaged [34] in the harsh testing environment. They are also not restricted to taking surface measurements only since a large amount of information at various heights in the boundary layer and streamwise locations can be obtained from a single image, unlike PCB and heat flux sensors. Early researchers were able to capture single images of schlieren and shadowgraph photographs of the rope-like structures ([42, 65–67]. Potter and Whitfield first observed these waves from shadowgraph images and reported

that "long distances of quite regular rope- or chain-like laminar or incipiently transitional flow pattern frequently preceded what was considered to be boundary-layer transition" [65]. These were only later identified as second mode instabilities by Smith [67] due to their observed wavelength being approximately twice the boundary layer thickness.

Laurence et al. applied image processing techniques to extract quantitative information from schlieren images, including the wavelength and velocity of second mode wave packets [54, 68, 69]. For a 7^o half-angle cone model with a blunted nose tip radius of 5 mm at a total enthalpy of 3.4 MJ/kg and unit Reynolds number of $6.2\text{x}10^6$/m, second mode wavepackets were visualised by Laurence et al. for a 60 mm segment of the cone, shown in Fig. 2.14.

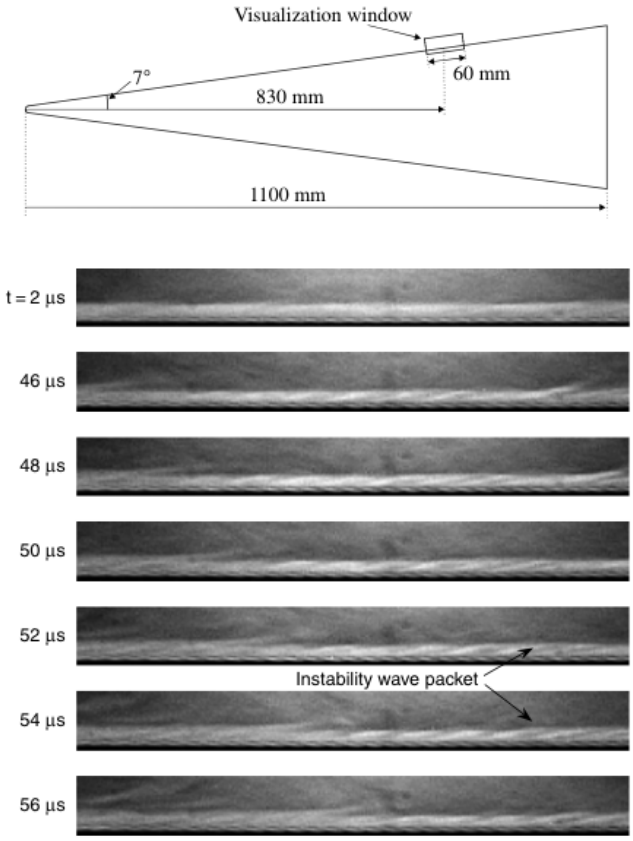


Figure 2.14: Schematic of the cone model (top) and second mode instability wavepackets within the boundary layer (bottom) from Laurence et al. [68]

Note that in the schlieren images, the regular structures occurring in the pixels immediately above the cone surface are non-physical artefacts (diffraction halos

around the model which occur in high knife-edge cut-offs when there is an opaque edge in the test area parallel to the knife-edge, described in detail in [62]). The normalised pixel intensities along a single row corresponding to $\frac{y}{\delta} = 0.5$ are plotted in the form of an x-t diagram in Section 2.4.2. Power spectra of the pixel intensities along individual rows above the cone surface were obtained and is shown in Fig. 2.15, at a single time instance. The expected peak in power spectrum near $\frac{\delta}{y} = 0.5$ are clearly present and the amplitude reaches a maximum near $\frac{y}{\delta} = 0.5$ before tapering off towards the boundary-layer edge. The weaker peaks at longer wavelengths are likely from low-frequency disturbances from tunnel noise (as these were also seen in the laminar spectra) or non-uniform illumination. Wavepacket propagation speed was determined from two-dimensional cross-correlation between images. Wave structure angle (the inclination of the lines of constant phase in the x-y plane) was also obtained by one-dimensional spatial correlations between neighbouring rows of a single image [68]. This showed the first possibilities of deriving structural and propagation characteristics of second mode instabilities from high-speed schlieren imaging.

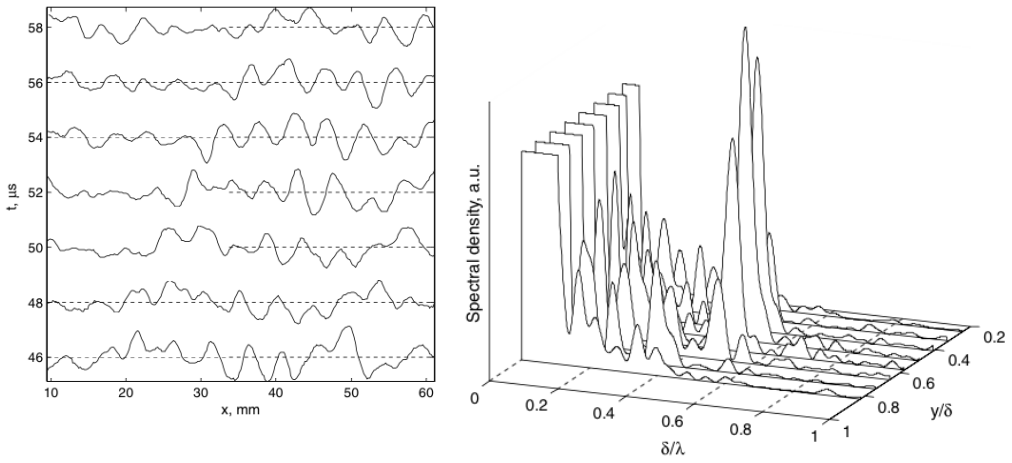


Figure 2.15: x-t diagram showing the normalised pixel intensities and development of instability waves (left) and energy spectral density as a function of normalised inverse wavelength for various heights in the boundary layer at $t = 54\mu s$ (right) [68]

Butler & Laurence [70, 71] applied the SPOD (spectral proper orthogonal decomposition) method of Towne et al. [72] to 5^o half-angle cone models with compression and expansion corners at Mach 6 and unit Reynolds numbers ranging

from 3-5.3 (10^6/m). Some results are selected for discussion and the processed schlieren images are shown in Fig. 2.16. The power spectral density (PSD), which describes the power of a signal in terms of it's frequency components and the SPOD results are shown in Fig. 2.17.

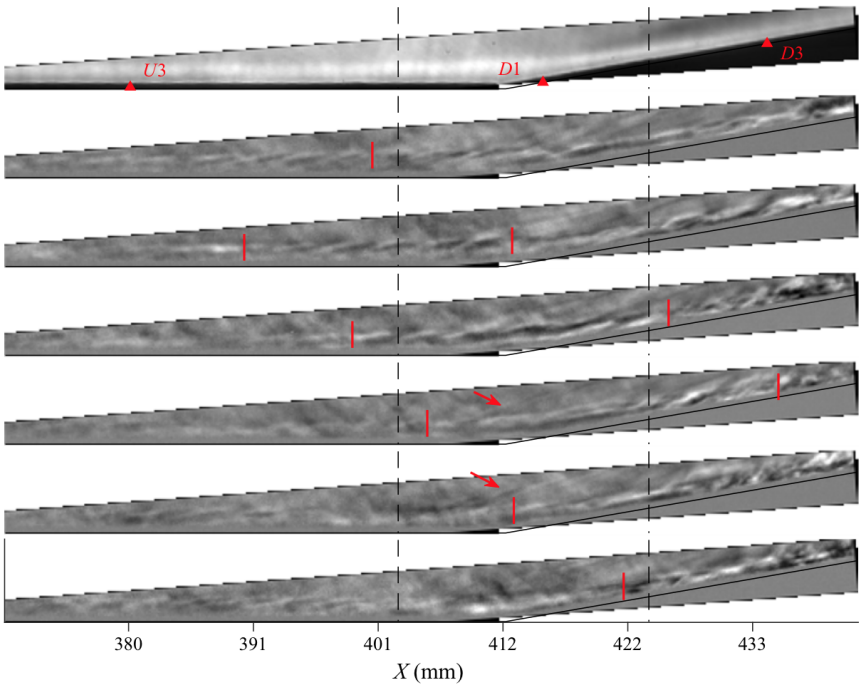


Figure 2.16: Processed schlieren images over a cone with compression corner at Mach 6, unit Reynolds number of 4.94-5.31(10^6)/m, total specific enthalpy approximately 0.89 MJ/kg [70]

The transition to turbulence for this condition is apparent from the schlieren images and spatial PSD contours. High frequency content (integrated between 225-325 kHz) grows steadily before decaying downstream of the separation from X = 403-413 mm. The flow reattaches, and the high frequency content amplifies and spreads rapidly off-wall. At lower frequencies similar behaviour is seen, from the PSD integrated over 80-110 kHz, with little distinct shear-generated instabilities. Considering the SPOD results in Fig. 2.17, bottom, a set of orthogonal modes which oscillate at distinct frequencies may be identified. The highest-ranked modes which represent the greatest energy content are shown. The upper mode shape at 289 kHz shows that second mode content is well resolved upstream of the corner, dispersing upon separation before amplifying at reattachment with the energy extending well

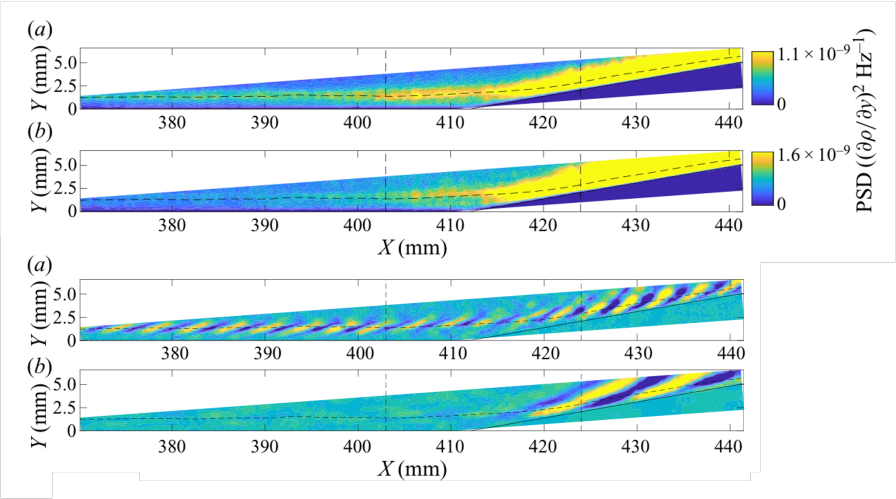


Figure 2.17: Average PSD at the unit Reynolds number 4.94-5.31(10^6) condition (top) for a frequency range of (a) 225-325 kHz and (b) 80-110 kHz. SPOD mode shapes (bottom) at (a) 289 kHz and (b) 90 kHz [70]

away from the surface. The low frequency content (90 kHz) displays no evidence of shear-generated instabilities but shows strong growth at reattachment. These results demonstrated the use of SPOD to confirm the structure and growth of both low and high frequency content.

Butler & Laurence also applied both SPOD and bispectral analysis methods to a similar cone geometry with an abrupt expansion instead of compression. Results from the same test condition as reported for the compression corner experiments are selected.

Schlieren is suitable for detecting harmonics of the fundamental frequency but as Butler & Laurence [71] point out, the subharmonic frequencies indicating the interaction between first and second mode disturbances should not be interpreted from schlieren data because as an integrated line-of-sight technique, oblique modes are not well represented.

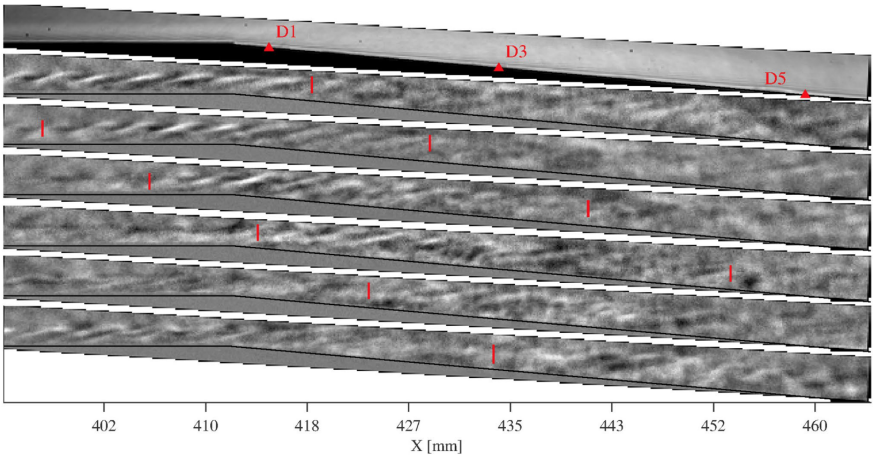


Figure 2.18: Processed schlieren images over a cone with expansion corner at Mach 5.95, unit Reynolds number of $5.31(10^6)$/m, total specific enthalpy approximately 0.89 MJ/kg [71]. Images are 10.7μs apart

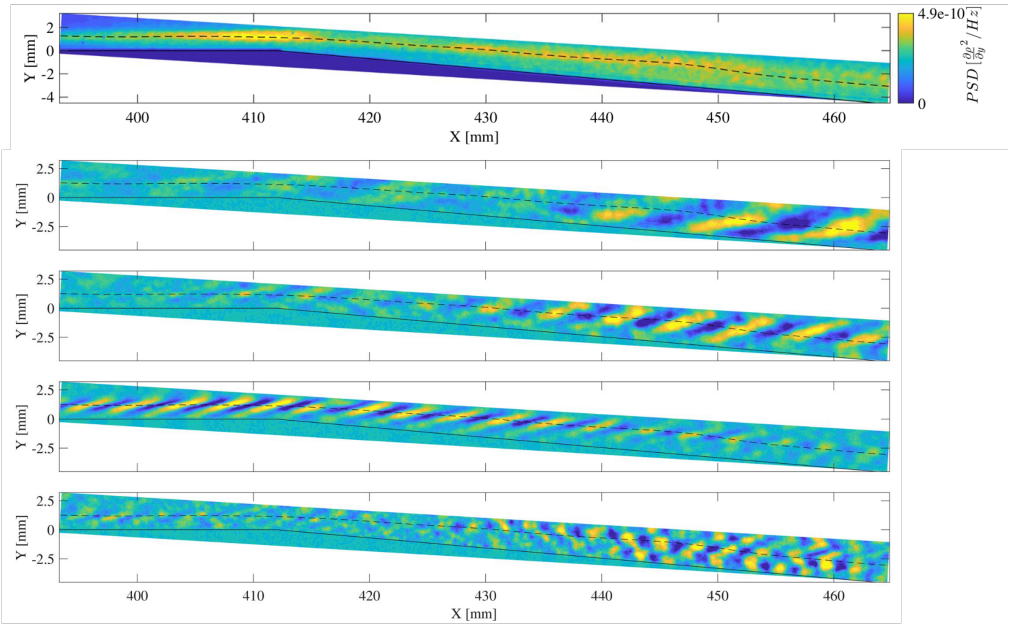


Figure 2.19: Spatial distribution of second-mode fundamental PSD (top panel). SPOD mode shapes (bottom 4 panels) at 117 kHz, 204 kHz, 274 kHz and 344 kHz [71]

2.5 Transition Mechanisms on Blunt Geometries and Entropy Layer Effects

One notable effect particular to hypersonic flows over a vehicle is the significant entropy layer. Shock waves in hypersonic flows are extremely strong, beginning at the nose of a blunt body, or at the attachment point over a sharp wedge and decreasing in strength further away from this point downstream. Since the entropy

increases across a shock, and this increase is greater the stronger the shock is, an entropy gradient tends to build and flow over the surface of the body much like a boundary layer. By Crocco's theorem, an entropy gradient results in strong vorticity which may interact with the actual boundary layer [12, 73].

Nose tip bluntness has the effect of introducing a bow shock at the front of the vehicle. This is normal at the nose tip and curves further downstream. An image of this captured on a 7^o half-angle cone at approximately Mach 7 in the Oxford High Density Tunnel is shown in Fig. 2.20.

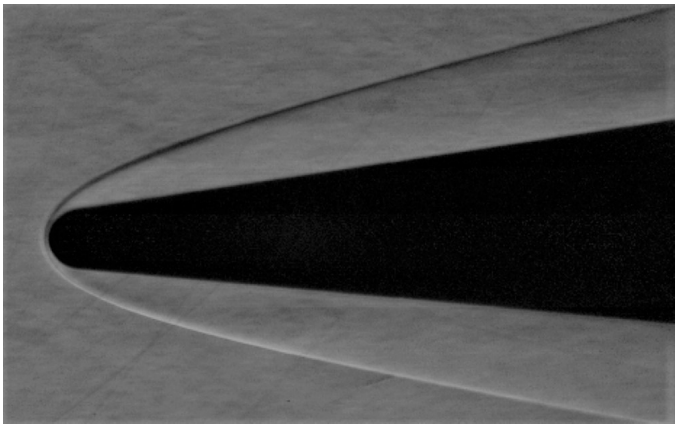


Figure 2.20: Schlieren image of a bow shock over a blunt cone, from experiments performed in the Oxford High Density tunnel on a 7^o cone at Mach 7

As a consequence of this, each adjacent streamline will experience a different entropy rise. This results in an entropy layer over the body which significantly influences the boundary layer edge properties. The distance from the nose tip at which entropy layer effects are no longer significant at the edge of the boundary layer is called the entropy layer swallowing distance, X_{SW}. Theoretical swallowing distances for various conical geometries and freestream Mach numbers are given by Rotta [74], shown in Fig. 2.21.

For any Mach number and selected conical geometries, the entropy swallowing distance may be determined using Fig. 2.21 and the dimensional parameter is given by:

$$\frac{X_{SW}}{(Re_{unit,\infty})^{1/3}(R_N)^{4/3}} \tag{2.2}$$

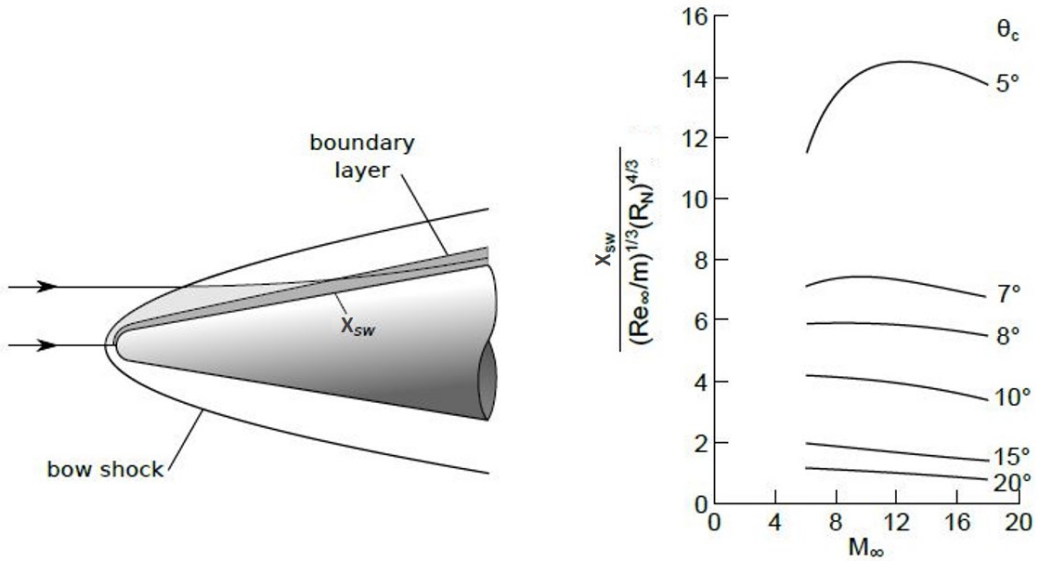


Figure 2.21: Schematic illustrating entropy swallowing distance (left) and swallowing distance parameter (right), from [12] (originally [17] and [74])

where R_N is the Reynolds number based on nose tip radius. For sharp, slender geometries boundary layer transition can usually be attributed to the amplification of hydrodynamic instabilities such as first or second mode waves, stationary and travelling crossflow instabilities and centrifugal instabilities (Görtler vortices). For blunt bodies however, the growth of modal instability waves is not supported. First mode instabilities are stable because of the strong favourable pressure gradient and edge Mach number values are too low to support second mode disturbances. The convex curvature also prevents amplification of Görtler vortices, while crossflow velocities remain small [75]. The mechanisms for transition over blunt geometries remain not as well understood. This is partly due to the difficulties in generating freestream conditions capable of causing transition on blunt geometries [76]. Stetson [77] performed experiments at Mach 6 with an 8^o half-angle cone using surface-mounted thermocouples and pressure sensors to measure the transition location. The model used nose tips varying from sharp to 15 mm radius. The results showed that as the nose tip radius increased, the transition location shifted downstream up to a sufficiently high nose tip bluntness, at which point the onset of transition moved upstream. This process is termed "transition reversal". These results were simulated by Jewell & Kimmel [78] using the STABL (Stability and Transition for

hypersonic Boundary Layers) CFD software suite. They showed that increasing nose tip bluntness and entropy-swallowing length resulted in a monotonic damping of the amplification (N factors) associated with second-mode instabilities, which is consistent with the observation of transition onset being displaced downstream up to a critical range of values. Similar suppression of second-mode growth was shown by Marineau et al. [79] and Maslov et al. [80] in cases where the entropy swallowing length was downstream of the transition onset location. While linear modal stability analysis predicts that the boundary layer continues to become more stable with increasing nose bluntness, experiments indicate the transition reversal process, where further downstream movement in transition actually slows and eventually reverses.

Since linear modal stability theory is not able to predict the experimentally observed behaviour for blunt cones, a potential explanation could be found in non-modal stability theory. Non-modal, or transient, growth means that disturbances can experience locally high amplification while overall being asymptotically stable. Paredes et al. [18] found that disturbances within the nose tip vicinity undergo a non-modal amplification which increased with increasing nose tip bluntness. These features were significantly amplified while first mode, second mode and entropy-layer modal instability amplification was marginal. Unlike second mode waves which appear as rope-like structures with peak disturbance magnitudes within the boundary layer, planar and oblique waves experiencing non-modal growth have a peak in disturbance magnitude between the entropy layer and boundary layer edges [19]. Using laser-induced fluorescence-based schlieren on a 7^o half-angle blunt cone at Mach 11.8, Grossir et al. [20] visualised these elongated structures which extended out beyond the boundary layer edge (Fig. 2.22). This is in agreement with the hot-wire measurements on a blunt cone reported by Stetson, where large fluctuations were recorded outside of the boundary layer at locations away from the nose tip [81] and attributed to inviscid instabilities growing within the entropy layer induced by the bow shock over the blunt nose tip.

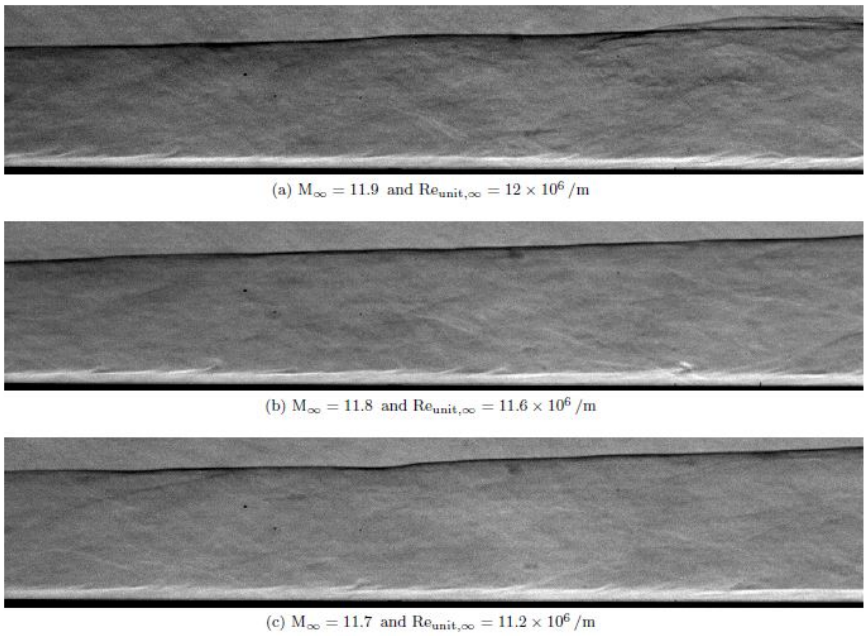


Figure 2.22: Elongated structures extending beyond the boundary layer, visualised by Grossir et al. using LIF based schlieren on a 4.75 mm nose tip radius cone at Mach 11.7-11.9 [20]

Recent experiments were performed by Kennedy et al. [76] on a 7^o half angle cone in Mach 6 flow with interchangeable nose tips of varying bluntness from sharp to 5.08 mm radius. It was found that for nose tips below a radius of 2.54 mm, second mode instabilities were the dominant transition mechanism but this was not so for nose tips above that radius. For these, second mode waves were no longer visible within the boundary layer and instead features which were elongated and steeply inclined developed between the edges of the boundary layer and entropy layer. Schlieren visualisation was used to capture these features, along with surface pressure measurements which revealed high-frequency oscillations associated with the trailing edge of these instabilities.

2.6 Summary

A review of the relevant literature on boundary layer transition and the mechanisms of transition for general and hypersonic boundary layers has been described here. Measurement techniques, with an emphasis on schlieren image processing techniques has been covered and recent work in the field has shown that useful data can be

extracted. While significant progress has been made, there is little data available for very thin boundary layers, where second mode instability frequencies may exceed the capability of traditional pressure transducers, and for cases where non-modal instabilities are present. This is in part due to the difficulty of establishing adequate conditions for these instabilities to form. These conditions can be established in the Oxford T6 Stalker Tunnel, but first requires commissioning in reflected shock tunnel mode, which is one of the major contributions of this thesis. Schlieren image processing techniques have been applied by some researchers, but the methods do not remain widely used, despite the advantage of being non-intrusive. Additionally, camera technology has significantly progressed and the use of cameras with higher frame rate and resolutions may provide a wealth of information in harsh flows for which traditional sensors would be damaged or not reliable. Current and new schlieren image processing techniques will be developed and applied to a dataset collected from the Oxford High Density Tunnel in order to test these techniques at first use which also provides useful data on second mode instabilities. This forms a guide in which methods are reviewed and outlined, along with an investigation on the effect of certain camera parameters, which is the second major contribution. Finally, the test conditions commissioned in T6, together with the image processing techniques developed and tested in HDT will come together to uncover information on the boundary layer transition mechanisms present under the harsh testing environment of the T6 tunnel, where traditional sensors are not viable.

Part II: Hypersonic Testing Facilities and Reflected Shock Tunnel Commissioning

2.7 Introduction

Wind tunnel testing has existed for the investigation of air flow over solid bodies since the 19th century, first credited to Frank H. Wenham (1824-1908), a Council Member of the Aeronautical Society of Great Britain [82]. Early experimental work on boundary layer transition specifically for aircraft design has taken place as early as the 1930's [83]. These facilities are of key importance and allow for the replication of flight conditions where in situ measurements from flight tests are infeasible due to the high costs and complexity involved.

For hypersonic testing, major effort has been devoted to the study of various key phenomena such as boundary layer transition, gas-surface interaction and flow radiation [84] and ground testing facilities are a crucial step in the process of understanding these effects, particularly as the environment can be better controlled and a broader range of measurement techniques can be used. A review of the different types of ground testing facilities, as well as the particular hypersonic facilities existing at Oxford is given here. Details and differences of both facilities (the High Density Tunnel and the T6 Stalker Tunnel) are explored, with a focus on the T6 Stalker Tunnel as this facility was first commissioned in a mode of operation suitable for boundary layer experiments and scaled model testing by the author.

Certain parameters need to be matched in order for flight representative results to be obtained. The main parameters and their represented effects are

- Viscous Effects

  Unit Reynolds number: $Re_{u,\infty} = \dfrac{\rho_\infty u_\infty}{\mu_\infty}$

- Compressibility Effects
  Mach number: $M_\infty = \frac{u_\infty}{a_\infty}$
- Thermodynamic Effects
  Total enthalpy: $H_0 = H_\infty + \frac{u_\infty^2}{2}$
- Binary Scaling Law (this states that flows with the same gas composition, free-stream enthalpy and product of density and length scale are characterised by the same binary chemistry, non-equilibrium processes and diffusive transport over proportional length scales [85, 86])
  Binary scaling parameter: ρL

2.7.1 Types of Hypersonic Test Facilities

A brief introduction to selected types of hypersonic facilities and their basic operation is given here, for further details on a wider variety of facility types see for example Chazot et al. [84].

Blowdown facilities are composed of a plenum holding a reservoir of constant stagnation pressure test gas, often heated. The test gas is then released and expanded through a contoured nozzle. A regulator valve coordinates the pressure equilibrium. Typical flow times range from a few seconds to a few minutes. The Oxford High Density Tunnel belongs to this class of facility and is further explored in later sections.

Shock tubes, along with the remaining facilities outlined here and the Oxford T6 Stalker Tunnel, belong to a class known as impulse or pulse facilities. The basic setup consists of two tubes filled with two different gases, separated by a diaphragm which is a partition typically made of steel or aluminium which can rupture at a certain pressure. The first tube, known as the "driver tube" typically contains a light gas, such as helium, held at a high pressure. The second tube, or "driven tube" contains the test gas at much lower pressure. Increasing the pressure in the driver tube leads to the diaphragm bursting which initiates a shock wave. The shock wave propagates through the low pressure gas in the driven tube and oppositely,

expansion waves propagate back through the high pressure region. The post-shock conditions of the travelling shock wave are observed at the tube exit. Expansion tunnels are similar to shock tubes with the exception that an acceleration section is added, which is an additional region of very low pressure gas separated by two diaphragms. This allows for an unsteady expansion of the test gas. If a nozzle is added to the end of this then it is known as an expansion tunnel. These facilities offer the highest flow velocities but the shortest test time.

Reflected shock tunnels are similar to shock tubes but with the addition of a divergent (non-reflected shock tunnel) or convergent-divergent nozzle (reflected shock tunnel) at the end in order to increase the Mach number and improve performance. In a reflected shock tunnel stagnated gas is generated when the shock reflects off a boundary at the end of the driven tube and this is used to generate high pressure and temperature conditions. The downside is short duration test times, on the order of milliseconds. This process is further explored in detail with respect to the T6 Stalker Tunnel in Reflected Shock Tunnel (RST) mode in Section 4.2.

To reach even higher enthalpies and flow velocities, a free piston can be used to compress the driver gas in a rapid quasi-isentropic compression, with the advantage of a compact driver configuration and minimised contamination from heaters [84]. This method was pioneered by Stalker in the early sixties [87–89]. A schematic of the original T3 free piston driven shock tunnel is shown in Fig. 2.23, from [90].

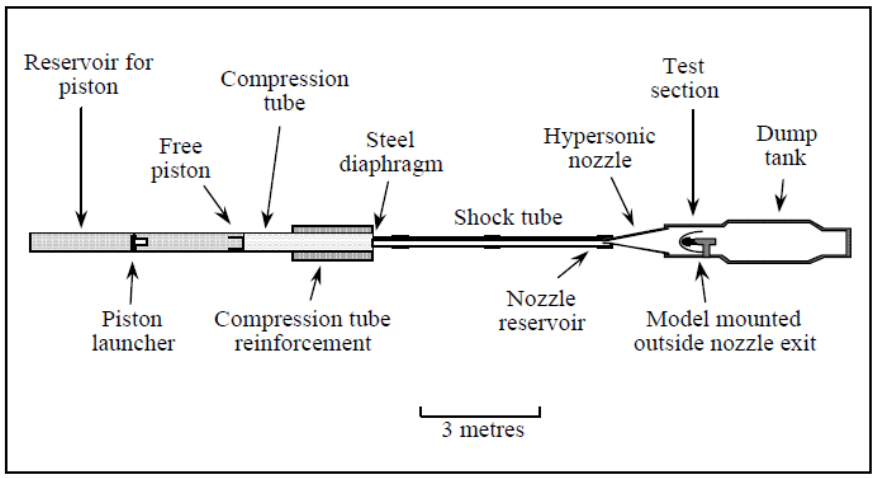


Figure 2.23: Schematic of original T3 free piston shock tunnel, from [90]

RST facilities operate worldwide for example T6 (Oxford) [91, 92], T5 (Caltech) [93], T4 and X3R (University of Queensland) [94, 95], HELM (Bundeswehr University) [96, 97], HEG (DLR Göttingen) [98] and HIEST (JAXA Kakuda) [99, 100]. For a comparison of such facilities, see [84, 90].

2.8 Hypersonic Facilities at the University of Oxford

Particulars of the main hypersonic facilities (High Density Tunnel or HDT and T6 Stalker Tunnel) at the University of Oxford are described here as this thesis involves experiments which were performed in both facilities. More detail is included for the Oxford T6 Stalker Tunnel as this was commissioned in the reflected shock tunnel mode of operation by the author [91]. This work has also been included in [92].

2.8.1 Oxford High Density Tunnel

The HDT or High Density Tunnel was originally developed by RAE, UK, in the 1960's and acquired by the University of Oxford in 2012. It was originally operated as a cold hydrogen driven shock tube and tunnel [101] before being refurbished as a cold hypersonic aerodynamic facility [102], shown in Fig. 2.24. It is operated as a type of blowdown tunnel called a Ludwieg tube or Light Isentropic Compression heating (LICH) tunnel with relatively long duration flows at high Reynolds number. The test gas is heated electrically to increase the total temperature to a maximum of 573 K in order to keep it just above liquefaction after expansion through the nozzle. It provides a low-disturbance ("quiet") flow environment by having a high pressure source of test gas so that a clean flow with minimal perturbations can be produced. Higher Mach numbers can be achieved with the addition of a light piston compression stroke in the process (LICH tunnel), however, this introduces further flow disturbances. It can operate over a range of Mach numbers from 3-7, unit Reynolds numbers of 7-53 x $10^6/m$ and wall to total temperature ratios of 0.56-1 with test durations up to 70 ms [103]. HDT has a 17.4 m long steel barrel with internal diameter of 152.4 mm. A bespoke fast-acting plug valve assembly separates

this barrel from a converging-diverging nozzle. The valve is operated by venting a high pressure source of air from behind the plug which allows the test gas to push the plug open and pass through radial cut-outs. The test gas then expands through the nozzle and exhausts into the test section and then a 28 m^3 vacuum tank.

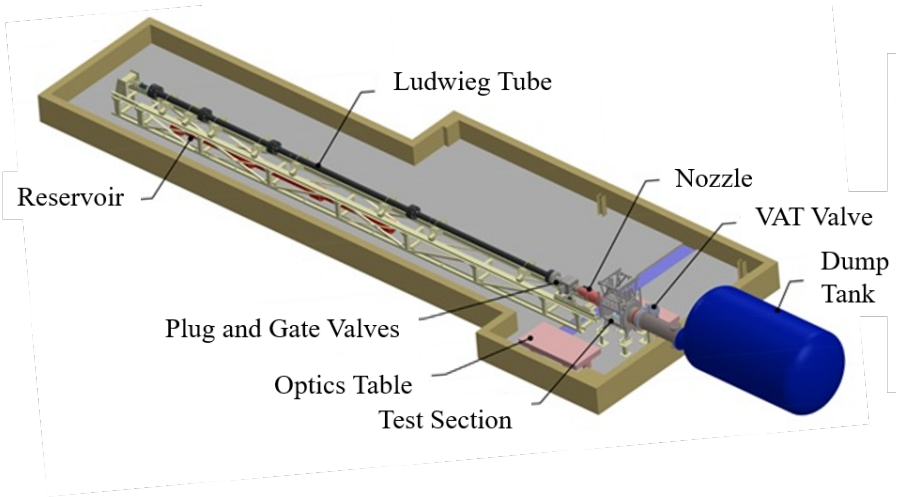


Figure 2.24: Schematic of Oxford High Density Tunnel [102]

Successive expansion waves propagate into the high pressure region when the plug valve opens. The test time is therefore steady until the expansion waves reflect off the far end of the tube and pass through the nozzle again. This results in multiple quasi-steady periods of flow, referred to as "plateaus" between expansion processes. This allows for a sweep of conditions in a single shot [103].

2.8.2 Oxford T6 Stalker Tunnel

T6 is a free piston driven, high total pressure and high total enthalpy facility. It is a combination of the driver section of the T3 tunnel and the driven section (shock tube, nozzles and test section) of the Oxford Gun Tunnel. It features an interchangeable tertiary barrel section which allows for operation in three different modes, each with a distinct purpose and inherent differences in test times, flow speed, thermochemistry similitude and ability to explore fundamental flow physics. These three fundamental modes are reflected shock tunnel, expansion tunnel and shock tube mode. The tunnel features a reservoir with 2.1 m^3 volume and a

compression tube which is 6 m long and has an internal diameter of 300 mm from the original T3 tunnel. The T3 tunnel had a 7.7 m long shock tube with an internal diameter of 76.2 mm. The shock tube of T6 comprises of two driven sections with a total length of 7.1 m and an internal diameter of 96.3 mm but features an orifice of diameter 76.2 mm between the compression and driven tubes to limit the rate of gas exhausting through the diaphragm at rupture. Before firing, the piston is seated on the launcher and the rear of the piston is evacuated, while high pressure reservoir gas is filled behind it and lower pressure driver gas in front. The reservoir gas is prevented from entering the cavity or the compression tube by two d-ring seals. To release the piston, pressure is applied to the cavity allowing the piston to move forward and the reservoir gas to rapidly enter the compression tube behind the piston. The driver and driven sections are separated by a primary diaphragm, typically a steel or aluminium plate, which is ruptured when the piston compresses the gas to a sufficiently high pressure against the primary diaphragm. The compressed gas drives a shock down the driven or shock tubes.

A brief description of the modes of operation is provided here, along with a figurative comparison in Fig. 2.25.

Shock Tube Mode

Here the driver gas is compressed against the primary diaphragm which ruptures and sends a shock wave through the shock tube and into the test section.

Expansion Tube Mode

When the facility operates as an expansion tube, the gas is once again shock heated when the driver gas is compressed against the primary diaphragm, creating an incident and weak reflected shock in the shock tube section. The flow then undergoes an unsteady expansion through the acceleration tube and may further undergo a steady expansion through a nozzle before entering the test section.

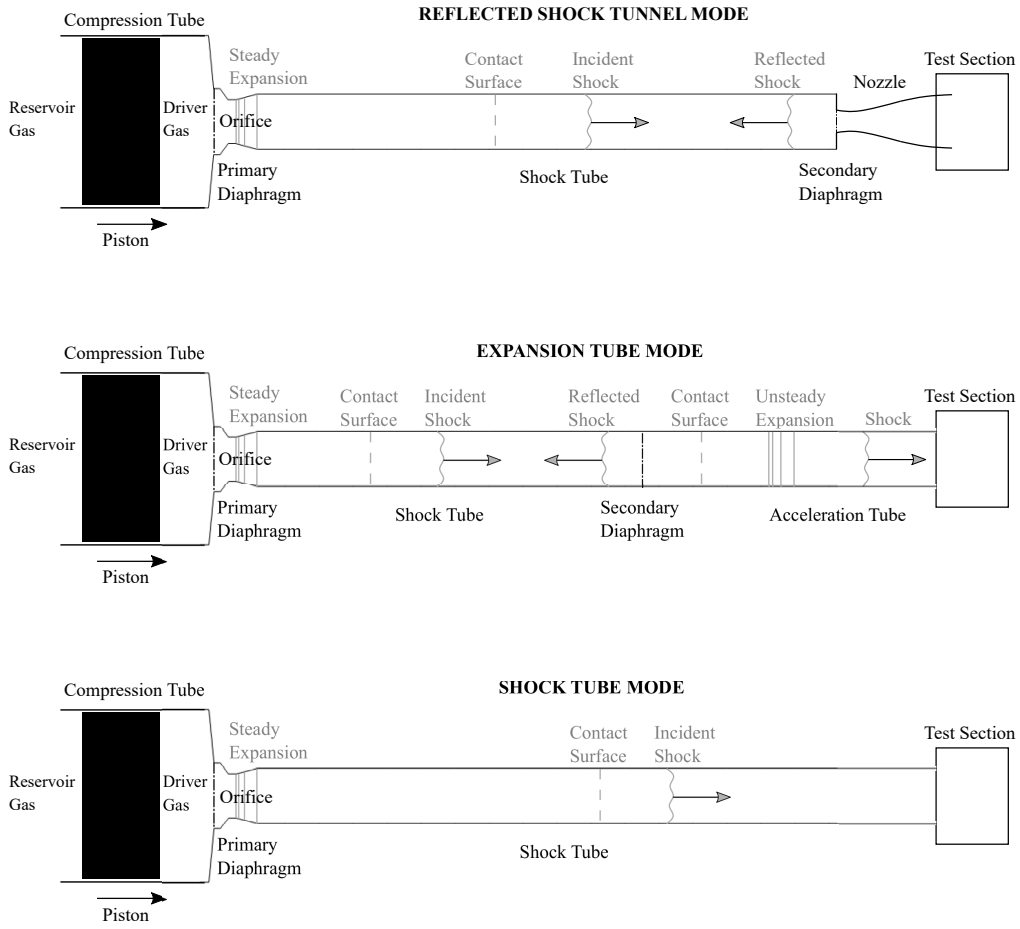


Figure 2.25: T6 facility mode comparison

Reflected Shock Tunnel Mode

Reflected Shock Tunnel (RST) mode allows for development of high total enthalpy and total pressure conditions by compressing the driver gas against the primary diaphragm which ruptures, sending an incident shock through the shock tube section. The gas is shock heated through stagnation after the reflected shock. The stagnated flow is then expanded through the nozzle and into the test section. The driver gas follows, with the boundary between the driver gas (usually Helium/Argon or Nitrogen/Argon) and the test gas (usually air) known as the contact surface.

This thesis will focus on the condition development and commissioning of the facility in reflected shock tunnel (RST) mode, which is shown in Fig. 2.26. In a free-piston driven shock tunnel facility, the piston is driven forward to compress

the driver gas, typically a helium/argon mixture which then ruptures the primary diaphragm. This sends a shock through the test gas, which is stagnated through a reflected shock process. The compressed test gas supplies a steady expansion through the nozzle and into the test section.

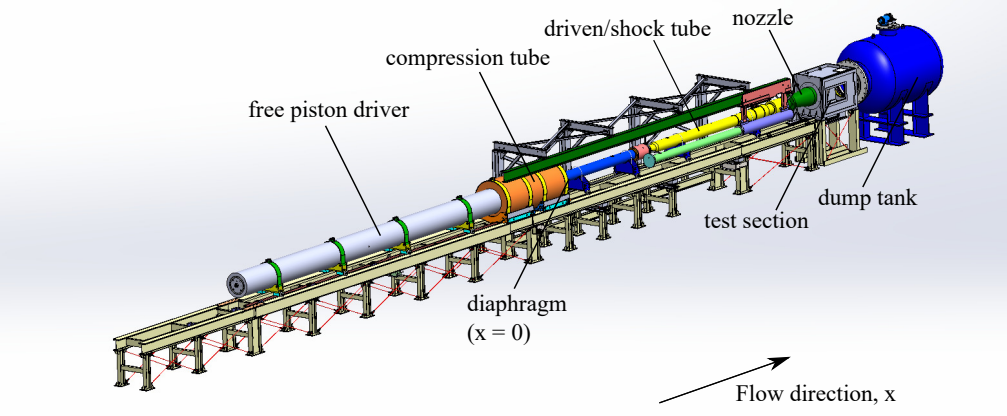


Figure 2.26: CAD model of the Oxford T6 Stalker Tunnel in the RST configuration

2.8.3 Tailoring and Tuning

In the development of conditions for a reflected shock tunnel, two aspects are the primary focus: tailoring and tuning. These are briefly explained here, preceding the methodology followed to attain tailored and tuned conditions in Section 4.2.

Tailoring refers to a selection of driver gas conditions such that when the reflected shock wave interacts with the contact surface (the boundary between the driven and driver gases), there is minimal disturbance created, the aim being to match the acoustic impedance between the driver and test gas [104]. In this way, conditions in the test section are maintained for a greater time without corruption of the desired pressure and temperature by expansion or shock waves propagating from the interaction. A comparison of tailored versus non-tailored conditions can be seen by plotting the pressure or ln(P) on a position-time axis, as shown in Fig. 2.27, adapted from [105].

Once tailored conditions have been achieved, the problem of tuning can be solved. Tuning refers to a selection of reservoir and driver gas conditions such that:

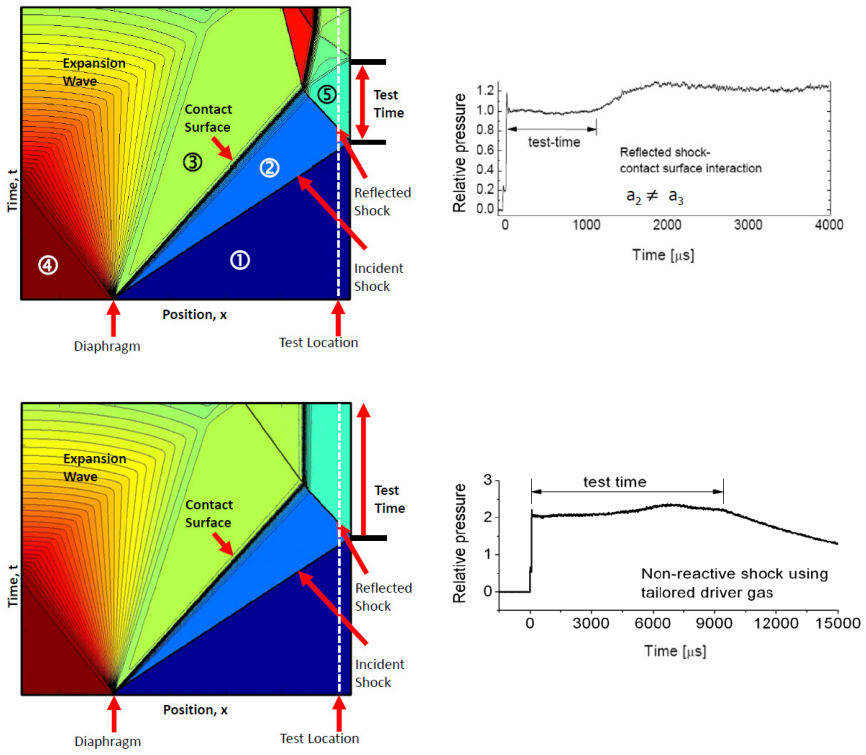


Figure 2.27: Non-tailored (top) versus tailored (bottom) comparison, adapted from [105]

1. The loss in driver gas pressure (and hence the loss in test time) as the gas flows out of the compression tube and into the test section following the rupture of the diaphragm is compensated for by increasing the driver gas pressure at rupture in excess of the required amount. This is known as "overdriving" [106]. The driver gas pressure is typically pushed to reach about 10% higher than the rupture pressure [107]. The desirable behaviour of pressure over rupture pressure versus non-dimensionalised time is shown in Fig. 2.28a.

2. The choice of driver and reservoir gas pressure combination results in the piston reaching the end of the compression tube with a speed within acceptable limits so as not to cause damage to the tunnel. A diagram illustrating typical piston trajectories is shown in Fig. 2.28b [108]. A soft landing condition, in which the piston initially slows to a stop as the driver gas is compressed before re-accelerating as the diaphragm bursts and gas is exhausted out of the compression tube is the optimal condition.

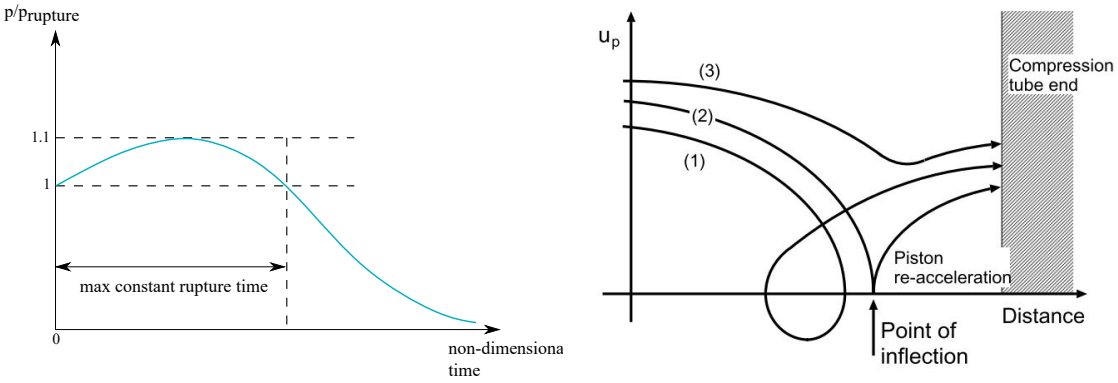


Figure 2.28: (a) Ratio of driver gas pressure to diaphragm rupture pressure versus non-dimensional time for an overdriven condition. (b) Typical piston trajectories [108], (1) Rebound Landing (2) Soft Landing (3) Direct Impact

2.9 Summary

An overview of selected hypersonic testing facility types is presented here, as well as descriptions of the specific facilities of interest at Oxford University (HDT and T6). An in-depth explanation of T6 which is a multi-modal facility is presented, with emphasis on the Reflected Shock Tunnel mode of operation since it is the most relevant for investigations carried out in this thesis. A description of the HDT facility was also given, since it provided a proving ground for the development of methodologies which were later applied in T6. Basic principles of tuning and tailoring are introduced which will be applied in later sections outlining the methodology formulated for commissioning of the T6 tunnel in RST mode.

3
Experimental Setup

Contents

3.1 Introduction 46
3.2 HDT Model 47
3.3 T6 Model 48
3.4 T6 Pitot Rake 51
3.5 Instrumentation 53
3.5.1 Piezoelectric Pressure Sensors 53
3.5.2 Piezoresistive Pressure Sensors 53
3.5.3 Thin Film Heat Transfer Gauges 55
3.6 Data Acquisition System 55

3.1 Introduction

This section outlines the model geometries used in each tunnel and gives a brief description of the type of sensors and instrumentation used in each one. The Pitot Rake model used to characterise the flow during T6 commissioning is also described here. The flow conditions and schlieren setups for each tunnel are described in their respective experimental campaign sections Chapter 6 and Chapter 7. For boundary layer experiments three axisymmetric cone models were used, each suited to the different testing environments of each tunnel. The naming convention used

for the cone is illustrated in Fig. 3.1. The angle of attack is denoted α and the azimuth is Φ, shown on the model in Fig. 3.1.

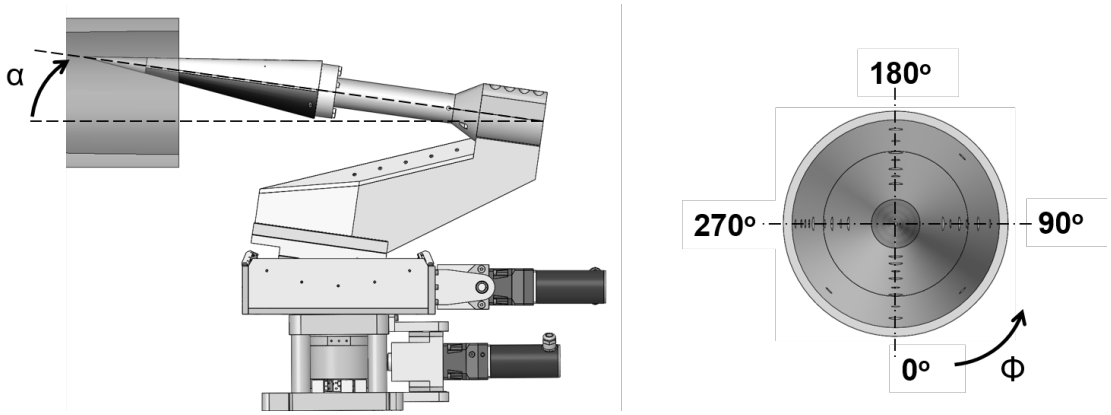


Figure 3.1: Naming convention for cone model showing angle of attack α and azimuth Φ

3.2 HDT Model

For experiments in HDT, a 7^o half angle cone was used with a nose tip radius of 1.25 mm and length of 550 mm, with a base diameter of 140 mm. This corresponds to a 50% scaled HIFiRE-1 flight vehicle [109]. The model was installed on a traverse system, allowing for micro-adjustments in angle of attack and yaw angle, and instrumented with 5 static pressure sensors (Kulite XTEL-140M and XCE-062) and 10 high-frequency piezoelectric pressure sensors (PCB132B38 and PCB132B39). A schematic and picture of the model installed in HDT is shown in Fig. 3.2. For further details on this model, see [103].

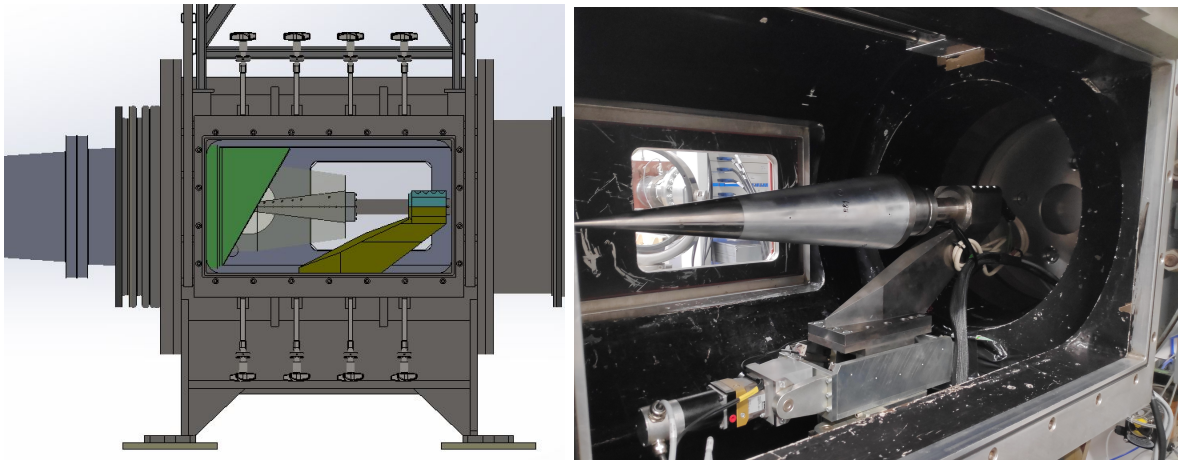


Figure 3.2: Model in HDT

Table 3.1: Sensors and location for HDT model

Sensor Name	Location from theoretically sharp nose tip (mm)	Ray Φ (^{o})
PCB1	219.5	0
PCB2	219.5	180
PCB3	219.5	90
PCB4	442.0	0
PCB5	471.0	0
PCB6	500.0	0
PCB7	521.5	0
PCB8	456.5	90
PCB9	456.5	270
PCB10	521.5	180
Kulite1	427.7	0
Kulite2	456.5	0
Kulite3	456.5	315
Kulite4	456.5	45
Kulite5	485.7	0

3.3 T6 Model

Due to the smaller volume test section and nozzle exit, the model used for the experiments in T6 is a smaller scaled cone model (approximately 407 mm in length) in order to avoid blockage and over-pressurisation of the test section. The model was made in two halves, with one half manufactured from PEEK (polyether ether ketone). PEEK enables the use of IR thermography as it has a high emmissivity and low thermal conductivity [110]. A labelled, exploded view of the main cone

assembly is shown in Fig. 3.3. Nose tips of various sizes were used, made from EN36B steel, these are summarised in Table 3.2.

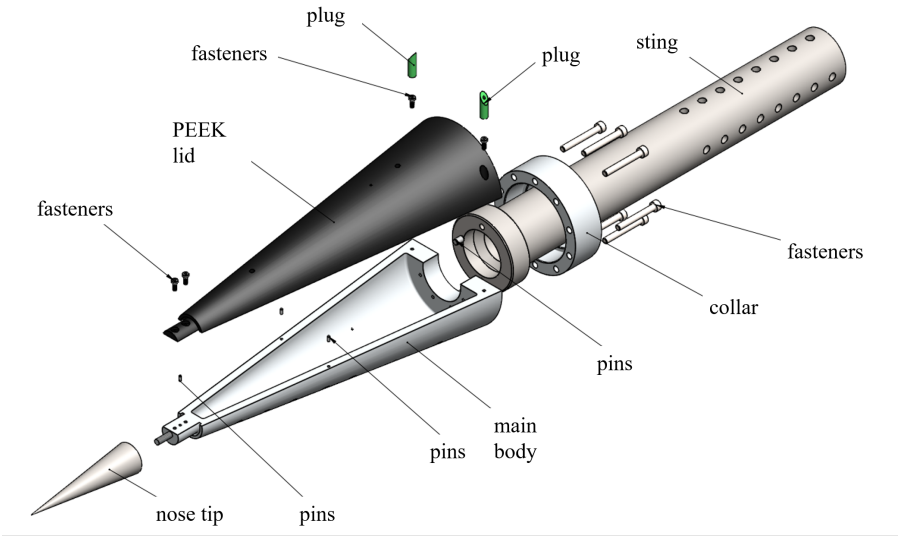


Figure 3.3: Labelled exploded view of T6 cone model

Table 3.2: Nose tips for T6 cone

Nose tip	Nominal Radius (mm)
A (Sharp)	0.05
B (Scaled)	0.852
C	1.095
D	1.25
E	2.5
F	3.4
G	6
H	9.5

Nose tips B, C and F were primarily used in this study. Simulations of the T6 Mach 7 nozzle were performed by T. Sopek [92] in order to verify that the cone was positioned correctly in the core flow and that the shock angle would not interfere with the region of analysis. A CAD model of the cone with the simulation Mach number contours and expected shock angle overlaid is shown in Fig. 3.4.

The cone installed in the T6 tunnel is shown in Fig. 3.5. The model was instrumented with 12 thin film heat transfer gauges, 6 PCB132A31's and 4 Kulite XCS-062-10A's but for this application only the static pressure sensors were used.

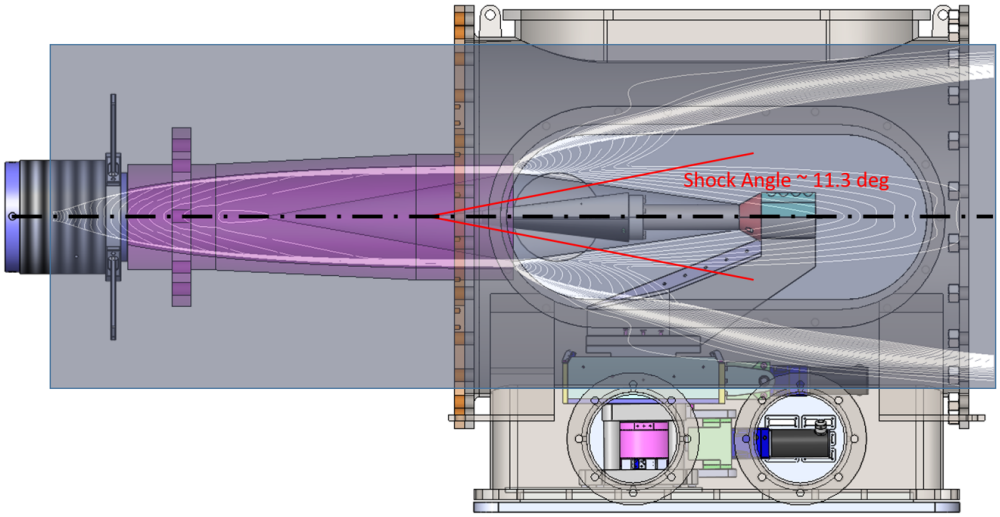


Figure 3.4: T6 cone in tunnel CAD with nozzle Mach number contours overlaid (nozzle simulations by T. Sopek)

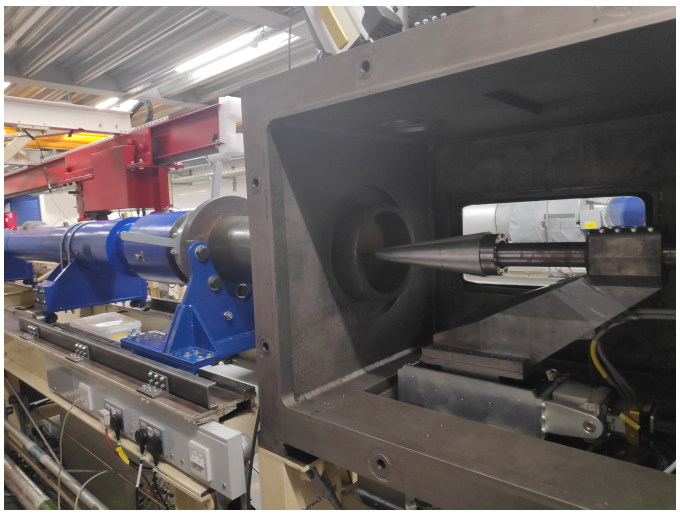


Figure 3.5: Cone model in T6

The Kulites measure static pressure and are used for micro-alignment. While high-frequency PCB sensors were fitted in the model, it is expected that the frequencies experienced in T6 are too high for these to be of use and so blanks were put in their place for testing in T6. Blanks were fitted into the HTG locations as well to prevent them from being damaged. An identical model without the holes for PCB and heat transfer gauges was also available to reduce the risk of shocks forming from the sensors and interfering with the flow. This model had 4 Kulites installed for micro-alignment at 202 mm from a theoretically sharp nose tip. Sensors and

locations for these two models are summarised in Table 3.3.

Table 3.3: Sensors and locations from theoreically sharp nose tip for T6 models

Cone Model 1					
Sensor	Location (mm)	Ray Φ (^{o})	Sensor Name	Location (mm)	Ray Φ (^{o})
HTG1	124.6	0	PCB1	151.1	45
HTG2	151.1	0	PCB2	179.0	45
HTG3	179.0	0	PCB3	206.9	45
HTG4	206.9	0	PCB4	240.2	45
HTG5	240.2	0	PCB5	267.6	45
HTG6	267.6	0	PCB6	355.8	45
HTG7	326.3	0	Kulite1	311.3	0
HTG8	341.1	0	Kulite2	311.3	45
HTG9	355.8	0	Kulite3	311.3	180
HTG10	378.0	0	Kulite4	311.3	315
HTG11	179.0	180			
HTG12	341.1	180			
Cone Model 2					
Kulite1	202	0			
Kulite2	202	90			
Kulite3	202	270			
Kulite4	202	180			

CAD manufacturing drawings of the fully instrumented model are included in Appendix F.

3.4 T6 Pitot Rake

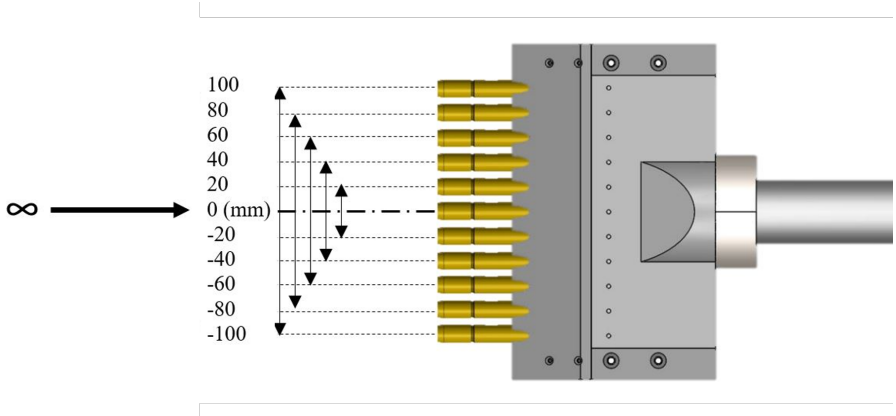


Figure 3.6: Pitot probe schematic and distances from centreline (mm)

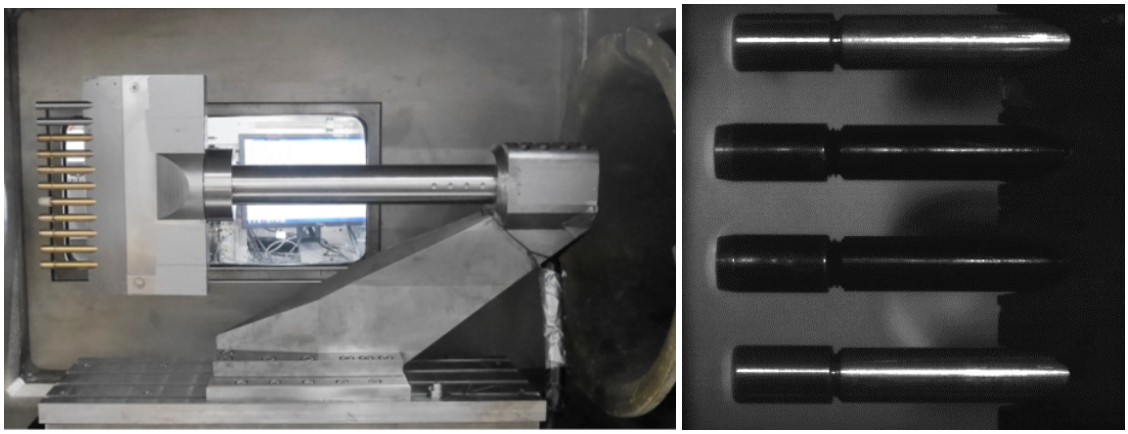


Figure 3.7: Image of pitot rake installed in T6, left ([111]), high speed image of pitot probes and bow shock formation during T6 test, right

A schematic of the Pitot rake used during commissioning of T6 with each Pitot probe distance from the centreline in millimeters is shown in Section 3.4. The probes are numbered from 1 down starting at the top. An image of the Pitot rake installed in the T6 tunnel is shown in Section 3.4, along with a high speed image of the pitot probes in the test flow for T6s89. The Pitot probes are used to measure the diameter of the core flow at nozzle exit and various distances downstream, along with the Pitot pressure to stagnation pressure ratio which is used to back out freestream properties such as the unit Reynolds number and exit flow velocity. The rake is typically instrumented with PCB 113B21's or 113B27's. For the first few commissioning shots a thermocouple (TC), thin film gauge (TFG) and diamond heat transfer gauge (DHTG) developed by Penty Geraets [112] was used to measure heat flux.

Table 3.4: Table showing Pitot probe setup

Pitot Rake Number	Radial Distance from Centreline (mm)	PCB type/Other	Max Pressure (MPa)
1	100	113B21	6.895
2	80	113B27	6.895
3	60	113B27	6.895
4	40	TFG	-
5	20	113B27	6.895
6	0	113B27	6.895
7	-20	TC	-
8	-40	DHTG	-
9	-60	113B27	6.895
10	-80	113B27	6.895
11	-100	-	-

3.5 Instrumentation

Three main instrumentation types were used: piezoelectric pressure microsensors by PCB Piezotronics, piezoresistive high temperature ultraminiature pressure transducers by Kulite Semiconductor Products and thin film heat transfer gauges manufactured by the University of Queensland. A brief description of each is given.

3.5.1 Piezoelectric Pressure Sensors

The piezoelectric pressure sensors are fast-response sensors which are primarily used for pressure fluctuation measurements in HDT and shock time of arrival as well as Pitot pressure measurements in T6. The specific sensors used for tunnel commissioning are described in Chapter 4. Type PCB132A31 sensors [49] are primarily used for higher frequency pressure fluctuation measurements in the cone for testing in HDT. These are mounted in neoprene tubes to vibrationally damp the sensors.

3.5.2 Piezoresistive Pressure Sensors

Four Kulite XCS-062-10A sensors [113] are fitted into the model. They use a fully-active four arm Wheatstone bridge which measures the strain on a diaphragm which deforms under pressure. These have four shielded cables, two for voltage

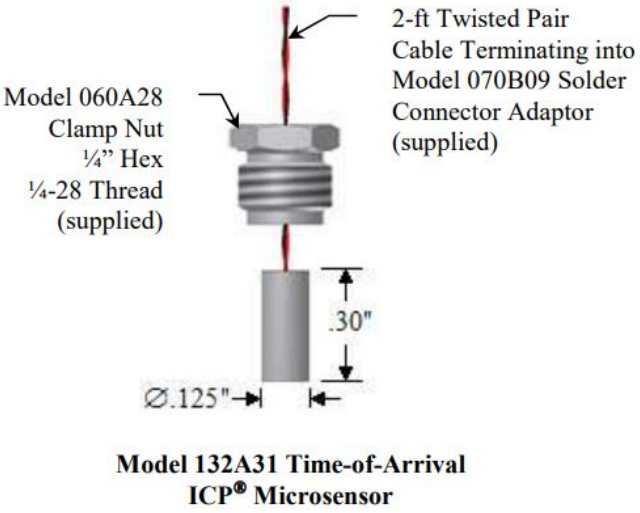


Figure 3.8: PCB132A31, from [49]

supply and two for the output signal. The sensors are used to measure static pressure over the surface of the cone for the purpose of alignment and are connected to a general single-channel Fylde FE-H379-TA high speed amplifier.

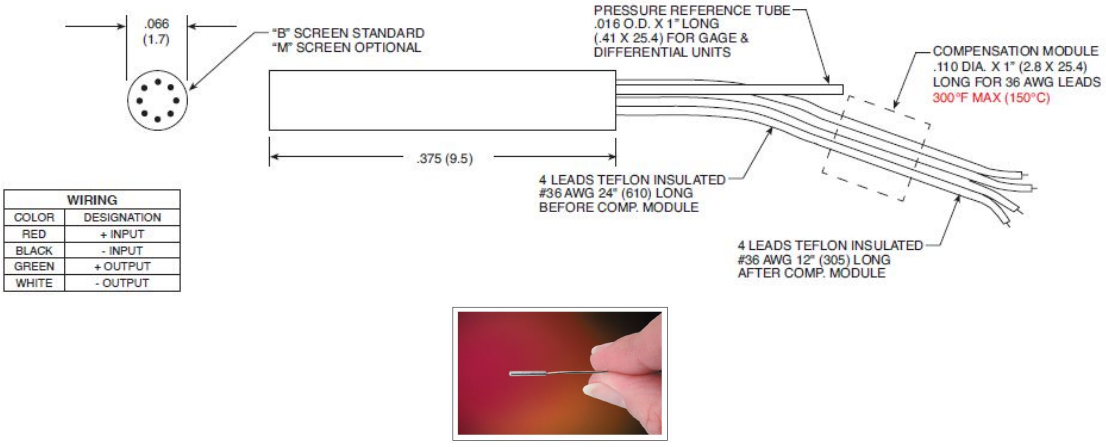


Figure 3.9: Schematic with dimensions of inches and mm in brackets (top) and image of of Kulite XCS-062 sensor (bottom) from [113]

This series of Kulite sensors can measure pressure fluctuations in the 100 kHz range but this is too low for the frequencies expected in both HDT and T6, and further is subject to sensor resonance [52].

3.5.3 Thin Film Heat Transfer Gauges

The University of Queensland has put significant effort into developing fast-response heat transfer sensors suitable for the short duration test time typical of hypersonic facilities (on the order of milliseconds). A thin metallic film acts as a resistance thermometer which records the temperature history and therefore heat transfer rate during a test. The assumptions are that the film is sufficiently thin and the substrate sufficiently thick that it behaves as a semi-infinite medium [114, 115]. Further details on the theory behind their operation can be found in [116]. An example of the gauge is shown in Fig. 3.10.

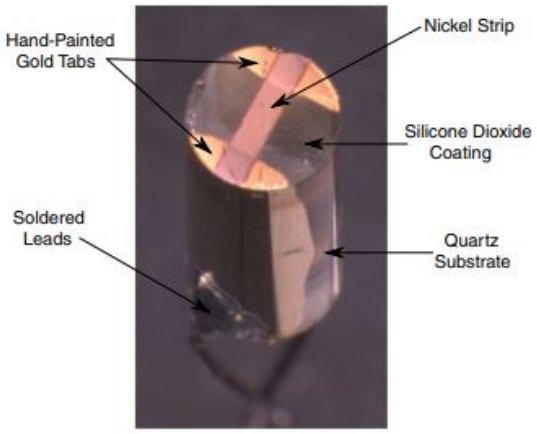


Figure 3.10: Image of UQ thin film gauge, from [114]

While thin film gauges were installed in the model used for testing in T6, they ultimately were subjected to too much damage from the flow and the transition data was not reliable.

3.6 Data Acquisition System

Data was recorded for experiments in both tunnels using a National Instruments PXIe-8135 controller with PXIe-6368 acquisition cards at 2MHz/channel.

4

Hypersonic Testing Facilities and Commissioning of the Oxford T6 Stalker Tunnel in Reflected Shock Tunnel Mode

Contents

4.1 Introduction 56
4.2 Condition Development Methodology 58
4.3 First L1D Results 65
4.3.1 Choice of Initial Driver Gas Pressure 66
4.3.2 Tuning and First Commissioning Condition 69
4.4 Experimental Setup 73
4.4.1 Blanking plate 73
4.4.2 Shock Timing Stations 73
4.4.3 Stagnation Probes 75
4.4.4 Steel Piston Refurbishment 75
4.4.5 Diaphragms 76
4.5 Experimental Results and Adjusted L1D Model 77
4.5.1 Blank-Off Tests 78
4.5.2 Shock Tube Tests 82
4.6 Initial Reflected Shock Tunnel Tests 83
4.7 Use of nitrogen-argon driver gas mixtures for extended test time 90
4.8 Summary of T6 RST Mode Conditions Commissioned 93
4.9 Selection of Appropriate Test Time 95
4.10 Conclusion 96

4.1 Introduction

The University of Oxford has recently commissioned the T6 Stalker Tunnel which is the highest speed facility in Europe [117]. It forms part of a series of free-piston shock tunnels first developed by the late Professor Ray Stalker at the Australian National University, which culminated in the T3 shock tunnel in 1986 [118]. Following the decommissioning of T3 after more than thirty years of operation, the driver section was acquired by Oxford University in 2014 and combined with the Bristol Siddley Gun Tunnel to form T6.

T6 is capable of operation in three main modes which will be outlined in further detail in the sections which follow. These modes are shock tube mode, expansion tube mode and reflected shock tunnel (RST) mode. At the start of this thesis, the tunnel had been commissioned in shock tube and expansion tube modes. A significant amount of this thesis work focused on developing and commissioning the tunnel in the reflected shock tunnel mode of operation which is the most suitable for use in boundary layer experiments as it has sufficient testing time for the flow to establish over a model.

While reflected shock tunnels do exist elsewhere, each tunnel is unique and the methodology followed for commissioning one tunnel cannot be directly applied to another. Particularly for T6, some subtleties existed which required the formulation of a novel framework for developing test conditions. Many approaches exist for developing and commissioning a tunnel in RST mode and the approach outlined here is the one which the author has formulated to reach the goal of working test conditions for use in testing scaled models in flight representative conditions.

A brief outline of the approach is given here. First, an extensive literature review was carried out in order to gain a fundamental understanding of the flow physics governing the reflected shock process, with the added complication of the interaction between two different gas species (driver and driven gas) and the finite reservoir

driving the shock process with the use of a free-piston driver. Both of these processes can severely restrict the test time achieved, as well as the safety of the facility if not properly controlled. The principles of tailoring and tuning (described in Section 2.8.3) describe these aspects in detail. Various formulations by authors who had commissioned other RST facilities were reviewed and aspects of the most relevant ones were gathered and applied to T6. An analytical framework was developed in Matlab to rapidly obtain a "first-cut" solution to the test conditions (reservoir fill pressure, driver fill pressure and composition, diaphragm rupture pressure, shock tube fill pressure) from desired test conditions (unit Reynolds number, Mach number and stagnation enthalpy). An approximate model of the piston dynamics was also included to estimate the reservoir and driver gas conditions for safe use of the piston. A model of the facility was then developed in L1D which is an open source, quasi-one-dimensional simulation software. The initial conditions obtained from the framework were fed into the L1D model, which allowed for a more accurate simulation of both the flow physics and the piston dynamics. A larger piston (90 kg) was refurbished and first used here to obtain a better "hold time" (maintenance of the rupture pressure as the gas exhausts through the burst diaphragm). This required adjustment of the computational model to adequately capture the new friction characteristics of the piston which significantly differed from the previous piston (36 kg). These characteristics could only be captured through experiments with the new piston and comparison of the rupture pressure traces to the facility model. Further experiments were done to relate the diaphragm rupture pressure to the score depth and material of the diaphragm used (outlined in Section 4.4.5).

Once these tests confirmed the facility simulation was accurate, small adjustments could be made to the parameters used in the model to optimise the resulting test conditions. Once an acceptable result was obtained the condition could be tested experimentally. This often also required small adjustments during the experiment, for example in shock tube fill pressure, as the facility model was close but could not capture all the flow physics. Finally, optimised conditions were reached and this

process could be repeated for a few different test conditions which are summarised at the end of the chapter in Table 4.10.

4.2 Condition Development Methodology

The method followed here will be applicable to a range of total enthalpy and pressure requirements. The test condition chosen for initial development is based on conditions from the HIFiRE-1 test flight, scaled for the model being used. The unit Reynolds number specification was later relaxed as it was found that lower conditions were more favourable for establishing observable boundary layers. This is a relatively low total enthalpy and high total pressure condition for this facility with the required properties shown in Table 4.1. Working back from the test section

Table 4.1: Initial conditions of interest

Nominal Mach Number	Unit Reynolds Number $\times 10^6$ (/m)	Total Enthalpy (MJ/kg)
7	18	2.4

is done in three parts, with the final goal of calculating the fill conditions required to achieve the given test flow. Part I is the calculation of the reflected and incident shock in front of the nozzle, Part II is the calculation of the expansion conditions through the orifice and Part III outlines the method used for tuning the piston. This is illustrated in Fig. 4.1. A flowchart showing the logic followed in the condition

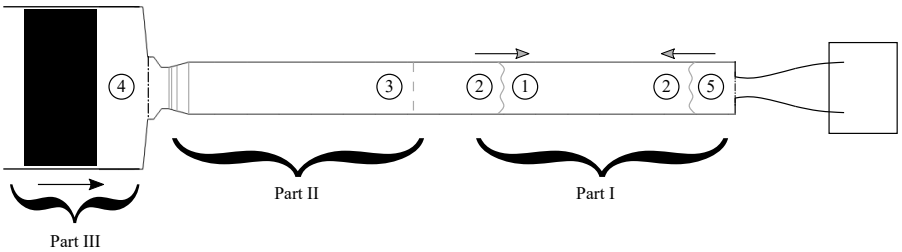


Figure 4.1: Flow features and numbering convention in reflected shock tube mode

development process is shown in Fig. 4.2.

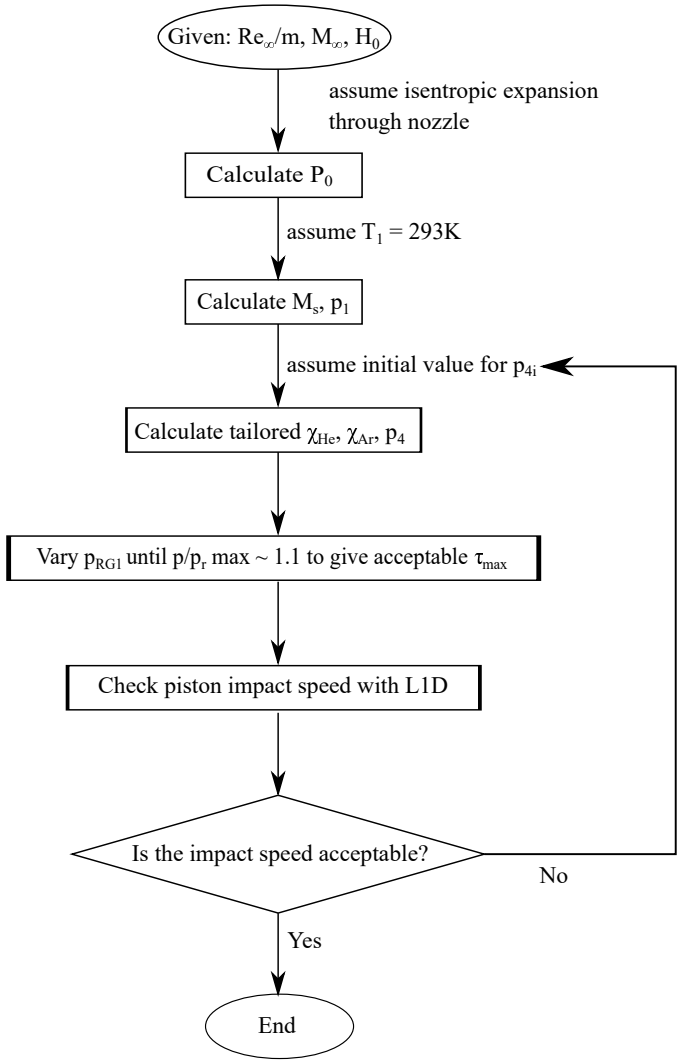


Figure 4.2: Flowchart showing general methodology followed in condition development for RST mode

Part I - Incident and Reflected Shock Properties

For clarity, Part I is magnified and shown in Fig. 4.3 with the numbering convention used in the calculations which follow. The arrows show the direction in the shock reference frame. The assumption of an isentropic expansion through the nozzle is used to calculate the stagnation condition P_0 from the test conditions in Table 4.1. The known quantities are then H_0, P_0 and T_1 (assumed to be 293 K). As a first value, using a perfect gas assumption and assuming a shock Mach number and shock tube fill pressure p_1 allowed for a rapid estimation of the incident shock conditions

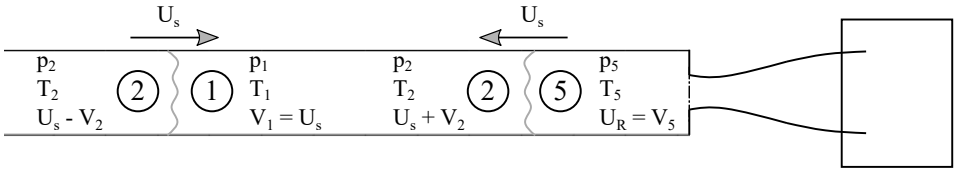


Figure 4.3: Numbering convention for Part I

which were later adjusted by Eq. (4.1), Eq. (4.2) and Eq. (4.3) [119]:

$$\frac{p_2}{p_1} = 1 + \frac{2\gamma_1}{\gamma_1 + 1}(M_s^2 - 1) \tag{4.1}$$

$$\frac{T_2}{T_1} = 1 + \frac{2(\gamma_1 - 1)}{(\gamma_1 + 1)^2}\frac{(M_s^2 - 1)(1 + \gamma_1 M_s^2)}{M_s^2} \tag{4.2}$$

where

$$V_1 = M_s\sqrt{\gamma_1 R_1 T_1} \tag{4.3}$$

The properties post incident shock and reflected shock could be calculated using the NASA Chemical Equilibrium with Applications (CEA) [120] programme, assuming equilibrium gas.

A potential method used to calculate the shock speed is outlined here.

1. Assume M_s
2. Assume p_1
3. Iterate through shock Mach numbers until H_0 converges
4. Iterate through initial shock tube fill pressures p_1 until P_0 converges
5. Recalculate final properties

This loop is repeated until the calculated value of H_0 and P_0 match to within the set tolerance.

Part II - Tailoring Conditions Including the Orifice

The orifice is incorporated using the method outlined in Gildfind et al. [121] which calculates properties such as M_3. Tailoring was done by varying the percentage of helium in the helium-argon driver gas mixture and imposing the tailored condition from the method outlined in Hong et al. [104] which calculates the tailored M_3. The two were compared to obtain the ideal driver gas composition for tailoring. The method is described here, with the simplified geometry and numbering convention shown in Fig. 4.4.

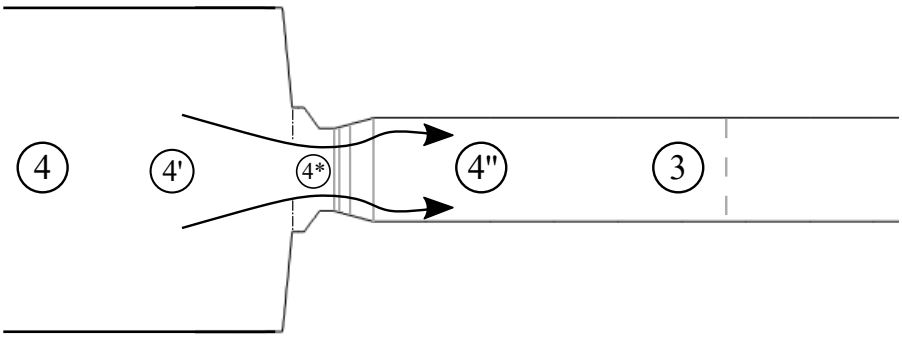


Figure 4.4: Numbering convention and simplified geometry with orifice

Following on from the conditions calculated above (or obtained from CEA):

$$u_2 = \frac{a_1}{\gamma_1}\left(\frac{p_2}{p_1} - 1\right)\left[\frac{\frac{2\gamma_1}{\gamma_1+1}}{\frac{p_2}{p_1} + \frac{\gamma_1-1}{\gamma_1+1}}\right]^{1/2} \tag{4.4}$$

Assuming that the orifice can be approximated as a converging-diverging or de Laval nozzle [122], it goes through a steady, isentropic expansion from Mach 1 at the throat (orifice) to supersonic conditions in the driven gas in region $4''$. Using the Mach-Area relation, M_4'' can be solved from:

$$\left(\frac{A_1}{A_{4^*}}\right)^2 = \frac{1}{M_{4''}^2}\left[\frac{2}{\gamma_4+1}\left(1 + \frac{\gamma_4-1}{2}M_{4''}^2\right)\right]^{\frac{\gamma_4+1}{\gamma_4-1}} \tag{4.5}$$

where A_1 and A_{4^*} are the areas of the driven tube and the orifice respectively. The initial driver gas conditions p_{4i} and T_{4i} are assumed to be known, or are

usually chosen based on tuning of the piston (this is further explained below). The conditions at rupture can be directly obtained from

$$p_4 = p_{4i}\left[\frac{\frac{u_2}{a_{4i}} + \frac{2}{\gamma_4 - 1}\left(\frac{p_2}{p_{4i}}\right)^{\frac{\gamma_4 - 1}{2\gamma_4}}}{\left(M_{4''} + \frac{2}{\gamma_4 - 1}\right)\left(1 + \frac{\gamma_4 - 1}{2}M_{4''}^2\right)^{\frac{-1}{2}}}\right]^{\frac{2\gamma_4}{\gamma_4 - 1}} \tag{4.6}$$

where a_{4i} is the initial speed of sound in the driver gas, obtained from a known initial temperature and composition. The composition of the driver gas is a mixture of argon and helium, so the specific gas constant is:

$$R_{4i} = \chi_{He}R_{He} + \chi_{Ar}R_{Ar} \tag{4.7}$$

from which

$$a_{4i} = \sqrt{\gamma_{4i}R_{4i}T_{4i}} \tag{4.8}$$

Following isentropic relations the rupture temperature can be calculated:

$$T_4 = T_{4i}\left(\frac{p_4}{p_{4i}}\right)^{\frac{\gamma_4 - 1}{\gamma_4}} \tag{4.9}$$

Similarly the temperature in region $4''$ can be obtained, from which $a_{4''}$ and $u_{4''}$ can be calculated. The properties in the expanded region are then:

$$u_3 + \frac{2a_3}{\gamma_3 - 1} = u_{4''} + \frac{2a_{4''}}{\gamma_{4''} - 1} \tag{4.10}$$

or subsequently from the velocity (and pressure) equivalence across the interface

$$\begin{aligned} u_3 &= u_2 \\ p_3 &= p_2 \end{aligned}$$

The temperature is once again obtained through the isentropic relation

$$T_3 = T_{4i}\left(\frac{p_3}{p_{4i}}\right)^{\frac{\gamma_4 - 1}{\gamma_4}} \tag{4.11}$$

The method up to this point was run for a number of He-Ar mixtures and M_3 was plotted against the expansion Mach number for the tailored condition which is a function of the pressure ratio across the reflected shock and the ratio of specific heats (constant for the driver gas mixture of interest). The tailored expansion Mach number is given by [104]:

$$\alpha_4 = \frac{\gamma_4 + 1}{\gamma_4 - 1} \tag{4.12}$$

$$M_3 = \frac{(\alpha_4 - 1)\left(\frac{p_5}{p_2}\right)}{\sqrt{(1+\alpha_4)\left(1+\alpha_4\frac{p_5}{p_2}\right)}} \tag{4.13}$$

The driver gas composition for the tailored condition is thus obtained, along with the rupture conditions.

Part III - Piston Dynamics

The method outlined in Hornung [107] was used to estimate the reservoir and driver gas conditions to achieve an acceptable test time and landing condition. The equations for the non-dimensional piston velocity, displacement and time are given by:

$$\xi = \frac{x}{D} \tag{4.14}$$

$$\kappa = \frac{u}{a_{RG1}} \tag{4.15}$$

$$\tau = \frac{t a_{RG1}}{D} \tag{4.16}$$

where a_{RG1} is the speed of sound in the reservoir gas. Assuming an isentropic compression, the initial condition of the driver gas is calculated by Eq. (4.17).

$$p_{4i} = \frac{p_4}{\lambda_c^{\gamma_4}} \tag{4.17}$$

Where p_4 is the rupture pressure calculated in the previous section. The initial pressure of the reservoir gas is guessed and the parameters b_1 and b_2 are obtained by:

$$b_1 = \frac{\pi P_{RG1} D^3}{4 m_p a_{RG1}^2} \tag{4.18}$$

$$b_2 = \frac{P_{4i}}{P_{RG1}} \left(\frac{L}{D}\right)^{5/3} \tag{4.19}$$

$$b_3 = b_1 \frac{P_{4i}}{P_{RG1}} \tag{4.20}$$

$$b_4 = b_1 b_2 \tag{4.21}$$

$$b_5 = \frac{9}{16}\sqrt{5/3} \left(\frac{b_1 b_2 M}{m_r}\right)^{1/2} \frac{d^2}{D^2} \tag{4.22}$$

m_r is the mass of the driver gas at rupture. The following non-linear system of ODE's is then solved using Matlab's ODE113 function, with the initial conditions as shown:

$$\dot{\xi} = -\kappa \tag{4.23}$$

$$\dot{\kappa} = b_1 \left[(1 - 0.2\kappa)^7 - b_2 \xi^{-5/3}\right] \tag{4.24}$$

$$\xi(0) = L/D \tag{4.25}$$

$$\kappa(0) = 0 \tag{4.26}$$

The system of equations to be solved post rupture are

$$\dot{\xi} = -\kappa \tag{4.27}$$

$$\dot{\kappa} = b_3 - b_4 \left(\frac{\mu}{\xi}\right)^{5/3} \tag{4.28}$$

$$\dot{\mu} = -b_5 \left(\frac{\mu}{\xi}\right)^{4/3} \tag{4.29}$$

subject to:

$$\xi(\tau_r) = \xi_r \tag{4.30}$$

$$\kappa(\tau_r) = \kappa_r \tag{4.31}$$

$$\mu(\tau_r) = 1 \tag{4.32}$$

The initial value of the reservoir gas pressure is varied to achieve as high a test time as possible, which can be determined by plotting the pressure trace at diaphragm

rupture. It should be noted that the actual reservoir gas pressure is likely to be much higher to account for friction losses and losses due to flow around the launcher, so this only gives an initial estimate.

4.3 First L1D Results

Using the method outlined in Sec. 4.2, initial preliminary conditions which gave an acceptable test time and piston landing condition were obtained. The relevant lengths and diameters of the tunnel used for the analysis are summarised in Table 4.2.

Table 4.2: T6 tunnel dimensions

Region/Number	Diameter (m)	Length (m)
1 (Driven Tube)	0.0963	7.1
4* (Orifice)	0.076	0.012
4 (Compression Tube)	0.3066	6

The initial distance between the piston and the diaphragm, L, is 5.75m. Using the method outlined in Sec. 4.2, the nozzle supply/stagnation pressure (P_0) was calculated to be 26.56 MPa, with an initial shock tube fill pressure of 229 kPa. These values were then run in the University of Queensland's quasi-one-dimensional gas dynamics code L1D which provided a higher fidelity model and allowed for slight adjustments to the condition based on the inclusion of equilibrium thermodynamic and viscous effects. The shock tube fill pressure was later adjusted to 220 kPa as this gave a slightly better combination of nozzle supply enthalpy and pressure. It was found that a loss factor was required to account for viscous effects and other losses when inputting the calculated conditions to L1D to obtain the correct nozzle supply conditions (this does not account for piston losses, just losses in the driven section). Hence the initial method output was adjusted using a 20% increase applied to the shock Mach number to account for losses and bring the estimate closer to that given by L1D.

A tailored case was obtained by assuming a driver gas pressure and varying the composition of the helium/argon mixture in the driver gas until the Mach number

of the expansion matched the tailored Mach number given by [104]. The choice of driver gas pressure is closely coupled with the tuning of the piston, and is discussed in the next section. With the tailored composition calculated, the rupture pressure of the diaphragm could then be obtained.

Using a driver gas pressure of 4.8 MPa, the composition which maximises testing time is a 19% helium/ 81% argon mixture by mass fraction for a given driver gas pressure.

The tailored case approximated by the code was then run in L1D, along with comparative cases where either too much or too little helium was added to the driver gas. As an example, the x-t diagram of log(P) for these cases are shown in Fig. 4.5.

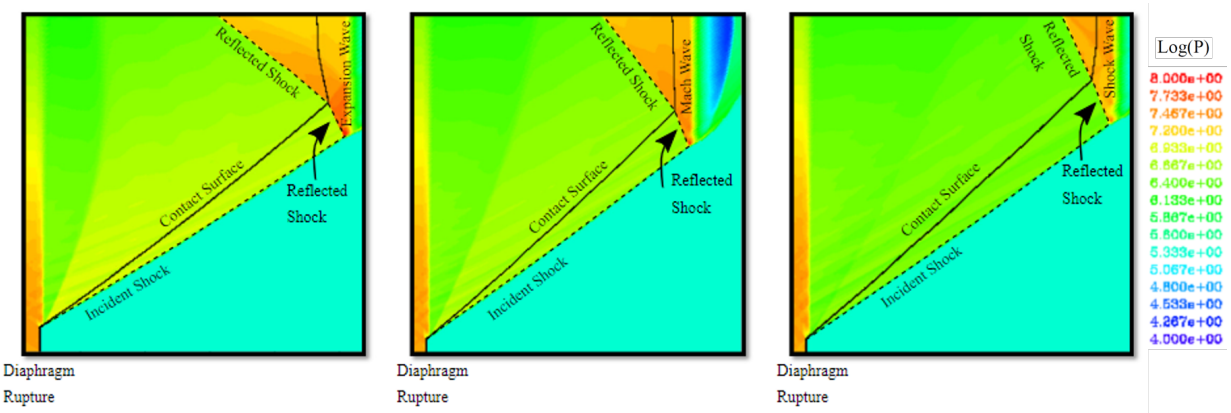


Figure 4.5: Overtailored, tailored and undertailored cases

4.3.1 Choice of Initial Driver Gas Pressure

The choice of initial driver gas pressure greatly affects both the tuned and tailored properties of the flow. For the given test condition, since the nozzle supply pressure required is quite high while the nozzle supply enthalpy is low, the initial pressure in the shock tube is relatively high. Two possible options then exist for the choice of the initial pressure in the driver gas, p_{4i}.

If the driver gas pressure is chosen to be lower than the shock tube pressure ($p_{4i} < p_1$), the advantage is that a lower reservoir gas pressure and diaphragm rupture pressure is required. However, the incident shock is slower while the reflected shock propagates faster upstream through the lower pressure gas and

interacts with the compressed driver gas before the piston reaches its maximum stroke. This causes the piston to rebound and on travelling forwards again, the low driver gas pressure is not sufficient to fully dampen the impact of the piston on the compression tube end. The hold time of the piston is thus reduced, as well as the usable test time at the nozzle supply end. For the case where the driver gas pressure is higher than the test gas pressure $p_{4i} > p_1$, a very high reservoir gas pressure is required to drive the shock. The rupture pressure of the diaphragm is also increased, and the helium percentage and compression ratio in the driver section is decreased to maintain tailored conditions. The incident shock is faster, while the reflected shock is slower through the higher pressure gas. During this time, the piston rebounds further and on return, the higher driver gas pressure reduces the piston impact speed. The slower shock then causes a larger secondary rebound. Due to the slower reflected shock, the nozzle supply conditions remain within the ideal limits for longer and hence the usable test time is increased, with a decrease in maximum piston impact speed. However, a much greater reservoir gas pressure is required which is not ideal. The alternate high driver gas pressure condition is shown in Fig. 4.6, Fig. 4.7, Fig. 4.8 and Fig. 4.9 for comparison with the final condition described in Section 4.3.2 where the above phenomena can be seen.

4.3.2 Tuning and First Commissioning Condition

It was ultimately decided that the lower driver gas pressure condition was a better option for initial commissioning tests. The initial output of the code and the final values which were decided on are shown in Table 4.3.

The value in parenthesis in Table 4.3 were the direct output from the theoretical calculation, subsequently adjusted in L1D to optimise the rupture pressure achieved. In particular, the reservoir gas pressure from the theoretical calculation is much lower, as this does not account for friction and pressure losses in the piston, which are substantial. A factor of approximately 2.7 MPa was added to the reservoir gas pressure when going from the theoretical calculation to the L1D simulation to

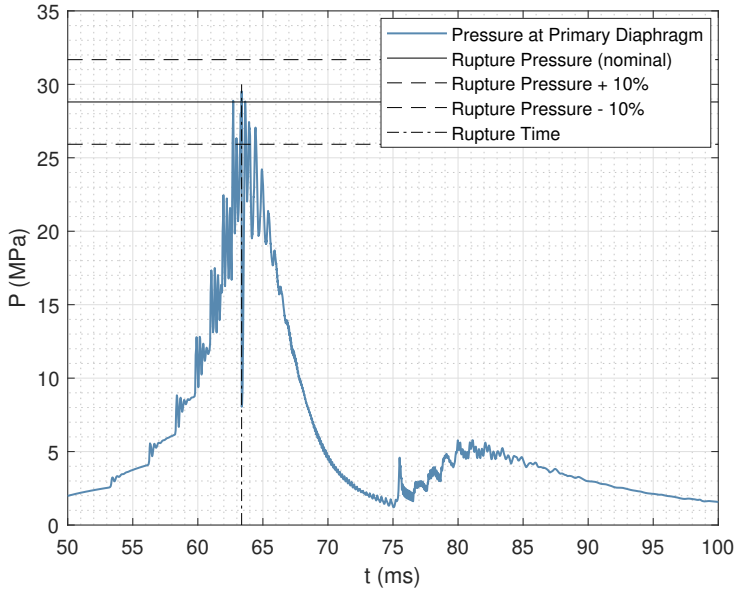


Figure 4.6: High RG alternate case, pressure at the diaphragm (MPa)

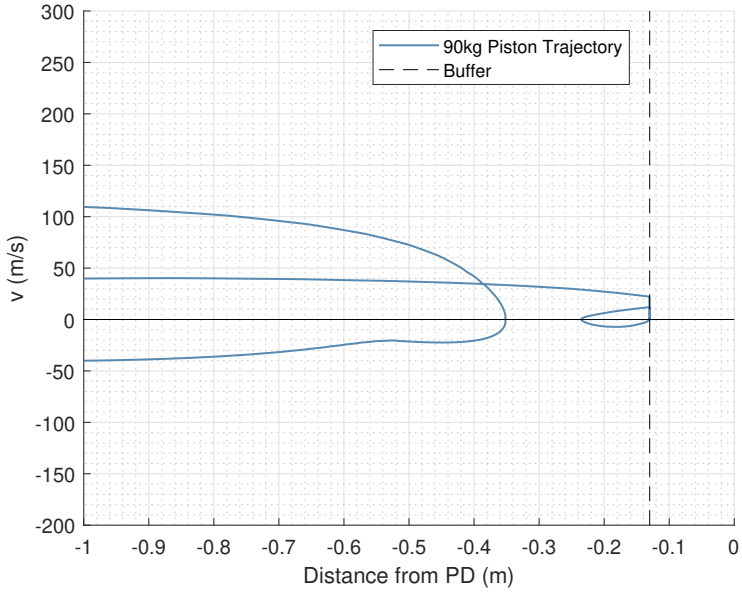


Figure 4.7: High RG alternate case, piston velocity (m/s) versus distance from the primary diaphragm (m)

achieve the same driven pressure.

With these conditions, the results from the L1D simulation are as follows. The rupture pressure is shown in Fig. 4.10, and piston trajectory in Fig. 4.11.

The nozzle supply pressure and enthalpy are shown in Fig. 4.10, and piston

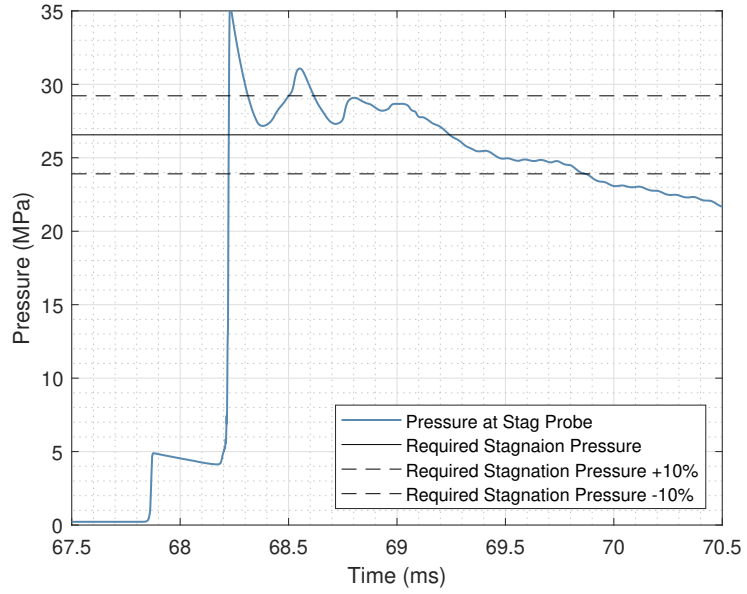


Figure 4.8: High RG alternate case, pressure at the stagnation region (MPa)

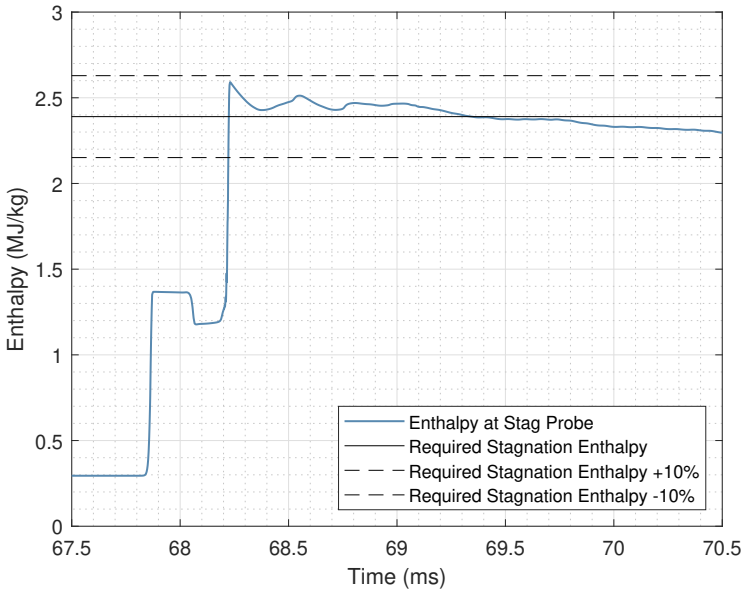


Figure 4.9: (a) High RG alternate case, enthalpy at the stagnation region (MJ/kg)

trajectory in Fig. 4.11. A usable test time of approximately 0.85 ms is theoretically predicted. Due to the reflected shock which causes the piston to rebound, a soft landing condition was difficult to achieve in this mode, with a piston speed of 30 m/s initially predicted (this was later reduced due to the higher friction losses found by changing pistons).

Table 4.3: Initial and final input conditions

	p_0 (MPa)	H_0 (MJ/kg)	p_{4i} (kPa)	p_{RG1} (MPa)	p_4 (MPa)	p_1 (kPa)	λ_c	χ_{He} for tailored conditions
Final Adjusted Conditions (L1D)	26.56	2.39	120	4.8 (2.1)	20.6	220	21.9	0.19
Method Output (20% Losses)	26.56	2.39	120	1.78	21.5	229	22.5	0.19
Method Output (No losses)	26.56	2.39	120	1.3	11.8	229	15.8	0.22

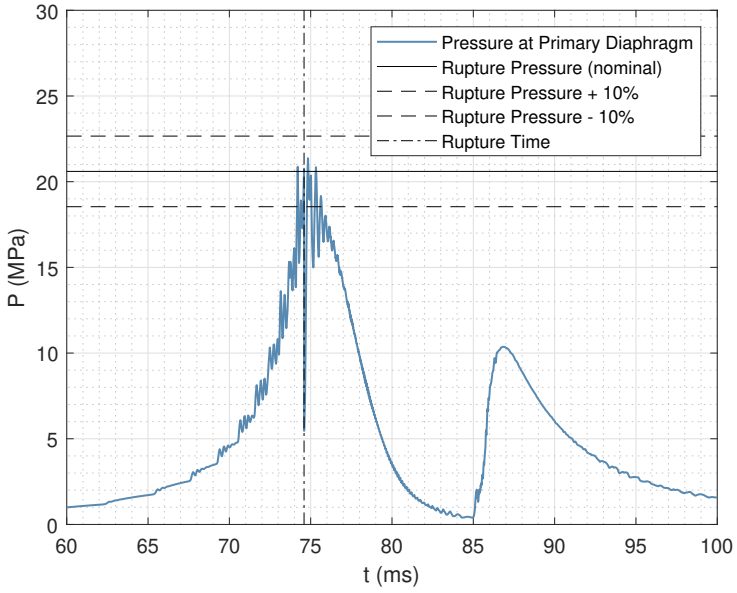


Figure 4.10: Final condition, pressure at the diaphragm (MPa)

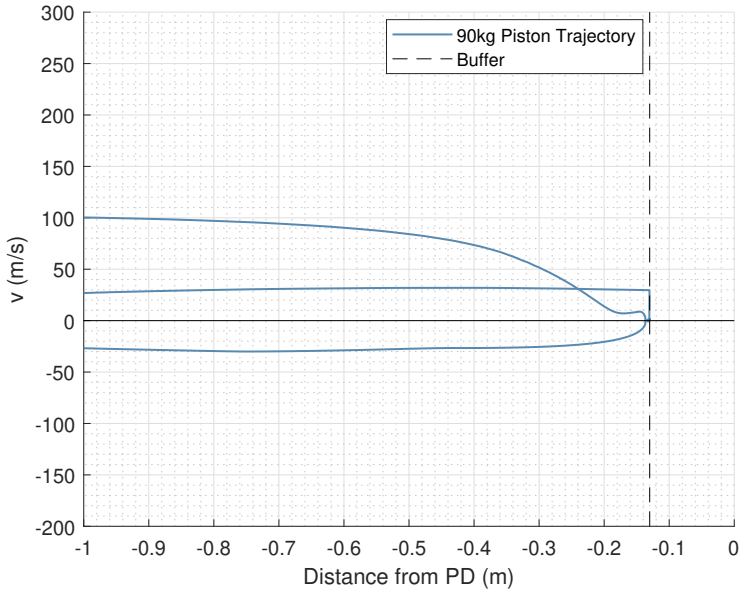


Figure 4.11: Final condition, piston velocity (m/s) versus distance from the primary diaphragm (m)

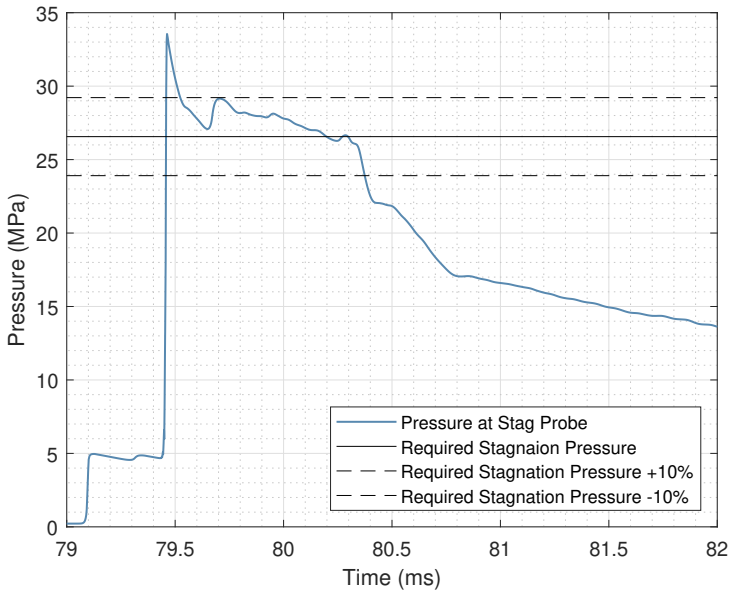


Figure 4.12: Final condition, pressure at the stagnation region (MPa)

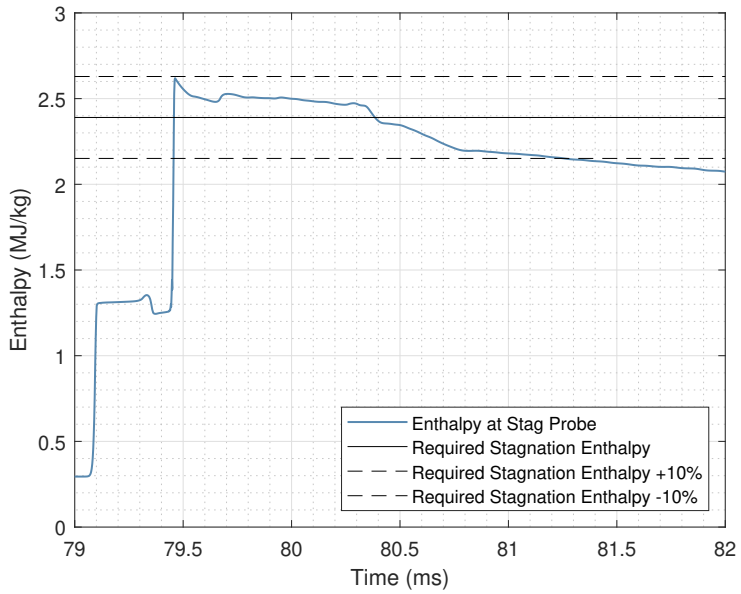


Figure 4.13: Final condition, enthalpy at the stagnation region (MJ/kg)

4.4 Experimental Setup

The Pitot rake model used is described in Chapter 3. Tunnel specific instrumentation and components are described here.

4.4.1 Blanking plate

For initial verification of the piston model, a blanking plate was used in place of the primary diaphragm, shown in Fig. 4.14. It was manufactured from S355 mild steel and 70 mm total thickness, allowing for a design pressure of 100 MPa. It was fitted with 6 nylon buffers, 60 mm in diameter and 55 mm in length to prevent the piston from damaging the blanking plate if need be. It housed a high pressure transducer (PCB Piezotronics CA102B03) in a custom brass mounting to vibrationally isolate the sensor from the facility, based on previous excessive noise observations by Gildfind [123] and Wagner [124]. Crush rods which give an indication of the piston trajectory were attached to the blanking plate. The blanking plate setup is shown in Fig. 4.14 and Fig. 4.15.

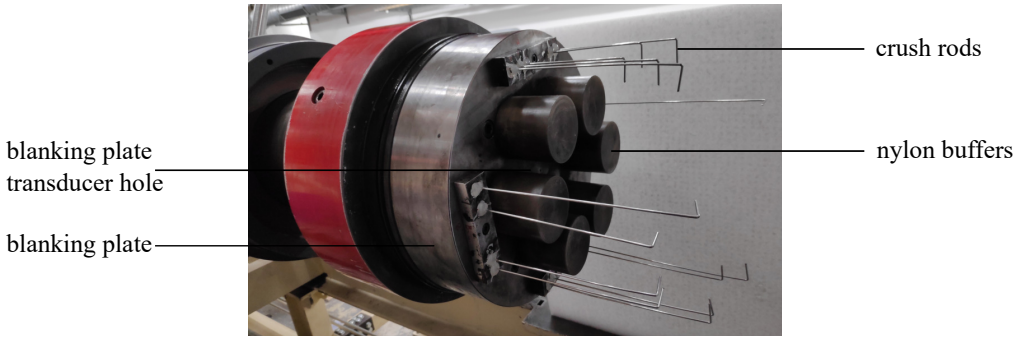


Figure 4.14: Blanking plate setup

4.4.2 Shock Timing Stations

The shock speed is obtained by pressure rise measurements from pressure transducers at shock timing stations along the shock tube and at the stagnation location. The second to last three locations are averaged to obtain the final shock speed used for the condition. These are at distances of 4.31, 5.06 and 5.81 m referenced from the primary diaphragm location. This is circled in the example shown in Fig. 4.16.

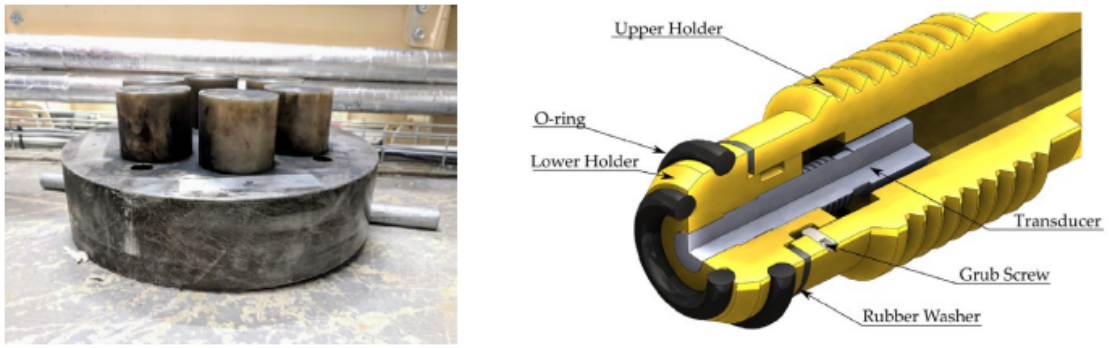


Figure 4.15: Blanking plate and buffers, post test (left) and detail of the blanking plate transducer mount (right), [92]

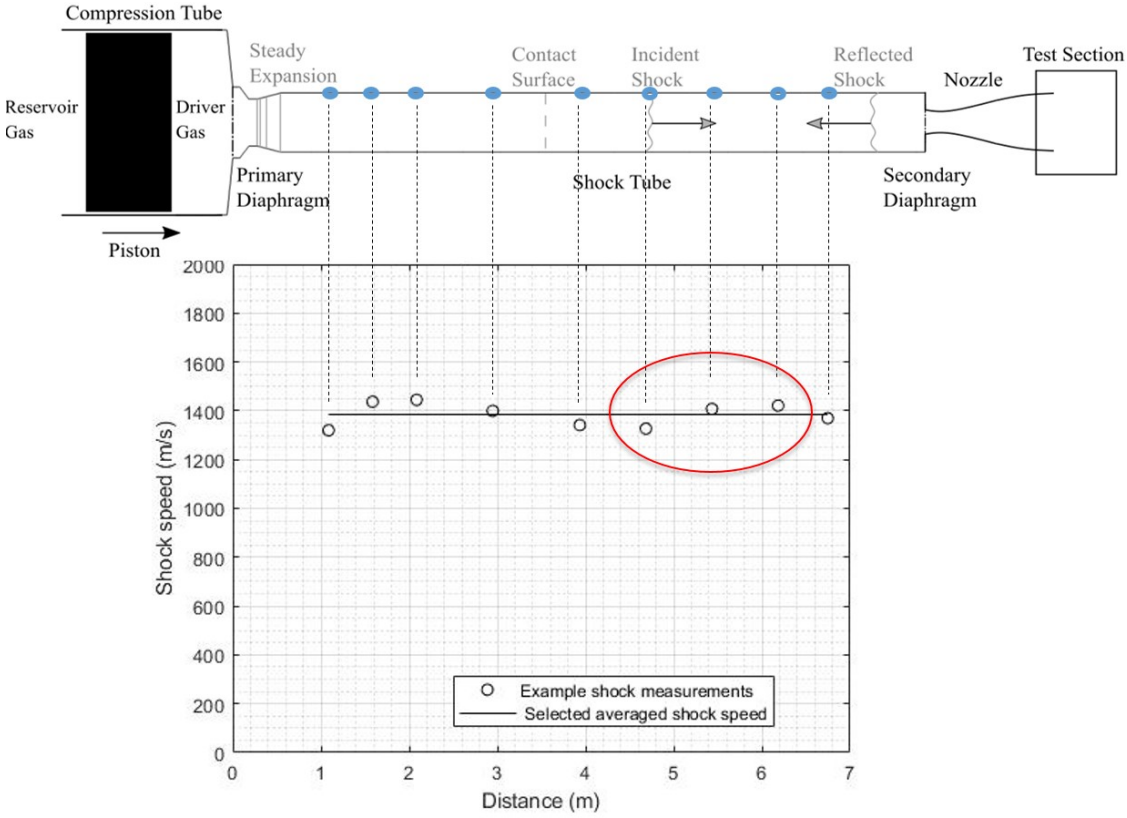


Figure 4.16: Schematic of shock timing station measurement locations and an example of the data selected to obtain the average shock speed

Typically, the Pitot rake is instrumented with PCB 113B23's or CA102B04's for the high post-shock pressures expected.

The pressure rise caused by the incident shock is manually identified for each sensor and the time between each rise is used along with the distance to calculate the shock speed.

Table 4.4: Table showing shock timing station distances from the primary diaphragm

STS Number	Distance (m)
1	0.8374
2	1.3361
3	1.8355
4	2.3355
5	3.5597
6	4.3095
7	5.0594
8	5.8095
9	6.5597

4.4.3 Stagnation Probes

The stagnation probes are fitted to the north and south locations of the stagnation block. These are copper coated inserts fitted into the tube at the region before the nozzle in order to rapidly dissipate the heat in the reflected shock region. Blank probes were fitted to the east and west locations when facing downstream. The probes used are described in Table 4.5.

Table 4.5: Table showing stagnation probe setup

Stag Probe	PCB type	Max Pressure (MPa)	Distance (m)
North	CA102B03	103.42	6.933
South	CA102B03	103.42	6.933

4.4.4 Steel Piston Refurbishment

A heavier weight piston than the existing 36 kg aluminium piston was required so the original 90 kg steel piston from the T3 tunnel was refurbished. This greatly increased the testing time. The refurbishment consisted of replacement of the wear rings, chevron seal and an FEA analysis of the effect of adding a threaded hole to the face of the piston. The internal rear ring was also replaced with an aluminium ring in order to prevent the original nylon ring from catching on the launcher D-ring seals. The refurbished piston as well as the meshed model is shown in Fig. 4.17 and a CAD drawing provided in Appendix G.

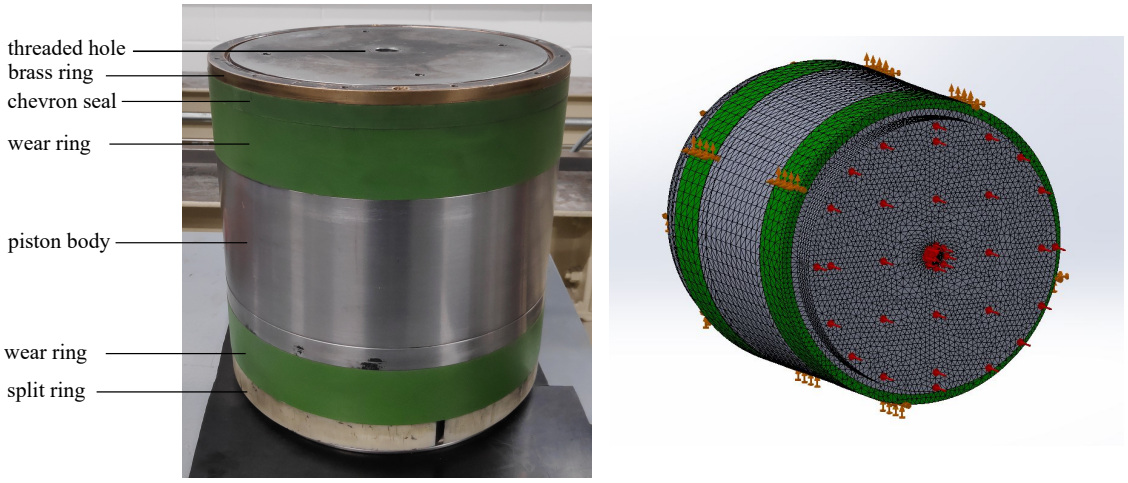


Figure 4.17: 90 kg steel piston, refurbished (left) and piston model in SolidWorks (right)

4.4.5 Diaphragms

The pressure at which the primary diaphragm ruptures is governed by the material yield strength and the depth of the score on the diaphragm, if scoring is used. The rupture process is particularly important to facilities of this type as the burst pressure strongly effects the dynamics of the piston and hence is critical to safe operation of the facility. Two options exist for diaphragms, either scored or unscored. Unscored diaphragms are plain metal sheets, while scored diaphragms have an X pattern machined onto the surface at a carefully controlled depth. Fig. 4.18 shows the before and after of an unscored diaphragm (top) and scored diaphragm (bottom). Scored diaphragms were used for these tests, for a number of reasons. The rupture pressure can be more finely controlled through the depth of the scoring. The rupture of a scored diaphragm is also cleaner, in that it will yield along the weaker score lines resulting in smaller and fewer fragments from the diaphragm breaking off and potentially damaging the tunnel or the model in the test section. Particularly for RST mode, damage to the copper coated components in the stagnation region and nozzle throat should be avoided. The score depth required to reach the desired rupture pressure was determined via the measured shock speed from experiments in the tunnel in shock tube mode. This is outlined in Section 4.5.2.

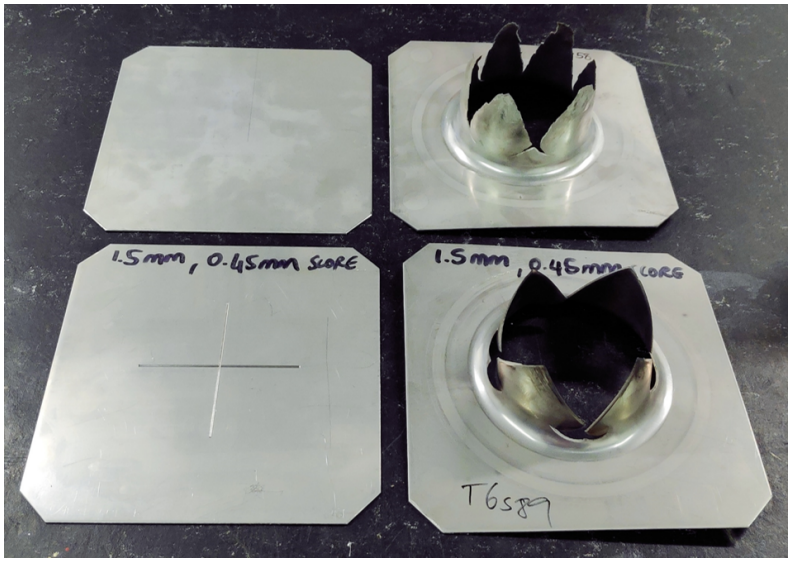


Figure 4.18: Example of unscored diaphragm (top) and scored diaphragm (bottom) before and after rupture

4.5 Experimental Results and Adjusted L1D Model

In order to validate the L1D model, particularly the piston seal friction factor and launcher loss factor which was initially assumed to be the same as for the lighter aluminium piston, blank-off tests were conducted to measure what would be the rupture pressure.

As the reservoir gas pressure for the condition was quite high and a new piston was to be used, a half blank-off test was initially run (shot 65) followed by the full blank-off condition (shot 66). The analysis which followed showed that the friction factor appeared to change a great deal between the first and second shots, which may be accounted for by the slight skimming down of the new wear rings and chevron seals after the first use. A second shot at the full condition was run (shot 67) to verify that the friction between shots was approximately constant, followed by an adjustment in L1D to match the increased friction of the steel piston and then the final blank-off test with the higher reservoir gas pressure to bring it up to the required condition (shot 68). A summary of the blank-off shots and their conditions is given in Table 4.6.

Table 4.6: Description of blank-off shots and conditions

Shot Number	Description	Reservoir P, MPa	Reservoir P, MPa (Actual) +- 2kPa	Driver P, kPa	Driver P, kPa (Actual) +-0.02
65	Half Condition	2.4	2.402	60	60.167
66	Full Condition	4.8	4.795	120	120.006
67	Full Condition	4.8	4.8	120	120.026
68	Loss Adjusted Condition	5.5	5.496	120	120.006

4.5.1 Blank-Off Tests

The initial L1D model using the aluminium piston friction factors was compared to the full condition test, shot 66. The model was subsequently adjusted to match the blank-off data ("First Adjustment"). A fourth order Gaussian curve was fitted to both the simulated and experimental data and compared on this basis, shown in Fig. 4.19. The higher frequency oscillations seen in both the experimental and numerical data were found to be time varying and therefore no one dominant frequency was found through an FFT. These are likely acoustic waves reflected off the piston face and blanking plate which increase in frequency as the piston approaches the end of the compression tube (ranging from approximately 3-10 kHz during the period shown).

The first adjusted factors were then compared to the Half Blank-Off test, shot 65. It was found that this L1D model overpredicted the peak pressure, which is an indication that after the first shot, the friction may have dropped as the piston was slightly worn after the first use. This is shown in Fig. 4.20. To verify that the behaviour of the piston remained relatively constant, a repeat of the full condition shot 66 was done and compared in Fig. 4.21. It was found that the error between them was within expected experimental variation.

Using the first adjusted factors, the reservoir gas pressure was increased from 4.8 MPa to 5.5 MPa to match the required condition. Shot 68 was done with this new reservoir gas pressure and the results compared in Fig. 4.22, which was found to be in good agreement with the pressure correlating to the required RST conditions.

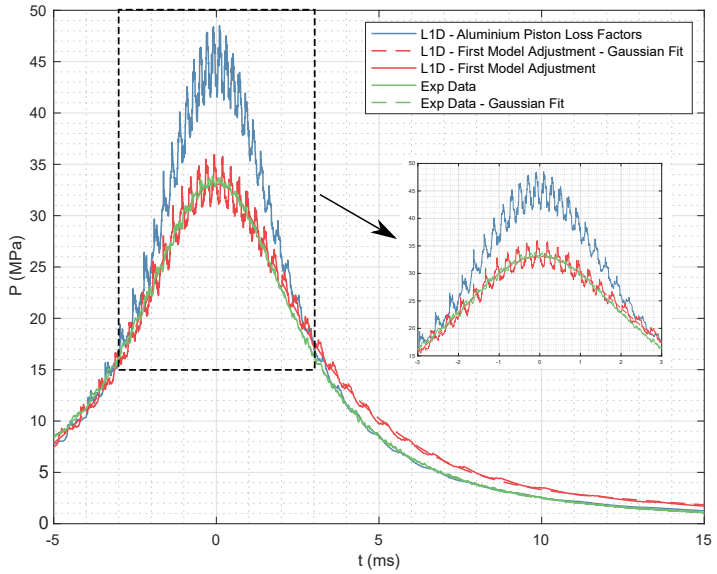


Figure 4.19: First adjusted model compared to T6 shot 66 and original model

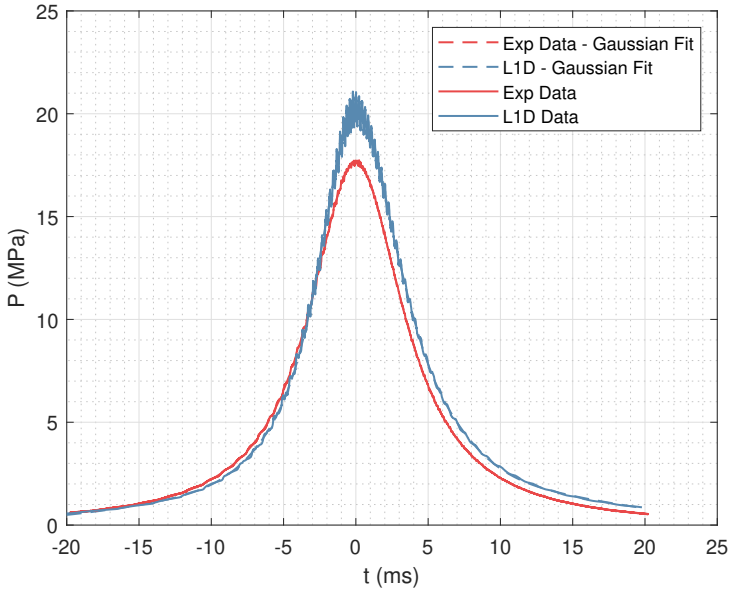


Figure 4.20: Comparison of half blank off experimental results versus L1D model with first adjusted factors

The crush rods provide an approximate indication of the piston trajectory, before and after pictures of these is shown in Fig. 4.23.

The loss factors were then further adjusted to their final value to more closely match the experimental data. Results were compared on three factors: full width at half maximum (FWHM, Fig. 4.24, left) which for a Gaussian curve

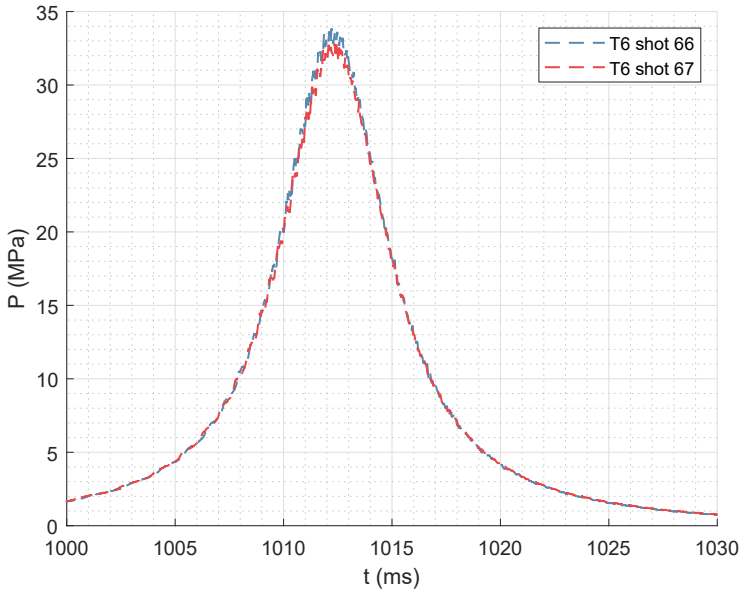


Figure 4.21: Comparison of shot 66 and shot 67

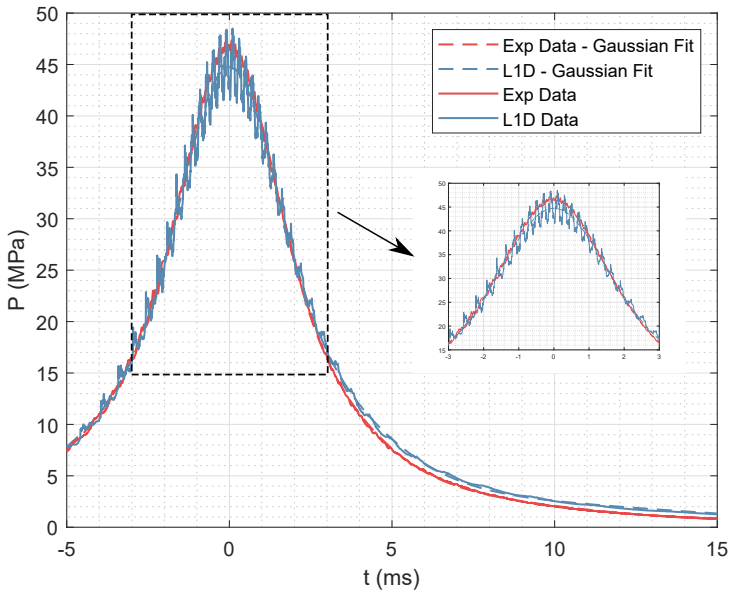


Figure 4.22: Comparison of shot 68 adjusted reservoir gas pressure to required conditions

works out to be $FWHM = 2\sigma\sqrt{2ln2}$ where σ is the standard deviation [125], experimental lag behind the L1D model (Fig. 4.24, centre) and peak pressure correlation (Fig. 4.24, right).

The results for shot 68 and a close up of the experimental lag is shown in Figure 4.25. The loss factors used should result in a model for which the experimental data lags the L1D prediction due to the pressure build up just in front of the

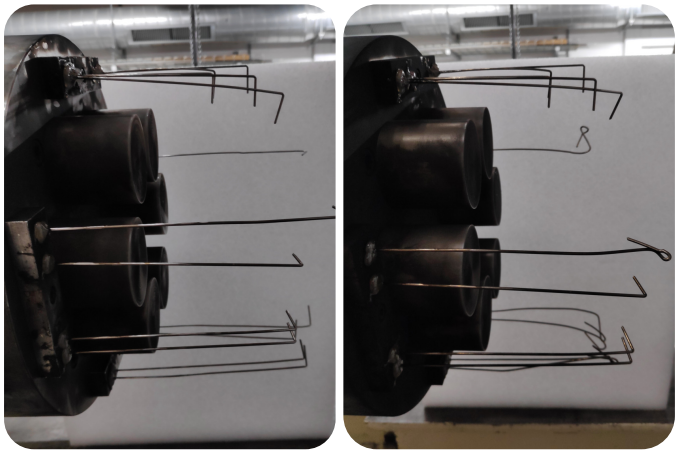


Figure 4.23: Shot 68 crush rods before (left) and after (right)

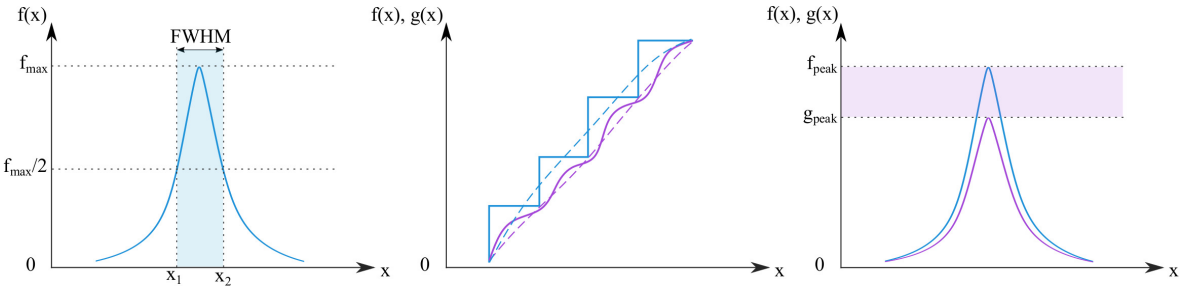


Figure 4.24: Full width at half maximum (left), experimental lag (centre), peak pressure comparison (right)

blanking plate probe.

This was then compared to all tests, with the fitted Gaussian curves for the experimental shots and L1D models compared in Figure 4.26. A summary of the original and adjusted friction factors is summarised in Table 4.7.

Table 4.7: Summary of original and adjusted loss factors

	Friction Seal Factor (f_{sf})	Launcher Loss Factor (l)
Aluminium Piston Factors	0.275	3.4
First Adjustment	1.1	3.7
Final Factors (Steel Piston)	0.88	3.7

As can be seen in Figure 4.26, the friction factors between tests seemed to decrease, which is to be expected for the first initial shots of the new piston. For the condition to be used in RST mode, good agreement was found using a friction seal factor of 0.88 and launcher loss factor of 3.7. The friction seal factor is significantly higher than the value used to model the lightweight aluminium piston.

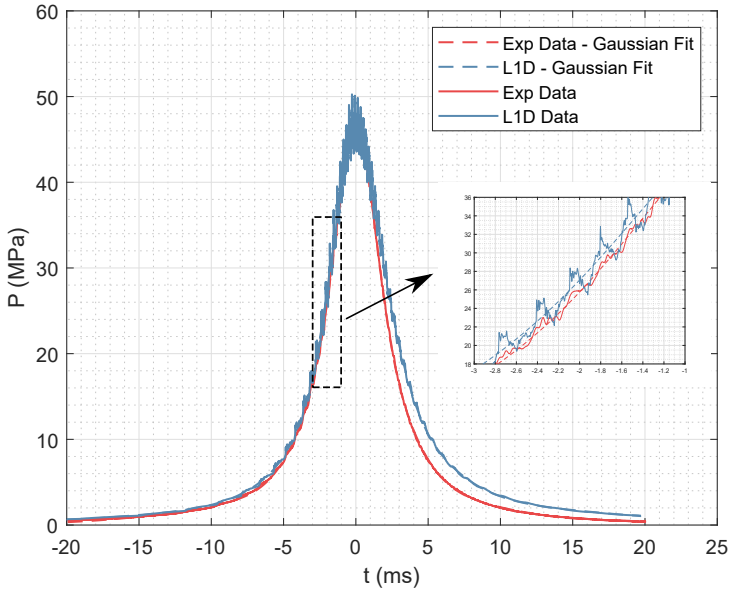


Figure 4.25: Comparison of shot 68 with final loss factors with close up to show experimental lag

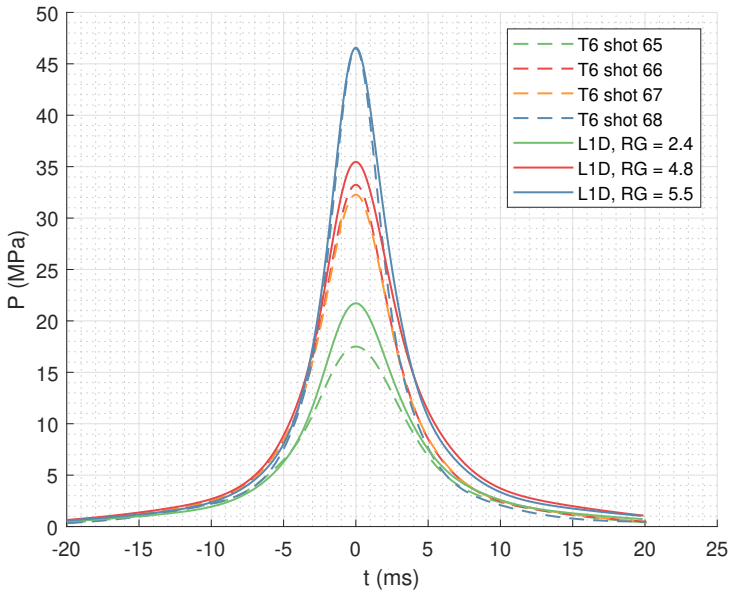


Figure 4.26: Comparison of fitted Gaussian curves of all blank-off tests with their corresponding L1D models using the final loss factors

4.5.2 Shock Tube Tests

Following the successful commissioning of the piston and blank-off tests, a shock tube test was conducted to investigate the diaphragm score depth needed to achieve the desired rupture pressure. From previous tests shock tube tests conducted by Collen

[111], it was estimated that a score depth of between 0.4-0.5 mm would be a close starting point. Preliminary results for the shock tube test with a 1.5 mm stainless steel diaphragm, scored to a depth of 0.4 mm is compared to the L1D prediction for the shock speed achieved with the nominal rupture pressure, diaphragm rupture at 20% increase and 20% decrease, shown in Fig. 4.27. This was also compared to the shock speed predicted by PITOT, the equilibrium gas rapid simulation program for free-piston driven expansion tube flows [126]. Favourable results were achieved for

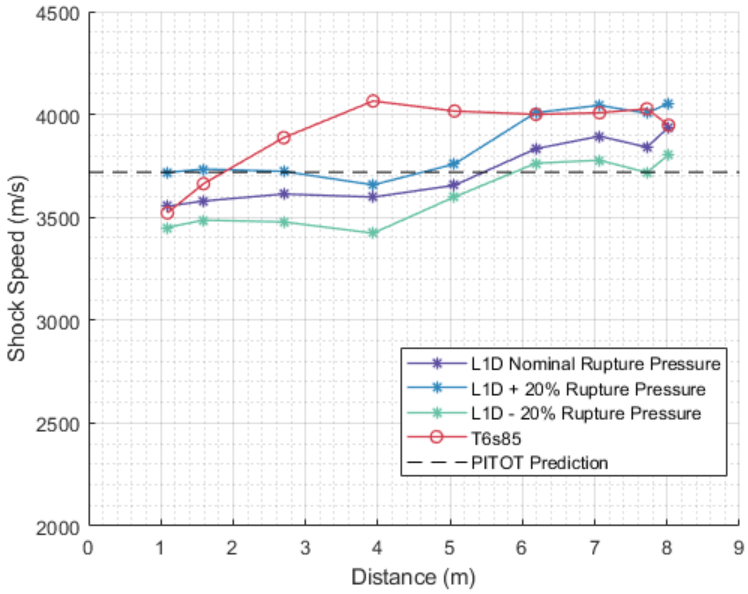


Figure 4.27: Shock speed achieved for Shot 85, compared to L1D and PITOT predictions

the overall shock speed. It is expected that some variation in the L1D predictions would occur, particularly near the primary diaphragm region (x = 0) as the rupture of the diaphragm is a complex process to model, but the shock speed at the end of the tube was well predicted at the nominal rupture pressure. From the L1d results, the diaphragm was determined to have ruptured later than predicted and so the final score depth used for the reflected shock tunnel test was 0.45 mm.

4.6 Initial Reflected Shock Tunnel Tests

A summary of the preliminary fill conditions is shown in Table 4.3 which includes conditions after the first blank-off test was completed and the final values used

for the first RST commissioning tests.

Table 4.8: Fill conditions from condition development

	p_{4i} (kPa)	p_{RG1} (MPa)	p_4 (MPa)	p_1 (kPa)	χ_{He}
Preliminary Condition	120	4.8	20.6	220	0.19
Post Blank-Off	120	5.5	20.6	220	0.19
Final RST	120	5.5	20.6	180	0.19

Three tests were successfully undertaken in RST mode with no damage to the piston, buffers or stagnation region. The initial test (Shot 86) was undertaken using the Preliminary Condition values in Table 4.8, resulting in a stagnation enthalpy and pressure of 2.43 MJ/kg and 27.8 MPa (also named Condition A0 in Table 4.10). This led to consecutive tests reducing the shock tube fill pressure to slightly reduce the stagnation pressure. Ultimately, this led to a final shock tube fill pressure of 180 kPa for shots 88 and 89 (listed as "Final RST" in Table 4.8 and Condition A1 in Table 4.10) but Condition A0 was kept as a useful alternative condition. The predicted versus achieved stagnation pressure (measured off the north pressure probe SP-N) is plotted in Figure 4.28 with the approximate test time highlighted. The measured stagnation pressure was 25.8-26.05 MPa for the two shots, within 2.6% of the desired nozzle supply pressure. In contrast to the L1D results which show a clear rise between incident and reflected shocks, an intermediate step is seen in the experimental trace. This is likely evidence of shock bifurcation, which forms due to the complex interaction between the boundary layer in the driven tube and non-planar reflected shock, similarly seen in some RST facilities compared by Mundt et al. [90], and in full-facility numerical studies by Goozee et al. [127]. Further results obtained by Goozee showed this to be affected by boundary layer thickness and end-wall geometry which explains why this step varies in severity between facilities [128].

Using ESTCj [129], the stagnation enthalpy was calculated to be 2.397-2.376 MJ/kg, within 1% of the desired condition. The ESTCj calculation was done

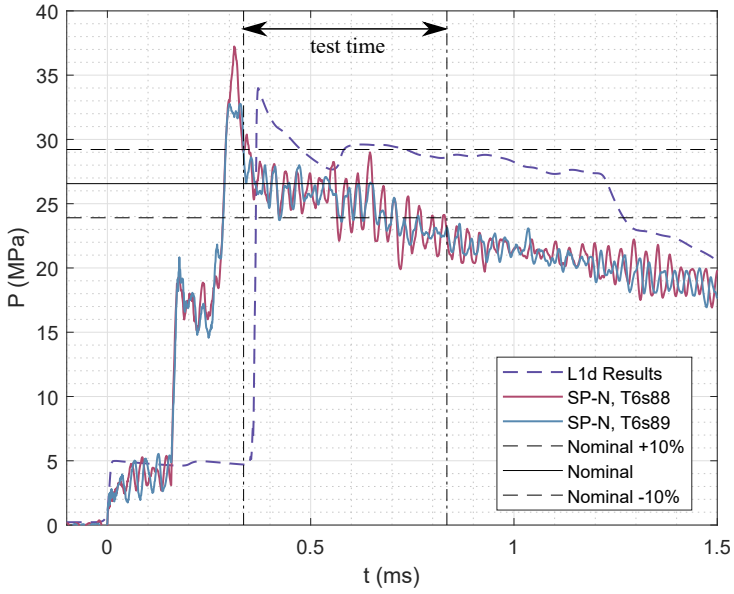


Figure 4.28: Nozzle supply pressure from RST shots 88 and 89 compared to predicted stagnation pressure with the approximate test time outlined

assuming equilibrium air of 5 species, the validity of which was explored using nozzle simulations and is addressed in later sections.

The shock speeds at each shock timing station, as compared to the L1D predictions, is shown in Figure 4.29. The shock speeds, using the shock timing stations closest to the nozzle supply, are approximately 1524 m/s and 1511 m/s for shot 88 and 89. The freestream Mach number which results is approximately 6.71 and 6.63.

The Pitot pressure was captured by six probes placed at varying positions along the Pitot rake in order to give an estimate of the core flow region. The Pitot pressure versus radial distance of the probes from the centre line of the test flow is shown in Figure 4.30. The variation from the mean for the values of Pitot Pressure/Nozzle Supply Pressure for a radial distance up to 80 mm was 1.8% for shot 88 and 1.2% for shot 89, with a mean Mach number of 6.63 and 6.68. A core flow diameter of at least 160 mm was measured and a test time of 0.5 ms was achieved. Stagnation point heat flux was measured using Diamond Heat Transfer Gauges [112]. The gauges were flush mounted in cylindrical probes with a diameter of 10.5 mm with a corner radius of 0.25 mm. Measured heat fluxes are shown in Figure 4.31 along with

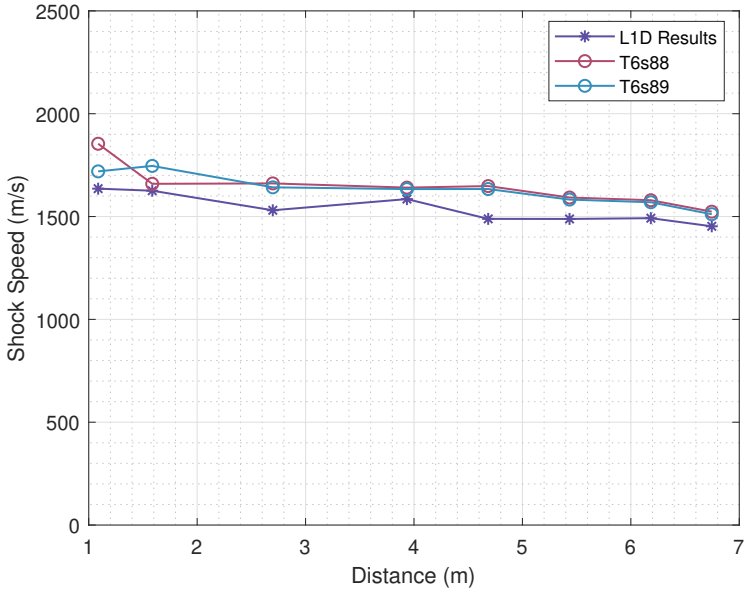


Figure 4.29: Incident shock speed (m/s) versus distance (m) for T6 in RST mode shots 88 and 89 compared to L1d prediction

a prediction based on the Fay Riddell correlation [130]. In these calculations, the flow is assumed to be in thermochemical equilibrium and an effective nose radius of 30.0 mm was used to account for the non-hemispherical geometry of the probe [131]. The heat flux is shown to be relatively steady during the test time, and agree within the measurement uncertainty of 10% of the predicted value for both shots.

RST Nozzle Simulations

The assumption of chemical and thermal equilibrium has been made in order to infer some nozzle conditions using ESTCj [129], in line with studies using other reflected shock tunnel facilities at similar conditions [90, 95, 132]. This is a code for estimating state-to-state properties in reflected shock tunnels. The limitations of this assumption are discussed here. A computational study of the Mach 7 nozzle was undertaken by T. Sopek using Eilmer4, which is an open source, Reynolds-averaged Navier-Stokes fluid dynamics solver [133] using the experimental results. It is further expanded and submitted for publication in [134] and published in [92]. Selected results relevant to this study are included here. The approach taken models the nozzle from the throat onwards following the methodology of previous

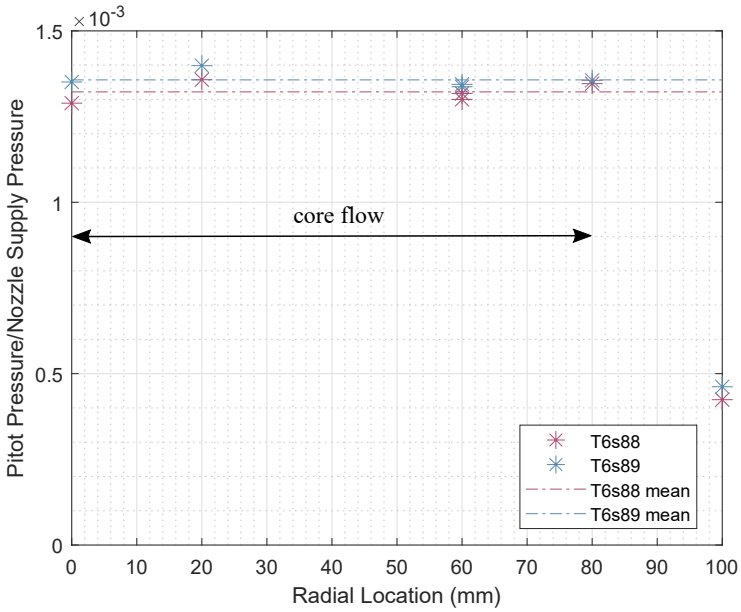


Figure 4.30: Pitot pressure versus radial distance (m) from centreline of Pitot rake

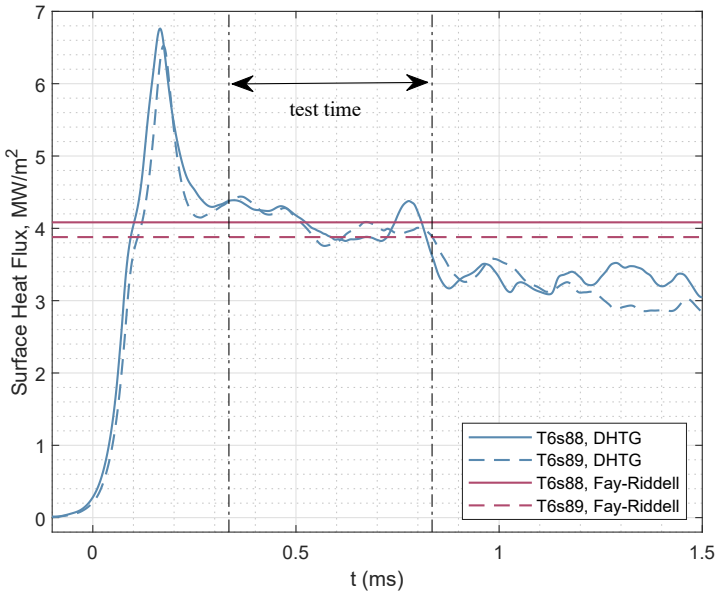


Figure 4.31: Stagnation point heat flux for shot 88 (solid lines) and shot 89 (dotted lines)

studies of similar facilities such as by Chan et al. [135]. Measured stagnation pressures were expanded to Mach 1 at the throat and the wall was assumed to be a constant temperature of 300 K. The k-ω turbulence model of Wilcox et al. was used [136] and wall functions from Nichols & Nelson [137] were implemented

to reduce computational time. The boundary layer transition location was varied until acceptable agreement with the measured Pitot pressures was achieved. The computational grid was composed of 600 and 80 cells in the axial and radial directions. Grid clustering was employed near the throat and in other regions where large flow gradients were expected. A grid convergence study is detailed in [134]. Simulations were performed with three different thermo-chemical gas models: equilibrium based on the 5-species air model from the CEA2 program of Gordon & McBride [138] (*equilibrium*), finite-rate chemistry based on Gupta & Thompson [139] (*chemical non-equilibrium*) and two-temperature thermo-chemistry based on the model of Park [140] (*thermo-chemical non-equilibrium*). Properties such as viscosity and thermal conductivity were calculated using the mixing rules of Gordon & McBride [138]. One purpose of the numerical simulation was to estimate the core flow extent, and this is shown by the Mach number contours through the nozzle and test section in Fig. 4.32. Data was extracted at the nozzle exit, indicated by the dashed white line. The Pitot to supply pressure and Mach number variation radially is shown in Fig. 4.33. This indicates that the core flow is at maximum 180 mm in diameter and extends to an axial length of 1050 mm. This matches well with the results obtained from the experimental campaign, which indicated a core flow of at minimum 160 mm (the resolution of the Pitot probes is such that only measurements every 20 mm radially could be taken).

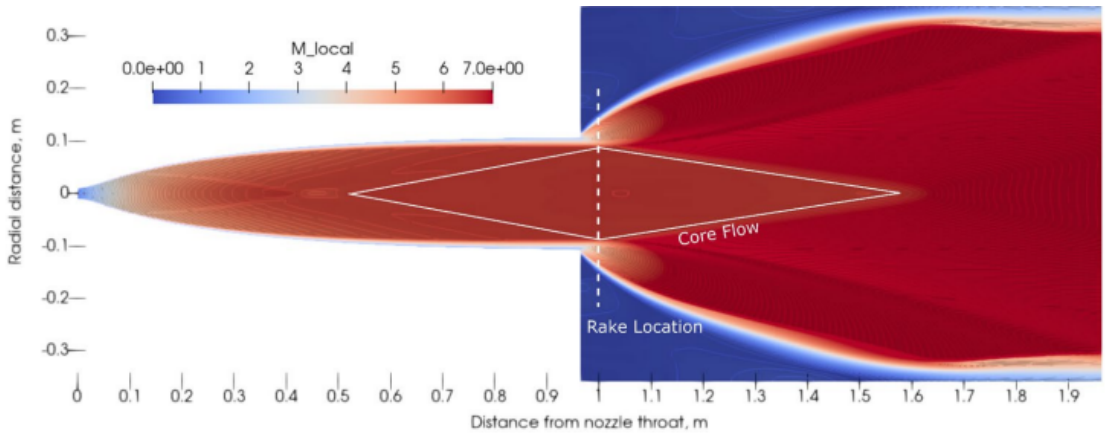


Figure 4.32: Contour plot of Mach number for the Mach 7 nozzle and test section, indicating the core flow region and Pitot rake location

The Pitot to supply pressure results show very good agreement between gas models and good uniformity through the core flow. However, the assumption of equilibrium flow does have an effect on the Mach number and static pressure. While the equilibrium and chemical non-equilibrium results agree well, the thermo-chemical non-equilibrium model shows some variation. Fig. 4.34 shows results modelling the static pressure and temperature at the nozzle exit.

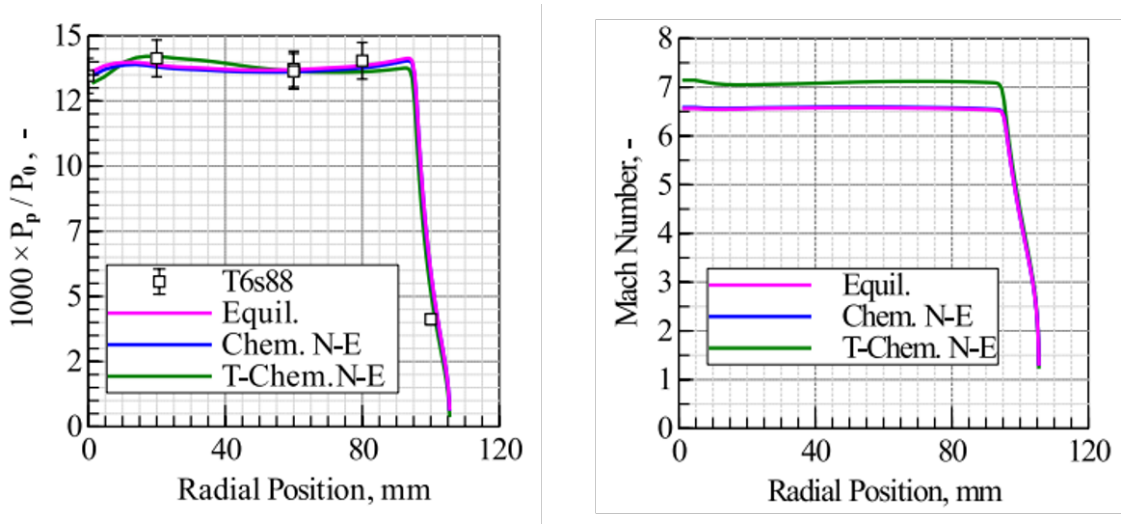


Figure 4.33: Pitot to stagnation pressure ratio (left) and Mach number (right) at nozzle exit

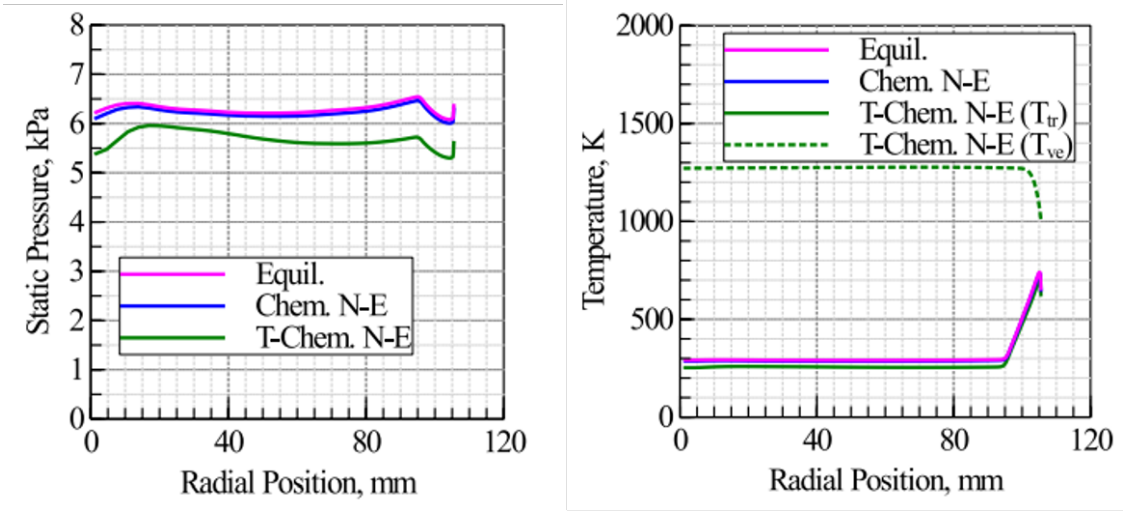


Figure 4.34: Static pressure profile (left) and temperature (right) at nozzle exit

The simulations reveal that the freestream static temperature is approximately 270 K for an equilibrium and chemical non-equilibrium flow, while for thermo-

chemical non-equilibrium the vibrational temperature is frozen at 1270 K. Thus, the assumption of equilibrium flow in the freestream requires further exploration to confirm the degree of thermal non-equilibrium for the conditions used here. This is planned in future but for now, freestream calculations were made based on equilibrium assumptions using ESTCj [129] with the knowledge that this may introduce some error in static pressure and Mach number.

4.7 Use of nitrogen-argon driver gas mixtures for extended test time

Following the initial RST mode tests, a method of increasing the test time and stagnation pressure was explored. The original condition was still used but the option of replacing the Mach 7 with the Mach 8 nozzle was also explored, with the added advantage that for establishing the first boundary layer experiments in T6, the larger nozzle exit area would result in a less noisy flow over the model.
Two options in terms of altering the condition were also considered, increasing the helium ratio and shock tube fill pressure with the aim of increasing the stagnation pressure and temperature, or the use of a nitrogen-argon driver gas. The former option was explored but due to the reduced test time, this was not used. The use of a nitrogen driver gas is explored in this section.

For stagnation enthalpies lower than around 3 MJ/kg, tailored conditions become more difficult to achieve because the sound speed of the driver gas needs to be significantly reduced, lower than can be achieved by a pure argon driver. A driver gas mixture of nitrogen-argon is proposed by Chan et al.[141] (an extension of the work by [142, 143]). This was investigated as a suitable means of extending the test time for the low enthalpy condition. The initial fill parameters (nitrogen-argon composition, burst pressure and shock tube fill pressure) were chosen following the method described in Chan et al.[141]. Since tuned driver conditions had been established in T6 and differ greatly from those in T4 because of the different tunnel geometries, the driver fill pressure and reservoir pressure were chosen for T6 based on previous tests rather than the values listed for T4. This was then modelled in

L1d and manually optimised to achieve a satisfactory result for testing ("Pre-Test Condition D" in Table 4.9). During the commissioning tests the shock tube fill pressure was slightly adjusted to improve the test time and the final shock tube fill pressure for this condition ended up being 30 kPa higher.

Table 4.9: Modifications to nitrogen driver gas conditions

Condition	Driver Composition (mass fraction)	Burst Pressure (MPa)	Shock Tube Pressure (kPa)
From Chan et al.[141]	17% N2/Ar	37	245
Pre-Test Condition D	15% N2/Ar	29	230
Post-Test Condition D	15% N2/Ar	29	260

The commissioning tests for the Mach 8 nozzle were performed with the Pitot rake at a distance of 40 mm from the nozzle exit ("Rake forward") and 230 mm from the exit ("Rake aft") to determine the extent of the core flow. Fig. 4.35 shows the stagnation pressure as well as the times at which the pressure rose or dropped ± 10% of the nominal for both Pitot rake locations. The shock speeds

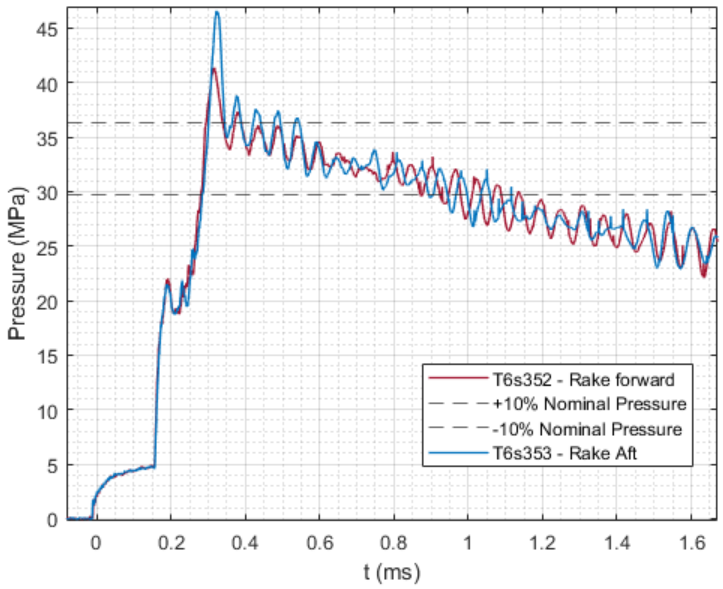


Figure 4.35: Stagnation pressure for forward and aft Pitot rake positions, Mach 8 nozzle and N2 driver condition D

are shown in Fig. 4.36, with the averaged values over the second to last three

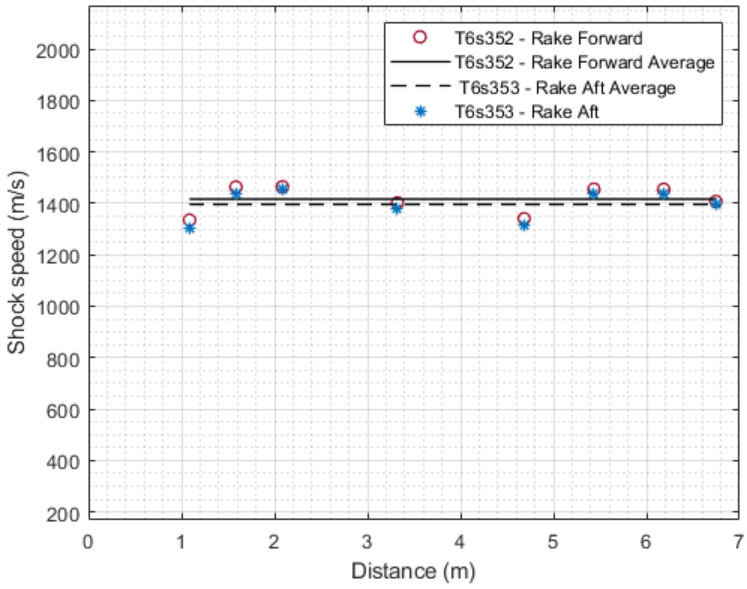


Figure 4.36: Shock speed for forward and aft Pitot rake positions, Mach 8 nozzle and N2 driver condition D

stations used. Fig. 4.37 shows the diameter of the core flow is at least 180 mm and extends to at least 230 mm from the nozzle exit. This confirms that the core flow is acceptable for testing of the cone model, but in order to fully characterise where the core diameter starts to decrease, additional Pitot rake tests should be done at distances further downstream.

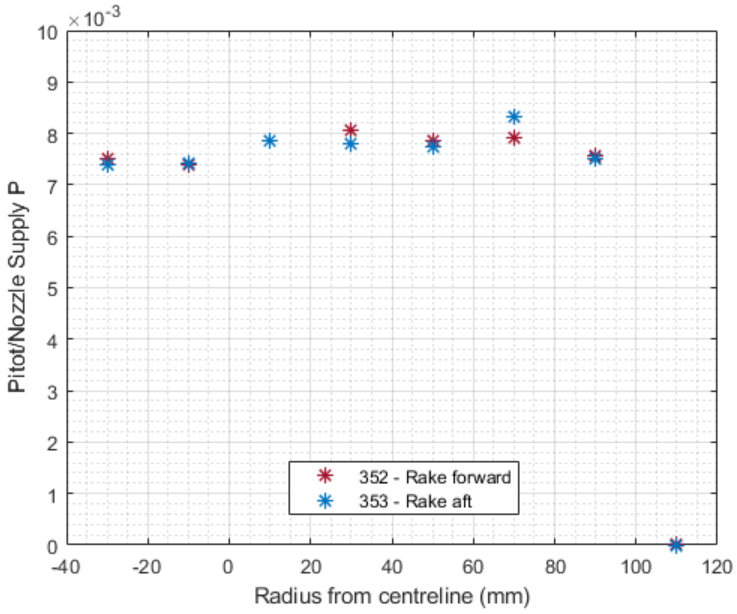


Figure 4.37: Pitot to nozzle supply pressure indicating core flow diameter for forward and aft Pitot rake positions, Mach 8 nozzle and N2 driver condition D

4.8 Summary of T6 RST Mode Conditions Commissioned

A summary of the conditions which have been commissioned in T6 RST mode to date are summarised in Table 4.10.

Table 4.10: Nominal conditions commissioned in T6 RST mode

Name	Res P (MPa)	Driver P (kPa)	Driver χ (mass)	Prim. Diaph (mm)	Burst P (MPa)	ST P (kPa)	Sec. Diaph (mm)	Stag P (MPa)	Stag H (MJ/kg)	$Re_{U,\infty}$ (e6/m)
A0	5.5	120	19% He/Ar	1.5 SS, 0.45 score	20.6	220	0.07 Mylar	28	2.43	12
A1	5.5	120	19% He/Ar	1.5 SS, 0.45 score	20.6	180	0.07 Mylar	26	2.40	10
B	5.85	120	40% He/Ar	1.5 SS, 0.45 score	20.6	350	0.07 Mylar	33	2.6	16
C	5.85	120	15% He/Ar	1.5 SS, 0.35 score	29	50	0.07 Mylar	19	5.3	2.6
D	6.0	100	15% N2/Ar	1.5 SS, 0.35 score	29	260	0.01 Mylar	33	2.3	15

4.9 Selection of Appropriate Test Time

When testing a model in a reflected shock tunnel, the selection of the appropriate test time is not obvious and becomes important since the flows are inherently transient in nature and typically on the order of milliseconds, depending on the condition, tunnel geometry and tailoring. In HDT this is not relevant because the test times are significantly longer and the flow has established long before the flow time plateaus over the conditions of interest (shown later in Section 6.2.2).

The test time is the period over which the desired flow properties remain relatively constant which is used to take the measurements of interest over the model. In T6 the processes which need to be considered are as follows: the slug of quasi-stagnant gas (nozzle supply gas) is expanded through the nozzle, which then requires some time for nozzle start up. The nozzle is considered to be started once the initial unsteady expansion has been swept out [144]. The flow then needs to establish over the model, which typically requires a number of flow lengths (for further details on the method see [145], [146], [147], [148]). The non-dimensional ratio of the length of flow that has passed to the length of the flow feature is given by G [147]:

$$G = U_c t_{est} / L_c \tag{4.33}$$

where G has a different values depending on the flow feature of interest based on correlations such as those for flat plates by Davies and Bernstein [149], L_c is the characteristic length and U_c is the characteristic velocity. The characteristic length is typically the length of the model, or to the selected sensor. G has been shown to vary from 2 for laminar flows and approximately 1 for turbulent flows [148]. For flat plates, approximately 3.3 flow lengths are required for skin friction measurements while G is 0.9 for pressure measurements [149]. Jacobs et al. [147] showed that the flat plate correlation could be extended to a generic scramjet configuration at high Mach numbers. The methodology for the selection of the appropriate test time applied to experiments in T6 is described later in Section 7.2.3.

4.10 Conclusion

An experimental campaign was launched to commission the Oxford T6 Stalker Tunnel in reflected shock tunnel mode. For given test flow requirements, the shock tube fill conditions and diaphragm rupture parameters were developed using a method which can be applied to a range of future test conditions at low enthalpies. Tailoring of the driver gas pressure and composition was done in order to maximise test time by minimising the interaction between the reflected shock and contact surface. The chosen pressures of the reservoir and driver gas were found to achieve acceptable tuned conditions of the piston. A refurbished 90 kg steel piston was commissioned and blank-off tests performed to verify the loss factors used in modelling the flow using the quasi-one-dimensional gas dynamics code L1d. This was important to ensure correct piston tuning as there are no brakes which can result in rebound motion after reflected shock arrival at the driver. The steel piston loss factors were then used to obtain the increased reservoir gas pressure which would achieve the required conditions, which was an increase of 0.7 MPa. A shock tube test was run to verify the score depth required to produce the desired rupture pressure of 20.6 MPa. Comparing results to the predicted shock speed, the diaphragm score depth was subsequently adjusted for reflected shock tunnel mode. The first commissioning shots of reflected shock tunnel mode were successfully performed and the results presented. The shock tube fill pressure was adjusted by approximately 18% to bring it closer to the required conditions. The final condition achieved was within 1% of the predicted nozzle supply enthalpy and 2.6% of the nozzle supply pressure, with a test flow time of approximately 0.5 ms and core flow diameter of at least 160 mm. Further test conditions were developed and are summarised in this chapter, including a nitrogen driver condition to improve the test time to approximately 0.7 ms for use with the Mach 7 or Mach 8 nozzles available. Commissioning tests were performed with the Mach 8 nozzle to provide a condition with reduced freestream noise and the results of these tests with forward and aft Pitot rake positions to characterise the core flow extent are presented.

This chapter concludes the first work done by the author to develop and commission

the T6 Stalker Tunnel in the Reflected Shock Tunnel mode of operation. This mode gives the UK it's first capability of performing hypersonic experiments over Mach 7 at total enthalpies which are flight representative. It demonstrates the capacity of T6 to perform as a multi-mode facility and allows for the future development of a range of further conditions which opens up a host of new avenues for hypersonic flight research.

Elements of the work done in this chapter are included in the following publications:

[91] S. D. Subiah, P. L. Collen, L. J. Doherty, R. T. Penty Geraets, A. Hyslop, and M. McGilvray. "Condition Development and Commissioning of the Oxford T6 Stalker Tunnel in Reflected Shock Tunnel Mode". In: International Conference on Flight Vehicles, Aerothermodynamics and Re-entry Missions & Engineering (2019)

[92] P. L. Collen, L. J. Doherty, S. D. Subiah, T. Sopek, I. Jahn, D. E. Gildfind, R. T. Penty Geraets, C. Hambidge, R. G. Morgan, and M. McGilvray. "Development and Commissioning of the T6 Stalker Tunnel". In: Experiments in Fluids (2021)

[134] T. Sopek, P. A. Jacobs, S. D. Subiah, P. L. Collen, and M. McGilvray, "Effect of non-equilibrium thermochemistry on Pitot pressure measurements in shock tunnels". Submitted to AIAA Journal (2022)

[150] P. L. Collen, L. J. Doherty, S. D. Subiah, A. Hyslop, and M. McGilvray, "Performance Capability Experiments in T6: A Hypervelocity, Transient and Multi-Mode Ground Test Facility for High-Enthalpy Aerothermodynamics Research," In: International Conference on Flight Vehicles, Aerothermodynamics and Re-entry Missions & Engineering (2019)

[151] P. L. Collen, "Development of a High-Enthalpy Ground Test Facility for Shock-Layer Radiation," DPhil Thesis, University of Oxford (2021)

5

Development of High-Speed Schlieren Image Processing Techniques

Contents

5.1 Introduction 99
5.2 The Morlet or Continuous Wavelet Transform 100
5.3 Image Pre-Processing 104
5.3.1 Schlieren Spatial Calibration 106
5.4 Frequency Detection Methods 107
5.4.1 Intensity Probe 107
5.4.2 Image Stitching 108
5.4.3 Cross Correlation 109
5.4.4 Semi-Global Matching 111
5.4.5 Gradient Convection Speed Method 112
5.5 Feature Detection Methods 113
5.5.1 CWT for Feature Detection 113
5.5.2 Bispectral Analysis 114
5.5.3 Spectral Proper Orthogonal Decomposition (SPOD) . . 118
5.6 Summary 121

5.1 Introduction

Second mode instabilities, described in Chapter 2 can be identified from schlieren images by clear 'rope-like' structures in the boundary layer, an example of which is shown in Fig. 5.1 from images captured in the HDT campaign which will be

explored later. They are typically characterised by their frequency, wavelength, structure angle and wavepacket convection velocity.

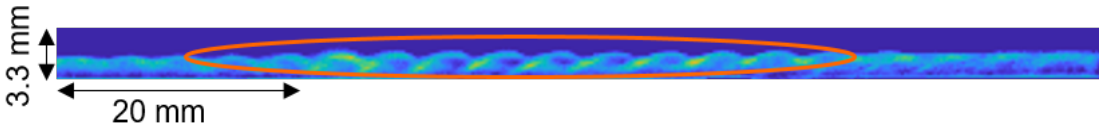


Figure 5.1: Example of second mode instability wavepackets on the surface of a 7^o half angle cone in Mach 7 flow (flow is from left to right) circled, colour map applied for clarity

Due to the acoustic nature of the waves, the density gradients produced are well suited to being visualized by schlieren imaging and this is particularly useful when the frequency of the second mode instabilities exceeds the limits of current pressure sensors. With the use of high speed cameras capable of capturing images at over a million frames per second, the identification and tracking of whole wavepackets and individual waves is possible, allowing quantitative data to be extracted through non-intrusive means. Methods which allow the extraction of these frequencies using much lower frame rates are also explored. These methods are particularly advantageous as even the highest speed cameras available are not always able to resolve these high frequencies directly. More straightforward methods of extracting the frequency from pixel intensities which will be described further, require the sample rate to be more than double the expected frequency to be extracted. Both high and low frame rate methods are applied specifically to the dataset obtained from the High Density Tunnel, for which the experimental setup (Chapter 3) and full results are presented in Chapter 6 where they can be verified with pressure transducers. Once the suitability of these methods are established, selected methods will be applied to the experiments undertaken in T6.

A variety of options can be found for processing schlieren imaging, ranging in complexity ([54, 68, 69, 152]) and including wavepacket identification with mass injection ([153]). Jewell et al. first proved the validity of using schlieren to measure disturbances for Mach 6 flow with thin boundary layers (on the order

of 0.5 mm) and the highest frequencies for which this method has been applied before now (up to 1MHz) [154] but little other data is available at or above these frequencies. Shumway and Laurence [152] highlighted methods for detecting both wavepackets and turbulent spots. The work presented here compares image processing methodologies which are suited to second mode instabilities captured at low frame rates (well below the frequency of the second mode instability) and high frame rates (well above the Nyquist limit).

5.2 The Morlet or Continuous Wavelet Transform

This section provides an explanation of the Morlet transform (also known as the Continuous Wavelet Transform or CWT) and a comparison of the methodology to a Fourier Transform. In cases where the signal is interrupted by transients which are physical features and need to be characterised, the CWT can provide more detailed frequency information than a short-time Fourier transform. It is thus particularly useful in the identification of discrete wavepackets convecting downstream. Studies such as those done by Shumway and Laurence [152] apply this method to schlieren images to identify discrete wavepackets and turbulent spots. A two-dimensional CWT can be applied to an image, which is essentially composed of signals with varying pixel intensities in space. The Morlet transform was developed by the geophysicist Jean Morlet in 1982 based on an intuitive approach and previous analysis of seismic time-frequencies. It was later formalised by mathematicians and renamed the Continuous Wavelet Transform. (For further details, see [155]). The analysis was traditionally formulated for one-dimensional time signals, but can be extended to two or more dimensions (such as x and y for an image) and retain the same properties as the 1D case [156]. The basics are explained here for a one-dimensional signal, for further details on the two dimensional implementation see [156].

Consider a sinusoidal wave with period X_0 (in blue) and it's cosine which starts on zero phase (red),

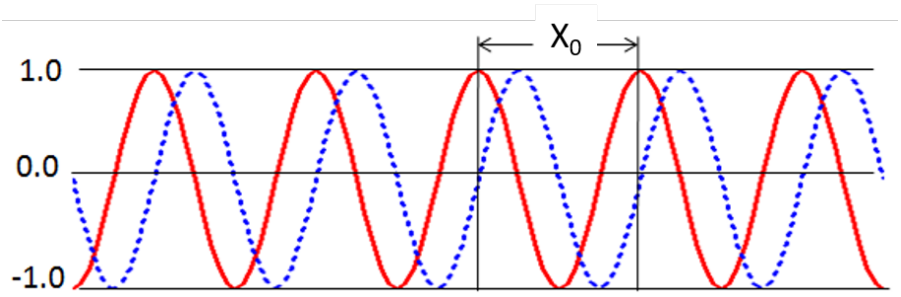


Figure 5.2: Example of a pure sinusoidal wave and it's cosine, or zero phase, function adapted from [155]

noting that it is infinite in length. The sinusoidal component can be expressed as

$$s(x) = exp(i\omega_0 x) = \cos\omega_0 x + i\sin\omega_0 x \tag{5.1}$$

where:

$$\begin{aligned} i &= \sqrt{-1} \\ \omega_0 &= 2\pi f_0 = \frac{2\pi}{X_0} \end{aligned} \tag{5.2}$$

f_0 and X_0 are the mean frequency and period [155]. ω_0 is the mean angular frequency.

Next consider a Gaussian envelope in x, Fig. 5.3, which is a smooth curve outlining the extremes of an oscillating signal which Morlet et al. wrote as:

$$g(x) = exp\left[-\left(\frac{2x\sqrt{\ln 2}}{\Delta x}\right)^2\right] \tag{5.3}$$

Δx is the width of the Gaussian envelope [157], defined as the distance between the envelope at half it's maximum amplitude.

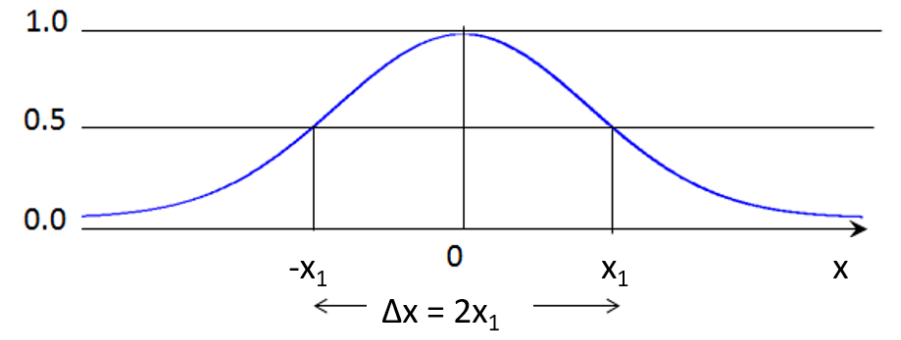


Figure 5.3: Example of a Gaussian envelope function with the width equal to the distance between half maximums (Δx), adapted from [155]

The product of these two functions, shown graphically in Fig. 5.4, can be written:

$$\psi(x) = exp\left[-\left(\frac{2x\sqrt{\ln 2}}{\Delta x}\right)^2\right] exp(i\omega_0 x) \tag{5.4}$$

The effect of the Gaussian envelope is also to restrict the signal to a finite length with decaying edges. For the frequency domain, this is shown by Morlet et al. [158] to be:

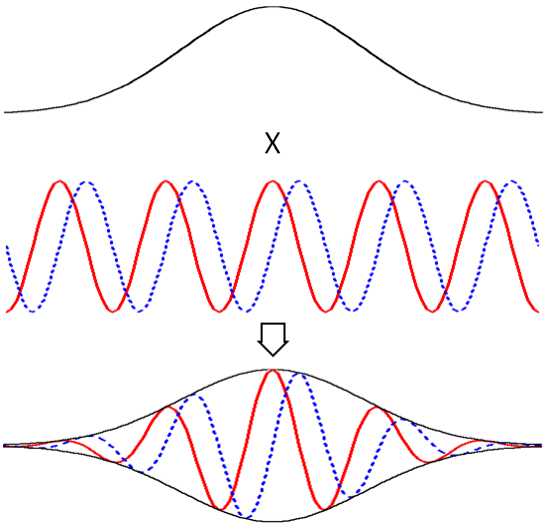


Figure 5.4: Graphical representation of the product of a Gaussian function (top) and sinusoidal waves (middle), resulting in the final wavelet (bottom) with amplitude envelope superimposed [155]

$$\Psi(\omega) = \frac{1}{2}\sqrt{\frac{\pi}{\ln 2}}\Delta x\ exp\left[-\left(\frac{\Delta x(\omega-\omega_0)}{4\sqrt{\ln 2}}\right)^2\right] \tag{5.5}$$

Morlet et al. also related the time width at half maximum amplitude to the mean period using a "shape ratio" k:

$$\Delta x = kX_0 \tag{5.6}$$

A graphical demonstration of the effect of different shape ratios while keeping the dominant period the same (20 mm) is shown in Fig. 5.5, left. The dominant period X_0 can also be varied, shown in Fig. 5.5, right, for a fixed shape ratio. This has a stretching effect while preserving the shape.

In addition, a directionality component can also be introduced to detect oriented features (the 2-D Morlet wavelet is directional) [156]. These parameters are varied until the closest identification of a wavepacket is obtained.

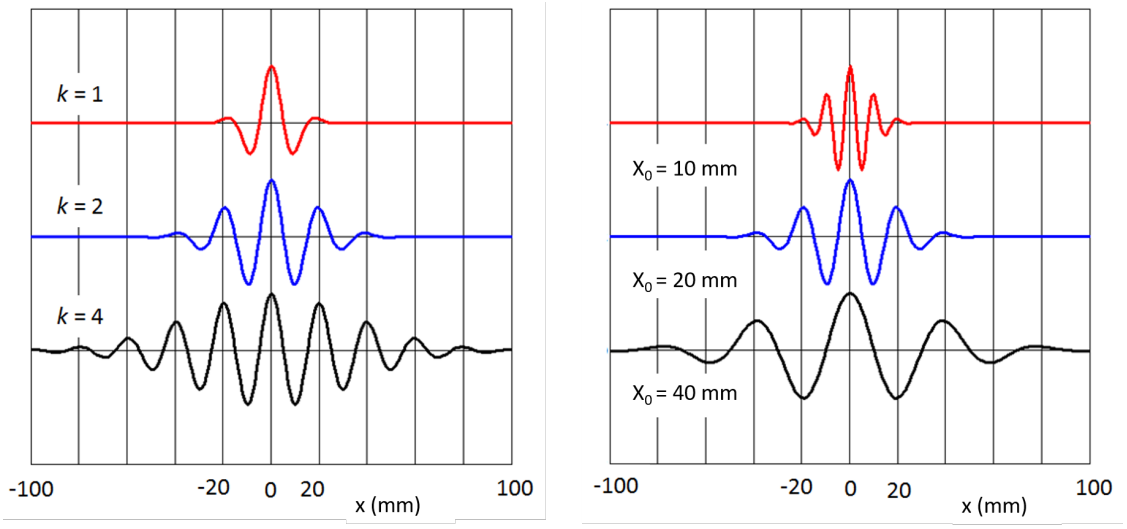


Figure 5.5: The effect of varying the shape ratio k (left) and the effect of varying the dominant period X_0 (right), adapted from [155]

5.3 Image Pre-Processing

This section details the initial steps taken to process the images before further analysis can be applied. It is summarised in Fig. 5.6 and described in detailed here with example images (shown in colour instead of grayscale for clarity).

This series of steps were done before the other processing techniques were applied in order to get the best possible image quality.

The images, backgrounds and spatial calibrations are loaded in. Background images were taken with the flow off, at the same camera and lighting settings set for the actual test. The background images are subtracted from their flow-on images in order to isolate the boundary layer. This process is shown in the series of images in Fig. 5.7. Next, the spatial calibration is done (described below in Section 5.3.1). In some cases, particularly for use in the Spectral Proper Orthogonal Decomposition (SPOD) analysis described later, or with extremely thin, high intensity boundary layers, it was necessary to also subtract an averaged image in order to enhance sensitivity and the presence of instabilities. This is similar to the process of "unsharp masking", described in Settles [62], where a copy of the image is blurred to remove detail then subtracted from the original in order to remove slowly varying gradations

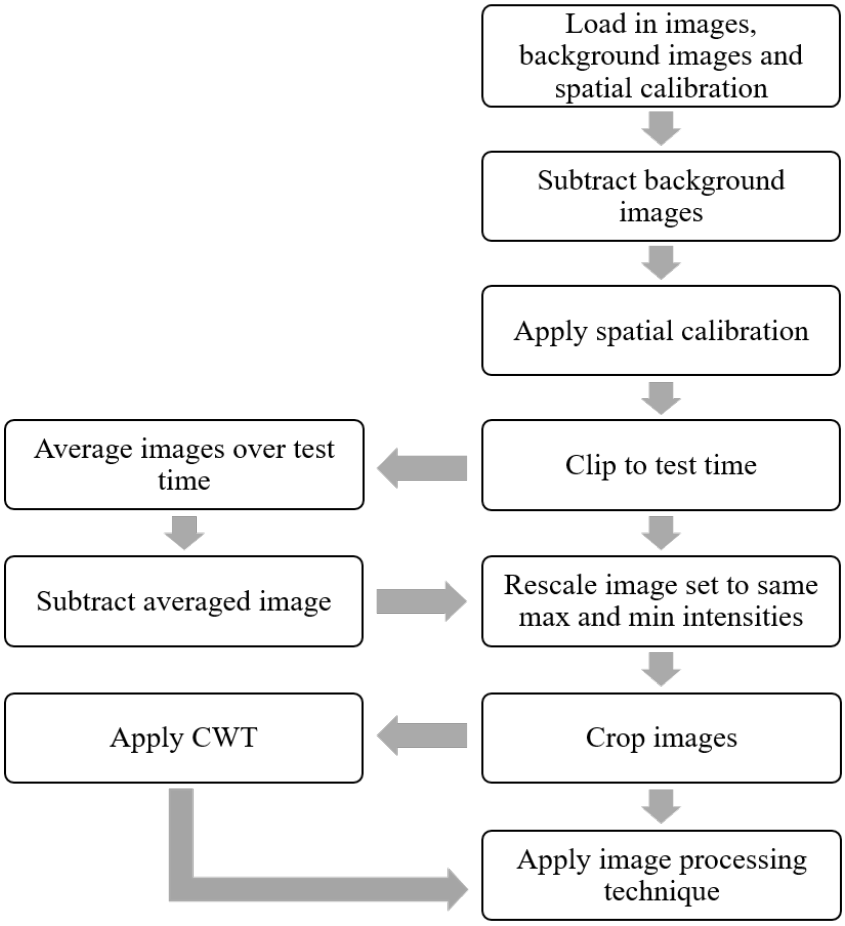


Figure 5.6: Flowchart summarising background image processing

and enhance detail. In this case, the flow-on images over the test time are averaged and then subtracted, shown in Fig. 5.8.

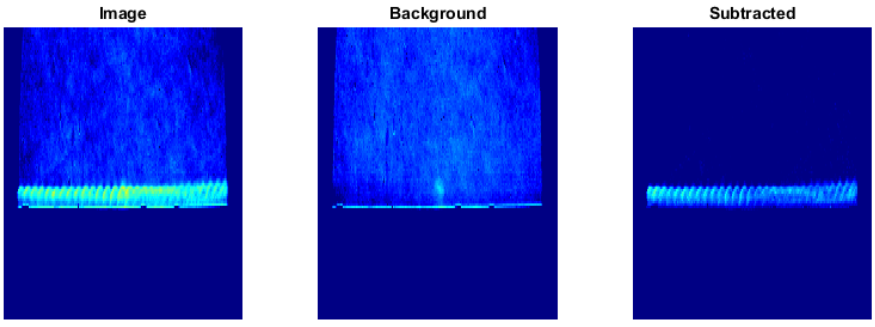


Figure 5.7: A selected example frame, it's background image and the subtracted image

The background-subtracted, or if applicable, mean-subtracted images are then rescaled in terms of intensity to the same maximum and minimum values in order

to account for any non-uniformity in the output of the light source and to improve the contrast of the images. An example of this is shown in Fig. 5.9.

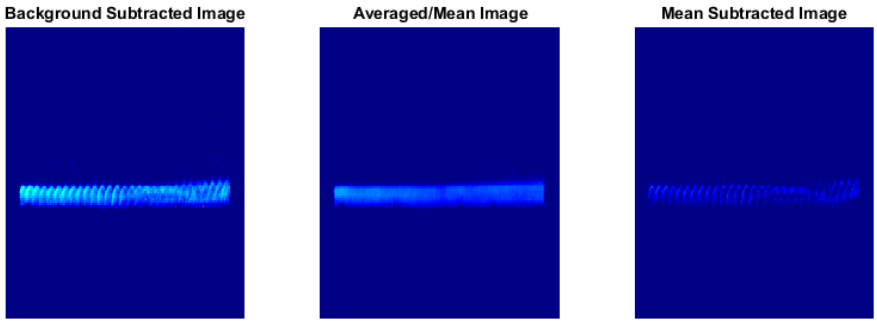


Figure 5.8: The background and mean subtracted images

The images are also cropped to the region of interest around the boundary layer, Fig. 5.9.

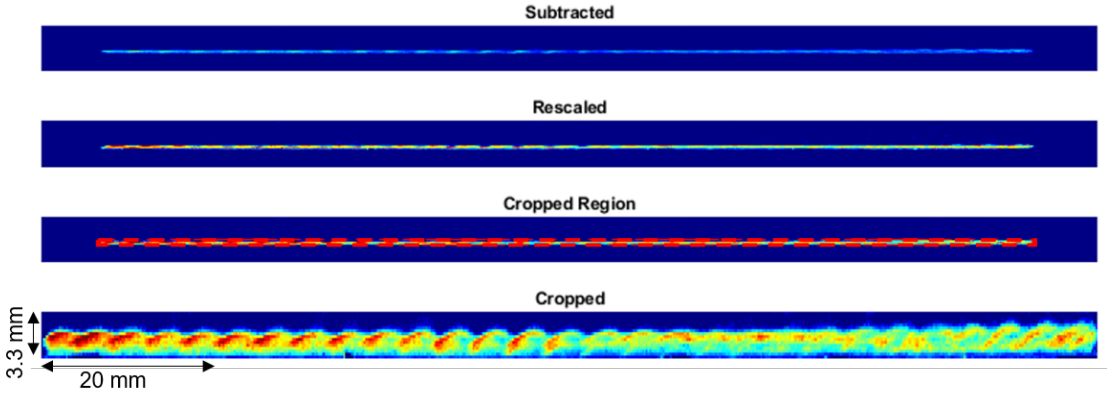


Figure 5.9: The subtracted image, its rescaled and cropped image. The cropped region is highlighted by the red dashed line

For some of the processing techniques used it is useful to first apply a continuous wavelet transform to the images to highlight the regions of clear wavepackets or enhance their signal. The wavelet transformed images are shown in Fig. 5.10.

5.3.1 Schlieren Spatial Calibration

The viewing location on the cone and the relation between a pixel on the image and the real distance on the cone was obtained by spatial calibration. An image of the cone with a known object placed at a known location (in this case a ruler

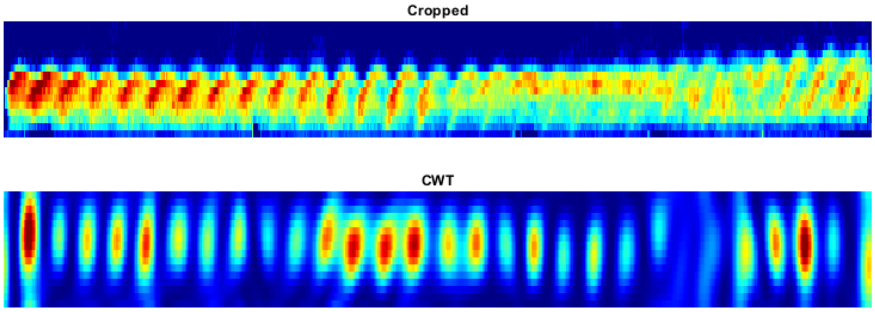


Figure 5.10: The cropped image and image with continuous wavelet transform applied. Dimensions are the same as Fig. 5.9, y axis enlarged for clarity

placed at the centre of a Kulite sensor) was taken at the same magnification settings as the flow-on test image. This was done for each experiment in HDT and T6 as the settings and viewing locations were different in each. An example of the spatial calibration image taken for shot 1922 is shown in Fig. 5.11. The width of the ruler was measured and related to the number of pixels representing the ruler width in the image in order to get a pixel-to-mm ratio. The axes of the schlieren images could then be determined in terms of real units. The surface of the cone was identified in the image by edge detection and then manual verification if the edge detection was not fine enough.

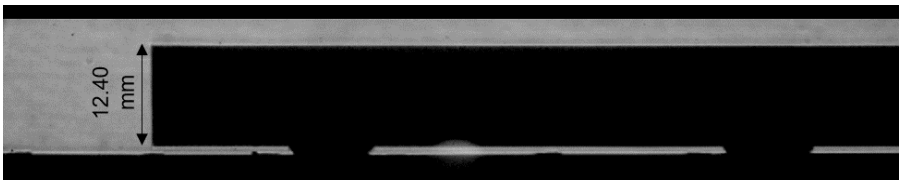


Figure 5.11: Spatial calibration image with ruler at location of Kulite 4, 458 mm from a theoretically sharp nosetip for shot 1922. x and y axes are equal

This concludes the image pre-processing which forms the basis of the techniques which follow. Some methods made use of the wavelet transformed images and some, such as the image stitching were applied to the background-subtracted images depending on whether clearer identification of the wavepackets was necessary.

The methodologies are divided into two main categories: Frequency Detection Methods and Feature Detection Methods. For frequency detection the following

methods are explored: cross-correlation, an intensity probe, image stitching, semi-global matching and the gradient convection speed. Feature detection methods include wavelet scalograms, bispectral analysis and Spectral Proper Orthogonal Decomposition (SPOD).

5.4 Frequency Detection Methods

5.4.1 Intensity Probe

The absolute value of the wavelet transform coefficients at a point corresponding to the location of PCB 5 ($\sim$ 470 mm from a theoretically sharp nose tip) is extracted for each successive frame. This is shown in Fig. 5.12 for a set of images and their transforms taken during the test time (t = 0 s) for shot 1922. The location of the pressure sensor for comparison is shown by the red marker. A power spectral density (PSD) following the method of Welch [159] is calculated for this signal and is scaled to the maximum value from the pressure data (between the limits of 100 kHz and 400 kHz).

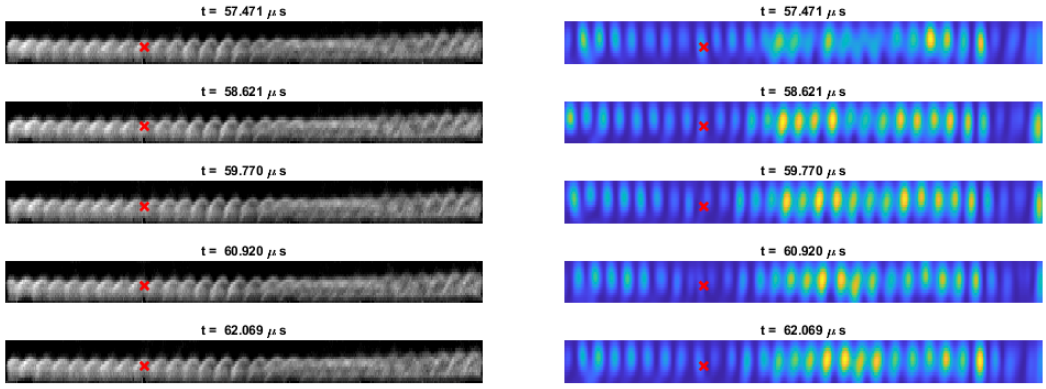


Figure 5.12: Schlieren images using (left) and wavelet transform of images (right) for shot 1922. The location of PCB5 is shown by the red marker. Dimensions are the same as Fig. 5.9

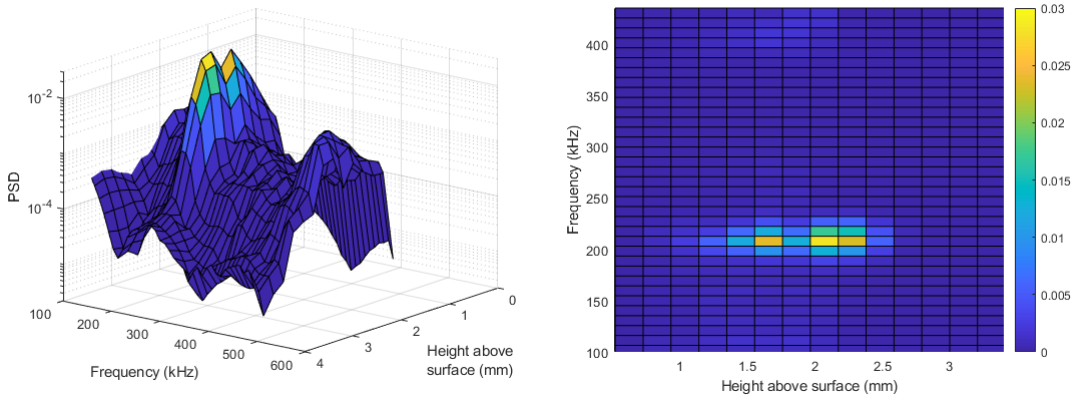


Figure 5.13: Surface map of PSD (flattened view on the right) for heights above the wall for pixel intensity traces

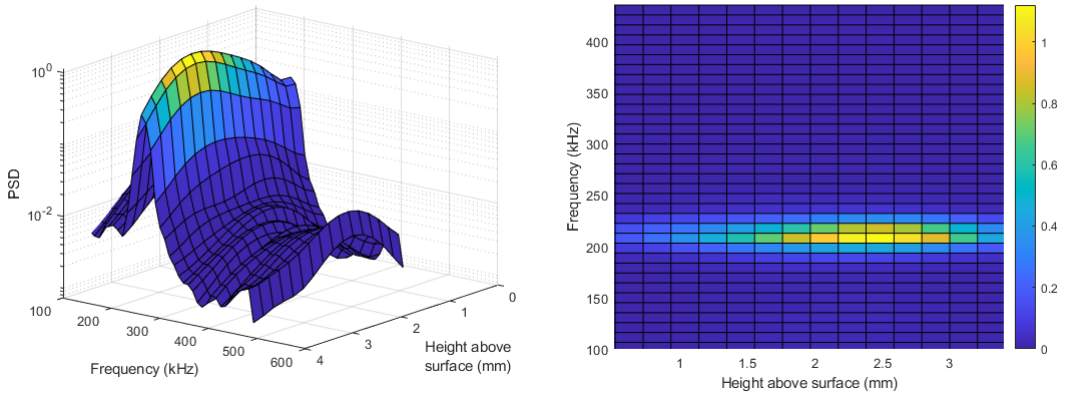


Figure 5.14: Surface map of PSD (flattened view on the right) for heights above the wall for Morlet transformed images

5.4.2 Image Stitching

This is similar to the cross correlation method in the identification of wavepackets, however the identified images are then stitched together and the pixel intensity is determined across a row in the boundary layer. Consecutive matched images are appended to the previous and the pixel intensity over a row of the entire image is extracted to determine the PSD. The new sampling frequency for the stitched image is given by:

$$F_s = X_{wp}/(\frac{1}{fr}) \tag{5.7}$$

Where X_{wp} is the wavepacket translation between frames and fr is the frame rate. If the field of view was not wide enough to track whole wavepackets, the entire image was stitched together (shown for 10 frames for shot 1932 in Fig. 5.15). Similar methods are referred to as temporal reconstruction and applied by authors

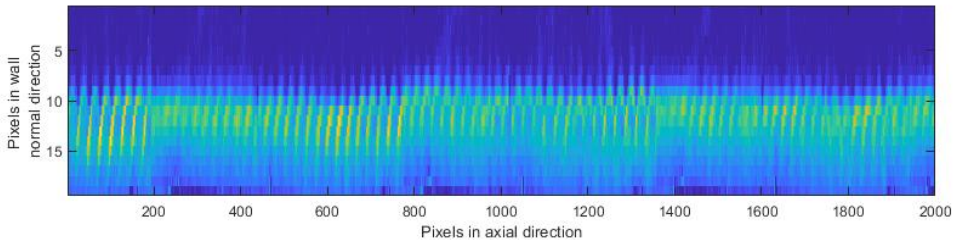


Figure 5.15: Stitched wavepackets for shot 1932

such as Kennedy et al.[160].

5.4.3 Cross Correlation

Cross correlation is an algorithm which determines when two regions closely resemble each other. A version of it has been demonstrated in studies for example in [46, 152] for the automatic identification and tracking of wavepackets. The methodology used in this implementation is outlined here. Given a matrix $\mathcal{X}$ (size $M \times N$), which in this case contains the pixel intensities of the whole image and a matrix $\mathcal{H}$ of size $P \times Q$ which is the smaller region or "template" image, their two-dimensional cross correlation is given by $\mathcal{C}$:

$$\mathcal{C}(k,l) = Tr\{\tilde{\mathcal{X}}\tilde{\mathcal{H}}_{kl}^{\dagger}\} \quad \begin{matrix} 1 \leq k \leq M+P-1 \\ 1 \leq l \leq N+Q-1 \end{matrix} \tag{5.8}$$

where Tr is the trace and † denotes the Hermitian conjugation. $\tilde{\mathcal{X}}$ and $\tilde{\mathcal{H}}_{kl}$ have elements:

$$\tilde{\mathcal{X}}(m,n) = \mathcal{X}(m-P+1, n-Q+1), \quad \begin{matrix} P \leq m \leq M+P-1 \\ Q \leq n \leq N+Q-1 \end{matrix} \tag{5.9}$$

$$\tilde{\mathcal{H}}_{kl}(p,q) = \mathcal{H}(p-k+1, q-l+1), \quad \begin{matrix} k \leq p \leq P+k-1 \\ l \leq q \leq Q+l-1 \end{matrix} \tag{5.10}$$

The maximum of the cross correlation should correspond to the estimated location of the image section. Further details can be found in [161]. A "template"

wavepacket is identified from a clear image (shown in Fig. 5.16 (left)) and then the cross correlation is applied to determine where a similar wavepacket occurs in each frame. This is then used in all frames to identify and track the wavepackets moving downstream, shown for a series of images for shot 1922 in Fig. 5.16 (right).

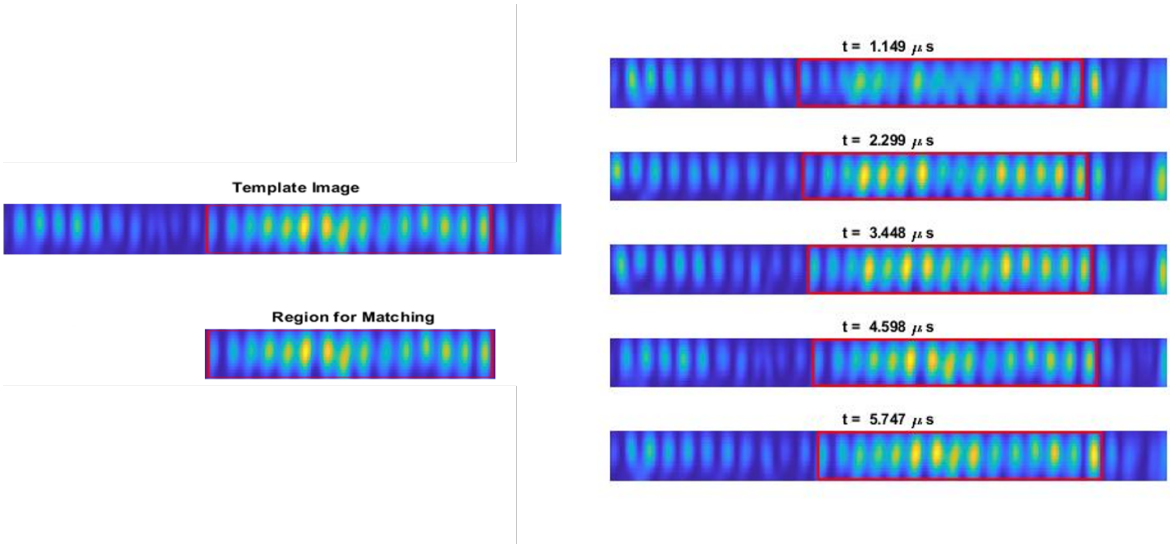


Figure 5.16: Template image and wavepacket section (left). Identified wavepackets for a series of images (right). Dimensions are the same as Fig. 5.9

The cross correlation indices are generated and the maximum is then converted into a translation in x between frames. The x translation together with the frame rate gives the wavepacket velocity. The wavelength is determined from the peaks in the pixel intensity across the "template" wavepacket and the frequency calculated. Since the method is optimal for images were the regions are not deforming, it is expected that some partial matches will occur due to waves morphing as the progress downstream, or enter/exit the field of view.

5.4.4 Semi-Global Matching

Semi-global matching has not been used for this application before but is explored as a novel possibility, subject to certain assumptions. The method computes the disparity (displacement of a point) between a pair of stereo images. The method considers the whole image and uses neighbouring pixels to calculate the disparity of each pixel in the image [162] (see [163–165] for further details). While it is

originally meant for use on images of the same object from different viewpoints, it is applied here with the assumption that the wavepackets do not deform significantly between frames. This is more suited to high frame rates where the image does not move or deform significantly over consecutive frames. The method was applied to shots 1922 and 1936 which were from two different cameras at 870 kfps. It is limited to a subset of frames with the wavepacket remaining in the field of view. The method was applied to 26 frames for both shots. A subset of 5 consecutive images is shown for both cases in Fig. 5.17.

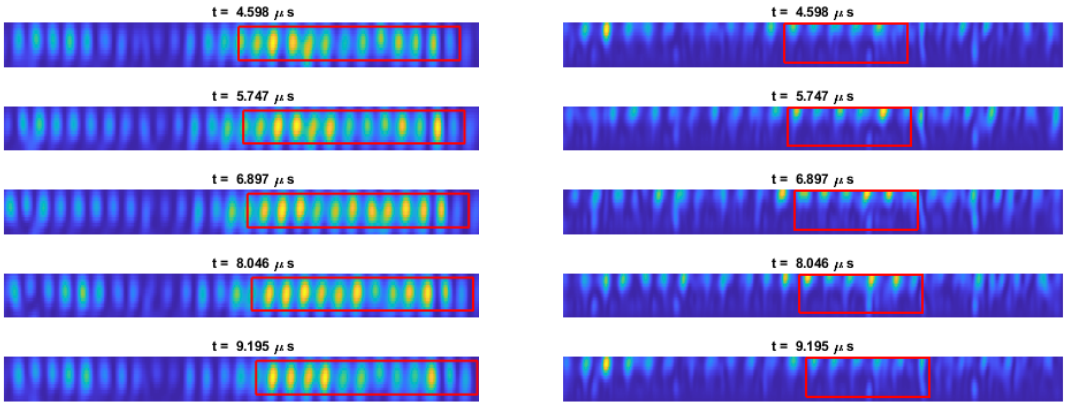


Figure 5.17: Subset of image frames and regions over which disparity was taken for shot 1922 (right) and shot 1936 (left)

The search space is defined by manually estimating an initial displacement between the first few images in order to limit false matches downstream. The disparity is averaged over a region which is moved across frames based on the disparity information from the previous frame, corresponding to the translation of the wavepacket downstream (shown in Fig. 5.17, right). The averaged disparity, or wavepacket translation, is then used along with the wavelength as in Section 5.4.3 to calculate the frequency.

5.4.5 Gradient Convection Speed Method

Another simple and novel method of determining the convection speed of a wavepacket is formulated here. By taking a row from each image and plotting them on a single

axis, the resulting image allows for the clear determination of the gradient which indicates velocity of the wavepacket. The resulting image for shot 1922 is shown in Fig. 5.18, with two example lines chosen from which to calculate the gradient. An additional method of identifying the gradient lines are by applying a Canny edge detection algorithm to the image and automatically identifying the longest line segment, which is the method applied to experiments in T6.

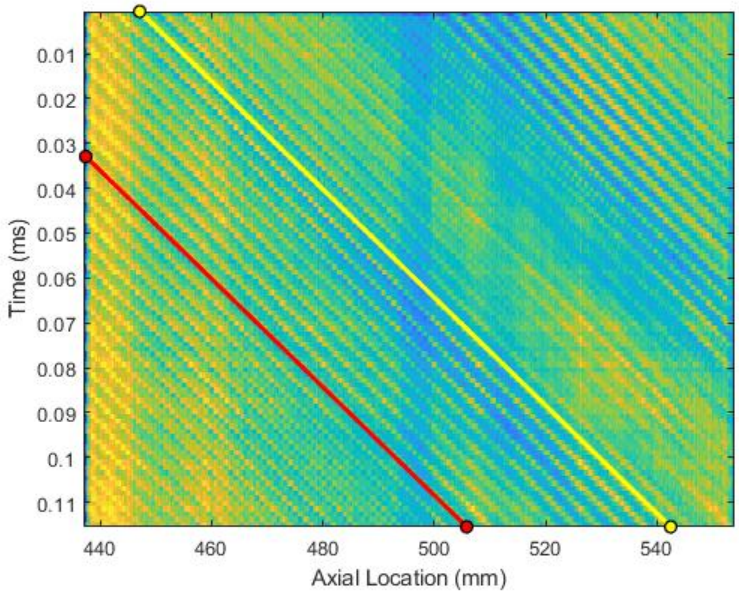


Figure 5.18: Resulting image with lines indicating the gradient for shot 1922

5.5 Feature Detection Methods

5.5.1 CWT for Feature Detection

To illustrate the application of the Morlet wavelet transform for detection of features in the boundary layer, it is applied two-dimensionally to an image of the second mode instabilities. The image is transformed by cross-correlating the image pixel intensity to the analysing function, i.e measuring the similarity between the two.

Consider an image from shot 1922, Fig. 5.19, where flow is from left to right.

A number of interesting features can be seen. In Region I (∼440-500 mm) there is a consistent set of waves with constant frequency. This then amplifies before collapsing into a turbulent spot (Region II, ∼500-530 mm). It becomes

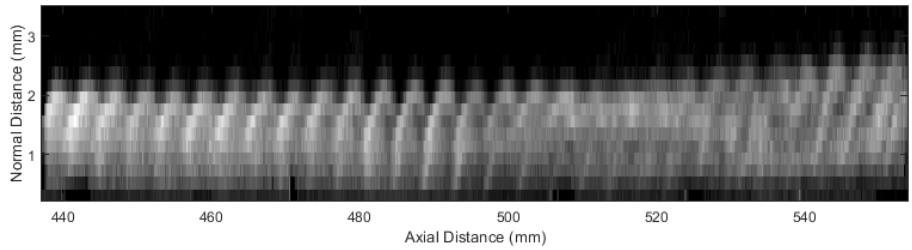


Figure 5.19: Example image, shot 1922

hard to identify after this but Region III (from ∼540 mm) could potentially be another, highly amplified wavepacket. If a row is taken across this image towards the edge of the boundary layer, at approximately 1.65 mm above the surface, the pixel intensity can be plotted axially for each section, shown in Fig. 5.20, with identification of a turbulent spot shown in Fig. 5.21.

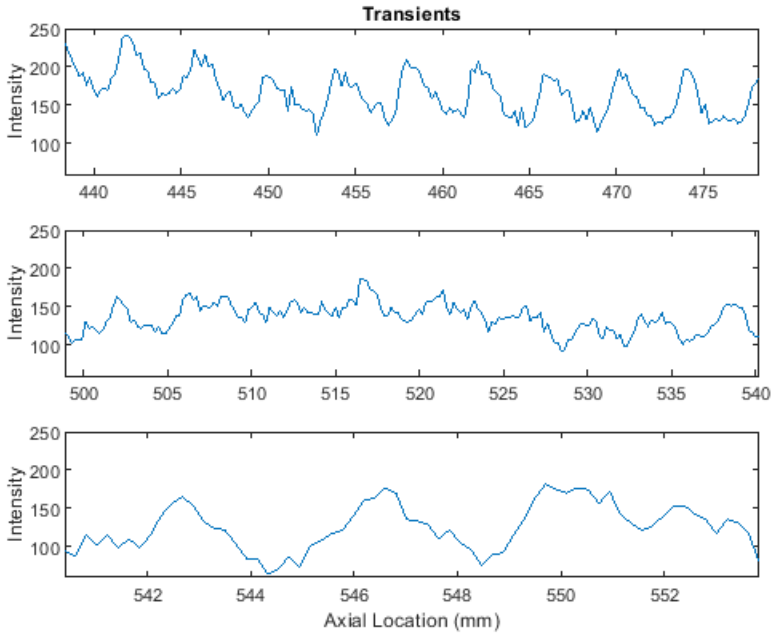


Figure 5.20: Pixel intensity across a row in regions I-III

5.5.2 Bispectral Analysis

While tools like the power spectrum are useful in identifying dominant frequencies, they cannot provide information about phase coupling (a nonlinear growth mechanism) and whether or not peaks at harmonically related positions are in fact phase

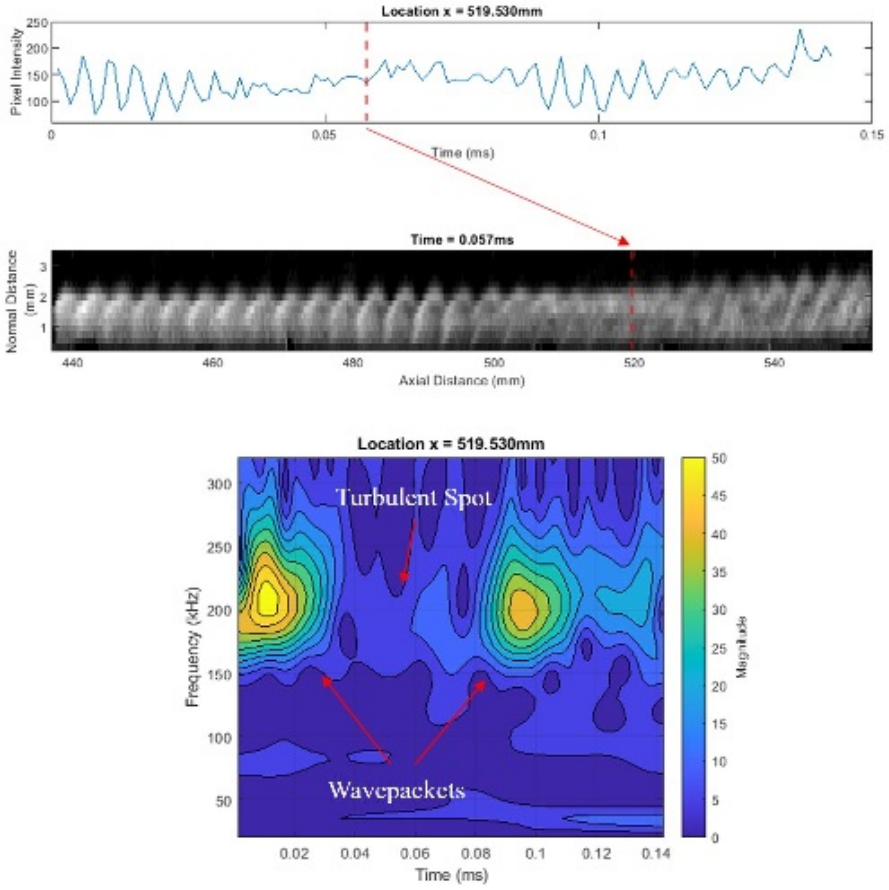


Figure 5.21: Identification of turbulent spot

coupled. Thus, techniques which can identify nonlinear effects are investigated, and their suitability for use on schlieren imaging is explored.

Bispectral analysis, including the bispectrum and bicoherence index, have been used to examine nonlinear effects in fields as varied as biomedicine, plasma physics and fluid mechanics [35]. A brief outline of the method of bispectral analysis applied to schlieren images is given here, using the open source implementation by Swami et al. [166].

The bispectrum is a natural extension to the method of estimating the power spectrum. While conventional estimators of the power spectrum are relatively simple and easy to implement, they are limited in that they cannot resolve closely spaced harmonics, particularly for small samples.

Consider three signals x, y and z with their Fourier Transforms $X(f_1 + f_2)$, $Y(f_1)$ and $Z(f_2)$ as a function of their dominant frequencies f_1, f_2 and $(f_1 + f_2)$. The

third-order cumulant series gives an indication of correlation (generally, cumulants of zero indicate statistical independence). The Fourier transform of the third order cumulant gives the natural estimate of the general cross-bispectrum:

$$I_{xyz}^{N}(f) = \sum_{k=-N-1}^{N-1} \sum_{l=-N-1}^{N-1} \hat{C}_{xyz}(k,l) e^{-i2\pi f_1 k} e^{-i2\pi f_2 l} = \frac{1}{N^2} X_N^*(f_1+f_2) Y_N(f_1) Z_N(f_2) \tag{5.11}$$

The bispectrum and biperiodogram is a special case obtained when x = y = z. Smoothing is added by including a lag window function, w(t,s) which can further be scaled by a factor SF, $w_{SF}(t,s) = w(t/SF, s/SF)$ so that the smoothed estimate is obtained:

$$\hat{S}_{xyz}(f_1,f_2) = \sum_{k=-N-1}^{N-1} \sum_{l=-N-1}^{N-1} \hat{C}_{xyz}(k,l) w_M(k,l) e^{-i2\pi f_1 k} e^{-i2\pi f_2 l} \tag{5.12}$$

The squared bicoherence is a normalised, squared version of the bispectrum which is a convenient way of quantifying the degree of phase coupling. As described by Brillinger [167] and Swami [166], and used for a similar application by Butler & Laurence [71] it is computed by:

$$|b(f_1,f_2)|^2 = \frac{|\hat{S}_{xxx}(f_1,f_2)|^2}{\hat{S}(f_1)\hat{S}(f_2)\hat{S}(f_1+f_2)} \tag{5.13}$$

The result of the bispectral analysis is a hexagonal area of the type shown in Fig. 5.22 [168]. For two dominant frequencies f_1 and f_2, the darker shaded area shows the principal region corresponding to sum interactions of $f_3 = f_1 + f_2$, this contains most of the information of interest. The hatched region corresponds to difference interactions $f_3 = f_1 - f_2$. The white region has the same information as the principal region. The lighter grey areas indicate the complex conjugates.

A simple example is considered here to illustrate the usefulness and interpretation of the results. Consider an audio signal of laughter data, which is known to be highly phase and frequency coupled, from [166]. The audio signal and its bispectrum are shown in Fig. 5.22.

To more clearly identify dominant peaks, we can look at a diagonal slice through the bispectrum (Fig. 5.24).

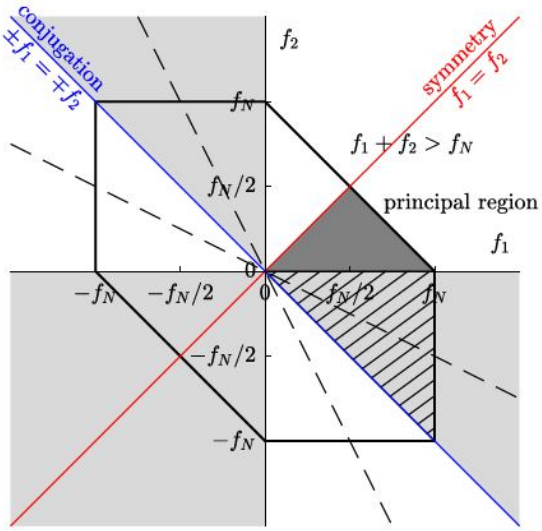


Figure 5.22: Example of a standard bispectrum [168]

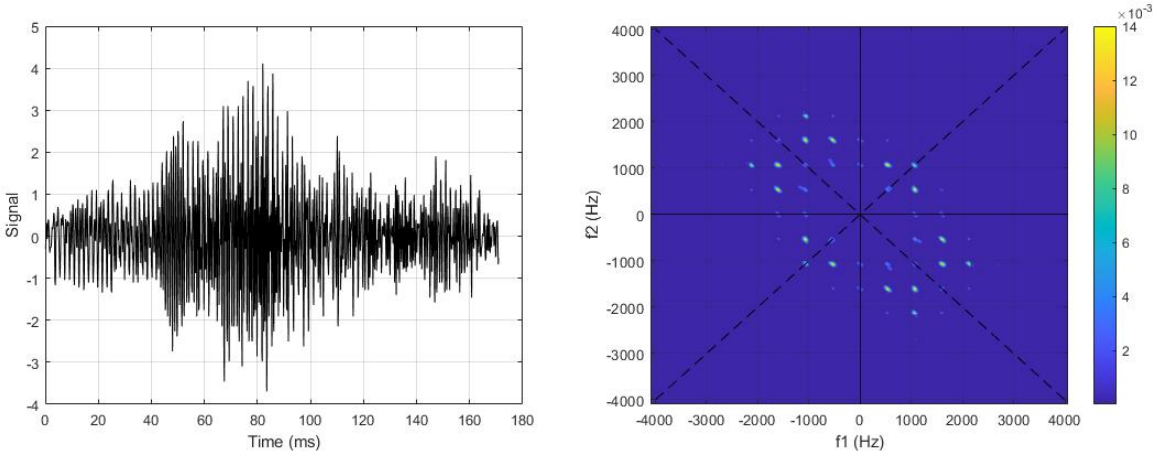


Figure 5.23: Audio signal data example from Swami et al.[166] (left) and bispectrum (right)

The peaks are identified at approximately $f_1 = 500$ Hz, $f_2 = 1000$ Hz and $f_3 = 1500$ Hz. From the bispectrum we can also see another peak at ~ 2000 Hz. The conclusion is that there is self-coupling with harmonics of frequencies kf_0 with $f_0 \approx 500Hz$ and $k = 1, 2, 3, 4$.

5.5.3 Spectral Proper Orthogonal Decomposition (SPOD)

Spectral Proper Orthogonal Decomposition, or SPOD, is an efficient way of identifying coherent structures and their evolution in a flowfield [168]. The method breaks down a flowfield into a set of orthogonal modes which oscillate at distinct

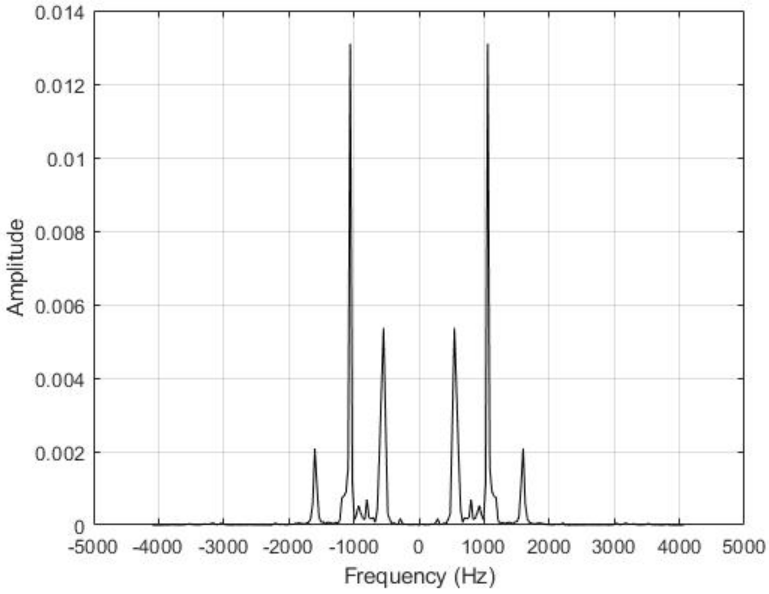


Figure 5.24: Diagonal slice through bispectrum

frequencies. The SPOD method is described here from [72], [168], [169] and [170], implemented using the algorithm created by Schmidt, Towne and Colonius (for the computational methodology, see [72, 171]). The method has also been applied for similar applications in studies such as [70], [71] and combined with bispectral analysis in [170]. This is not to be confused with the method of the same name developed by Sieber et al.([172]). SPOD is an extension of the original POD (Proper Orthogonal Decomposition) introduced by Lumley [173, 174].

An overview of the method is described here. Suppose we would like to find a deterministic vector field $\varphi(z)$ (meaning non-random, ie. given the same input the model always produces the same output exactly) which has the maximum projection on a random vector field $q(z;\varpi)$, where q is the variable we are concerned about, such as density or velocity, and depends on z. ϖ which could be x, t, or some subset of this. If both q and φ belong to a Hilbert space $\mathcal{H}$ with inner product $\langle\cdot,\cdot\rangle$, and $\Xi\{\cdot\}$ is the expectation operator (the weighted average of possible values, weighted according to the probability of that event occurring), then the objective is to maximize the eigenvalues Λ:

$$\Lambda = \frac{\Xi\{|\langle q(z;\varpi), \varphi(z)\rangle|^2\}}{\langle \varphi(z), \varphi(z)\rangle} \tag{5.14}$$

The eigenvalues are ordered ($\Lambda_1 > \Lambda_2 > \Lambda_3...$), making the representation optimal or "proper". This is what makes POD the most efficient way to break down a field of finite total energy, in terms of the energy. It can be shown that the function $\varphi(z)$ must satisfy the eigenvalue problem:

$$\langle \tilde{\mathbf{C}}(z, z'), \varphi(z') \rangle^* = \Lambda \varphi(z) \tag{5.15}$$

where $\tilde{\mathbf{C}}$ is the two-point correlation tensor

$$\tilde{\mathbf{C}}(z, z') = \Xi\{q(z; \varpi) q^*(z'; \varpi)\} \tag{5.16}$$

The asterisk denotes the complex conjugate of a scalar or the Hermitian transpose of a vector/tensor. So far, this is the basis of the standard POD method. For our application, the flow field depends on both space and time, and we seek modes of the same, which is where SPOD comes in. For any two elements u and v in $\mathcal{H}$ and spatial domain Ω, the appropriate inner product becomes:

$$\langle u, v \rangle_{x,t} = \int_{-\infty}^{\infty} \int_{\Omega} v^*(x, t) \mathbf{W}(x) u(x, t) dx dt \tag{5.17}$$

where $\mathbf{W}$ is the weight. The quantity to maximise is:

$$\Lambda = \frac{\Xi\{|\langle q(x, t), \varphi(x, t) \rangle_{x,t}|^2\rangle}{\langle \varphi(x, t), \varphi(x, t) \rangle_{x,t}} \tag{5.18}$$

The eigenvalue problem is

$$\int_{-\infty}^{\infty} \int_{\Omega} \tilde{\mathbf{C}}(x, x', t, t') \mathbf{W}(x') \varphi(x', t') dx' dt' = \Lambda \varphi(x, t) \tag{5.19}$$

where the two-point space-time correlation tensor is

$$\tilde{\mathbf{C}}(x, x', t, t') = \Xi\{q(x, t) q^*(x', t')\} \tag{5.20}$$

For the spectral eigenvalue problem, the correlation tensor depends only on the difference between two times, Δt:

$$\tilde{\mathbf{C}}(x, x', t, t') \rightarrow \tilde{\mathbf{C}}(x, x', t - t') \rightarrow \tilde{\mathbf{C}}(x, x', \Delta t) \tag{5.21}$$

The space-time dependent $\tilde{\mathbf{C}}(\mathbf{x}, \mathbf{x}', \mathbf{\Delta t})$ can be transformed into the frequency domain through a Fourier transform, resulting in the cross-spectral density tensor $\mathbf{\Gamma}$:

$$\mathbf{\Gamma}(x, x', f) = \int_{-\infty}^{\infty} \tilde{\mathbf{C}}(x, x', \Delta t) e^{-i2\pi f \Delta t} d\Delta t \tag{5.22}$$

and

$$\tilde{\mathbf{C}}(x, x', \Delta t) = \int_{\infty}^{\infty} \mathbf{\Gamma}(x, x', f) e^{i2\pi f \Delta t} df \tag{5.23}$$

Now instead of a single eigenvalue problem, we have one for each frequency. For any frequency f', the function $\varphi(x,t) = \psi(x, f')e^{i2\pi f' t}$ is a solution of the eigenvalue problem of Eq. (5.19) with eigenvalue $\Lambda(f')$, where $\psi(x, f')$ and $\Lambda(f')$ satisfy the spectral eigenvalue problem:

$$\int_{\Omega} \mathbf{\Gamma}(x, x', f') \mathbf{W}(x') \psi(x', f') dx' = \Lambda(f') \psi(x, f') \tag{5.24}$$

This is the SPOD eigenvalue problem for which the eigenfunctions are obtained. An example of the analysis applied to a real fluid flow problem is described here to illustrate the use of the SPOD analysis. Schmidt et al. [168] apply the method to the results of a LES simulation of a turbulent jet. The instantaneous fluctuating and mean pressure field is shown in Fig. 5.25.

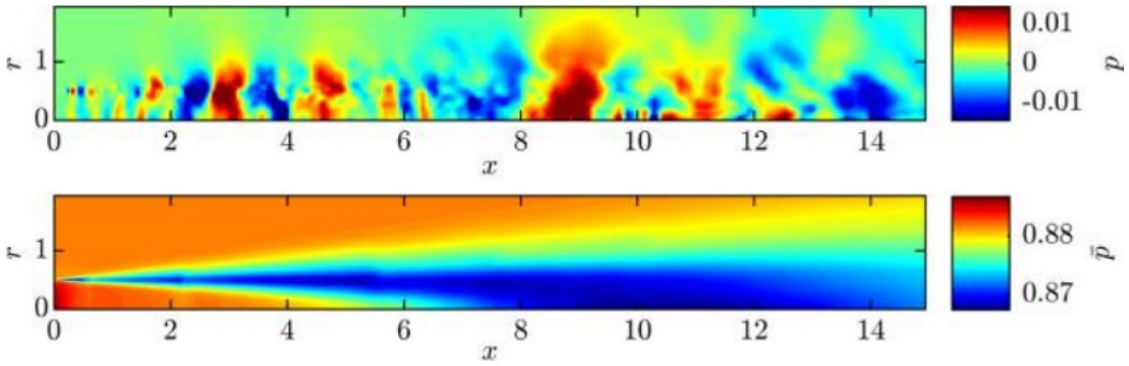


Figure 5.25: Fluctuating pressure component (top) and mean pressure field (bottom) of a Mach 0.4 isothermal turbulent jet from LES [168]

The columns represent the first and second SPOD modes respectively. The first three ranked representative frequencies are shown from top to bottom (fD/U = 0.1, 0.6, 1.5). The leading SPOD modes in the left column for different frequencies show that all leading modes take the form of a wave train or wavepacket. The

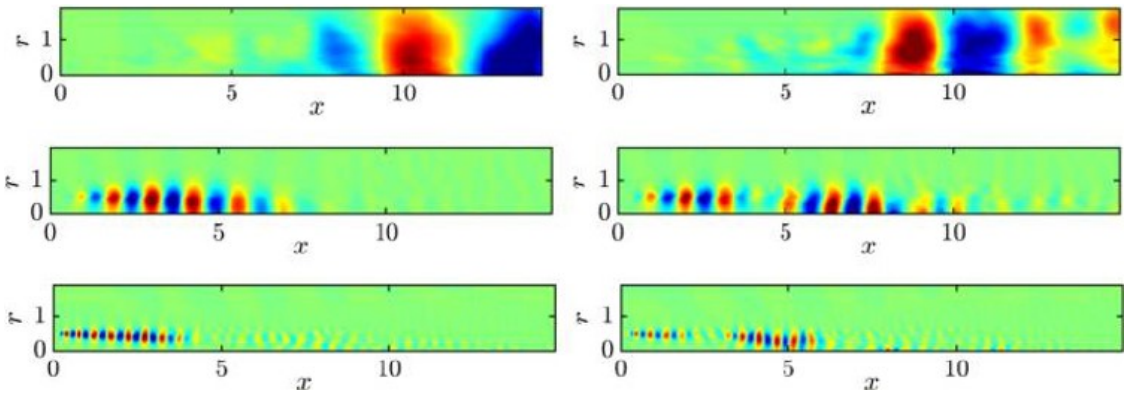


Figure 5.26: SPOD eigenfunctions/modes of a turbulent jet LES data for representative frequencies of fD/U of 0.1 (top row), 0.6 (middle row), 1.5 (bottom row) [168]

SPOD analysis is particularly useful in separating spatially and temporally scaled structures in the jet. The higher frequency wavepackets are located further upstream. For lower frequencies around fD/U of 0.6 the dominant coherent structure is the well-known Kelvin-Helmholtz instability and at lower frequencies still, Orr-type waves even further downstream are identified. A good indicator for the dominance of a specific mechanism is a large difference between the eigenvalues of the first and second SPOD modes [168], in this example for $fD/U \approx 0.6$ which shows that the Kelvin-Helmholtz instability is the physically dominant mechanism. This highlights the usefulness of the SPOD analysis in extracting underlying physical flow features. A physical inspection of the modes can often reveal structures such as vortex shedding, flow instabilities and acoustic resonances. One downside of the SPOD method is that the maximum frequency for which information can be extracted is subject to the Nyquist limit.

5.6 Summary

This chapter explores some selected image processing techniques which have been developed to extract quantitative and qualitative information from schlieren images captured at frame rates above and below the expected frequency of second mode instability wavepackets. The images are first processed by subtracting the background flow-off images, and if necessary an averaged flow-on image. This is done to enhance the presence of wavepackets or other features and reduce the

noise from freestream fluctuations. Example images demonstrating the method are provided. For some cases it is useful to apply a two-dimensional continuous wavelet transform to the images. For signals which are interrupted by transients (such as the presence of turbulent spots) the CWT provides more detailed frequency information than a Fourier transform. This use of this technique in highlighting wavepacket groups and turbulent spots is described and shown. Various frequency detection methods are presented, some of which have been applied before by other researchers and some of which are novel. Methods of extracting quantitative information such as the frequency and convection speed of second mode instabilities include simply extracting the intensity of pixels at points within the boundary layer, plotting a distance-time image and extracting the gradient to calculate the convection speed, stitching together the wavepackets tracked over successive images, using a cross-correlation algorithm to identify wavepackets convecting downstream and applying semi-global matching. The use of these methods in extracting quantitative information, and their advantages and limitations at different frame rates is explored. It is useful to note that the methods of convection speed gradient plotting, image stitching, cross-correlation and semi-global matching can provide velocity and frequency information when sampling frequencies are less than the expected second mode frequencies. Feature detection methods which are useful in highlighting the presence of turbulent spots, nonlinear interactions and other coherent structures in the flowfield are presented. These methods include the aforementioned Continuous Wavelet Transform, bispectral analysis which identifies phase coupling indicating nonlinear growth mechanisms and Spectral Proper Orthogonal Decomposition which breaks down the flowfield into orthogonal modes indicating coherent structures. The theory behind them is described and their application to simple examples is shown. Feature detection methods are inherently limited to frequencies less than half of the sampling frequency. The chapter which follows this one applies the methods developed to a full dataset of images from an experimental campaign conducted in the Oxford High Density Tunnel at conditions which result in lower frequencies of second mode instabilities. The purpose of this is to demonstrate the use of these

techniques under optimal conditions so that they can be compared against each other and against data from pressure transducers. Selected methods outlined here are applied to cases with different cameras and camera parameters such as frame rate and resolution in order to explore the effect on the quality of information obtained.

6

Schlieren Image Processing Techniques in the Oxford High Density Tunnel

Contents

6.1 Introduction 123
6.2 Experimental Setup 124
6.2.1 Schlieren and Camera Setup 124
6.2.2 Flow Conditions 126
6.3 Theoretical Prediction 129
6.4 Schlieren Frequency Detection Results Using Different Cameras 130
6.4.1 Cross Correlation 130
6.4.2 Image Stitching 133
6.4.3 Intensity Probe 135
6.4.4 Semi-global Matching 136
6.4.5 Gradient Convection Speed 137
6.4.6 Comparison of Frequency Detection Methodologies . . . 137
6.5 Schlieren Feature Detection Results Using Different Cameras 140
6.5.1 Wavelet Scalogram 140
6.5.2 Bispectral Analysis 142
6.5.3 Spectral Proper Orthogonal Decomposition (SPOD) . . 143
6.5.4 Comparison of Feature Detection Results 144
6.6 Parameter Comparison using Single Set of Data 145
6.6.1 Original Dataset 145
6.6.2 Effect of Decreasing Resolution 145
6.6.3 Effect of Decreasing Frame Rate 150
6.6.4 Effect of Clipping Frame Time 153
6.6.5 Comparison of parameter effects 158

6.7 Conclusion 159

6.1 Introduction

This chapter outlines the use of the schlieren processing techniques developed in Chapter 5, as well as an analysis of how various parameters such as resolution and frame rate affect the result. This was applied to experiments conducted in the Oxford High Density Tunnel where the lower second mode frequencies could be compared against pressure transducer measurements.

6.2 Experimental Setup

The cone model used here is described in Chapter 3. This section outlines the specific schlieren and camera setup and flow conditions used for the experimental campaign.

6.2.1 Schlieren and Camera Setup

A schematic of the schlieren setup used in HDT is shown in Fig. 6.1. A pulsed Cavitar C013 v1.0 Cavilux Smart UHS laser is used as the light source, emitting visible red light at a wavelength of 640 ±10 nm.

A variable aperture iris is placed in front of the laser source to control the amount of light that is passed through and provide additional sensitivity adjustments. This is reflected off a ϕ300 mm parabolic/concave mirror which collimates the light source and reflects off a ϕ300 mm flat mirror approximately 1.5 m apart. The side of the schlieren setup with the light source upto the first flat mirror is called the source side, while the side from the opposite flat mirror onwards is termed the detection side. The collimated light passes through the test section and is reflected off a flat mirror on the other side to another ϕ300 mm parabolic mirror, placed 4.55 m away. This refocuses the image to a point at the focal length of the mirror, approximately 64" (1.63 m) away. At the focal point a horizontal knife edge was placed. The detection system from knife edge to camera, was tilted at

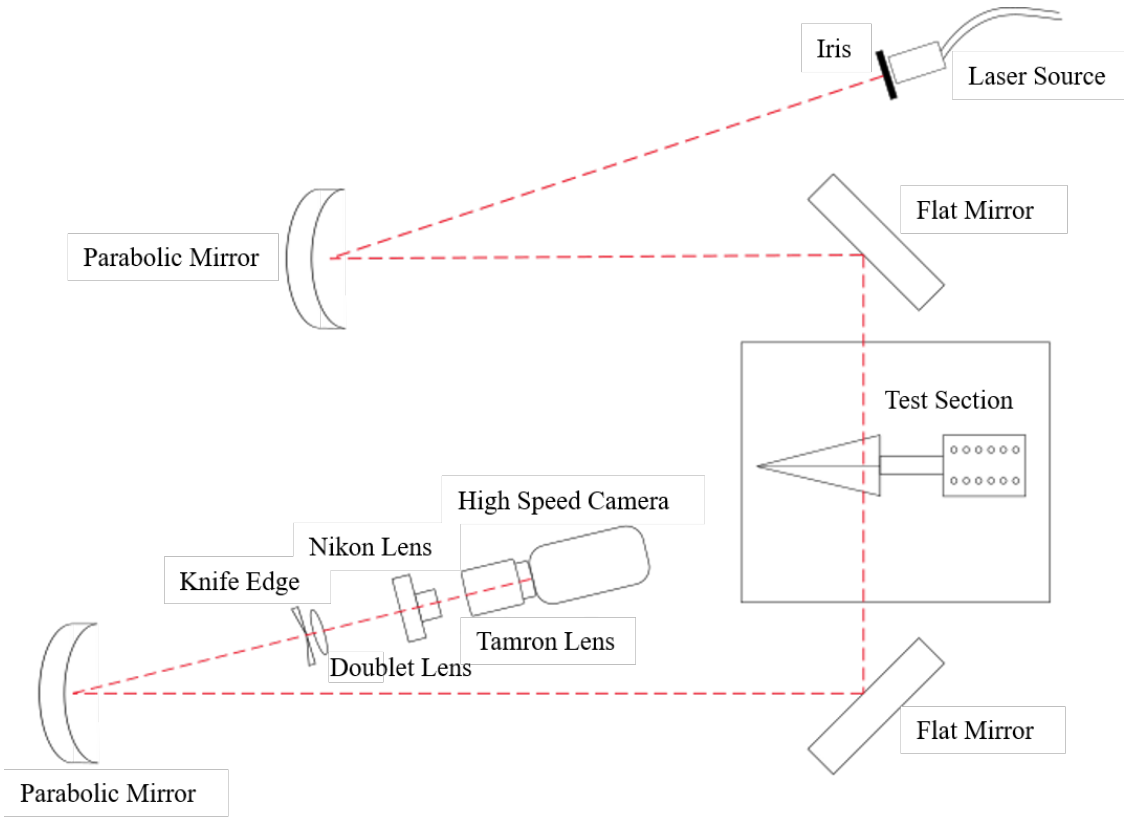


Figure 6.1: Schematic of schlieren setup in HDT, optical path lengths and objects are not to scale

approximately 7^o from horizontal to align with the surface of the cone model. The knife edge blocks off approximately half of the light, with rays that are not deflected by density gradients in the test section blocked by the knife edge while rays which are deflected by a change in density have a chance of passing through. Thus, higher and lower intensities corresponding to fluctuations in density gradient normal to the knife edge are recorded. A ϕ 1" achromatic doublet lens with anti-reflective coating in the 400-700 nm range and focal length of either 75 mm, 100 mm or 150 mm is placed directly after the knife edge, depending on the space restrictions of the system. In this configuration a 150 mm focal length lens was used. The achromatic lens is used to achieve a tighter focus on the imaging plane [175]. Two back-to-back variable focus lenses are used to focus the image on the camera sensor plane. The first is a Nikon AF Nikkor 50 mm f/1.4D lens followed by a Tamron AF 70-200 mm f/2.8 lens (set at 135 mm). Images of the schlieren source and detection sides in

HDT are shown in Fig. 6.2.

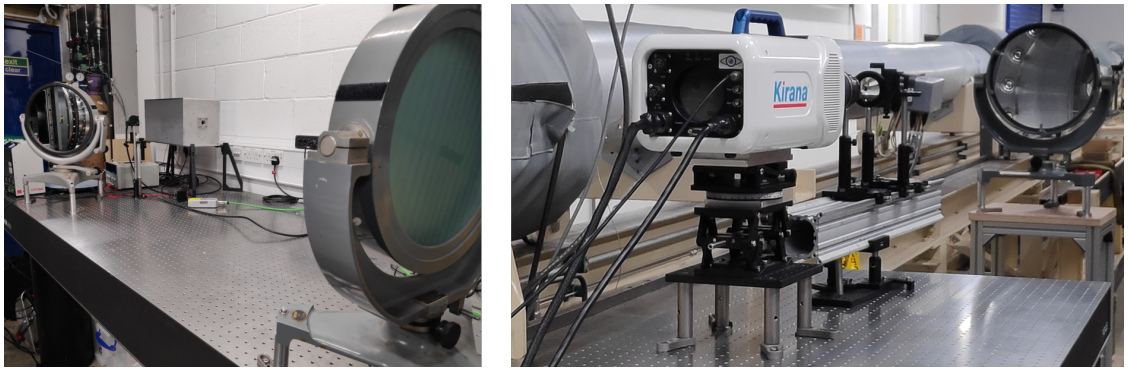


Figure 6.2: Images of the schlieren set up in HDT, source side on the left and detection side on the right

Three different high speed cameras were used, the Phantom TMX 7510 [176], Kirana5M [177] and Photron AX200 [178]. All were monochrome, using the same lens setup. The exposure times and resolutions were adjusted based on the frame rate (the maximum allowed resolution was used for each camera at each frame rate). The camera type and setting, including the maximum field of view for each shot is shown in Table 6.1.

Table 6.1: Camera and schlieren settings for each shot

Shot Number	Camera	Frame Rate (kfps)	Resolution	Field of View x (mm)
1928	Phantom TMX 7510	30	640x128	435-550
1932	Photron AX200	30	512x384	432-513
1926	Phantom TMX 7510	100	640x128	435-550
1930	Photron AX200	100	256x160	411-477
1924	Phantom TMX 7510	500	640x192	437-550
1937	Kirana5M	500	924x768	452-536
1931	Photron AX200	540	128x32	450-475
1922	Phantom TMX 7510	870	640x128	437-550
1936	Kirana5M	870	924x768	452-536

6.2.2 Flow Conditions

Experiments were performed in the Oxford High Density Tunnel (HDT) which is a Ludwieg tube that can achieve flight-representative Mach numbers and unit

Reynolds numbers, but not enthalpy, wall-to-total temperature ratios or velocities [102]. It is further detailed in Chapter 4.

The HDT facility produces distinct plateaus of relatively long flow durations over which the test conditions remain approximately constant. Perfect gas conditions ($\gamma = 1.4$) and isentropic expansion is assumed through the nozzle. The stagnation pressure for each shot is measured using a Kulite XT-190SM sensor located in the nozzle plenum. Static conditions are then calculated using the stagnation properties based on isentropic relations. Unit Reynolds number is calculated using these freestream conditions.

Existing Pitot surveys of the conditions characterising Pitot to supply pressure ratios are used to calculate the Mach number according to:

$$\frac{P_P}{P_0} = \left(\frac{M^2(\gamma+1)}{M^2(\gamma-1)+2}\right)^{\frac{\gamma}{\gamma-1}} \left(\frac{\gamma+1}{2\gamma M^2-(\gamma-1)}\right)^{\frac{1}{\gamma-1}} \tag{6.1}$$

A linear relationship $\frac{P_P}{P_0} = f(P_0)$ can be obtained using a range of supply pressures, shown in Fig. 6.3 from [103] such that

$$\left(\frac{P_P}{P_0}\right)_{M_{nozzle}=7} = -5.5734e-7P_0 + 1.6833e-2 \tag{6.2}$$

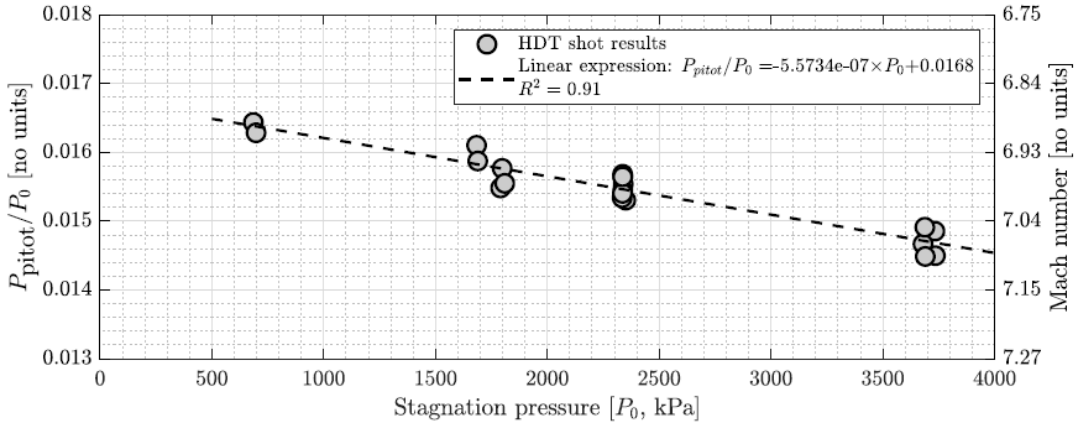


Figure 6.3: HDT facility Pitot to supply ratio as a function of supply pressures, dashed line indicates relationship used for Mach 7 nozzle, from [103]

In practice, a barrel fill pressure must be specified to achieve a target supply pressure, and correlations shown in Fig. 6.4 are used to account for losses over the

plug valve so that the experimenter can specify the fill pressure for the plateau used. For Plateau 3 used here, this is:

$$P_{fill} = 1.2142 P_{0,plat3} + 29.231 \tag{6.3}$$

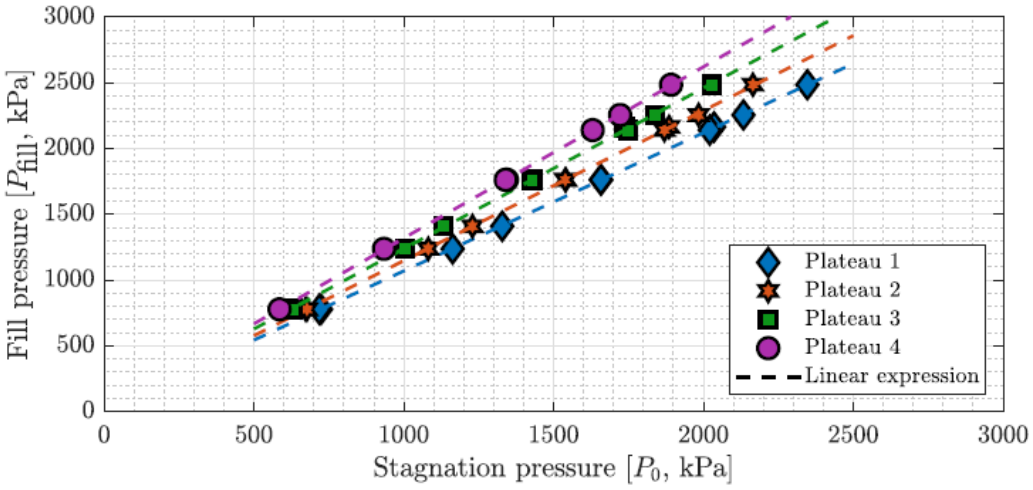


Figure 6.4: Required fill pressure as a function of target supply pressure for each facility plateau, from [103]

For the experiments conducted here, a barrel fill pressure of 2000 kPa and fill temperature of 500 K was used, resulting in a supply pressure of approximately 1600 kPa and Mach number of 6.93. The measured stagnation pressure for each shot is used to calculate the Pitot to supply pressure ratio and hence Mach number using this distribution.

To calculate the unit Reynolds number, Keyes' viscosity model could be used in HDT [179], described by:

$$\mu_{Keyes} = \frac{1.488e-6\sqrt{T}}{1+\dfrac{122.1(10^{-5/T})}{T}} \tag{6.4}$$

This model is suggested when T< 100 K [180]. Static pressure and temperatures are calculated according to isentropic relations and density ρ_∞ can be obtained using perfect gas assumptions so that $\rho_\infty = \dfrac{P_\infty}{RT_\infty}$. Freestream velocity can be obtained from the calculated Mach number according to $V_\infty = M_\infty\sqrt{\gamma RT_\infty}$.

For this analysis the third plateau was used and the region of test time is highlighted in red in Fig. 6.5. The nominal flow parameters did not vary much between shots and over the test time identified for plateau 3, they are summarised in Table 6.2. The entropy swallowing distance X_{SW} is calculated based on Reynolds number using Eq. (2.2) described in Section 2.5. The cone edge conditions are calculated using the Taylor-Maccoll relations [181], which assume a sharp cone geometry but are acceptable for this purpose. For facilities of this type, the test time is orders of magnitude larger than the flow establishment time (approximately 0.0009 s using two flow lengths) and selection of appropriate test time within the plateau is not as important as for the shorter total test times (on the order of ms) experienced in T6. The selection of appropriate test times in T6 is described in Section 7.2.3.

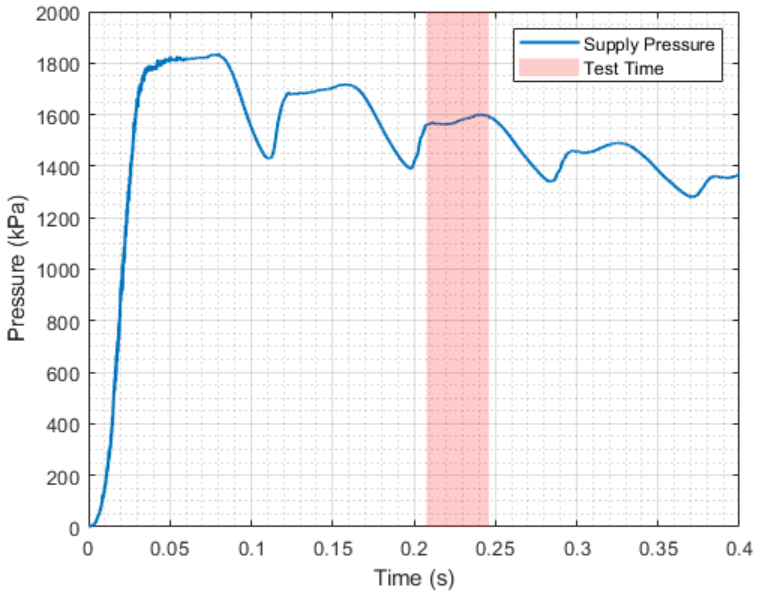


Figure 6.5: Stagnation pressure and Mach number traces with test time indicated for shot 1922

Table 6.2: Nominal Test Conditions for HDT Experiments

P_{fill} (kPa)	T_{fill} (K)	P_0 (kPa)	M_∞	M_e	T_w/T_0	$Re_{U,\infty}$ (10^6/m)	R_N (mm)	X_{SW} (mm)
2000	500	1600	6.93	5.87	0.68	10.5	1.25	213

6.3 Theoretical Prediction

An approximation of the expected second mode frequency can be calculated from an approximation of the boundary layer thickness and the edge velocity.

The boundary layer thickness can be roughly deduced from the maximum intensity of the boundary layer of a schlieren image [152]. Note that this is an estimation and the boundary layer thickness obtained based on density gradient will be less than the standard $99\%U_e$ boundary layer thickness but provided an adequate indication of the boundary layer for this purpose. For 1922, this occurred at approximately 1.75 mm. The expected frequency can then be estimated from the observed relation:

$$f \approx \frac{0.9U_e}{2\delta} \tag{6.5}$$

which gives an estimated second mode frequency of 225 kHz. Note that this empirical parameter of 0.9 has been observed to vary between 0.8-1.0U_e in other studies [41, 43, 46]. This is compared to the result from PCB sensor 5 which gave a peak frequency range over the experiments of 208-216 kHz.

6.4 Schlieren Frequency Detection Results Using Different Cameras

The results obtained for each method (where applicable) from three different high speed cameras are presented here. A summary of the methods developed which are applied to these datasets is shown in Fig. 6.6.

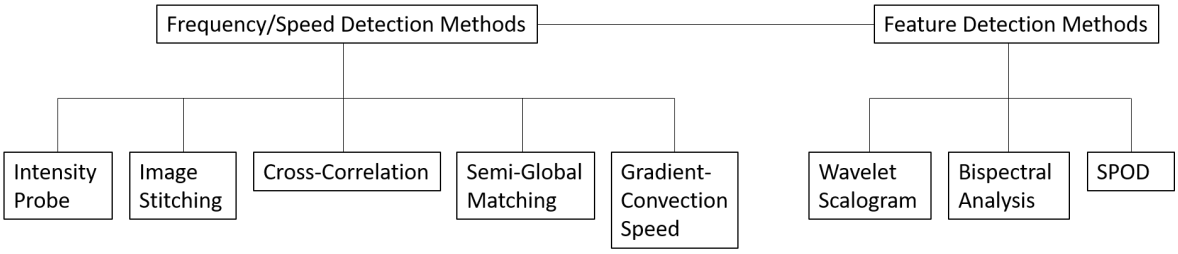


Figure 6.6: Summary of methods used in analysis of high speed schlieren images

6.4.1 Cross Correlation

The cross correlation method allows for the automatic detection of wavepackets using a template image. It is used to extract the convection speed based on most probable matches, and together with the wavelength which can be extracted from a single wavepacket, the frequency can be obtained. Authors such as Casper [46] and Shumway [152] have applied similar methods. The cross correlation method described in Section 5.4.3 was applied to the datasets summarised in Table 6.1. All of the cases were analysed, however only selected figures for the lowest and highest frame rate cases are shown in detail here (30 kfps and 870 kfps). Details of the cross-correlation histograms for the other experiments can be found in Appendix A. The frequencies resulting from the wavepacket matches over the set of viable frames is grouped into bins of 10 kHz width over the range of 100-400 kHz. The frequencies corresponding to the number of matched wavepackets is shown in Fig. 6.7 for shots 1928 (left) and 1932 (right), both at 30 kfps on two different cameras, alongside the measured frequency from PCB 5 for each shot and the fitted distribution centred around the mean. The same is shown for shots 1922 (left) and 1936 (right) in Fig. 6.8 which was sampled at 870 kfps.

Grouping the number of matched wavepackets into histograms allow for the interpretation of the results in terms of image quality. A broader distribution indicates a large number of partial matches, while a narrow distribution with a mean closely matching the modal value shows wavepackets which are distinct and easily tracked.

Partial matches may occur and this can be seen in Fig. 6.9 where the frequency for each frame is shown. Clusters of data points are apparent at approximately 0.5 and 1.5 times the expected frequency (corresponding to a match of the trailing half and leading half of the same wavepacket).

A summary of the percentage error from the pressure sensor results for each cross-correlated case is shown in Fig. 6.10. The mean and modal values are compared, with the error bars corresponding to the bin edges of the modal frequency. Note that the number of matched images is much lower with the Kirana camera shots as

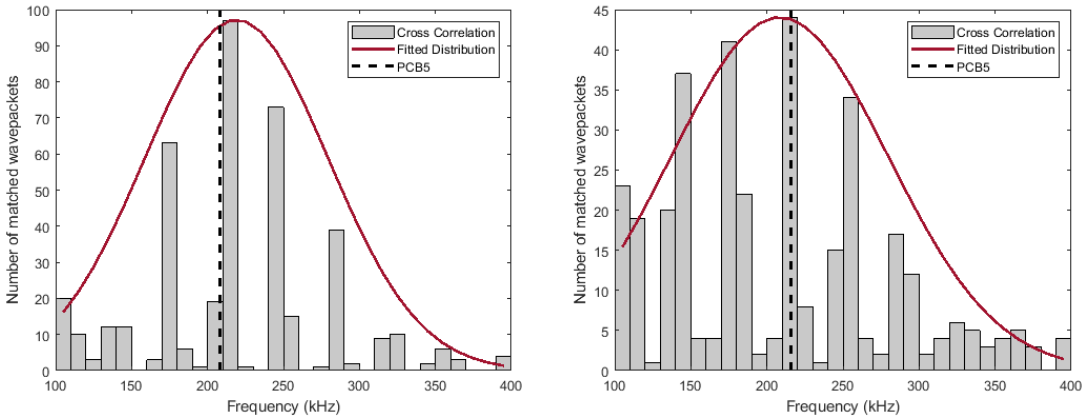


Figure 6.7: Histogram showing number of matched wavepackets at frequencies for frame rates of 30 kfps for shot 1928 (left) and 1932 (right)

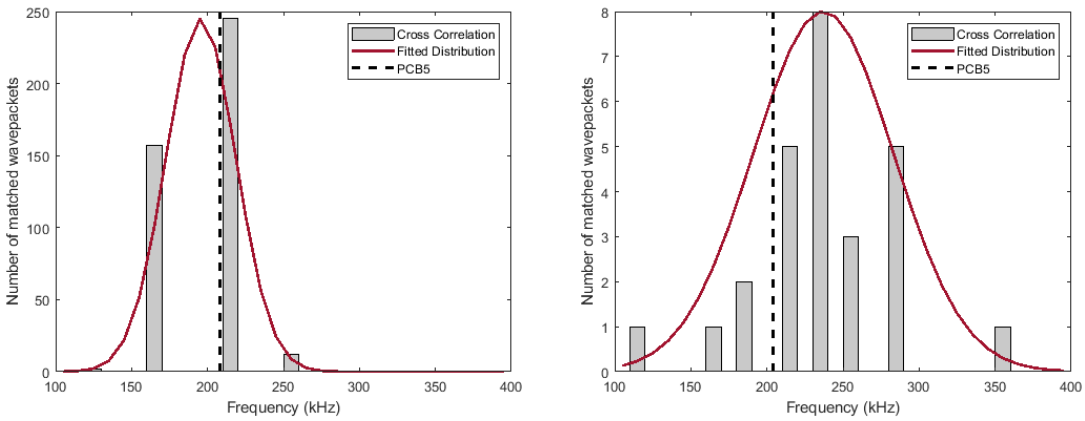


Figure 6.8: Histogram showing number of matched wavepackets at frequencies for frame rates of 870 kfps for shot 1922 (left) and 1936 (right)

it is limited to less than 180 frames so the overall number of viable images which could be analysed was lower.

At low frame rates, the mean frequencies of the overall data match well to the expected frequency (between 1%-6% error for 30 kfps shots), for both cameras used. The mean values are skewed because of partial or incorrect matches but they do not make a significant difference at these frame rates because the field of view and resolution provide good quality images for matching, provided that the field of view is wide enough to capture wavepacket progression, without being too wide as to contain multiple wavepackets in the same frame.

At the highest frame rates, in general the field of view and wavepacket displace-

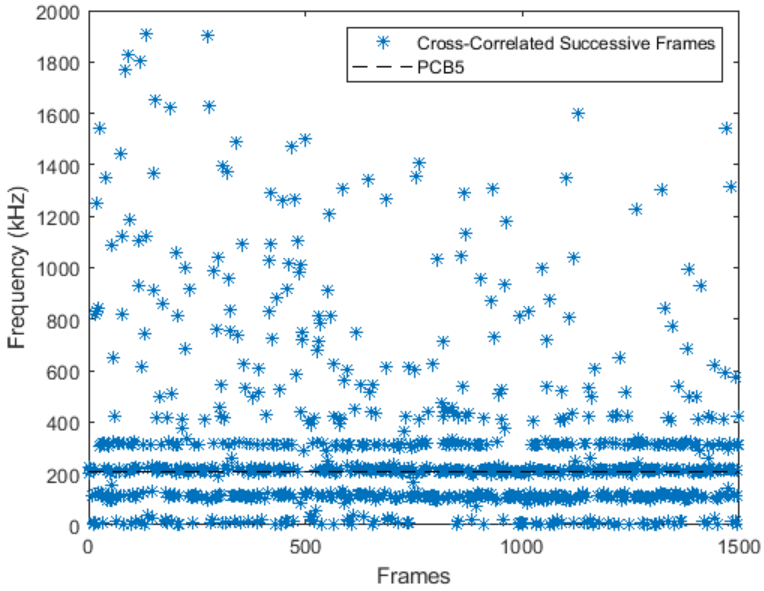


Figure 6.9: Frequencies for each cross-correlated frame in shot 1926

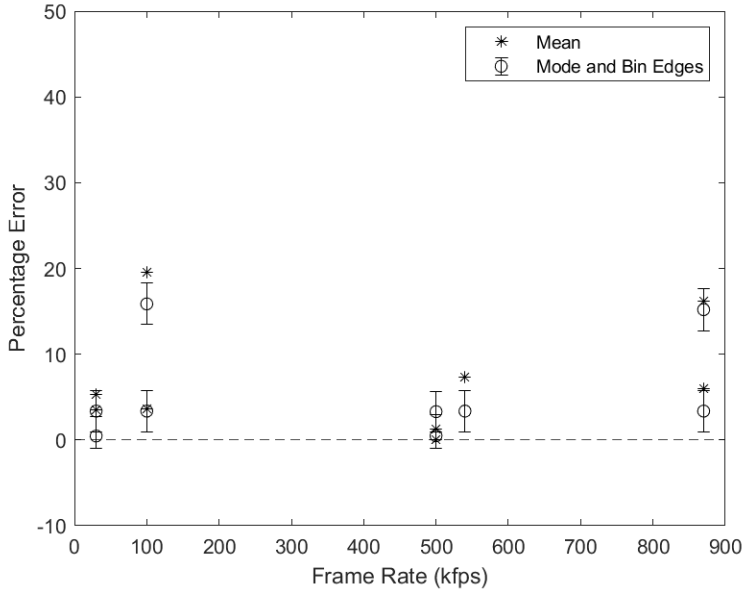


Figure 6.10: Percentage error from pressure sensor data for the cross-correlated results, both mean and modal values

ment is much smaller. A smaller section of the image is chosen, typically not an entire wavepacket but the higher intensity regions. While this gave a number of good matches, it also resulted in partial matches because an entire wavepacket could not be isolated, either due to the smaller field of view, or if the field of view

is large enough, then the cross-correlation algorithm has difficulty in distinguishing between multiple wavepacket groups. For the low frame rate methods, an entire region containing a complete wavepacket could be chosen as the template image which provides a better template for matching.

6.4.2 Image Stitching

The image stitching method was applied following the method outlined in Section 5.4.2 in order to generate a power spectral density particularly from results sampled at less than the expected frequency of the second modes. The power spectral density for the image stitching method is shown here for the 30 kfps and 870 kfps cases compared to the measured pressure fluctuations (PCB5). The results for the other experiments using using different cameras and frame rates between these are included in Appendix B. The maximum and minimum values of the PSD from the stitched images are scaled to the corresponding limits of the pressure fluctuations over the interval shown in order to directly compare the results since the PSD values of the stitched images are arbitrary.

In general, the results from the pixel intensities taken at mid-height of the boundary layer agree with less than 10% error from the pressure fluctuation results. The cases vary based on image quality and the field of view available, for example for shot 1932, the field of view was less than an entire wavepacket and so, instead of successive wavepackets being stitched together, the entire field of view was used. This still gives a decent indication of the second mode frequency (approximately 200 kHz versus the pressure fluctuations results of 216 kHz). For shot 1936, the image quality seemed to effect the sharpness of the PSD extracted. The image stitching results do show however, that given images of sufficient quality and field of view (shots 1928 and 1922), very good indications of the second mode instability frequency can be obtained despite having vastly different image frame rates (30 kfps versus 870 kfps). This is positive evidence that the image stitching methodology would be applicable to testing in T6 where second mode frequencies may be close to, or exceed the maximum frame rate that the available high speed cameras are capable of.

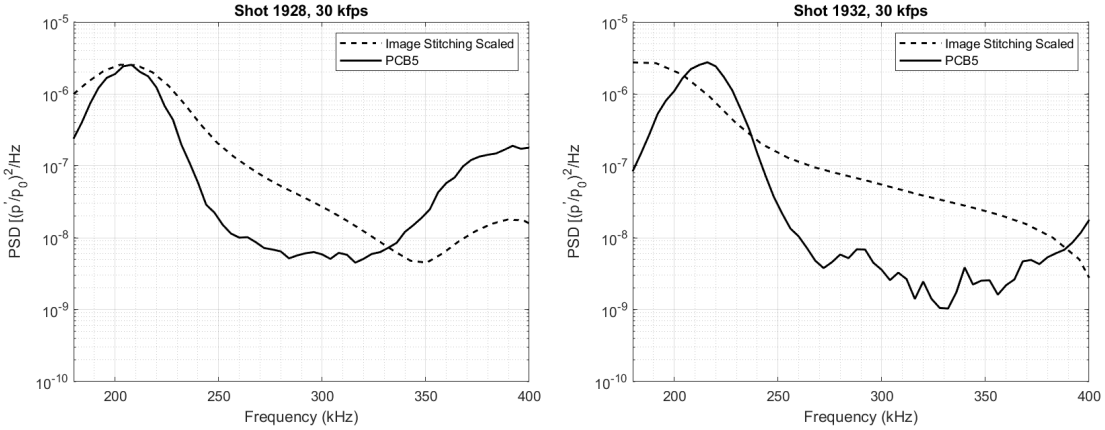


Figure 6.11: Image stitching results for frame rates of 30 kfps for shot 1928 (left) and 1932 (right)

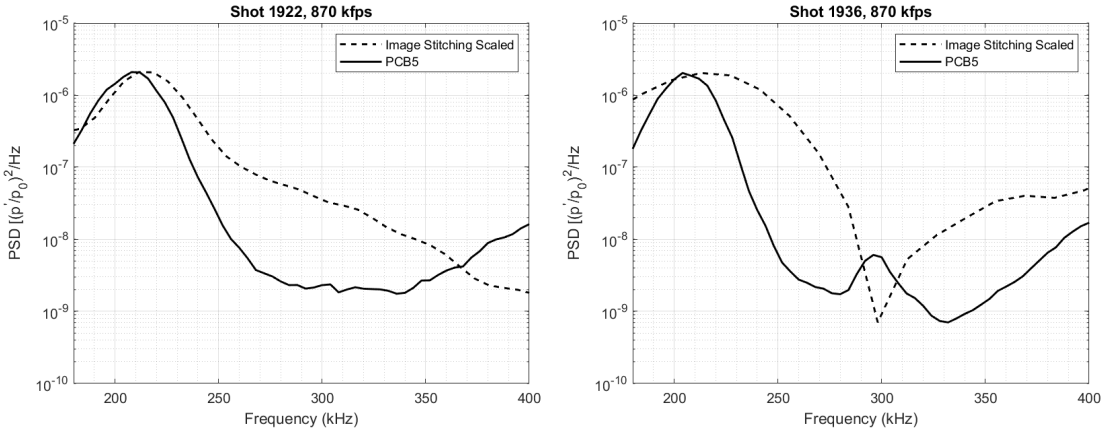


Figure 6.12: Image stitching results for frame rates of 870 kfps for shot 1922 (left) and 1936 (right)

6.4.3 Intensity Probe

The power spectral density for the intensity probe method described in Section 5.4.1 is shown in Fig. 6.13, compared to PSD from the measured pressure fluctuations (PCB5). The schlieren PSD values are scaled to the peak values from the pressure results (PCB5) since the intensity value for the images are arbitrary. This method was the most simplistic, and generally compared well to the pressure transducer results (with less than 10% error) but it is limited to cases where the frame rate is more than double the expected frequency.

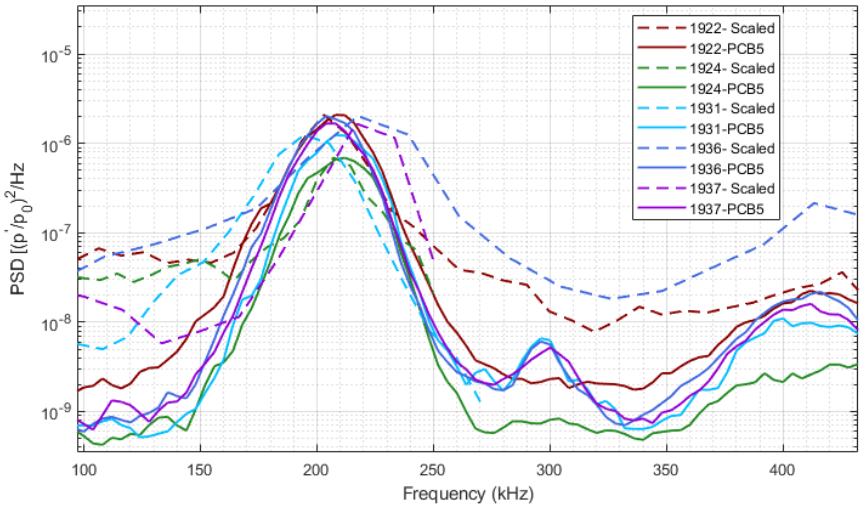


Figure 6.13: Intensity probe schlieren results (normalised against the maximum pressure sensor values for each shot) compared to pressure fluctuation results

6.4.4 Semi-global Matching

A novel application of the semi-global matching method is described here, with further details in Section 5.4.4. Two cases are shown to demonstrate the use of semi-global matching, shots 1922 and 1936, both at frame rates of 870 kHz. It was not used on the other images, as described here, it is effective only under a narrow set of circumstances. It does however provide an additional method by which to validate other results. The disparity map (the translation for each pixel in the image compared to the previous image) is shown in Fig. 6.14, left. The bounded region indicates where the wavepacket is expected to occur, which is translated based on the value of the mean disparity from the previous image. The disparity value is averaged over the wavepacket region for the selected frames, shown in Fig. 6.14 (right).

An example of a case for which the method is not suitable is shown in Section 5.4.4 and the disparity map for these in Fig. 6.15 (right). The averaged disparity is shown in Fig. 6.15 (left).

This method was applied to the highest frame rate cases because the small displacement and deformation of a wavepacket over frames is the best candidate for semi-global matching. As discussed in Section 5.4.4, this method was originally meant for use on images of the same object from different viewpoints, so it is

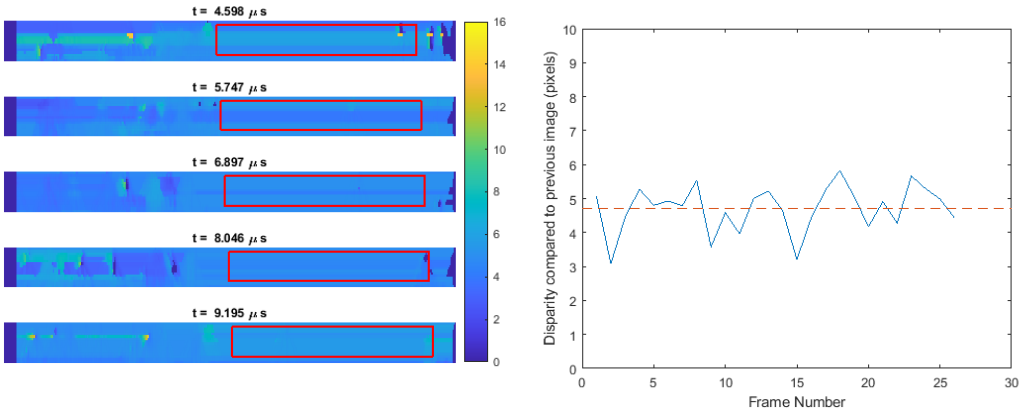


Figure 6.14: Semi-global matching disparity map indicating disparity values (left) for a subset of images and the averaged value of disparity over frames (right) for shot 1922

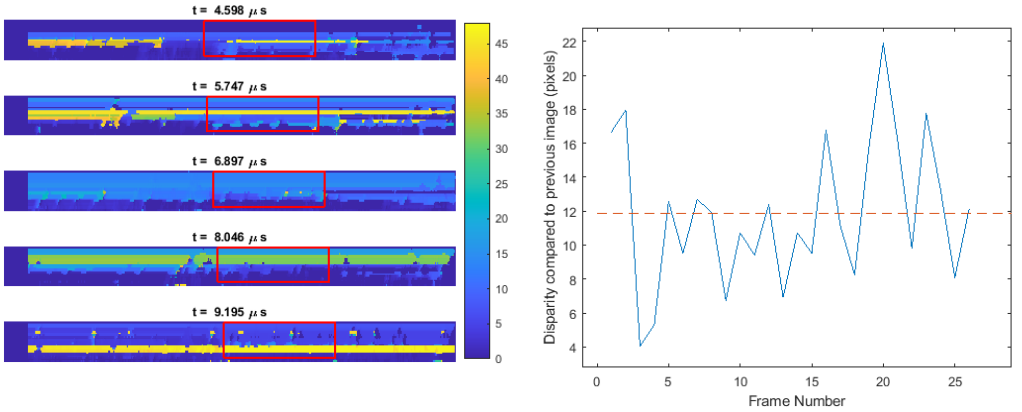


Figure 6.15: Semi-global matching disparity map indicating disparity values (left) and averaged value of disparity over frames (right) for shot 1936

applied based on the assumption that the wavepackets do not deform significantly between frames, as such, it is also extremely sensitive to image quality. Even so, the translation for shot 1936 varies greatly for each pixel in the selected region when compared to the uniform disparity for shot 1922. The resulting frequency estimate for shot 1922 is less than 1% off from the measured result, while for shot 1936, the error is 32%. While both images are taken at the same frame rate, the image quality differs significantly between them and this method is particularly sensitive to low image quality.

6.4.5 Gradient Convection Speed

The gradient method described in Section 5.4.5 was applied to the shots which allowed the use of this method and the results were compared to the convection speed identified using SGM for shot 1922 (shown in Fig. 6.16). In some shots the image quality or field of view did not result in clear gradients so these were not included. The results were included for the Phantom and Kirana camera shots at 500 and 870 kfps as these produced images with detectable gradients. This method provided good results, with errors from the SGM method between 3%-7%.

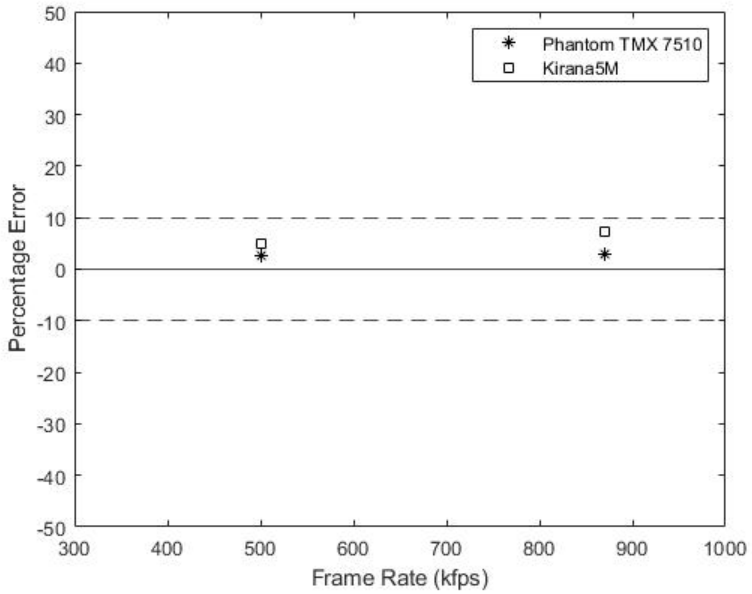


Figure 6.16: Convection speed percentage error difference from shot 1922 SGM method

6.4.6 Comparison of Frequency Detection Methodologies

The percentage errors between the peak frequencies for the three main methods (intensity probe, image stitching and cross correlation) are shown against the frame rate in Fig. 6.17. Semi-global matching and the gradient convection speed methods are not included as they are not applicable to all cases and provide a reliable result only under limited conditions. They can be used as a means of validating other methods, provided the image quality is good enough and/or the deformation of the wavepackets is low.

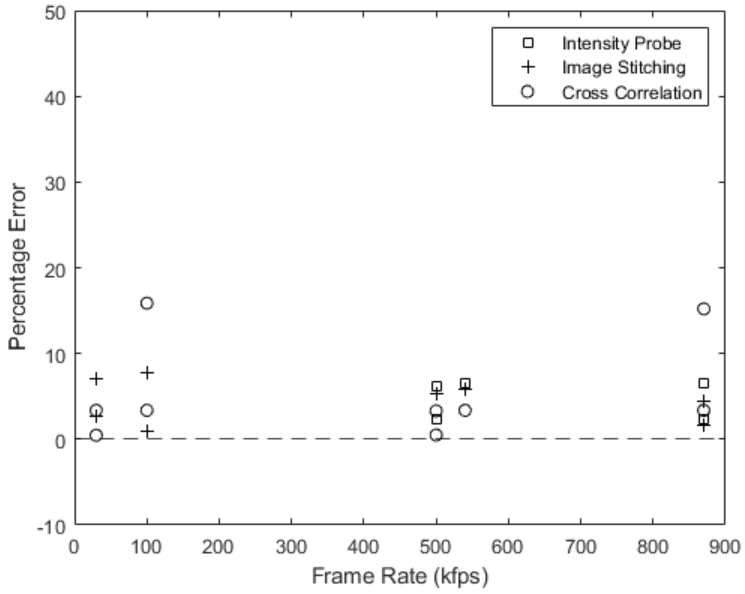


Figure 6.17: Percentage error from pressure sensor data for intensity probe, image stitching methods, and cross correlation (modal values)

The results for the intensity probe and image stitching methods all provide errors below 10% from the measured values. The intensity probe method is fairly reliable and provides a rapid estimation of the wavepacket frequency, with the disadvantage of only being applicable to images taken at frame rates above the Nyquist limit. While the cross correlation method provides good results for some images and is particularly useful at frame rates below the Nyquist limit, the error from the measured result is highly dependent on the image quality, the field of view and the deformation of the wavepackets. Low image quality and partial matches can heavily skew the results, regardless of the frame rate, as in shots 1930 and 1936. As found by Shumway et al. [152] for a similar method, algorithms of this type work best when there are distinct wavepackets in the field of view. The image stitching method provides a rapid and fairly reliable estimation of the wavepacket frequency without having to modify the raw images too much. While this is also dependent on image quality, it is not as affected as the wavepacket tracking methods. While wavepacket tracking methods are useful, they may have a higher error and future improvement for both the cross-correlation and semi-global matching methods would be to include consideration of the deformation of the wavepackets by scaling

and rotation of the template image.

Methods were introduced to analyse the frequency content of wavepackets in a hypersonic boundary layer using three different cameras and different frame rates below and above the Nyquist limit. Those that rely on algorithms to match wavepackets moving downstream in general have the highest error for certain cases and they are very sensitivity to image quality (cross correlation and semi-global matching). Errors when compared to the measured pressure data were below 10% for the image stitching and intensity probe results. These experiments have shown that the methods, when used in conjunction, can provide a fairly accurate estimation of the frequency of second mode instabilities. This informs the use of these techniques for conditions where frequencies may be above the limit of pressure sensors but can be analysed using schlieren at lower frame rates.

6.5 Schlieren Feature Detection Results Using Different Cameras

The nonlinear effects from pressure transducer data versus schlieren images from shot 1922 is compared using wavelet scalograms and bispectral analysis. SPOD is shown separately without transducer data since it is a 2-dimensional method which is not applicable to 1-dimensional pressure signals. The axial locations of the PCB transducers is shown in Fig. 6.18, along with the wall-normal locations within the boundary layer used in the wavelet scalogram analysis of the schlieren images.

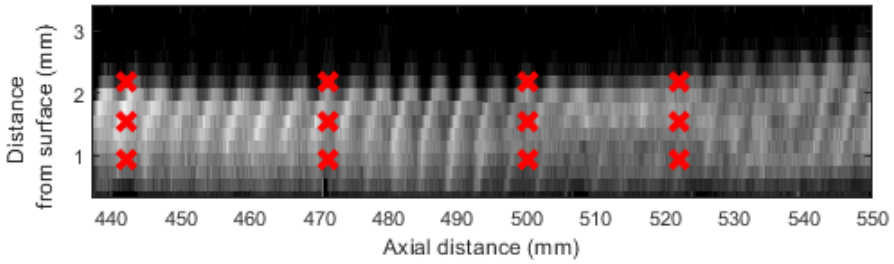


Figure 6.18: Indication of PCB axial locations and equivalent marker positions on a frame from shot 1922

6.5.1 Wavelet Scalogram

Wavelet scalograms allow for the detection of the most representative frequencies in a signal [182]. They are the absolute values of the CWT plotted against time and frequency. These are obtained for the pressure transducer data and shown in Fig. 6.19 axially along the cone surface. This is compared to the wavelet scalograms from schlieren images of shot 1922 (Fig. 6.20) at the equivalent locations and over the same time frame. The schlieren images allows scalograms to be applied at various heights within the boundary layer which is an advantage over pressure transducer data as the evolution of wavepackets both axially and normal to the surface can be examined. Note that the y-axis scales on the data are different because the scalogram can be computed theoretically up to approximately 1 MHz from the PCB data, but only just under 400 kHz for the schlieren data due to the different sampling rates. The pressure transducer scalogram is shown up to a higher frequency to highlight the weak signals occurring at 400 kHz, which could be a result of self-coupling of the dominant frequency at 200 kHz. This becomes more apparent when examining the bispectral analysis in the next section, which can be computed above 400 kHz for both sets of data.

The scalograms for the remaining shots at various heights in the boundary layer and along the cone surface are included in Appendix C.

6.5.2 Bispectral Analysis

The bispectra of the PCB pressure signals axially along the cone is shown in Fig. 6.21 (left) and the bispectrum applied to a single PCB signal (PCB5) at approximately 457 mm is shown in Fig. 6.21 (right). This is compared to the bispectra from the schlieren data at each axial location Fig. 6.22 (left) and the same axial location of PCB5 and central marker location above the surface (457 mm, 1.76 mm) in Fig. 6.22 (right).

The bispectra for the other experiments are included in Appendix D.

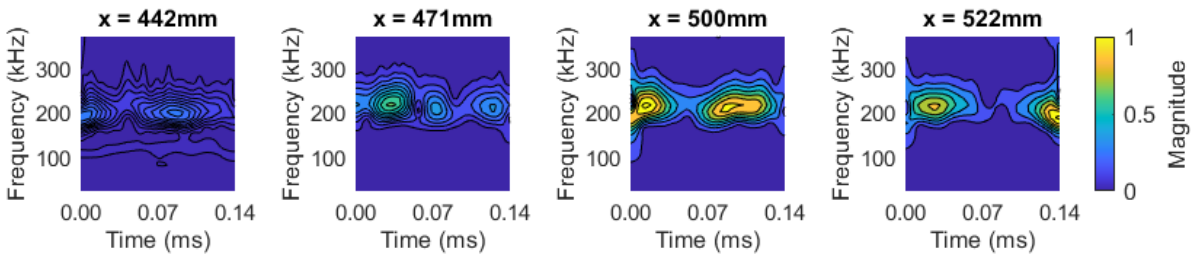


Figure 6.19: Wavelet scalograms from pressure transducer data

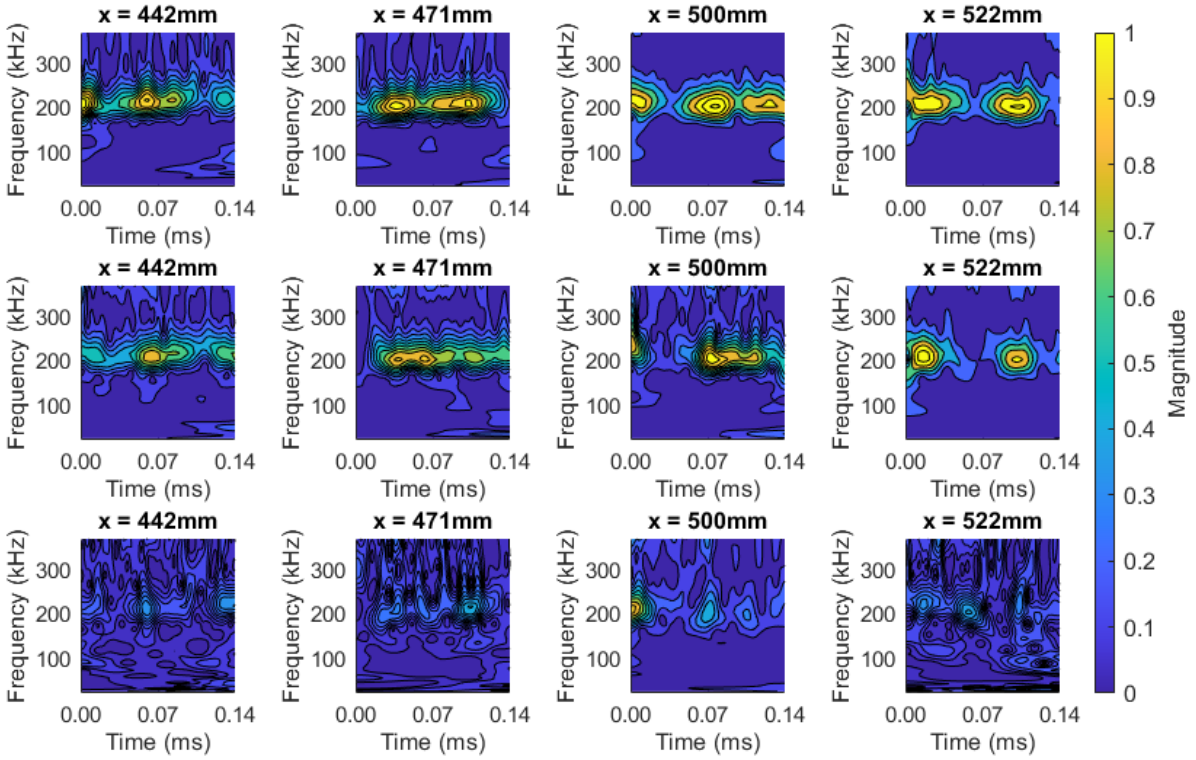


Figure 6.20: Wavelet scalograms from schlieren images, shot 1922, at equivalent PCB locations, corresponding to the wall normal locations in Fig. 6.18

6.5.3 Spectral Proper Orthogonal Decomposition (SPOD)

Hann windows of length 12 were used and the first 3-7 ranked modes are shown as the first 2 modes did not show coherent structures. For shot 1922, subharmonics are seen at 145 kHz, and some studies have identified interactions between the first and second modes as a significant nonlinear process preceding transition for sharp cones [183]. However, Butler & Laurence [71] indicate that the presence or absence of first mode interactions from schlieren images should be taken with

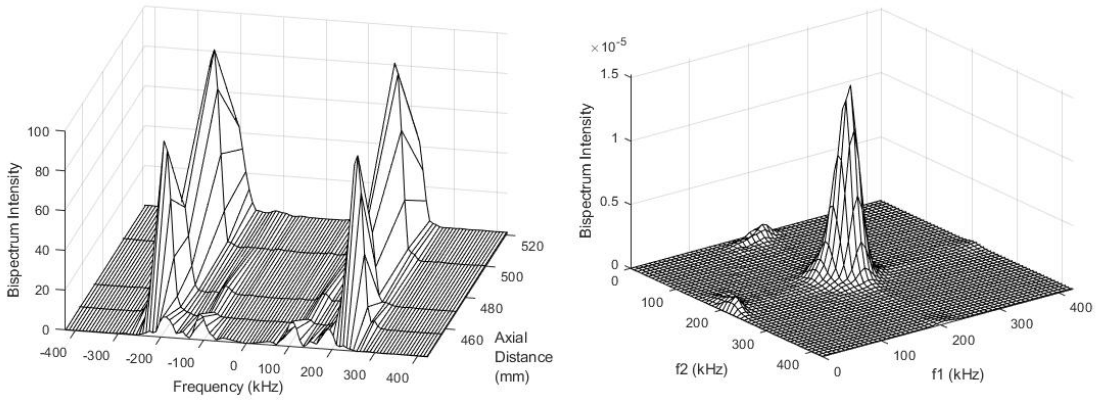


Figure 6.21: Bispectrum for shot 1922 from PCB data at sensor locations from theoretically sharp nose tip (left) and bispectrum for single PCB location at approximately 457 mm (right)

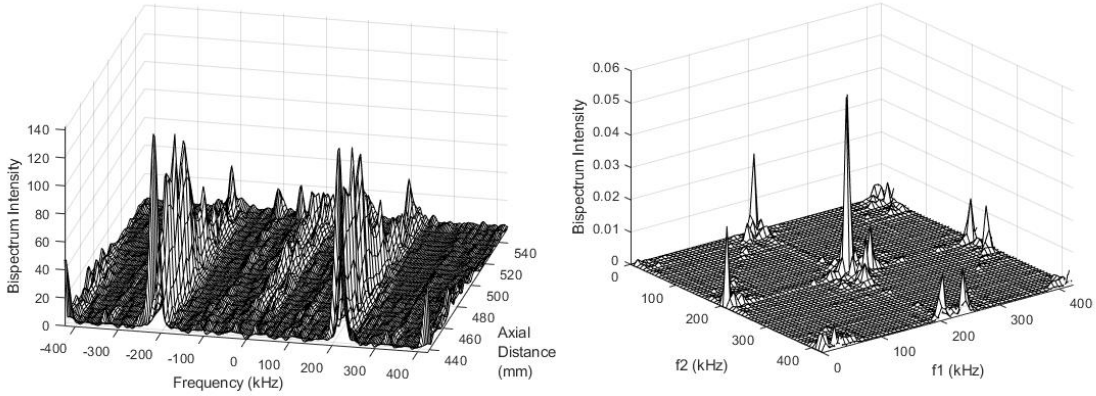


Figure 6.22: Bispectrum for shot 1922 from schlieren data at axial locations from theoretically sharp nose tip (left) and bispectrum for at a single PCB location at approximately 457 mm (right)

some scepticism as it is a line of sight method. However, given the structures seen at 362 kHz, this would seem to be an interaction between the 145 kHz and 217 kHz dominant frequencies. Further, self-coupling of the 145 kHz mode could be seen in the structures at 290 kHz. Self-coupling of the higher frequency 217 kHz signal is indicated with the frequencies at 435 kHz.

Appendix E shows the SPOD results for the remaining experiments.

6.5.4 Comparison of Feature Detection Results

Feature detection methods were applied, where applicable, to the datasets collected at different frame rates. Three methods were explored, wavelet scalograms, bispectral

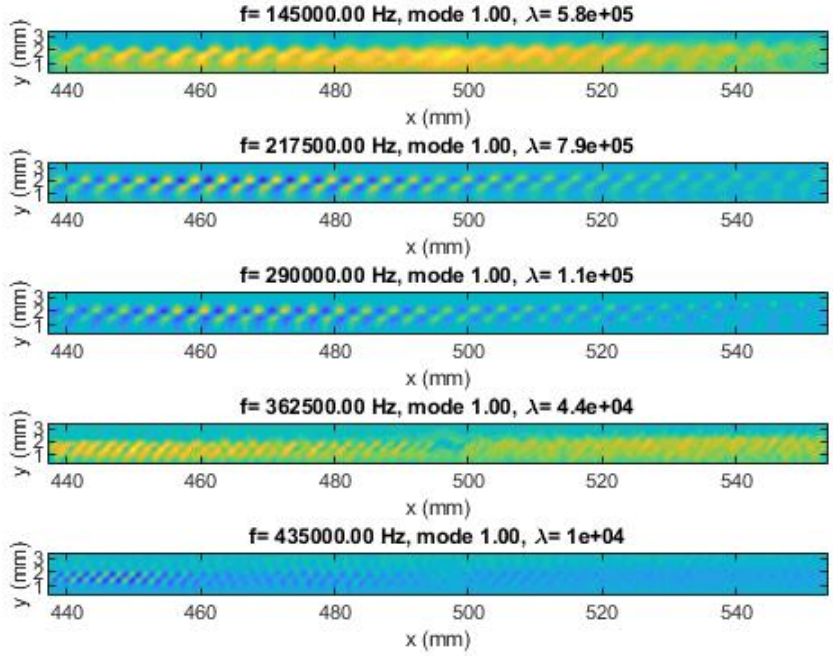


Figure 6.23: SPOD analysis for shot 1922 at 870kfps

analysis and spectral proper orthogonal decomposition (SPOD). Wavelet scalograms are useful for the identification and examination of the evolution of wavepackets and turbulent spots over time and may also weakly identify nonlinear interactions. Bispectral analysis is more suited to this however, and is particularly useful in identifying harmonics and coupling of frequencies. SPOD analysis is useful in identifying and highlighting the evolution of coherent structures in a flowfield. The major disadvantage of these methods is that they are only able to provide information up to half of the sampling frequency, so if self-coupling of second mode frequencies is present, it is only identifiable if the images are captured at four times the expected second mode frequency. While this is possible for the frequencies of instabilities in the test conditions of HDT, in T6, frequencies on the order of 1 MHz are expected, requiring a camera able to operate at over 4 Mfps. The Kirana5M is capable of this, but the system is limited by the trigger signal pulsing the laser and the image quality at this rate.

6.6 Parameter Comparison using Single Set of Data

An additional smaller study was done to determine the importance of different parameters on the quality of information able to be extracted from the data. A set of parameters were varied using the dataset with the clearest images in order to determine which settings had the most effect on the quality of information which could be extracted. These parameters included:

1. Resolution (in wall normal, axial and both directions)
2. Frame Rate
3. Number of Frames

The cases were assessed to determine if the simplest method to detect the dominant second mode frequency could be applied (intensity probe) and whether nonlinear information could be extracted using bispectral analysis.

6.6.1 Original Dataset

The original dataset used for the analysis is shot 1922 which was taken with the Phantom TMX-7510 camera, at a resolution of 566x16 pixels (post background processing) and a frame rate of 870 kfps, for 1000 frames which corresponded to approximately 1ms of test time. The images from this shot showed very clear wavepackets and provided a good dataset to determine the effects of changing parameters.

6.6.2 Effect of Decreasing Resolution

The resolution of the set of images was artificially decreased using bicubic interpolation where each output pixel value is a weighted average of pixels in the nearest 4-by-4 neighbourhood across rows, columns or both. The intensity probe method applied to sets of data with:

1. Decreasing resolution in the wall normal direction ("Y" cases, Table 6.3), shown for a frame in Fig. 6.24

Table 6.3: Cases and resolutions for de-sampling in height above surface

Case	Resolution in X	Resolution in Y
0 (Original Set)	566	16
Y1	566	8
Y2	566	6
Y3	566	4
Y4	566	3

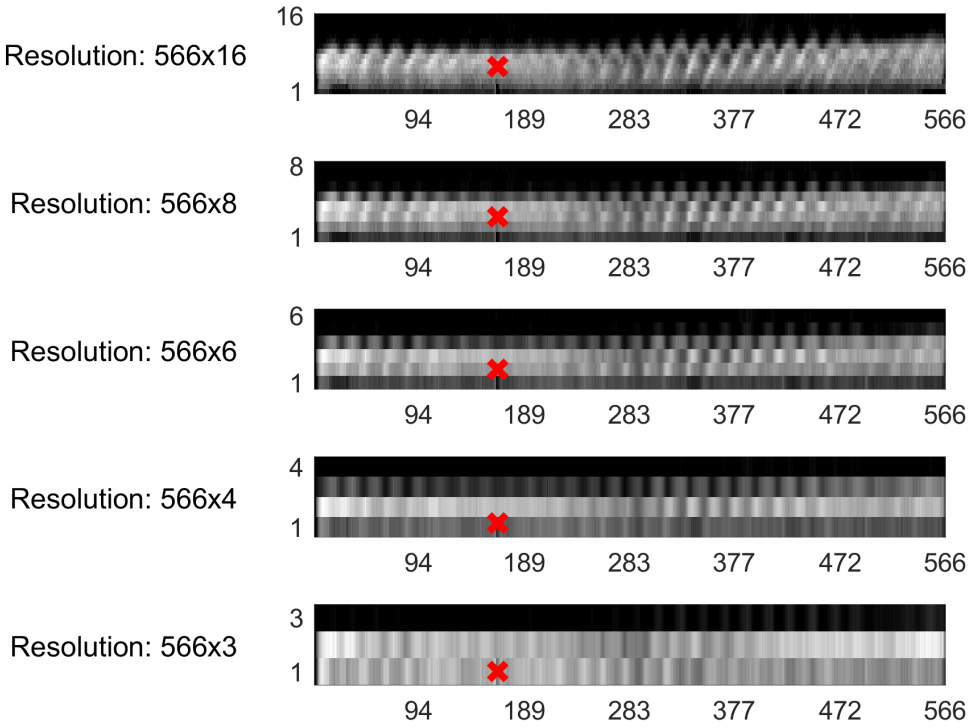


Figure 6.24: Snapshot of original and de-resolved images in wall normal direction (axes are in pixels)

2. Decreasing resolution in the axial direction ("X" cases, Table 6.4), shown for a frame in Fig. 6.25

Table 6.4: Cases and resolutions for de-sampling in axial direction

Case	Resolution in X	Resolution in Y
0 (Original Set)	566	16
X1	283	16
X2	189	16
X3	142	16
X4	95	16
X5	71	16
X6	57	16

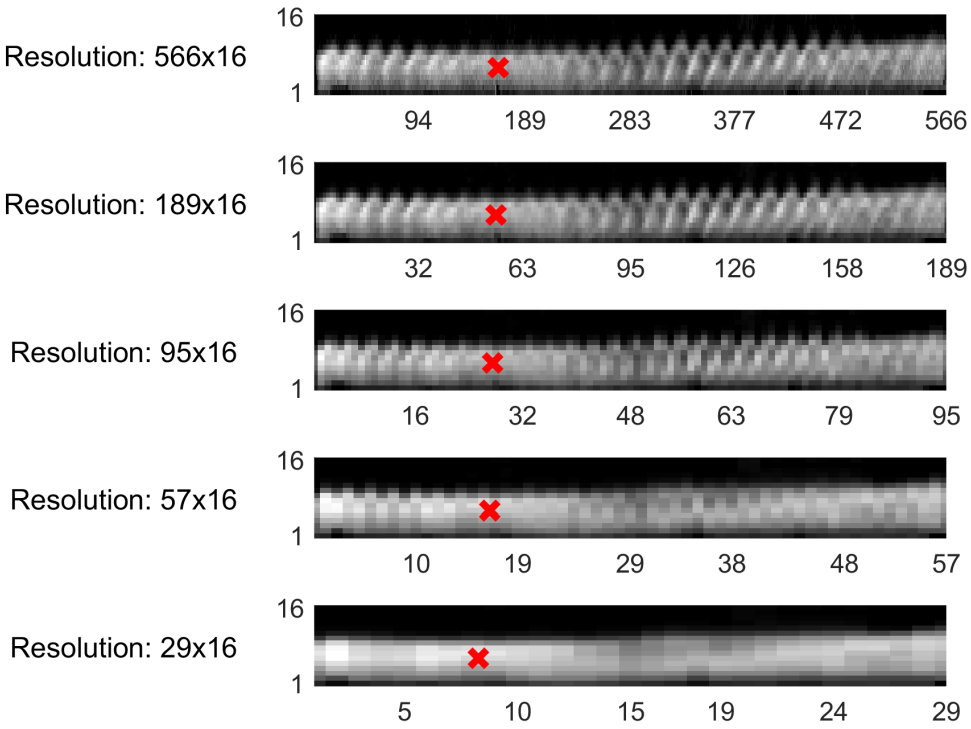


Figure 6.25: Snapshot of original and de-resolved images in axial direction (axes are in pixels)

3. Decreasing resolution in both wall normal and axial directions ("XY" cases, Table 6.5), shown for a frame in Fig. 6.26

Table 6.5: Cases and resolutions for de-sampling in both wall normal and axial directions

Case	Resolution in X	Resolution in Y
0 (Original Set)	566	16
XY1	283	8
XY2	189	6
XY3	142	4
XY4	95	3

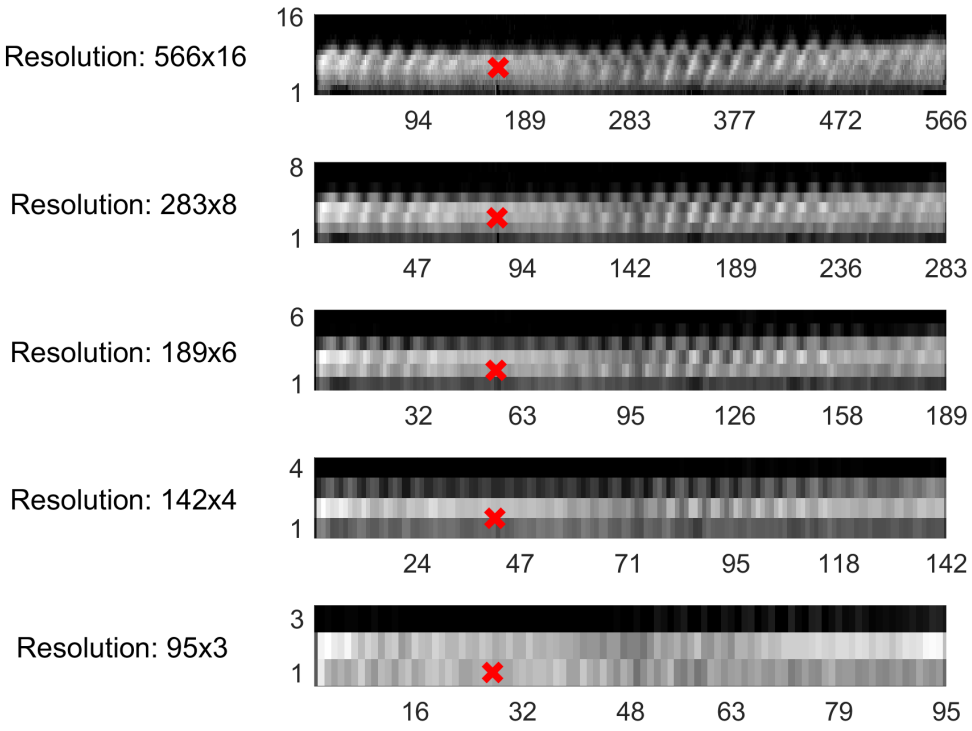


Figure 6.26: Snapshot of original and de-resolved images in wall normal and axial direction (axes are in pixels)

Wall Normal Direction

A snapshot of the original image is shown, along with the same image at varying pixel resolutions along the wall normal direction in Fig. 6.24. The marker indicates the position of the intensity probe and corresponds to location on the model of PCB 5.

The power spectral density for each case is compared in Fig. 6.27.

The bispectrogram and diagonal slice through the bispectrum for each case is compared in Fig. 6.29 and Fig. 6.28.

Axial Direction

Similarly for images which are decreased in pixel resolution along the axial direction of the same image, the series of de-resolved images is shown in Fig. 6.25. The marker indicates the position of the probe again corresponding to the location of PCB 5. The PSD for each case is compared in Fig. 6.30. The diagonal slice through the bispectrum and bispectrogram for each case is compared in Fig. 6.31 and Fig. 6.32.

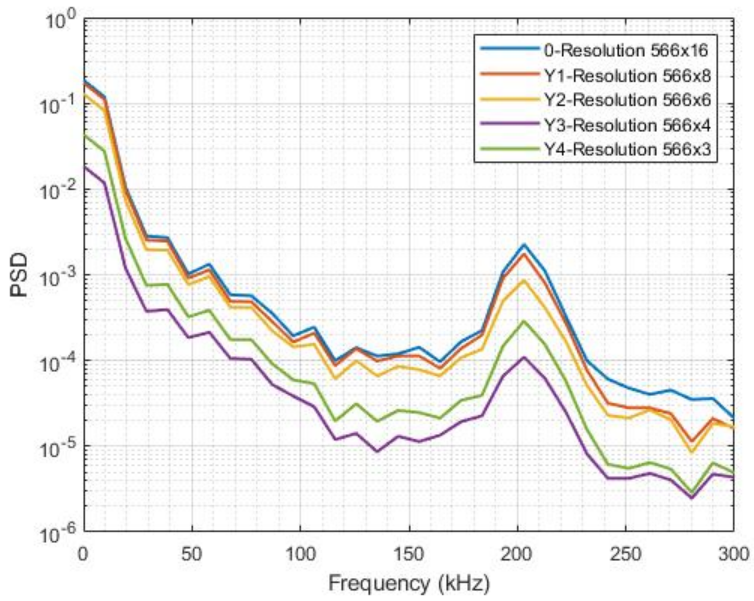


Figure 6.27: Power spectral density comparison of de-resolved images in wall normal direction

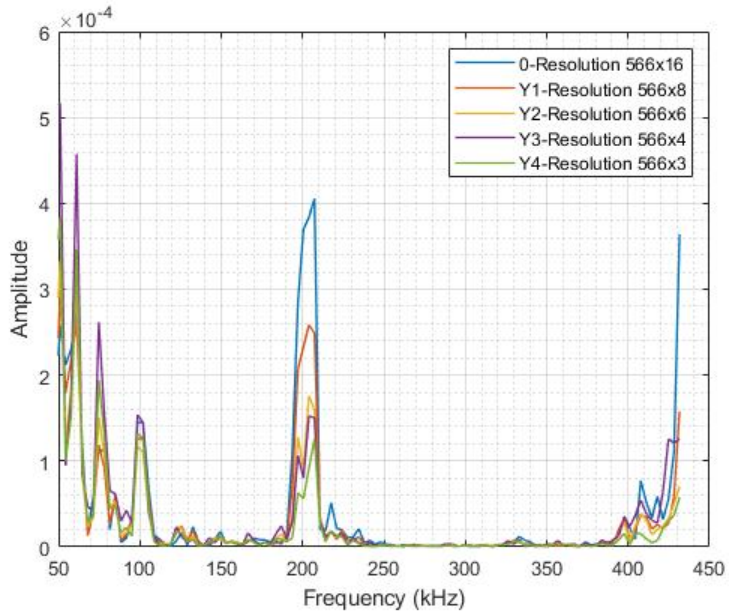


Figure 6.28: Diagonal slice through the bispectrum for cases in the wall normal direction

Wall Normal and Axial Direction

Next, the resolution of the images was varied in both the wall normal and axial direction, shown in Fig. 6.26.

The PSD for each case is compared in Fig. 6.33.

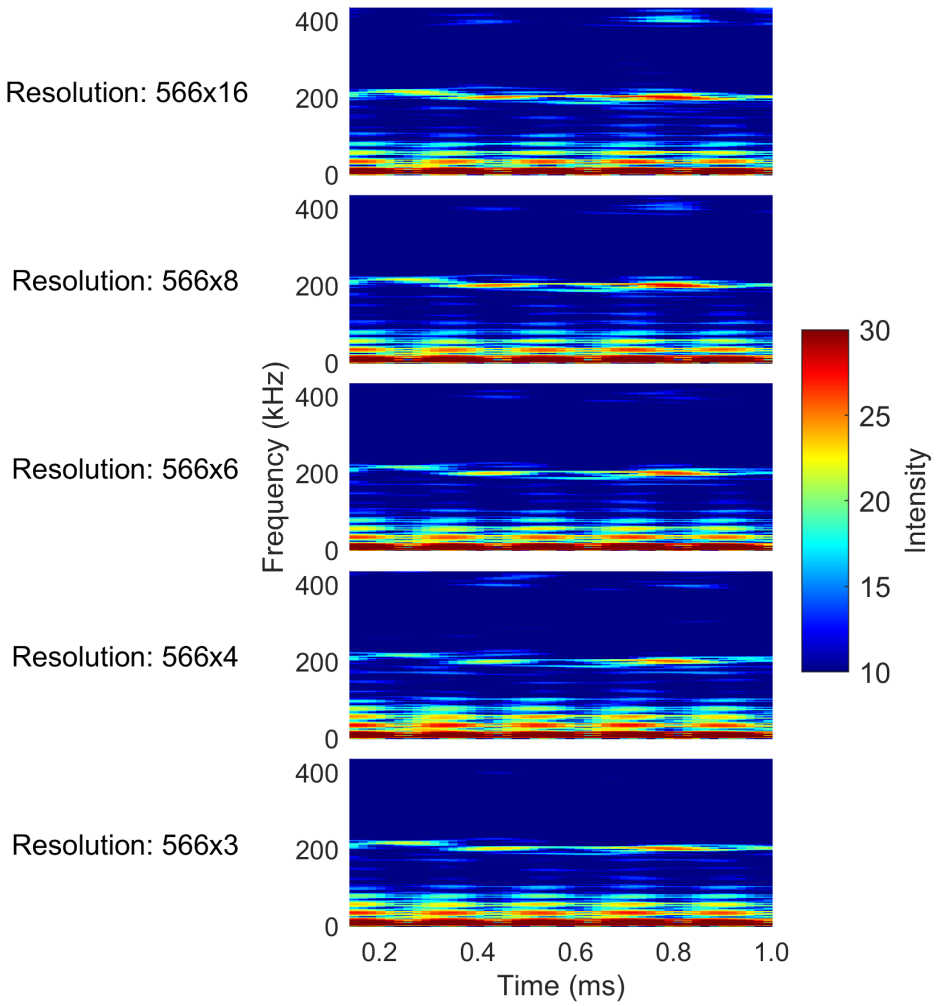


Figure 6.29: Bispectrogram for cases in the wall normal direction

The bispectrogram and diagonal slice through the bispectrum for each case is compared in Fig. 6.35 and Fig. 6.34.

6.6.3 Effect of Decreasing Frame Rate

The effect of reducing the frame rate was investigated by comparing the results from the intensity probe method applied to downsampled sets of data at:

1. The original frame rate (870 000 frames per second)

2. Half of the original frame rate (435 000 frames per second)

3. A third of original frame rate (290 000 frames per second)

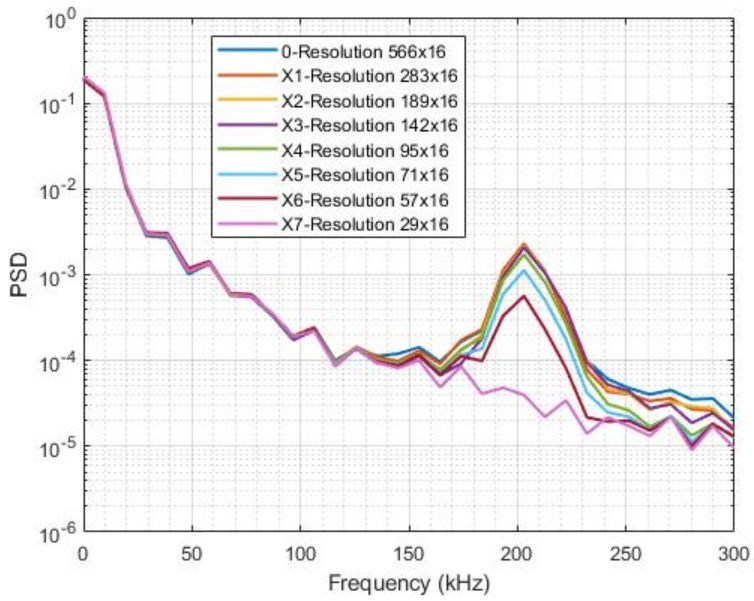


Figure 6.30: Power spectral density comparison of de-resolved images in the axial direction

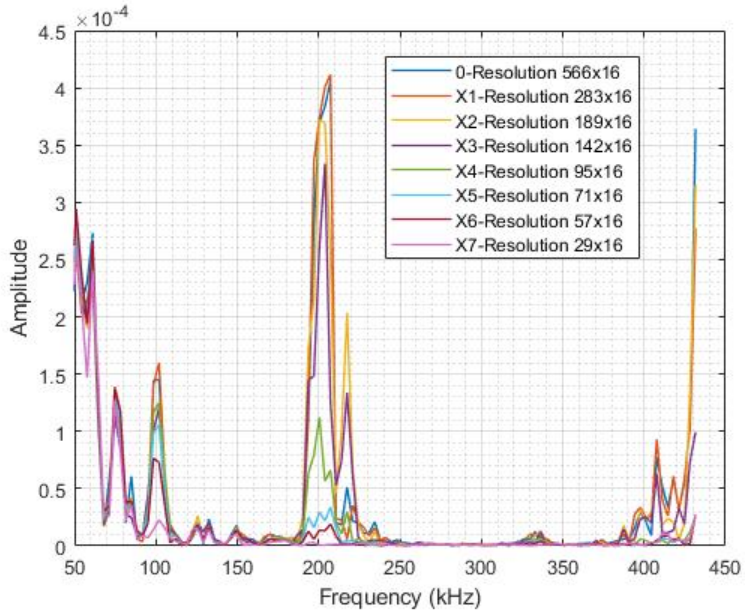


Figure 6.31: Diagonal slice through the bispectrum for cases in the axial direction

The parameters of the downsampled set is summarised in Table 6.6.

The PSD at different frame rates is compared in Fig. 6.36.

The bispectral analysis was not applied to frame rates lower than the original dataset as one step down in resolution results in a sampling frequency of 435 kfps,

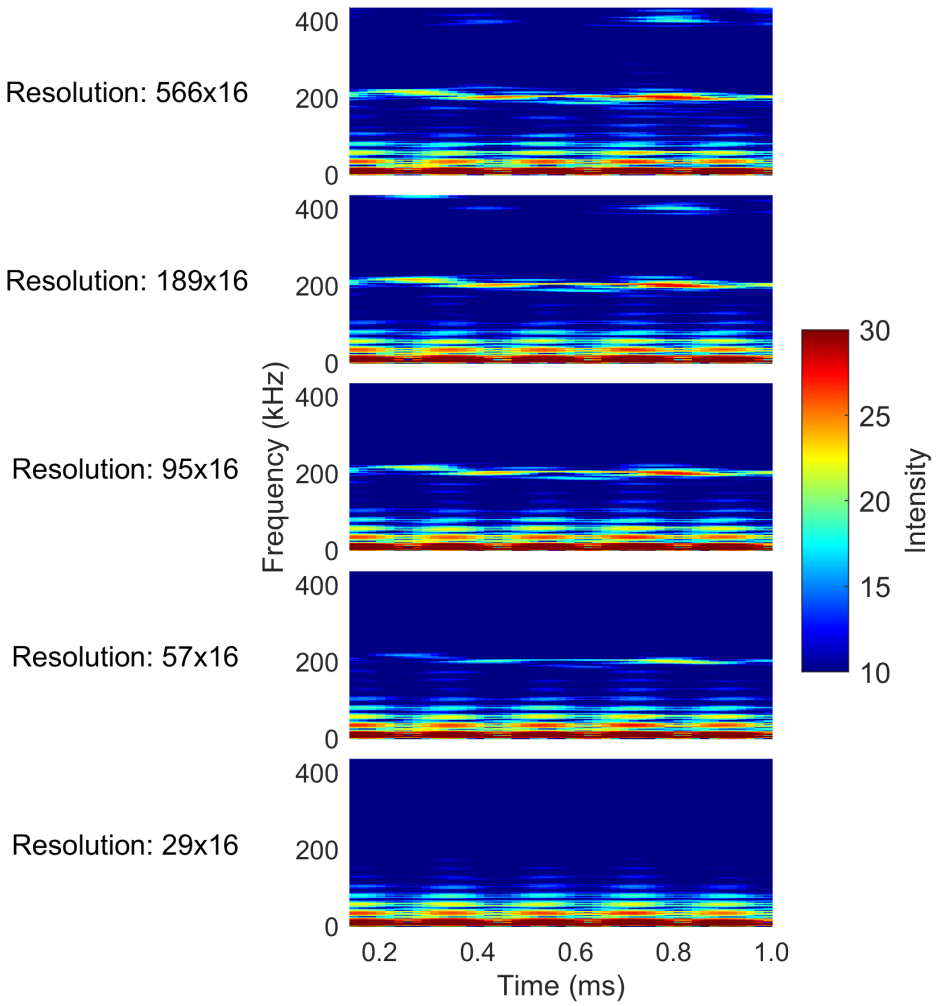


Figure 6.32: Bispectrogram for cases in the axial direction

Table 6.6: Cases and frame rates analysed

Case	Frame Rate (kfps)
0 (Original Set)	870
F1	435
F2	290

which would give a bispectrogram containing information only up to half of this frequency (∼217 kfps). This would give no indication of harmonics beyond the primary one so was not of use in this case.

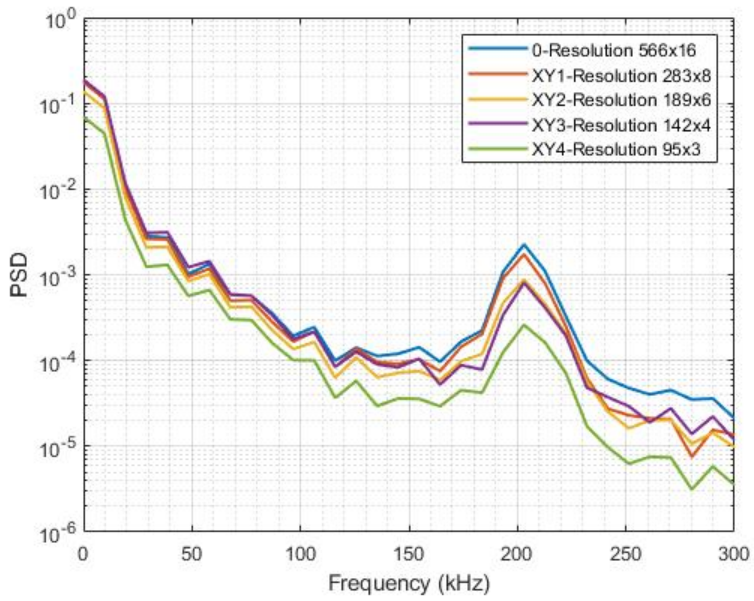


Figure 6.33: Power spectral density comparison of de-resolved images in the wall normal and axial directions

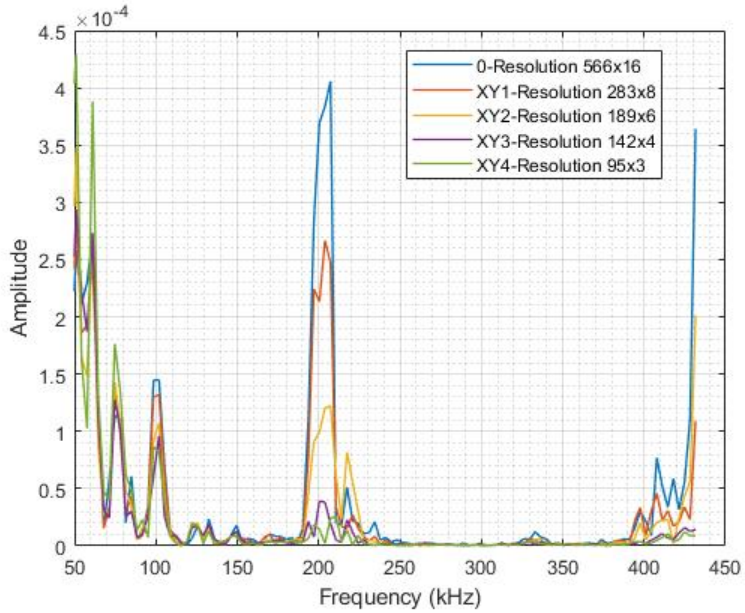


Figure 6.34: Diagonal slice through the bispectrum for cases in the wall normal and axial directions

6.6.4 Effect of Clipping Frame Time

Intensity probe method applied to sets of data with halving number of frames. Summarised in Table 6.7.

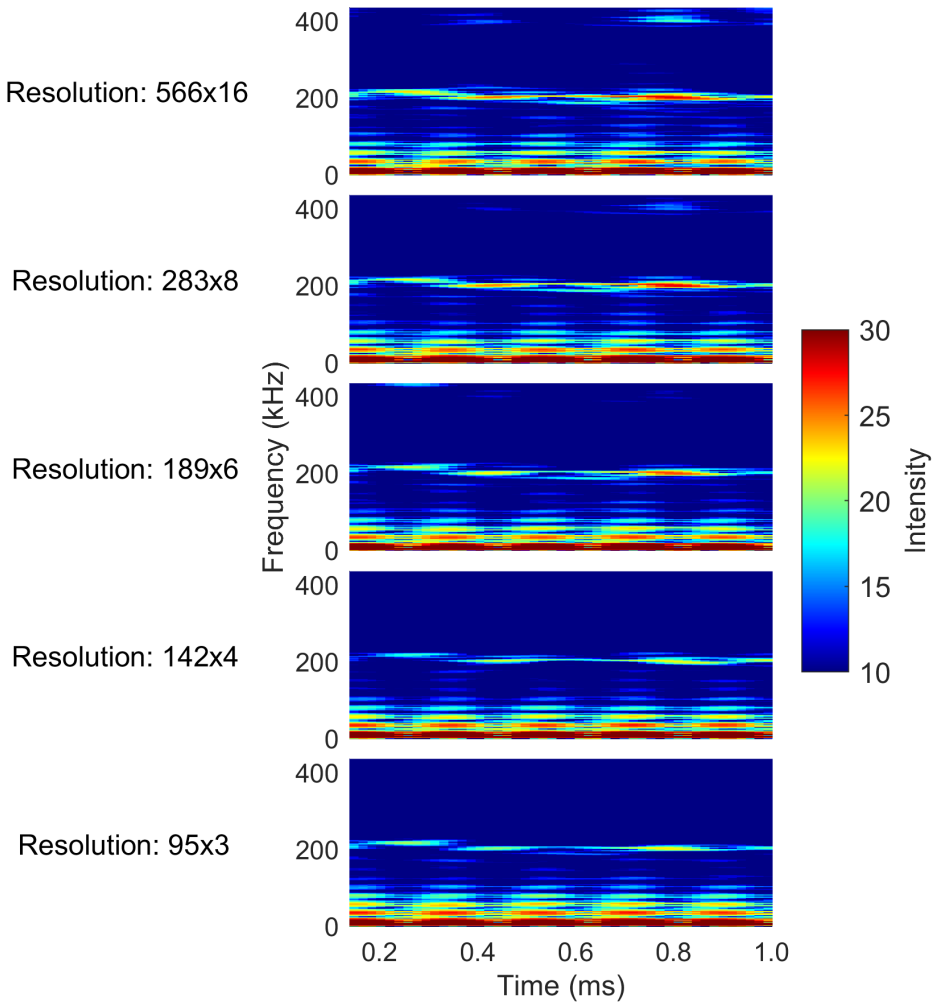


Figure 6.35: Bispectrogram for cases in the wall normal and axial directions

Table 6.7: Cases and frames analysed

Case	Number of Frames
0 (Original Set)	1000
T1	500
T2	250
T3	125
T4	63
T5	32

The PSD at different frame numbers is shown in Fig. 6.37

The bispectrogram and diagonal slice through the bispectrum for each case is compared in Fig. 6.39 and Fig. 6.38.

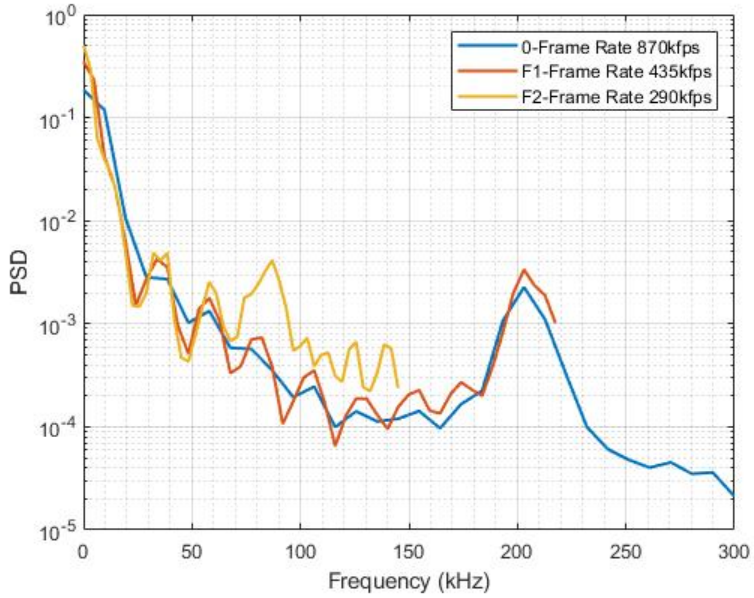


Figure 6.36: PSD comparison at different frame rates

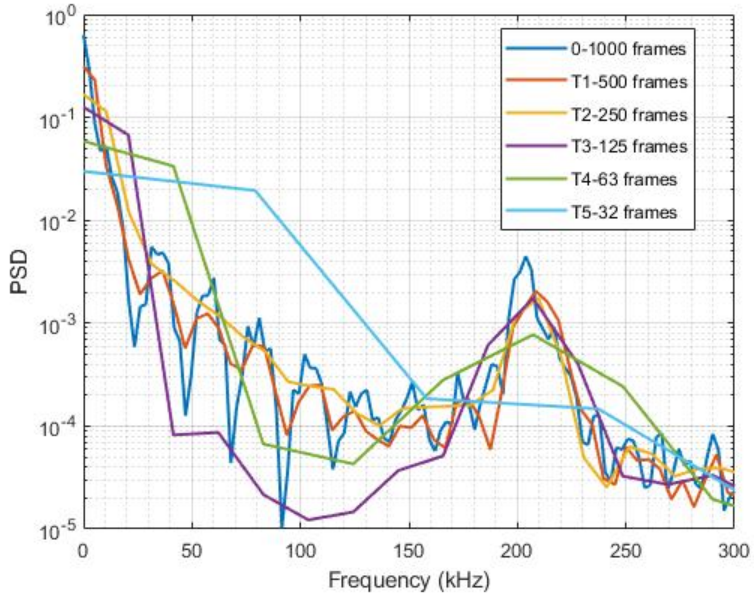


Figure 6.37: PSD comparison at different number of frames

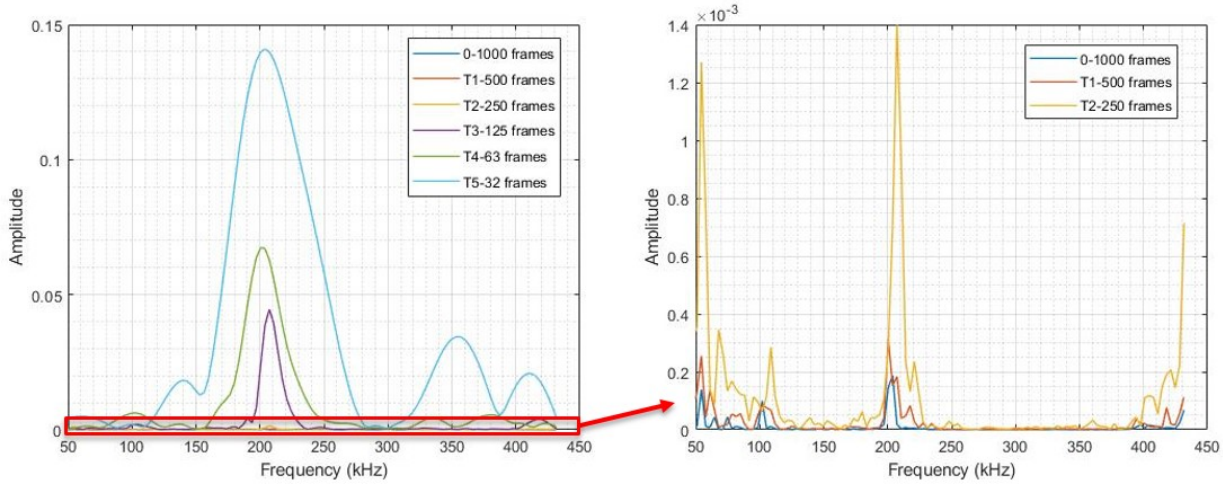


Figure 6.38: Diagonal slice through the bispectrum for different number of frames (zoomed in on the right)

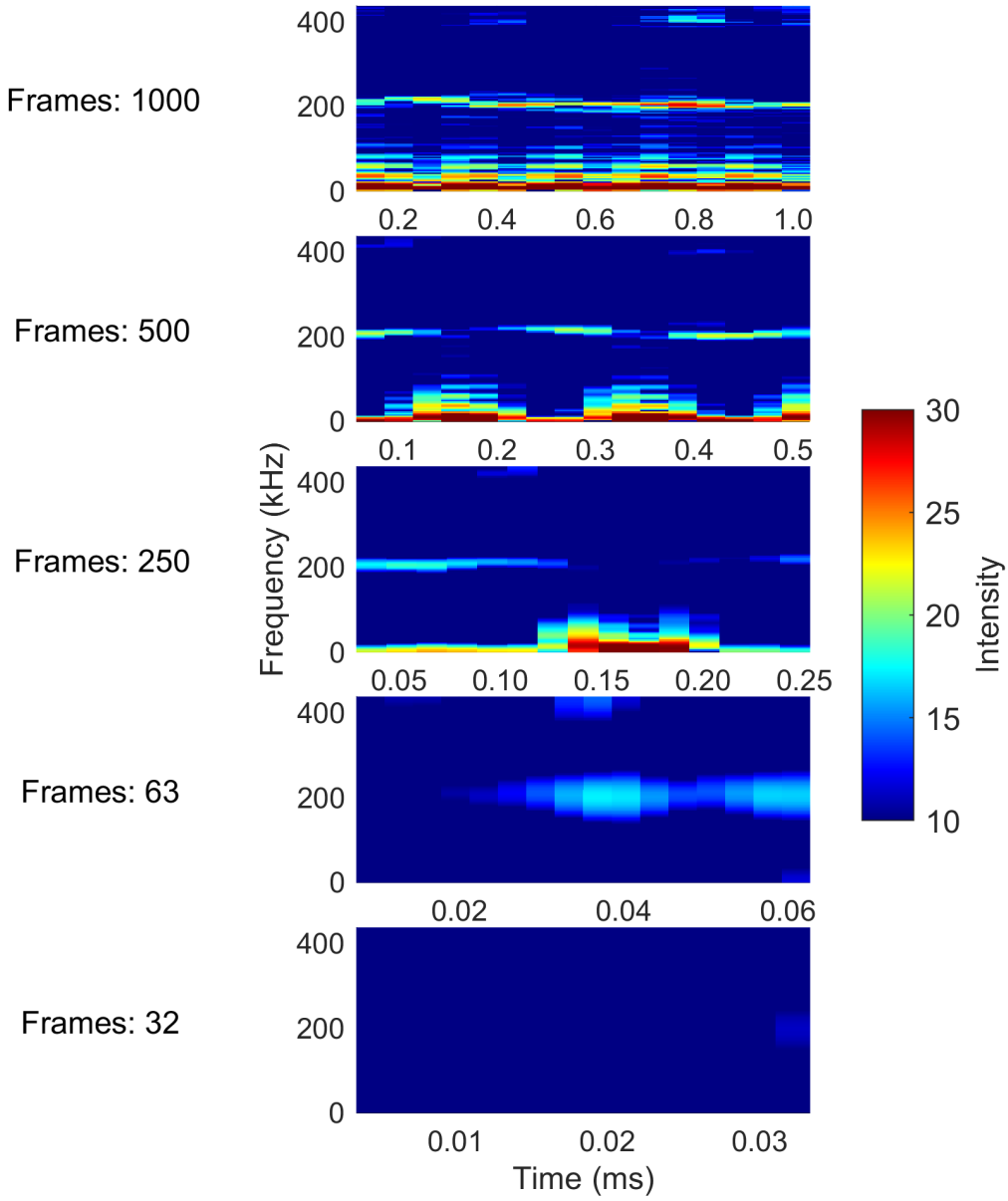


Figure 6.39: Bispectrogram for cases for different number of frames

6.6.5 Comparison of parameter effects

A smaller investigation was done with the aim of determining the camera setting that has the most effect on the quality of information extracted by two processes, the intensity probe and bispectral analysis. A high quality set of schlieren images was taken from shot 1922, using the Phantom TMX 7510 camera at 870 kfps. These images were artificially modified and the analysis run on each case. First, the effect of changing pixel resolution axially, normal to the surface and in both directions was explored. Adjacent pixels in each image were combined using a weighted average of each 4-by-4 cell in the specified direction. Then the pixel intensities were extracted and a power spectral density plot obtained to determine frequency information. A bispectral analysis was applied to compare the quality of nonlinear information retained with the decreasing resolution. In general, the results indicated that de-resolving images very quickly loses nonlinear information. This is more quickly lost when reducing resolution in the wall-normal direction than the axial direction. The opposite is seen when looking at the dominant frequency through the PSD. Here, reducing the resolution in the wall normal direction is much more robust than the axial direction. For resolutions in the axial direction, the method works but only to the point where the resolution is less than a wavelength. Next, the limitations introduced by reducing frame rate were explored. The images were sampled at half and a third of their original frame rates but this very quickly reduced the frequency and nonlinear information which could be extracted as both of these methods are subject to the Nyquist limit. In terms of the number of frames analysed, provided the frame rate is high enough, a small number of frames (63 in this case) was enough to provide an accurate estimate of the second mode frequencies. For nonlinear information however, the method proved unstable for anything less than 125 frames. In summary, frame rate when compared to resolution and number of frames is by far the limiting factor, particularly when nonlinear information is required.

6.7 Conclusion

Various methods for frequency and feature detection of second mode instabilities in the Oxford High Density Tunnel have been developed and compared with the results from pressure sensors. Second mode instabilities have been clearly established on a 7^o cone mode model with a nose tip radius of 1.25 mm and captured using schlieren with three high speed cameras of varying resolution and frame rate capabilities. The advantages and limitations of each technique have been explored. The suitability of each technique for extracting information from images captured at frame rates above and below the second mode frequencies are discussed. Techniques which are useful for detecting features such as turbulent spots, nonlinear effects and coherent structures in the flow are also explored and applied to the data. A study was done artificially varying parameters such as resolution, frame rate and number of frames on an "ideal" set of images to investigate the effectiveness of two of the techniques under different settings.

7

Schlieren Image Processing Techniques in the Oxford T6 Stalker Tunnel

Contents

7.1 Introduction 161
7.2 Experimental Setup 162
7.2.1 Schlieren and Camera Setup 162
7.2.2 Flow Conditions 164
7.2.3 Selection of Appropriate Test Time 164
7.3 Theoretical Prediction 168
7.4 Processing Methodology 169
7.4.1 Cross-Correlation and Gradient Method 169
7.4.2 Wave Detection and Structure Angle 174
7.5 Second Mode Instability Results 176
7.5.1 $M_\infty = 6.6$, 0.852 mm Radius Nose Tip 176
7.5.2 $M_\infty = 7.6$, 1.095 mm Radius Nose Tip 178
7.6 Non-Modal Instability Results 182
7.6.1 $M_\infty = 7.6$, 3.4 mm Radius Nose Tip 182
7.7 Conclusion 190

7.1 Introduction

The image processing techniques developed in Chapter 5 and proven on the experimental campaign undertaken in the cold flow environment of HDT, presented in Chapter 6 were then applied to experiments in T6 using the conditions commissioned

in Chapter 4. While the low disturbance environment of HDT is useful as a means of generating more easily characterisable second mode frequencies, it is limited to much lower freestream enthalpies than in flight. Thus T6 was commissioned in RST mode to provide a more representative test environment. Testing in this tunnel posed a greater challenge however, due to the harsh nature of the flow, increased particulates from the diaphragms which may appear and fluoresce in images, much shorter test time which reduced the amount of frames which could be analysed, increased noise levels of the freestream due in part to the noise from the boundary layer over the nozzle wall which radiated into the test section and affected the transition process in the form of turbulent spots as well as thinner boundary layers over the model and much higher frequency wave packets. Nonetheless, both second mode and non-modal instabilities were captured with enough clarity to be characterised by some of the image processing techniques developed.

Experiments were first conducted with the nominally Mach 7 nozzle (flow Mach number of approximately 6.6), of which experiment T6s301 is the most viable for analysis. A refurbished Mach 8 nozzle was then tested (resulting in a flow Mach number of approximately 7.6) and this proved to be more successful for identifying clear wavepackets due to the reduced freestream noise as well as the longer test time provided by using a nitrogen driver condition (for further details, see Chapter 4). Nose tip radii of 0.852 mm, 1.095 mm and 3.4 mm were tested, and interesting results were obtained in both. In particular, second mode wavepackets were observed in the sharper nose tip cases, while non-modal instabilities due to the longer entropy swallowing distance were observed with the blunter nose tip. This is the first time both were established and observed in this tunnel. The processing methodologies are first detailed in Section 7.4, and the results for second mode and non-modal instabilities presented in the sections subsequent.

7.2 Experimental Setup

The 7^o cone model described in Chapter 3 was used. Four Kulite pressure transducers at opposing circumferential positions were used for alignment in yaw and angle

of attack but other than that, schlieren imaging was the primary means of data collection on the model. The model was set as close to zero angle of attack as possible using the traverse system.

7.2.1 Schlieren and Camera Setup

The schlieren and camera setup was similar to that used for the HDT campaign (described in detail in Section 6.2.1), with some differences due to the tunnel layouts, space constraints and available equipment. A schematic of the schlieren setup used in T6 is shown in Fig. 7.1. For this configuration, the same Cavitar C013 v1.0 Cavilux Smart UHS pulsed laser with a wavelength of 640 ± 10 nm is used as the light source, with an iris in front to adjust the sensitivity. The parabolic and flat mirrors have a diameter of 200 mm. The parabolic mirrors have a focal length of 6 ft (1.83 m). The achromatic doublet lens used here had a 100 mm focal length. Both Nikon and Tamron adjustable focus lenses were the same as used in the HDT setup. The detection system was also tilted to align with the surface of the cone model, at 7^o . Calibrated schlieren was not implemented at this time.

The camera settings are summarised in Table 7.1. The Phantom TMX 7510 camera was used at a frame rate of 1 Mfps with a maximum resolution of 640 x 64 which provided a decent field of view over the cone surface for shots T6s357 and T6s358. 1 Mfps was used because it provided a good compromise between a high frame rate and field of view.

The Kirana5M camera was used for shot T6s301 at a frame rate of 2 Mfps since this camera had a fixed field of view and the setting was limited instead by the maximum number of frames (180) and by the ability of the laser to pulse at this frequency. The entire camera and lens setup was tilted to the cone half angle to maximise the field of view and align the knife edge with the cone surface. The camera parameters are summarised in Table 7.1.

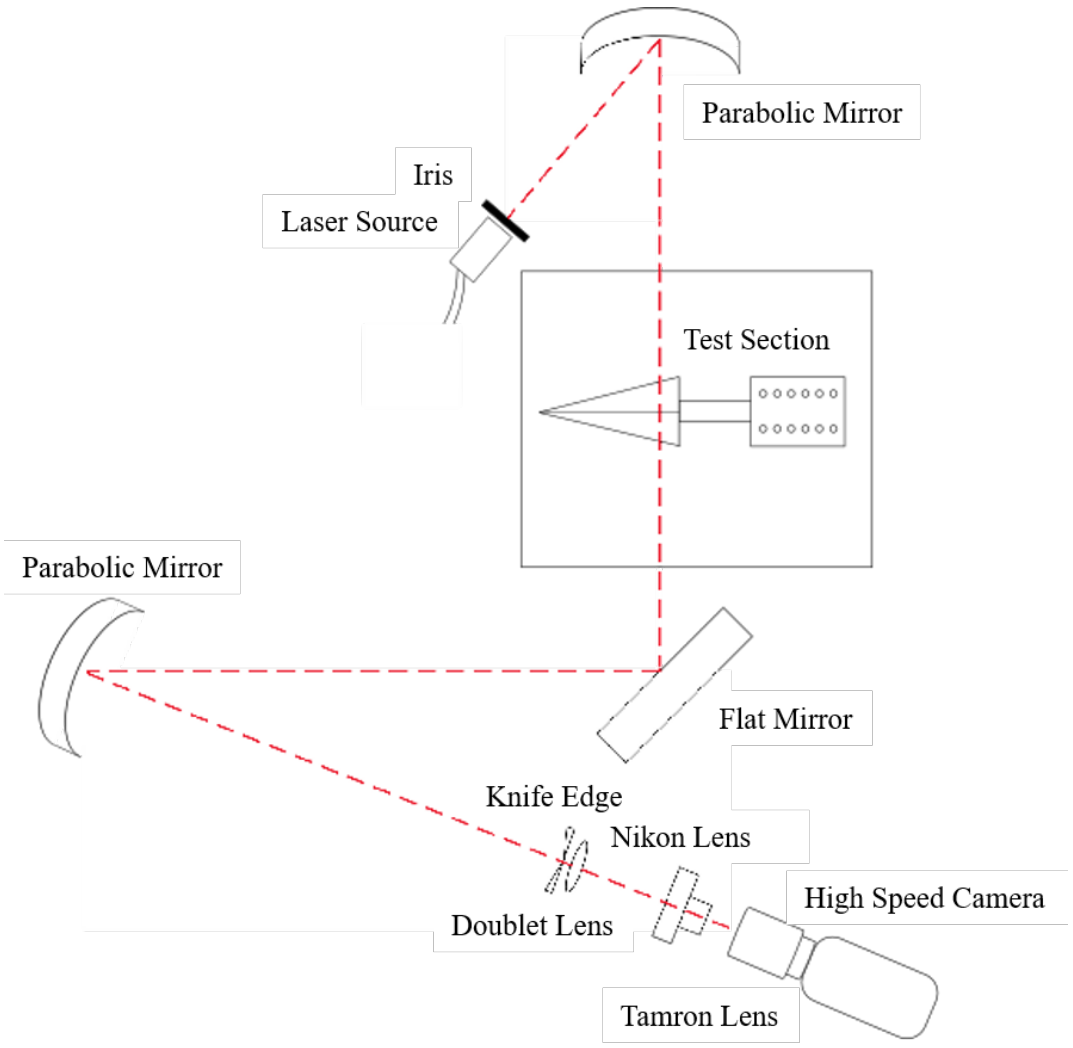


Figure 7.1: Schematic of schlieren setup in T6, optical path lengths and objects are not to scale

Table 7.1: Camera settings for T6

Shot Number	Camera	Frame Rate (kfps)	Resolution
T6s301	Kirana5M	2000	924x768
T6s357	Phantom TMX 7510	1000	640x64
T6s358	Phantom TMX 7510	1000	640x64

7.2.2 Flow Conditions

The test conditions and geometries (nosetip radii R_N) are summarised in Table 7.2 with the nominal test condition names in parentheses (corresponding to the table of nominal T6 test conditions in Table 4.10), along with the limits of the field of view (FOV) on the cone referenced from the theoretically sharp nose tip. Freestream

and total conditions such as stagnation enthalpy, unit Reynolds number and Mach number were calculated using ESTCj [129] with an equilibrium air assumption (the validity of this is discussed in Chapter 4) together with the measured values of stagnation pressure, Pitot to total pressure and shock speed from the Pitot rake campaigns. The entropy swallowing distance X_{SW} was calculated using Eq. (2.2) described in Section 2.5.

Table 7.2: Test conditions for T6 experiments

Shot	H_0 (MJ/kg)	M_∞	M_e	T_w/T_0	$Re_{U,\infty}$ (10^6/m)	R_N (mm)	X_{SW} (mm)	FOV x (mm)
T6s301 (A0)	2.40	6.60	5.82	0.15	11.8	0.852	132	210-270
T6s357 (D)	2.40	7.59	6.53	0.105	10.14	1.095	180	160-268
T6s358 (D)	2.43	7.61	6.55	0.105	10.12	3.4	800	162-270

7.2.3 Selection of Appropriate Test Time

For the inherently transient flow generated by shock tunnel facilities and the complex processes involved, the determination of the test time becomes important. Fig. 7.2 shows the pressure traces for the stagnation pressure, Pitot pressure obtained at the same conditions during the flow characterisation campaign normalised by the stagnation pressure and the model Kulite sensor static pressure also normalised by the stagnation pressure for T6s357. The Pitot and model sensor pressures are normalised by the stagnation pressure using a time offset to account for the flow transit time from the nozzle supply region to the sensor. The trigger time (at zero ms) corresponds to the rise in stagnation pressure. Note that this zero time reference is just used for the test time determination here and later references to time zero are from the start of the test time for each case.

The unsteady nozzle start up process is indicated by the stagnation pressure trace, from approximately 0-0.36 ms. The stabilisation of the Pitot to supply/stagnation pressure ratio indicates when the initial unsteady nozzle start up flow has been swept through the Pitot rake, corresponding to approximately 0.92 ms in the Pitot to supply pressure trace. This is traced through from the time offset in the Kulite sensor

to approximately 0.77 ms. The corresponding time for flow establishment over the model is then given by G, as described in Section 4.9 and Eq. (7.1), repeated here:

$$G = U_c t_{est}/L_c \tag{7.1}$$

G has been shown to vary between 1 for turbulent flow and 2 for laminar flows for pressure measurements [147]. While semi-empirical relations such as these make the assumption that turbulent flow starts immediately from the leading edge, in reality there is a small region of laminar flow first, for which a correction is usually applied but this has shown to be small [149]. As the flow of interest over the model is transitioning between these two cases the limits of G are applied to the Kulite pressure trace. This is indicated in Fig. 7.2 and shows the most and least conservative estimates for the start of the test time over the region of interest from which the schlieren images could be processed. The middle of these two cases was thus chosen as the start of the test time and examination of the schlieren images from this time shows consistent behaviour. The end of the test time is indicated in the stagnation pressure trace when the supply pressure starts to drop below 10% of the nominal value which is considered an acceptable threshold [146]. Sometimes the end of the test time is determined by the contamination of the test gas by the driver gas but since this occurs much later than the decay in nozzle supply pressure, the later was chosen. Thus, the total test time considered acceptable for clipping the schlieren frames of interest is indicated in Fig. 7.2 in the model sensor pressure trace. This was done for shot T6s357, shown here. In further results sections, time zero indicates the start of the appropriate test time over the model from this analysis.

The same methodology was applied to shots T6s358 (Fig. 7.3) and T6s301 (Fig. 7.4). The times indicated on subsequent images are referenced from the start of the available test time for each shot, except for shot T6s301. For this experiment, the Kirana5M camera was used, which has a limited number of frames of 180. At 2Mfps, this gave 0.09 ms of captured time but was started at 0.8 ms from the trigger time (the trigger being zero on Fig. 7.4). As indicated on the plot, this falls in

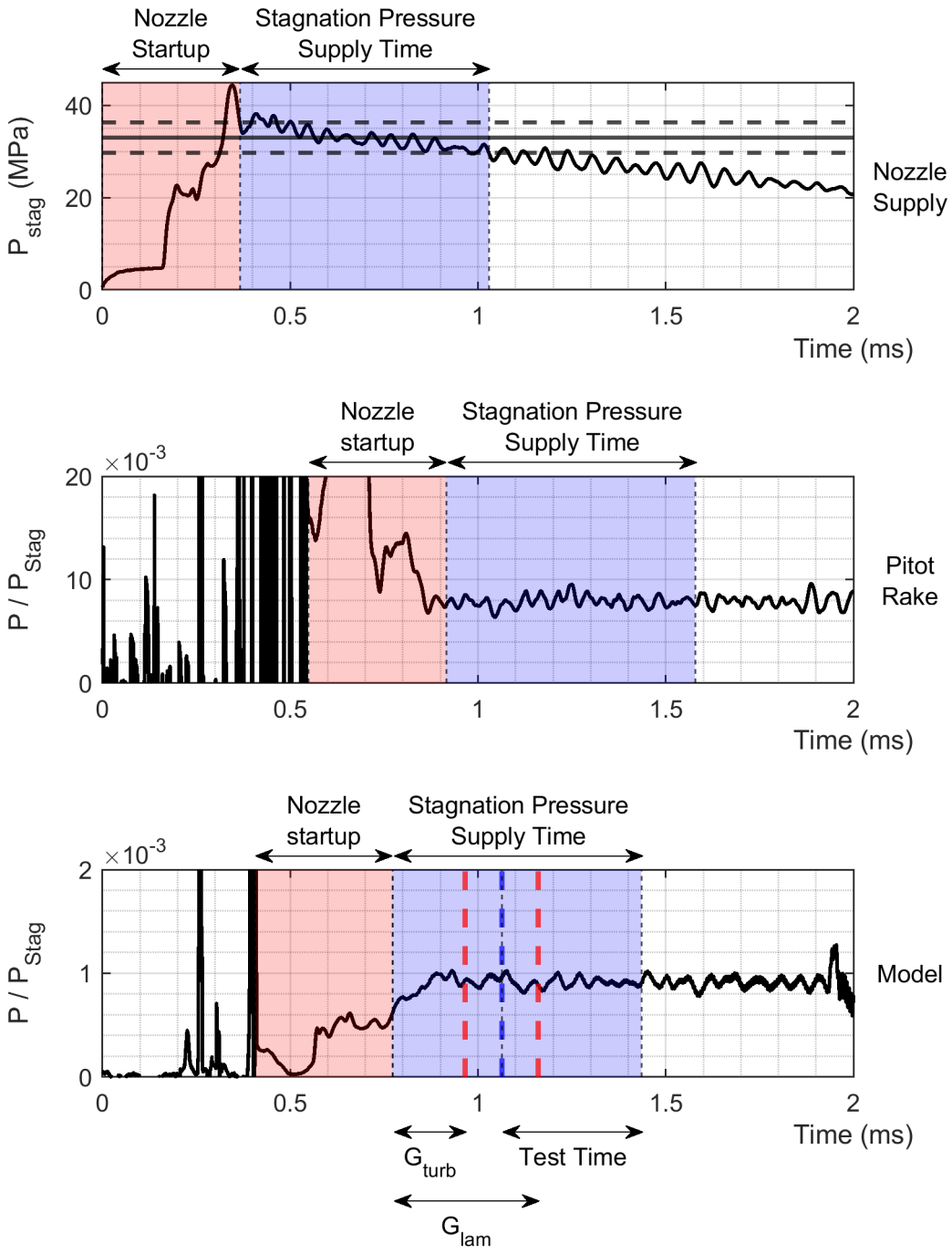


Figure 7.2: Test time analysis for T6s357

what is likely still the flow establishment time so while results from this experiment are included, they should be interpreted with some caution.

The shock speeds and characterised freestream conditions performed with a Pitot rake campaign are shown in Section 4.7 for Condition D (corresponding to T6s357 and T6s358, rake test T6s352 and T6s353), and in Section 4.6 for Condition

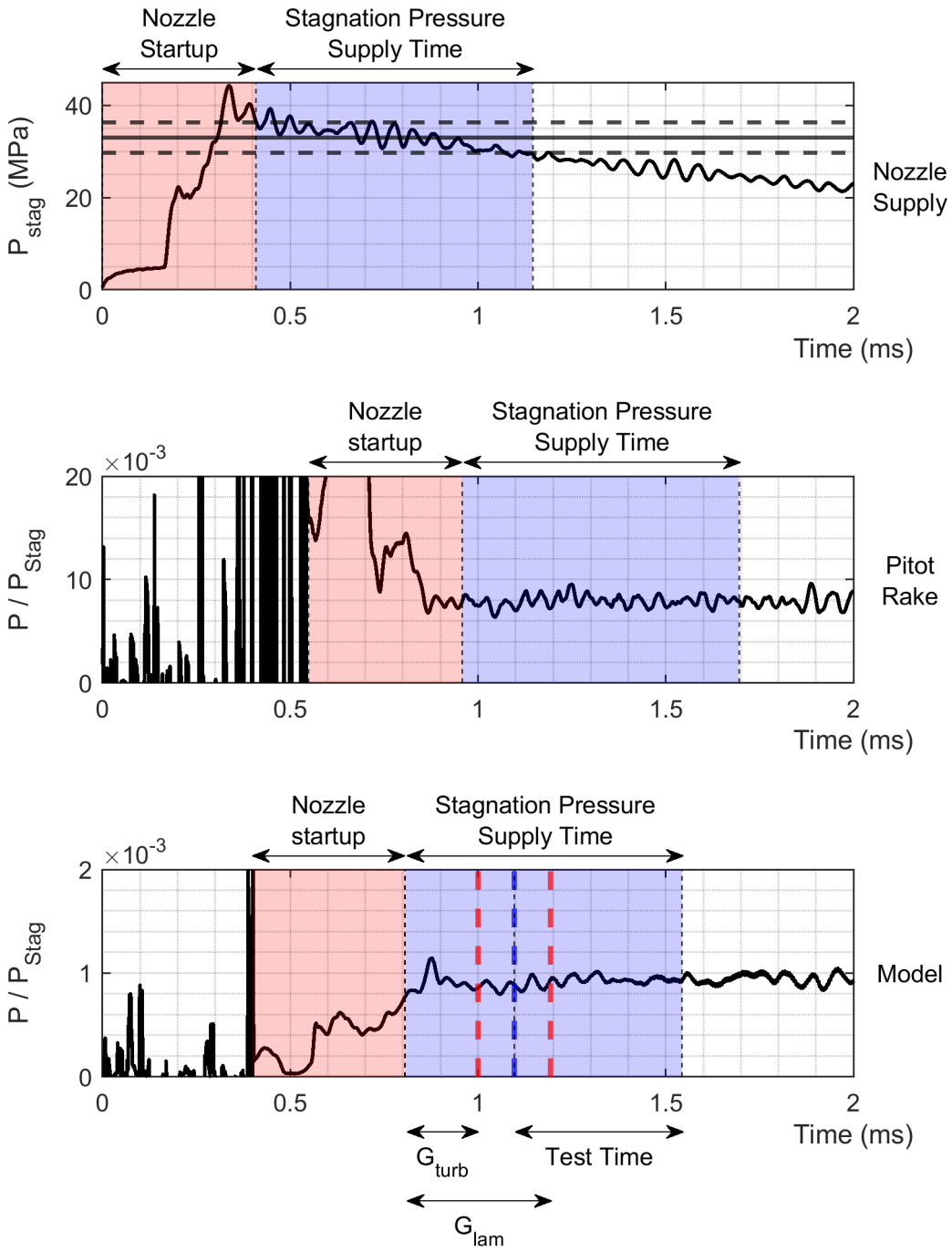


Figure 7.3: Test time analysis for T6s358

A0 (corresponding to T6s301, rake test T6s86).

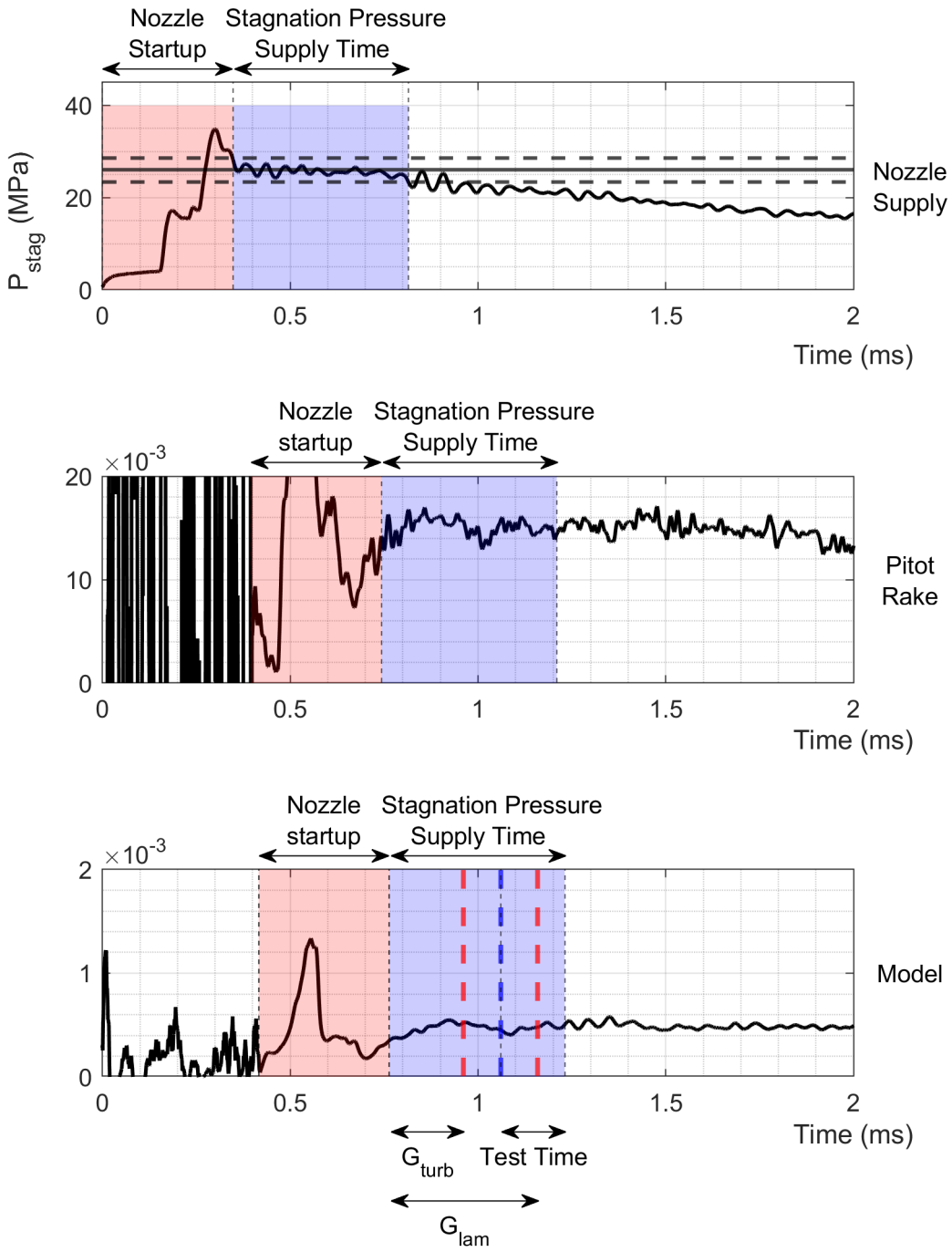


Figure 7.4: Test time analysis for T6s301

7.3 Theoretical Prediction

The boundary layer thickness can be roughly deduced from the maximum intensity of the boundary layer of a schlieren image [152]. Note that this is an estimation and the boundary layer thickness obtained based on density gradient will be less than the

standard 99%U_e boundary layer thickness but provided an adequate indication of the boundary layer for this purpose. For T6s357 ($M_\infty = 7.59$, $Re_{U,\infty} = 10.14\text{x}10^6$/m), δ occurred at approximately 1.0 mm and was taken from an image with the background but not the mean subtracted to provide a greater contrast for identification of the boundary layer edge. For the blunt cone geometry at the same condition (T6s358), the laminar boundary layer thickness was not captured in the field of view and so comparisons to the boundary layer thickness from the sharper cone results are made. The expected frequency of second mode wavepackets for this condition can then be estimated using Eq. (6.5), resulting in 925 kHz for shot T6s357 using a correlation of $0.9U_e/2\delta$. Since the factor of 0.9 is based on empirical observations and is known to range from 0.8-1.0 in other studies [41, 43, 46], this was adjusted down based on the value observed in the HDT campaign of schlieren measurements compared to pressure measurements (0.8). A revised estimated provided a second mode frequency estimate of 855 kHz (indicated by "Estimated Mean" in the resulting figures to distinguish it from the mean values of the cross correlation method). Similarly for test T6s301 ($M_\infty = 6.6$, $Re_{U,\infty} = 11.8\text{x}10^6$/m) the boundary layer was approximately 0.6 mm, resulting in a second mode frequency estimate of 1.4 MHz at this test condition.

7.4 Processing Methodology

7.4.1 Cross-Correlation and Gradient Method

The cross-correlation method developed in Chapter 5, Section 5.4.3, was applied to the pre-processed schlieren images to extract the second mode frequency, using the pre-processing method described in Section 5.3. It is interesting to note that unlike the HDT results, the wavepackets are not visibly identifiable with just background image subtraction, but start to appear when an average image is also subtracted. This could be due to greater intensity from the flow in T6 as well as the thinner boundary layer which make the wavepackets more difficult to detect by eye. A comparison of the same images with the background subtracted, Fig. 7.5, and additionally the mean image subtracted is compared in Fig. 7.6.

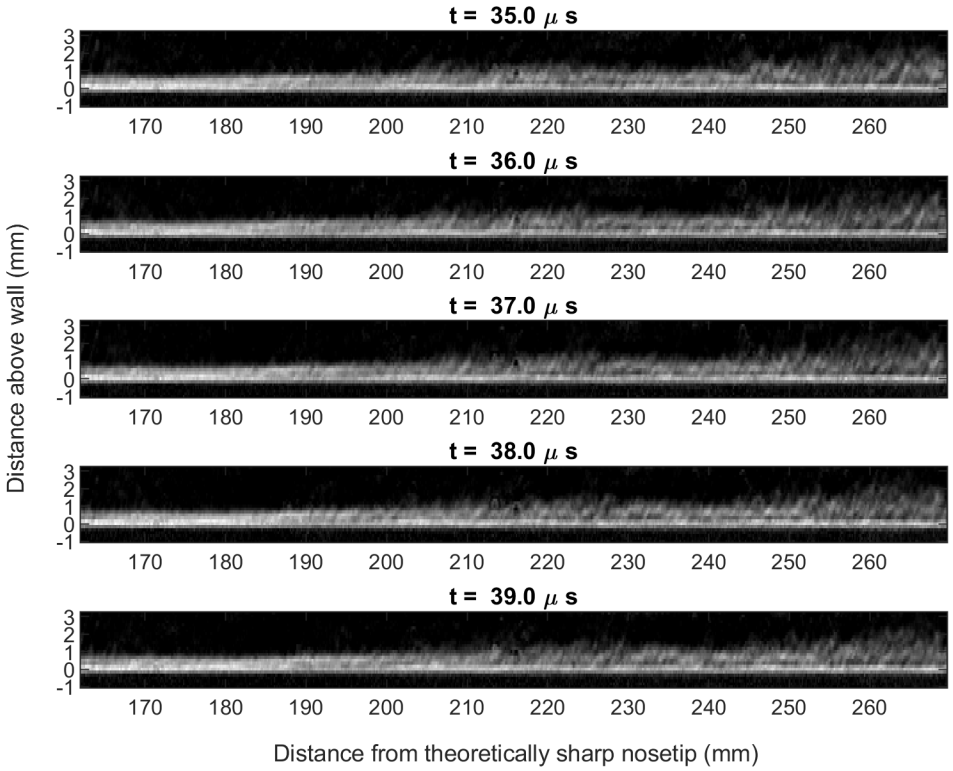


Figure 7.5: Series of images from shot T6s357, images have been processed by background subtraction. Time is referenced from the start of the test time for each condition

The template image and a clear isolated wavepacket which was used as the region for matching is shown in Fig. 7.7. This was approximately 8.5 mm in length and visually identified and selected from a range of schlieren images by it's "rope-like" structure which distinguished it from the surrounding boundary layer region.

This cross-correlation was then applied to the series of images in the test time. A selected series where the matching algorithm correctly identified successive wavepackets is shown in Fig. 7.8.

Similarly for the Mach 6.6 results, shot T6s301, the series of frames captured was analysed by subtracting both the background and mean images. It then becomes apparent that some structures convecting downstream are visible, but whether they are the formation of second mode wavepackets is more difficult to determine, partly due to the quality of the images. The template for cross correlation is shown in Fig. 7.9.

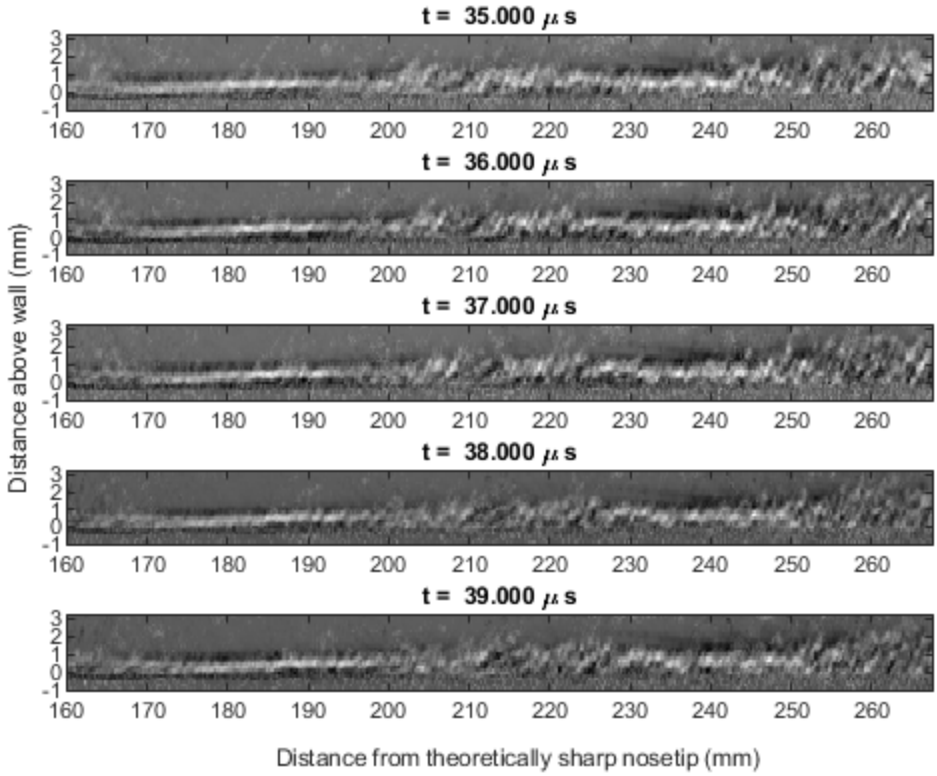


Figure 7.6: Series of images from shot T6s357, images have been processed by background and average image subtraction. Time is referenced from the start of the test time for each condition

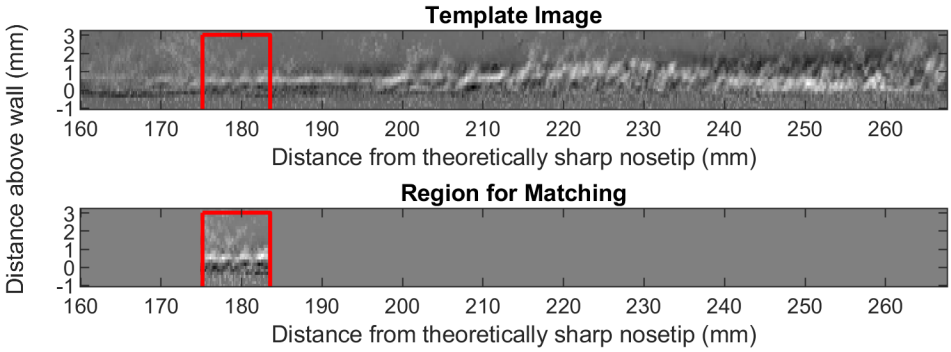


Figure 7.7: Template image for cross correlation, shot T6s357

A selected example of successful matches over successive frames (1 μs to 2.5 μs with an unsuccessful match at 3 μs is shown in Fig. 7.10.

The gradient convection speed method described in Section 5.4.5 was applied to shot T6s357 to determine the second mode wavepacket propagation speed for

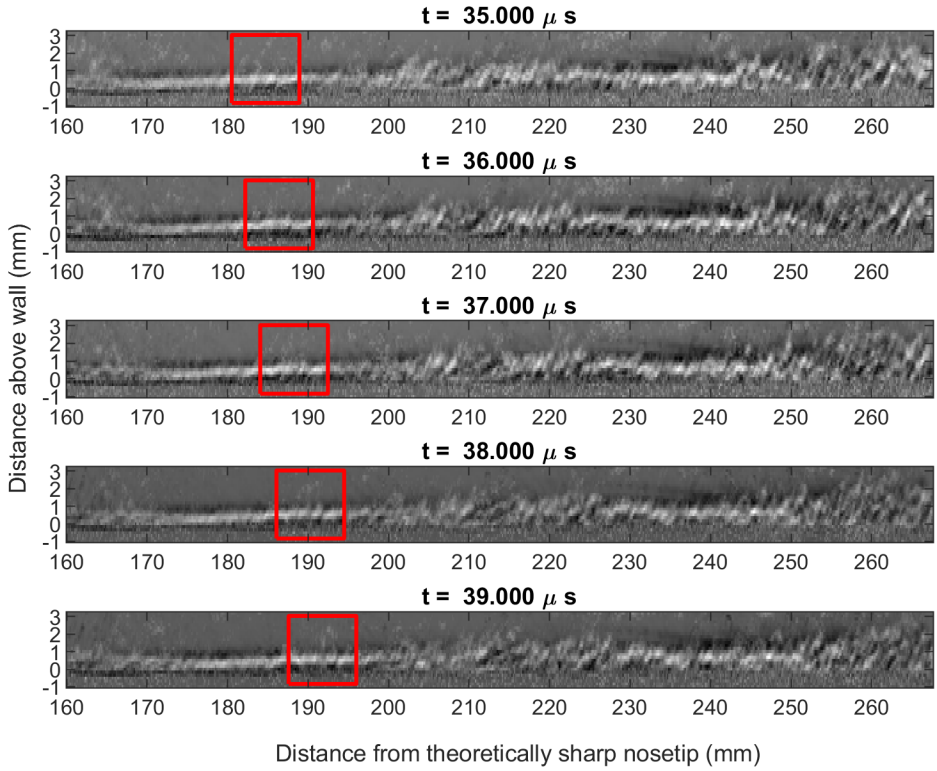


Figure 7.8: Matched wavepackets for a series of selected images, shot T6s357

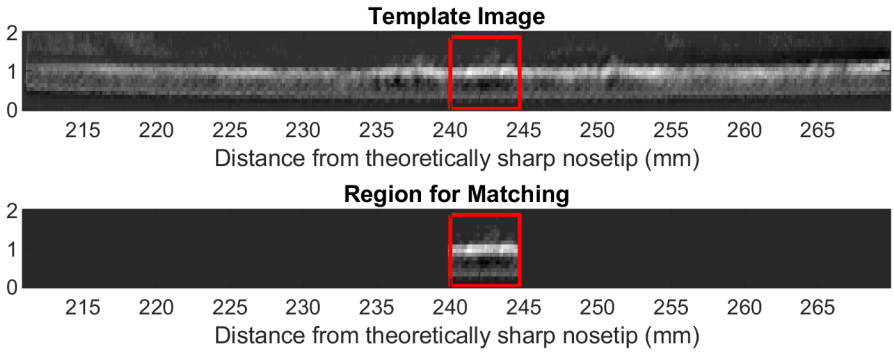


Figure 7.9: Template image for cross correlation, shot T6s301

three locations in the boundary layer. The non-modal instabilities are also a good candidate for use of the gradient convection speed method and this was applied at three locations above the surface, shown later in Fig. 7.31. It was not used in T6s301 because the image quality did not allow for a meaningful result to be obtained with this method. An additional Canny edge detection was applied to the gradient plots and the longest line segment detected was used for the gradient

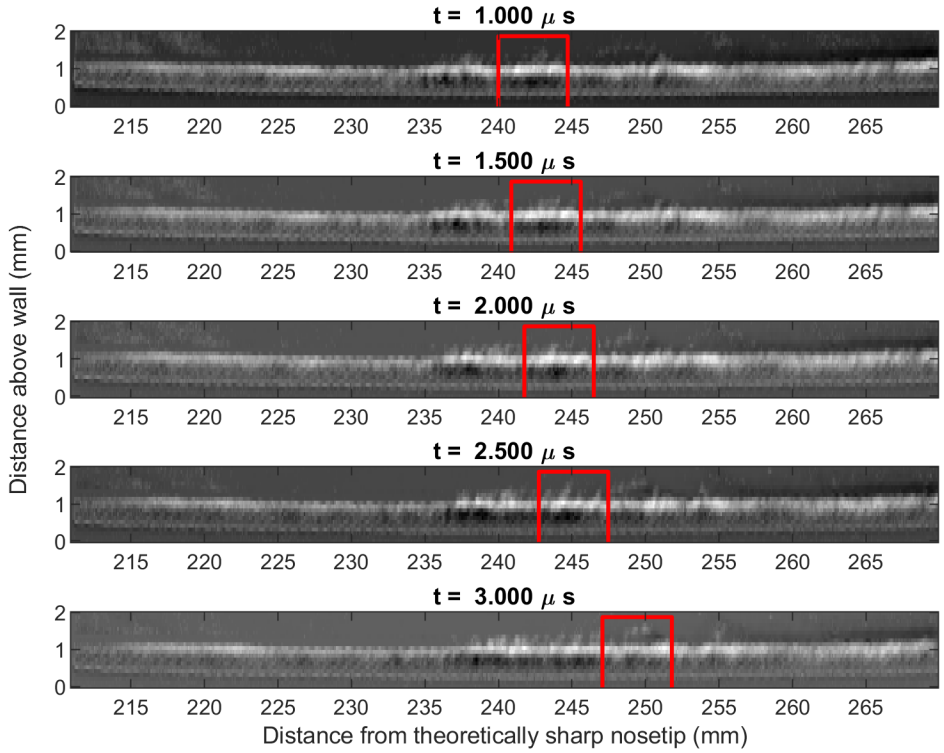


Figure 7.10: Matched wavepackets for a series of selected images, shot T6s301

calculation.

Elongated features were detected above the boundary layer height for experiments conducted with the blunt nose tip, similar in appearance to images captured by Grossir [184] and Kennedy [76]. The cross-correlation methodology was also applied to obtain the convection speed of these non-modal instabilities in the same way that the method is used to obtain the convection speed and frequency of the second mode instabilities, albeit with a single instability used as the template image instead of a full wavepacket. The template image used is shown in Fig. 7.11.

A selected example of successful matches over successive frames (35 μs to 39 μs is shown in Fig. 7.12.

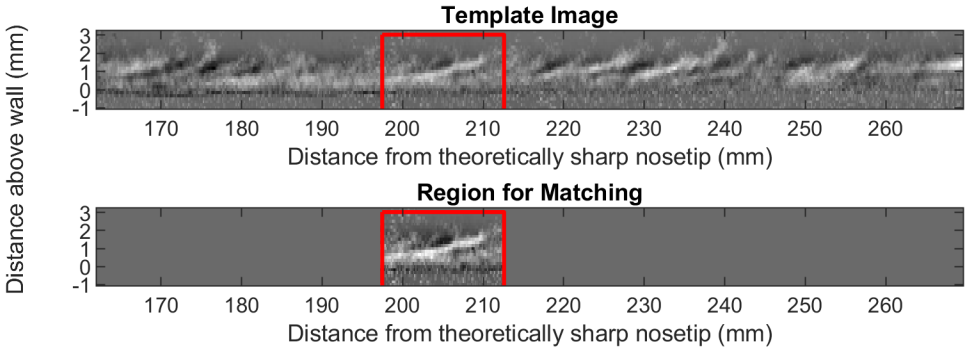


Figure 7.11: Template image for cross correlation, shot T6s358

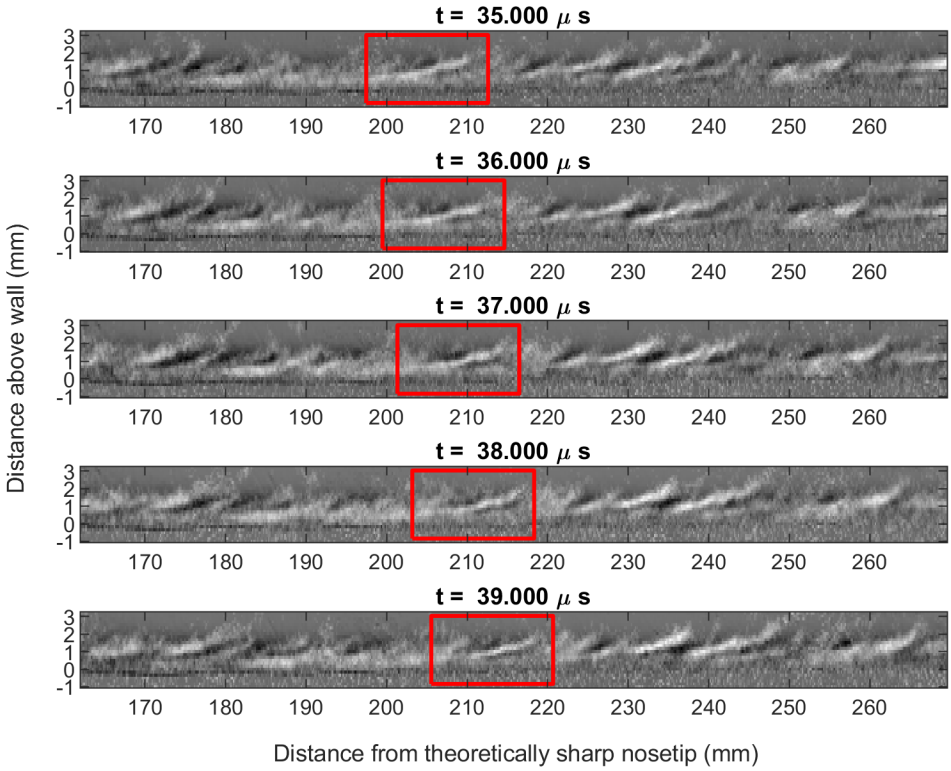


Figure 7.12: Matched wavepackets for a series of selected images, shot T6s358

7.4.2 Wave Detection and Structure Angle

A method of determining the angle of non-modal instability features was also developed and is outlined here as this was a key characteristic of these instabilities and the evolution in their angle could provide interesting indications of the state of the boundary layer. Fig. 7.13 shows a series of images illustrating the steps followed.

First, the standard background processing was done, which involved subtraction of the background and mean images (shown for an example frame in Fig. 7.13, a). A Canny edge detection algorithm was then applied to extract the edges of high intensity regions, which results in the green and magenta overlaid image highlighting the detected edges (Fig. 7.13, b). A single structure was then isolated, which is boxed in red and shown in Fig. 7.13, c. Since the automatic edge tracing is not perfect, some pixels may be missing, or pixels may occur at locations which are not along the instability or may trace the entire loop instead of just the upper edge. Thus, the frames are inspected and pixels are manually selected or removed to refine the points along the edge, shown for an example frame in Fig. 7.13, d. The edge to be traced was then selected (shown in cyan in Fig. 7.13, e).

A curve was then fitted to the refined edge using a least squares spline fit with shape primitives [185]. The fitted spline is shown compared to the refined edge in Fig. 7.13, f.

The local tangent was determined at five equally spaced points based on vertical height between the maximum and minimum y-coordinates of the edge. The angle between this tangent and the cone surface could then be calculated.

This was done for a single frame following different instabilities along the axial location. It was also applied to a single instability tracked over time through multiple frames to investigate the transient evolution, using the cross correlation method described previously.

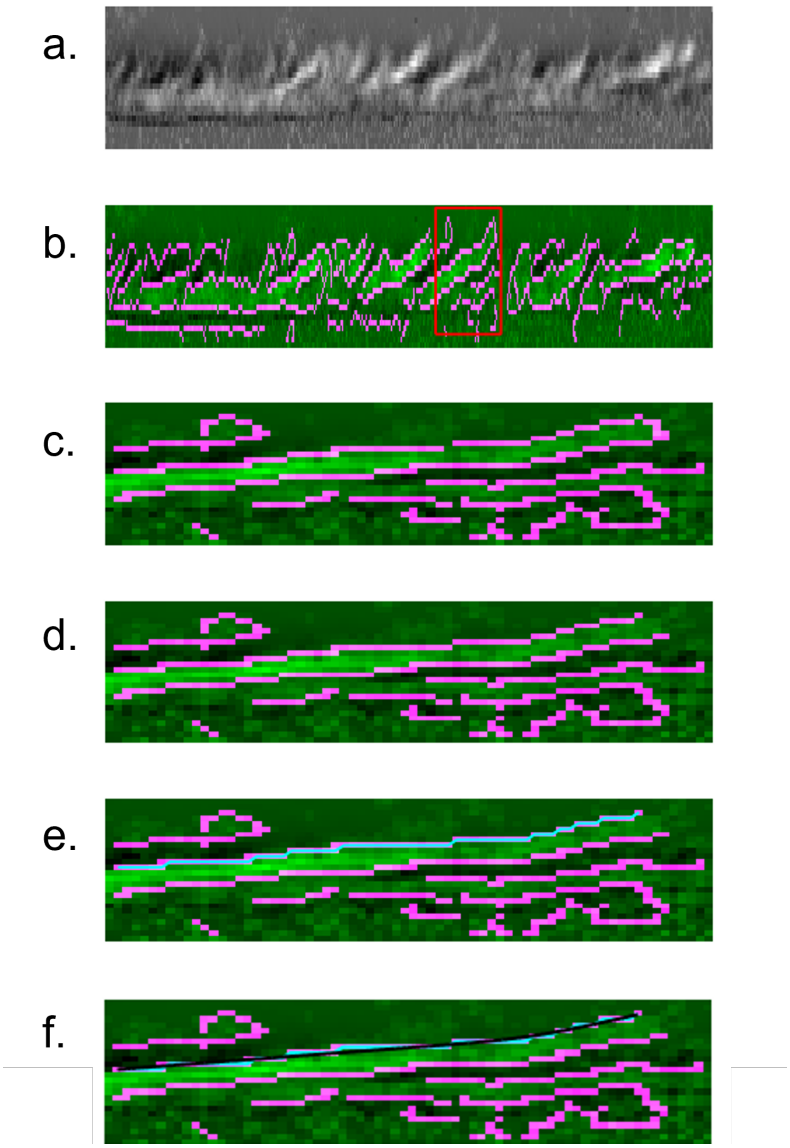


Figure 7.13: Images showing process of edge tracing. (a) Example pre-processed image (b) Edge detection applied and isolated region in red (c) Isolated region before edge refinement (d) Refined edge (e) Detected edge (f) Spline fit applied to detected edge

7.5 Second Mode Instability Results

7.5.1 $M_\infty = 6.6$, 0.852 mm Radius Nose Tip

The cross-correlation method described in Section 7.4.1, and previously applied in Section 6.4.1 to the HDT results was applied to determine the second mode frequency in shot T6s301. The frequencies corresponding to the matched frames for

shot T6s301 is shown in Fig. 7.14, left, and the histogram with fitted distribution is shown on the right. The estimated mean refers to the theoretically predicted frequency while the fitted distribution shows a normal density function fitted to the data and centred on the mean.

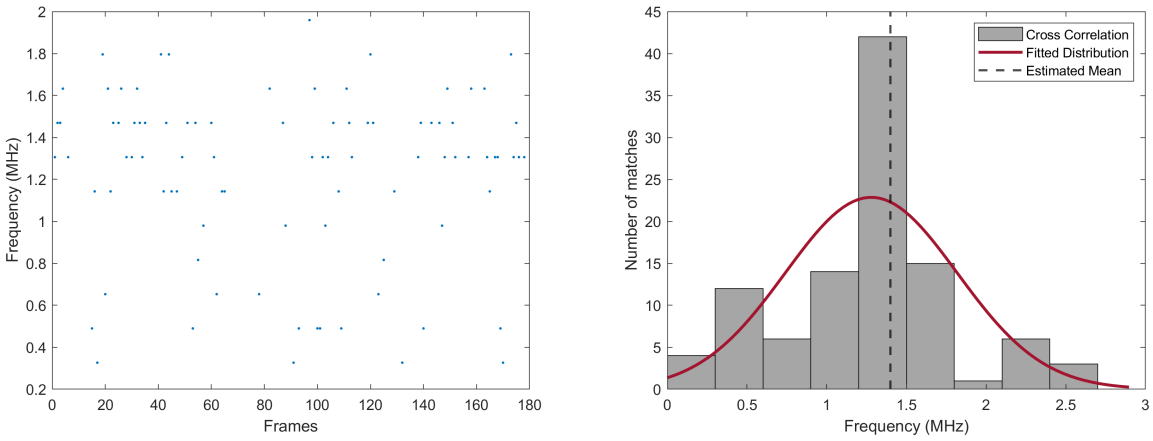


Figure 7.14: Cross correlated frequency results for each frame (left) and histogram (right) for shot T6s301

For this statistical method, a higher number of frames increases the precision of the estimate, so the 180 frames available for analysis is a major disadvantage. Some clear matches can still be seen in Fig. 7.14, left. These correspond to a modal frequency of 1.35 MHz and a mean frequency of 1.3 MHz which compared well to a theoretical prediction of 1.4 MHz.

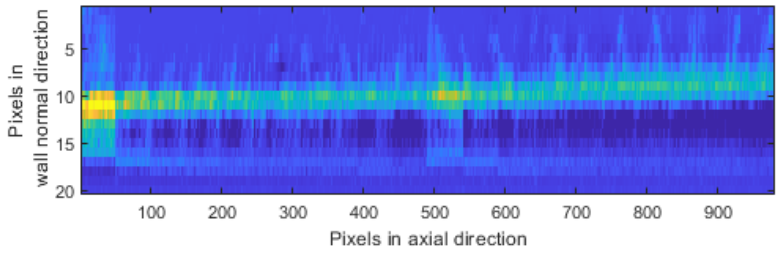


Figure 7.15: Stitched image of shot T6s301, first 20 frames in test time

The stitched image for shot T6s301, for the first 20 frames from the start of the test time is shown in Fig. 7.15. This is composed of the cross-correlated image matches for successive frames which are joined together. Further details on the

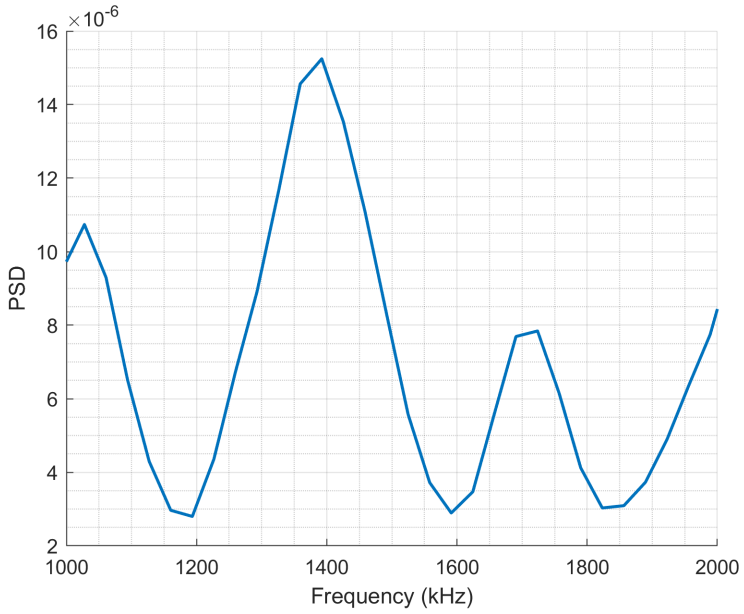


Figure 7.16: PSD for stitched image, shot T6s301

method can be found in Section 5.4.2. The PSD for the stitched image at the row corresponding to pixel 11 in the wall normal direction is shown in Fig. 7.16. It is shown between the frequencies of 1000 kHz - 2000 kHz since the expected second mode frequency is known from the theoretical prediction and frequency peaks outside of this are likely from partial or incorrect matches. The peak within these bands occurs at 1.39 MHz which compares very well to the predicted second mode frequency. Unfortunately the image quality was not high enough to generate gradient convection speed plot and individual gradients could not be automatically detected using this method so it was not included for this case.

7.5.2 $M_\infty = 7.6$, 1.095 mm Radius Nose Tip

For shot T6s357 the frequencies corresponding to the matched frames is shown in Fig. 7.17, left, and the histogram with fitted distribution is shown on the right. This has a modal frequency of 817.5 kHz, compared to a theoretical prediction of 855 kHz.

Breakdown of laminar flow occurs from 190 mm, visible in Fig. 7.6 coinciding with the approximate location of the entropy swallowing location which is consistent

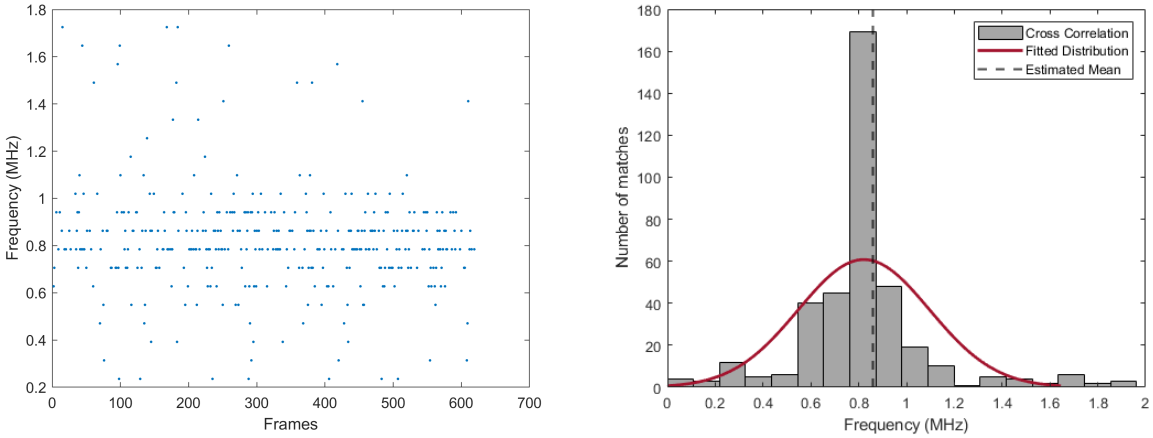


Figure 7.17: Cross correlated frequency results for each frame (left) and histogram (right) for shot T6s357

with results obtained by Stetson et al. [81] who showed that for even small amounts of nose bluntness there is a strong stabilising effect.

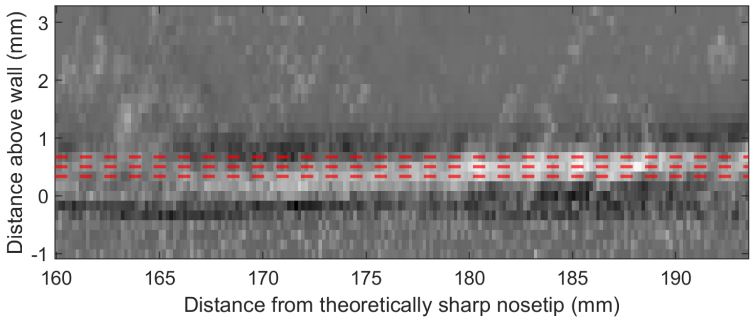


Figure 7.18: Locations for convection speed calculation, shot T6s357

The gradient method described in Section 5.4.5 was applied to shot T6s357, limiting the axial distance for each frame to approximately 190 mm to avoid the downstream turbulent region in the original field of view from interfering with the results. The average of results from three locations in the boundary layer corresponding to 0.67 mm, 0.5 mm and 0.34 mm above the surface were selected, shown in Fig. 7.18. These locations were far enough away from the surface that fluctuations were distinguishable but still within the boundary layer. The resulting time-location intensity plots and overlaid edge detection with the gradient line in white are shown in Fig. 7.19. The gradient line was automatically detected from the clearest joined line segment distinguishable from the edge detection algorithm. The

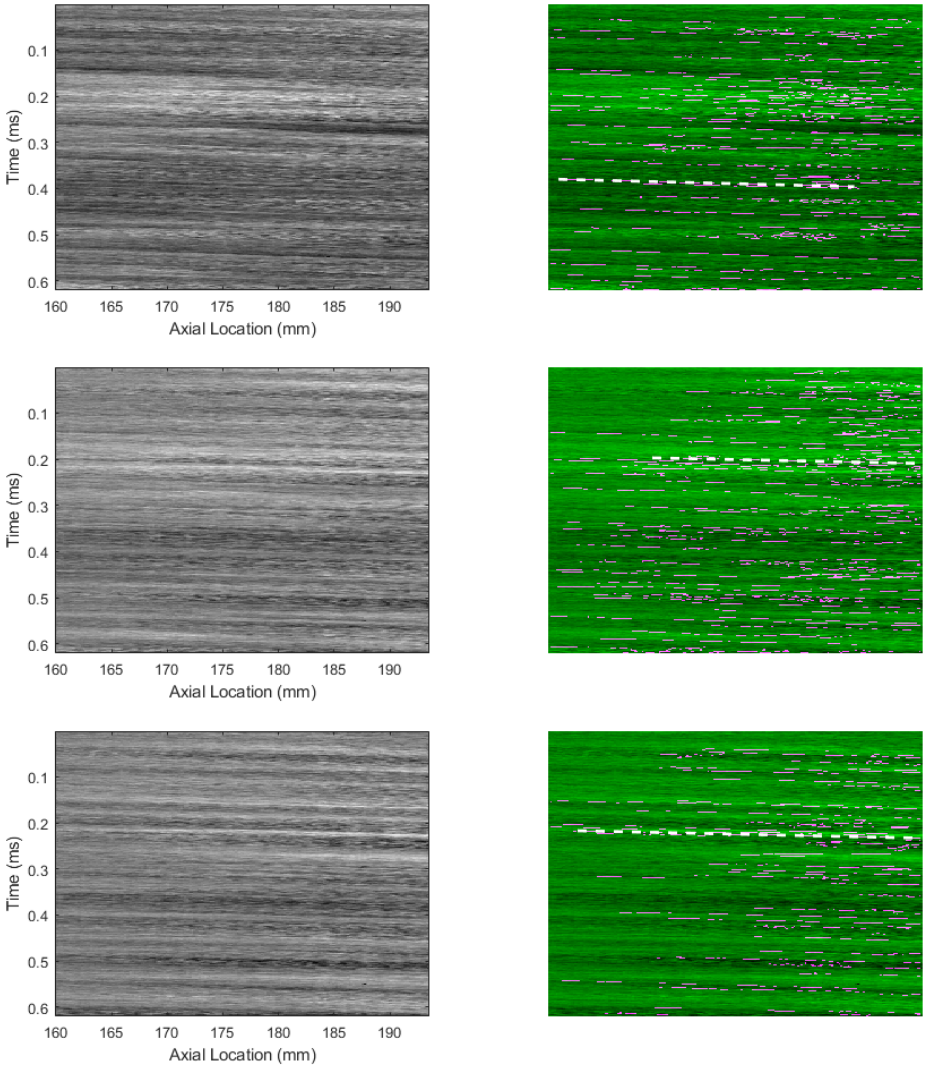


Figure 7.19: Time-location pixel intensity plots (left column) for shot T6s357 for selected rows at y = 0.67 mm (top), 0.50 mm (centre), 0.34 mm (bottom). Corresponding edge detection overlays and detected line for gradient calculation (right column)

mean convection speed obtained from this method is 1863 m/s with a maximum deviation of 10.8%. This corresponds to a 6.3% difference from the modal convection speed obtained through cross correlation and is 0.899 of the edge velocity. The corresponding frequency is 868 kHz.

The stitched image for the first 40 frames is shown in Fig. 7.20 and the corresponding PSD taken at pixel row 18 in Fig. 7.21. The peak for this shot occurs at 824 kHz, which is 3.6% from the theoretical prediction and agrees well.

A summary of the second mode frequency results using each method for both

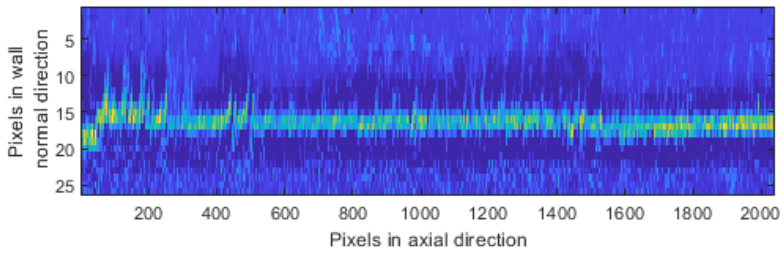


Figure 7.20: Stitched image of shot T6s357, first 40 frames in test time

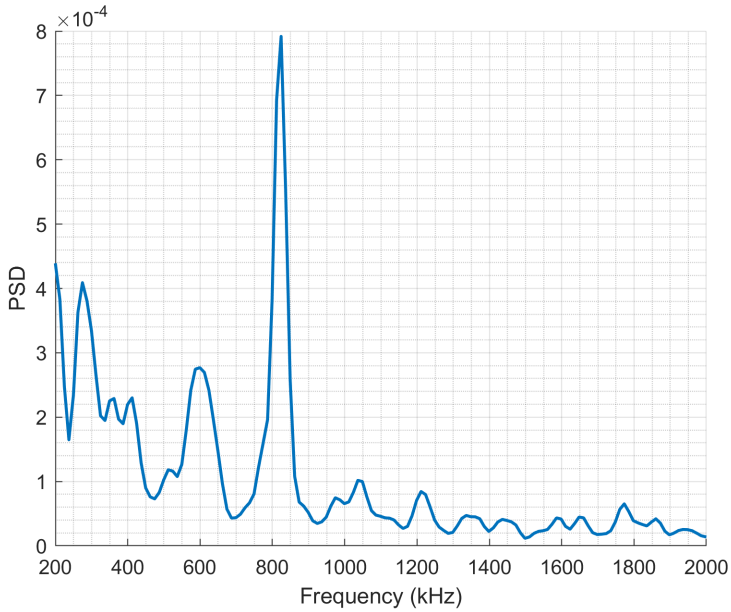


Figure 7.21: PSD for stitched image, shot T6s357

shots is provided in Table 7.3 along with the % error from the theoretical prediction in parentheses.

Table 7.3: Summary of second mode instability frequency results for T6 experiments using different methods

Shot	Frequency From Detection Method, MHz (% Error from theoretical)				
	Theoretical Prediction	Cross Corr (Mean)	Cross Corr (Modal)	Image Stitching	Gradient Plot
T6s301	1.40	1.30 (7.14%)	1.35 (3.57%)	1.39 (0.71%)	-
T6s357	0.855	0.83 (2.92%)	0.818 (4.33%)	0.824 (3.63%)	0.868 (1.52%)

7.6 Non-Modal Instability Results

7.6.1 M_∞ = 7.6, 3.4 mm Radius Nose Tip

An extensive analysis of the non-modal instabilities observed for the blunter nose tip case is applied here to fully characterise these structures. For this configuration, the predicted entropy swallowing length extended to almost double the length of the cone. The elongated structures seen in images from shot T6s358 (Fig. 7.12) extend upward over 2-3 times the boundary layer thickness that was seen in T6s357, the sharper nosetip case. This is similar to results observed by [20] and [76]. The structure angle for different instabilities in a snapshot frame, as well as for a single instability tracked over time is determined following the method described Section 7.4.2. A power spectral density at different axial locations is also calculated and analysed, as well as a scalogram based on the pixel intensity traces. A cross-correlation and gradient plot is also shown to determine the convection speed at which these instabilities are progressing.

Structure Angle

Fig. 7.22, top, shows an image taken at t = 10μs into the test time with the green regions in the top image highlighting the individual instabilities used for the following analysis. The edge detection method as described above was applied, and the image along with the refined detected edge and fitted spline is shown in Fig. 7.22, bottom.

The fitted curves representing the edges at selected locations are plotted in Fig. 7.23, along with their angles at a few equally spaced points above the surface. In general, the maximum angle of the structures occur well above the boundary layer, while at the boundary layer edge they are almost parallel. Comparing the instabilities upstream versus downstream, the upstream structures are steeper than downstream, and extend further above the boundary layer edge. At the first upstream location, the instability reaches a a maximum angle just under 23 degrees. (Note in this figure the x and y axes are not equally scaled for clarity so angles appear skewed). As the instabilities progress downstream the main structure (not including narrower parts that likely extend higher above the boundary layer)

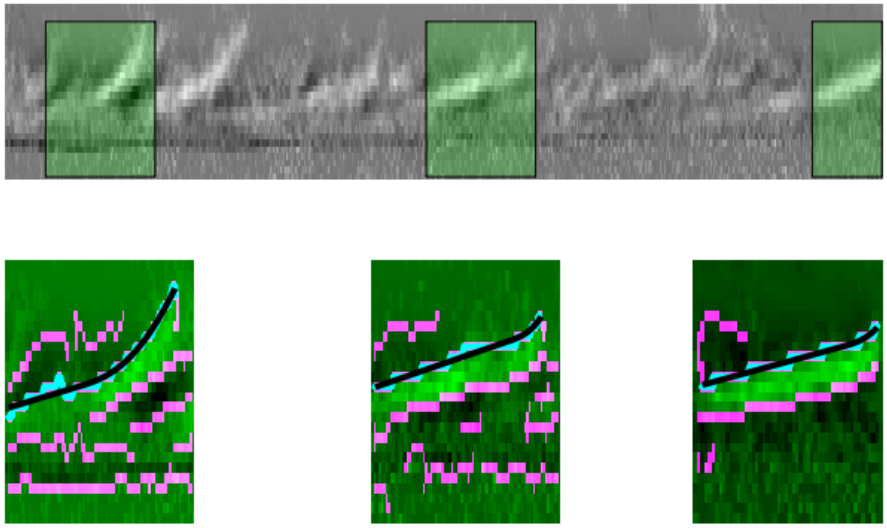


Figure 7.22: Image and regions for edge fit, t = 10μs (top). Edge and curve fit for each region (bottom)

starts to collapse and become shallower, seen by the maximum angle of around 13 degrees at the central axial location. At the most downstream location, just under 2 mm above the surface the main structure angle is almost 6 degrees, not including the the thinner, "wispy" edges which remain at 21 degrees. It is difficult to extract concrete trends from a single frame so the analysis was extending to tracking the same instability over a series of frames.

A single instability was tracked and analysed over time beginning from when it first enters the field of view and ending when it is at the most downstream location but still a complete structure shown for every tenth frame in Fig. 7.24. The analysis was applied to all 50 frames for which the structure was identifiable. The angles at four heights h above the surface are shown over time in Fig. 7.25. Linear trendlines were fitted to the data and these are shown by the dashed lines.

Gaps in the data from the highest h value indicates regions where the edge outline did not intersect at that height. At the highest and most upstream location, the structures extend to a steep maximum angle of 30 degrees well above the boundary layer. Examining the plots at each h value, it is clearly seen that the structure at each height is collapsing to a single angle as it evolves over time and progresses downstream. The structures physically evolve from more "wispy", steeper

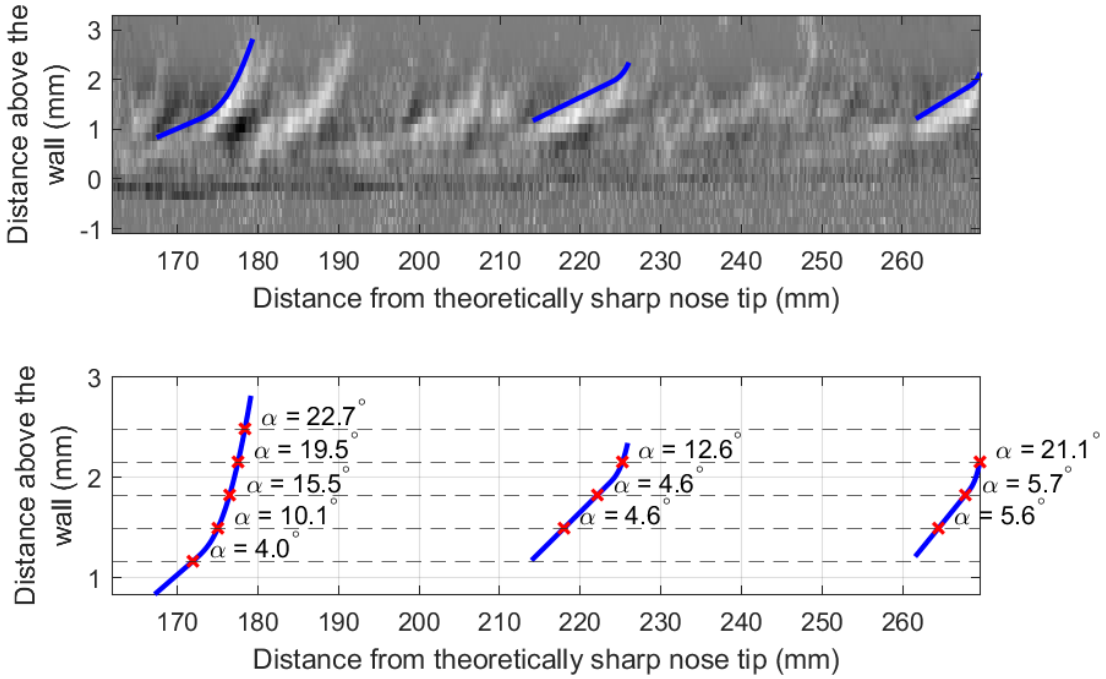


Figure 7.23: Extracted edge overlaid on image (top) and plotted with angles (bottom)

edges around 15-21 degrees to a shallow, flat linear structure approaching a constant angle of approximately 8^o, presumably preceding breakdown (which unfortunately was not clearly captured in this field of view).

PSD and Scalogram

The pixel intensity traces were extracted from the processed images at locations indicated on the image in Fig. 7.26. The power spectral density based on these intensities above the boundary layer is shown in Fig. 7.27. Unlike typical power spectra for images with second mode instabilities present, no dominant frequency can be identified, but rather a series of high-frequency peaks occur (170 kHz, 200 kHz, 230 kHz, 290 kHz, 330 kHz, 360-370 kHz, 440-460 kHz). This is expected, as pointed out by Paredes [19] and Kennedy et al. [76], non-modal instabilities are predicted to amplify over a wide range of frequencies typically between 100-800 kHz depending on the freestream conditions and cone geometry.

The scalogram at these locations is shown in Fig. 7.28. High intensity peaks

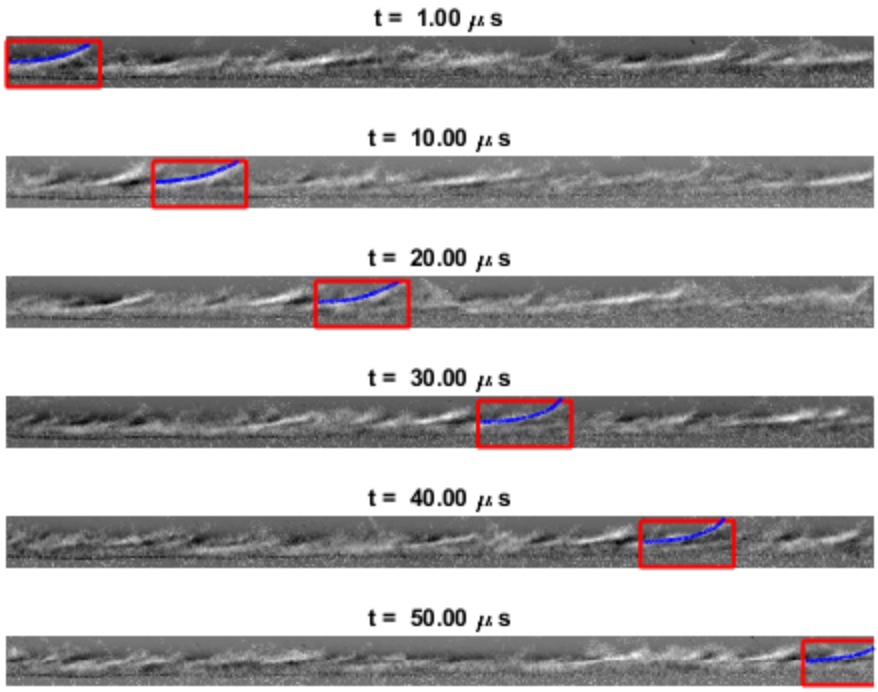


Figure 7.24: Tracked edges over multiple frames (only every tenth frame is shown here for clarity but the analysis was applied to 50 frames)

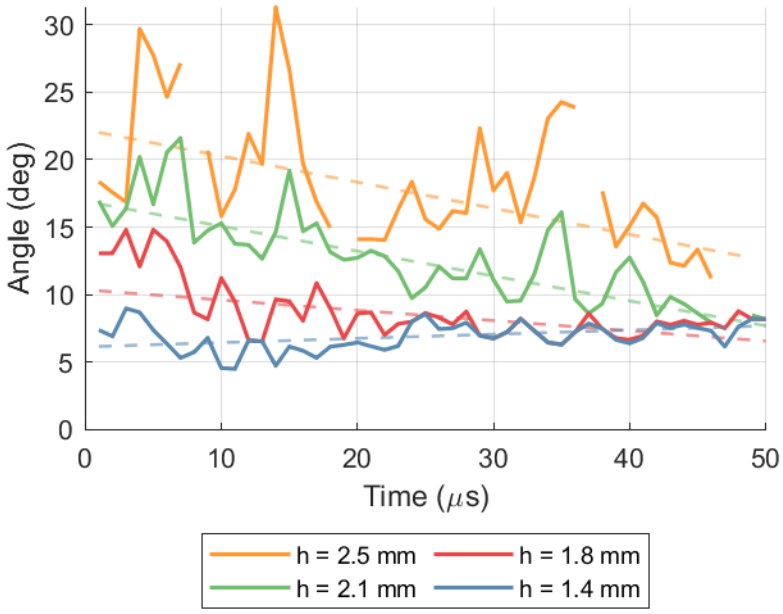


Figure 7.25: Evolution of single instability structure angle over time at different heights above the surface. Dashed lines show linear fit

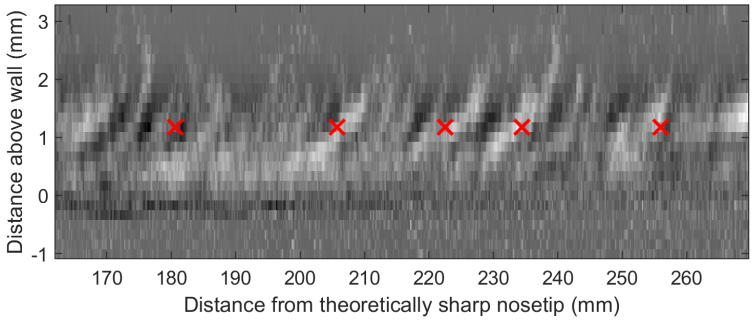


Figure 7.26: Locations for pixel intensity traces, shot T6s358

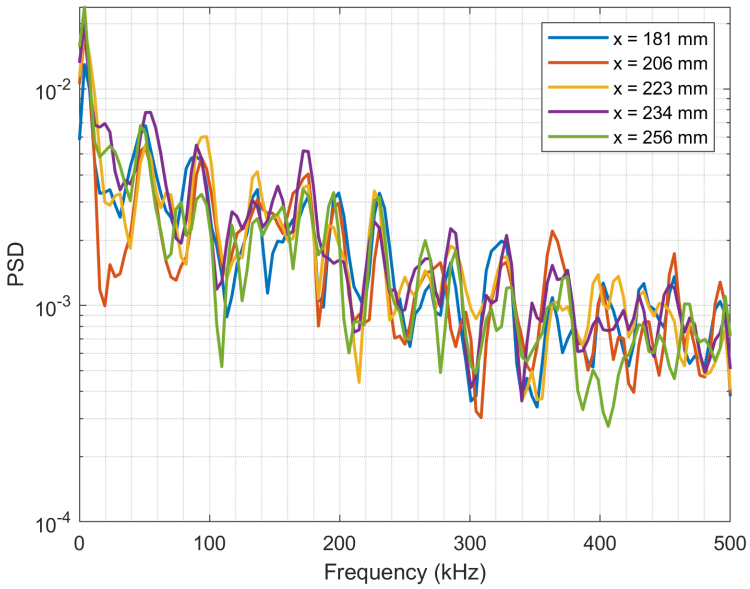


Figure 7.27: Power spectra from pixel intensity traces, shot T6s358

can be seen around 200 kHz, consistent with the presence of non-modal instabilities which are traced back and indicated in Fig. 7.29 for location x = 206 mm.

Convection Speed

The convection speed was obtained through two different means, cross-correlation and the gradient method. The cross-correlation matches are shown in Fig. 7.30, left, and the histogram with mean and fitted distribution is shown on the right.

The mean and modal values from the cross-correlation are 1923 m/s and 1950 m/s respectively (0.926 and 0.939 of the edge velocity).

The three locations for the extraction of the pixel intensities for the gradient

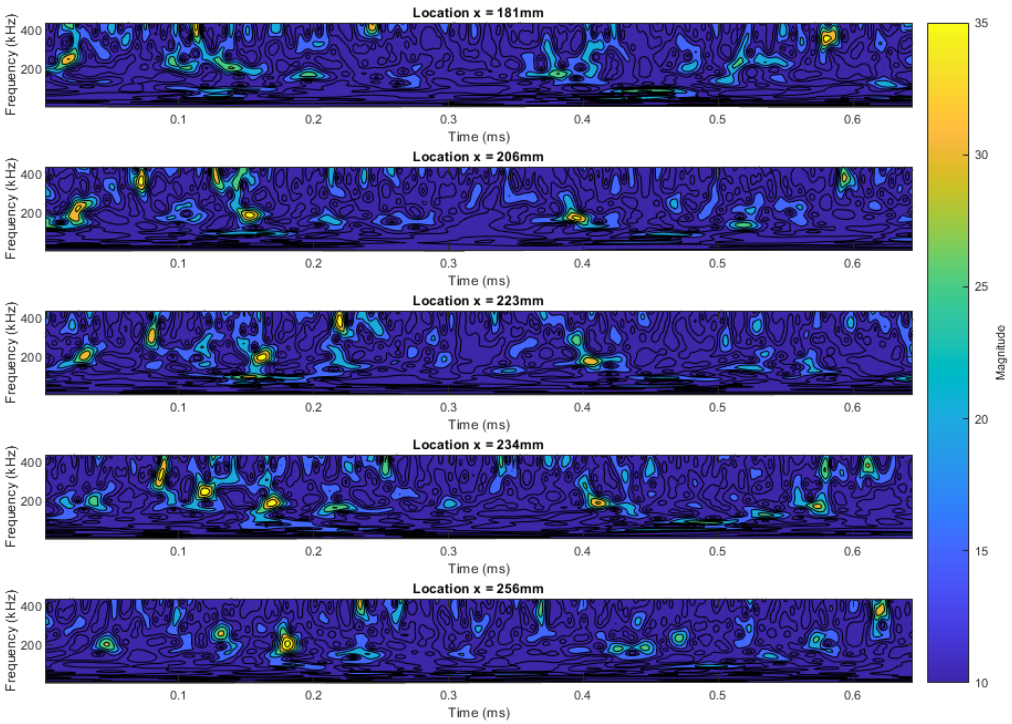


Figure 7.28: Scalogram based on pixel intensity traces

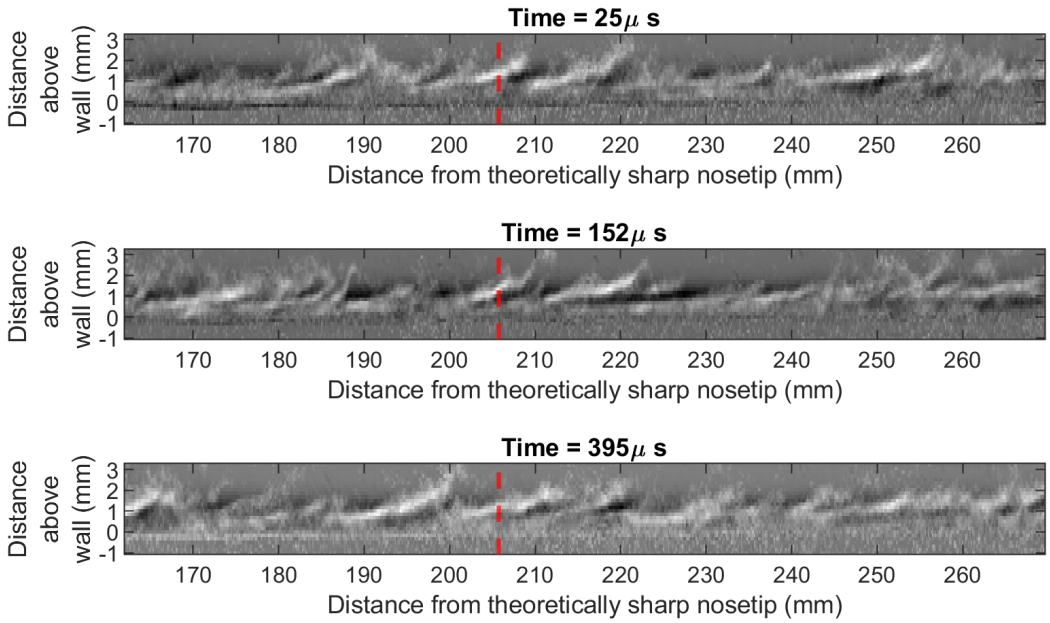


Figure 7.29: Regions of high scalogram intensity on images

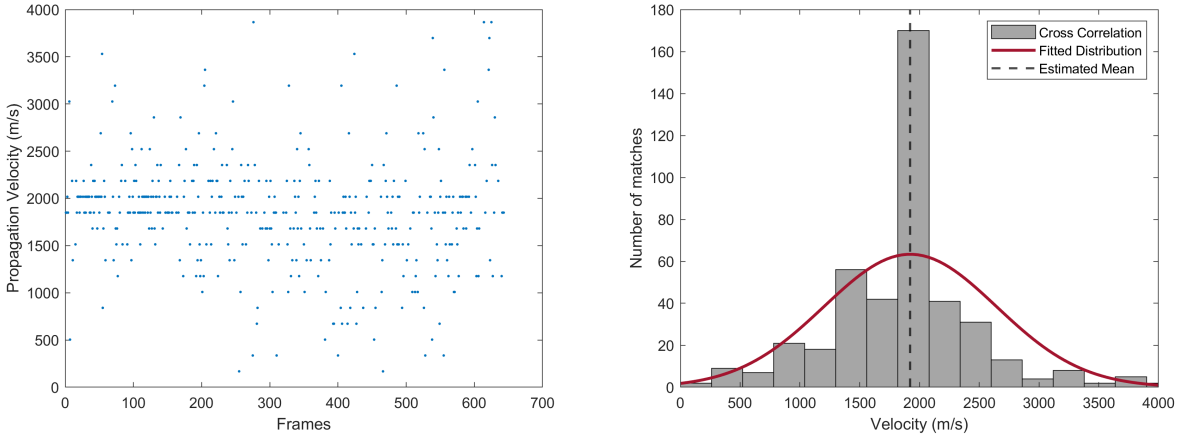


Figure 7.30: Cross correlated velocity results for each frame (left) and histogram (right) for shot T6s358

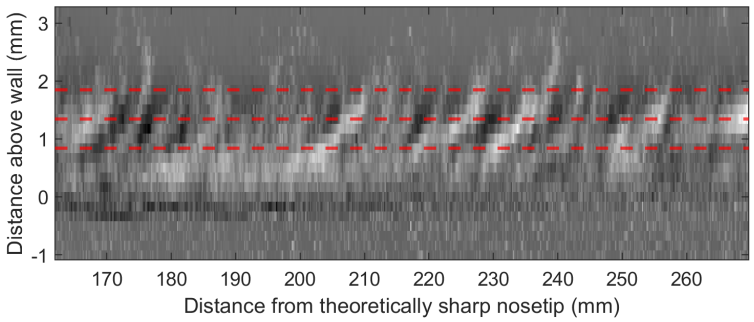


Figure 7.31: Locations for convection speed calculation, shot T6s358

method are shown in Fig. 7.31 and the corresponding gradient plots are shown in Fig. 7.32. For the gradient method the mean convection speed for these three locations is 1932 m/s (maximum deviation from mean of 0.87%) and mean convection speed to edge velocity ratio of 0.931.

The two methods of calculating the convection speed of these instabilities show good agreement. Overall the features characteristic of non-modal instabilities match well with those found by Kennedy et al. for different flow conditions ([76]), although convection speed to edge velocity ratio is slightly lower here compared to 1.03 reported by Kennedy et al. This could be attributed to a number of reasons, among them the effect of different freestream noise levels which have not been fully characterised for either study.

A summary of the non-modal instability convection speed to edge velocity ratio

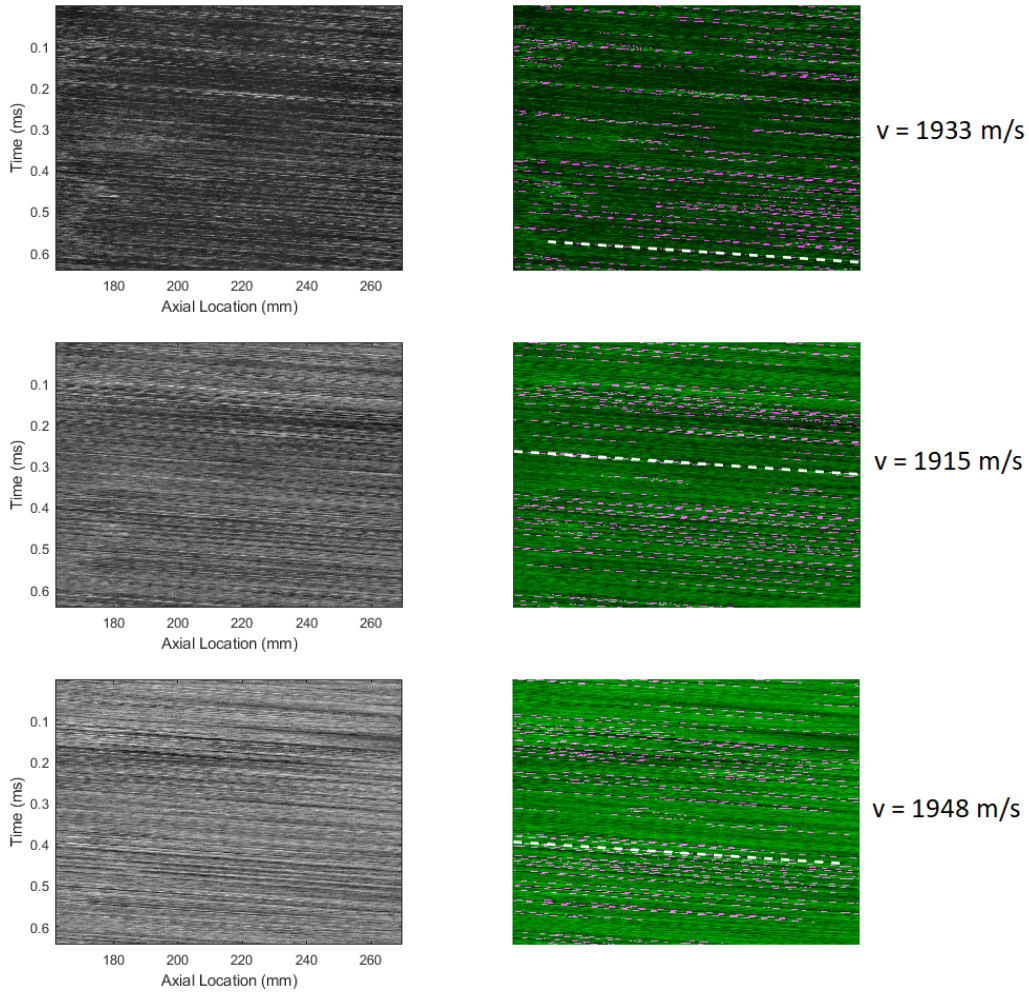


Figure 7.32: Time-location pixel intensity plots (left column) for shot T6s358 for selected rows at y = 1.85 mm (top), 1.34 mm (centre), 0.84 mm (bottom). Corresponding edge detection overlays and detected line for gradient calculation (right column)

using each method is provided in Table 7.4.

Table 7.4: Summary of non-modal instability convection speed to edge velocity ratio for T6s358 using different methods

Shot	Convection Speed/Edge Velocity from Detection Method		
	Cross Corr (Mean)	Cross Corr (Modal)	Gradient Plot
T6s358	0.926	0.939	0.931

7.7 Conclusion

Second mode and non-modal instabilities at high frequencies have been established and captured with the use of high-speed schlieren imaging for the first time in the Oxford T6 Stalker Tunnel. Three different nose tip radii and two different flow conditions which were developed for these tests were used. For sharper nose tip geometries these instabilities have been processed using selected methods developed in previous chapters in order to characterise the frequency of these second mode instabilities at Mach 6.6 and Mach 7.6 where the reliable frequency response of traditional pressure sensors would be exceeded. For the blunter nose tip configuration, non-modal instabilities have been captured and novel methods of extracting characteristics such as structure angle and convection speed have been developed and applied.

The second mode instabilities found at Mach 6.6 and Mach 7.6 (Re_{RN} of 10000 and 11000 respectively) have been visualised using two different high speed cameras, at frame rates of 1-2 million fps. The background flow-off images and an averaged flow-on image was subtracted, which greatly improved the quality of the images and enhanced the visibility of the wavepackets. Due to the high frequency of the instabilities expected, applying a PSD purely to the extracted pixel intensities over time would not provide any useful data, as the PSD is only calculated upto half of the sample frequency, which is much less than the expected second mode frequencies.

For the Mach 7.6 condition (T6s357) three successful methodologies were applied to extract the frequency information from these images. Cross-correlation was used to track successive wavepackets from a clearly identified "template" image. The most frequently matched results provided the wavepacket convection speed and together with the extracted wavelength, the frequency could be determined. Image stitching was also used using the tracked wavepackets joined successively and a PSD done on the stitched image. The gradient method was also used to obtain an additional verification of the convection speed and frequency. The methods agreed reasonably well, providing a frequency between 1.5-4.3% off the theoretical prediction of 855 kHz. This frequency was over 4 times the value of the second mode frequencies obtained

in the HDT results and while the boundary layer was significantly thinner in the T6 experiments, good agreement was achieved in characterising these instabilities without the use of traditional pressure sensors.

The results from the Mach 6.6 condition should be interpreted with some caution because the images were limited to 180 frames and captured during a time when the flow may still have been developing over the model and second mode instabilities were potentially in the early stages of development at this condition. The image quality was also not adequate to provide clear visible evidence of second mode packets and prevented the use of most of the methods developed, however structures were detected using cross-correlation and image stitching was also able to be applied. While the results from the cross correlation were negatively affected by the image quality (3.6-7.1% difference from the theoretical prediction), the image stitching proved very successful and agreed within 1%.

Non-modal instabilities extending well past the boundary layer edge were identified at Mach 7.6 with a nose tip radius of 3.4 mm. Methods developed from the image processing techniques for use on second mode wavepackets were successfully applied to characterise these instabilities. In particular, cross-correlation and gradient plots were used to extract the convection velocity and it was found that these instabilities progressed downstream at a velocity between 0.93-0.94 of the edge velocity. Edge detection and spline fitting were used to calculate the structure angle of instabilities as they developed downstream, spatially and over time. These structures were swept along at just below the edge velocity and flattened as they propagated downstream, from almost 30 degrees at the highest point upstream to approximately 8 degrees downstream. They tended to collapse and become more linear at a constant angle over time. In terms of spectral frequency content, no one frequency was dominant, but rather smaller peaks of intensity were seen over a wide range of frequencies. These were proven to be linked to the presence of non-modal instability structures by tracing sampled regions of high amplitude in the scalogram around 200 kHz to locations of individual high intensity non-modal instabilities in the captured images.

This study was somewhat limited, primarily due to the difficulties in establishing adequate flow and image capturing settings in the T6 Tunnel. For example, of the 9 experiments performed in a single campaign, only 2 were adequate for analysis. High freestream noise levels, particulates in the flow and short duration test times are the primary challenges to be overcome for future work. This chapter does however demonstrate the possibilities going forward for future studies and establishes a good base for the further investigation of instabilities in the T6 Tunnel for both second mode and on non-modal instabilities. Some proven methodologies are presented to be used for characterising and comparing these instabilities in future work. Two primary aims for future work are identified going forward: characterisation of the freestream noise levels, possibly with the use of focused laser differential interferometry (FLDI) and a comparison of different nose tip geometries on the characteristics of non-modal instabilities now that their presence has been established. The nosetip radius at which second mode instabilities dominate over non-modal instabilities would be useful future work. Another useful avenue of research would be a more in-depth investigation of the link between the characteristics of these non-modal instabilities and their eventual breakdown using a longer model and wider field of view.

8

Conclusions and Further Work

Contents

8.1 Contributions 193
8.2 Future Work 199

8.1 Contributions

This work was driven by three primary goals: to develop and commission the Oxford T6 Stalker Tunnel in Reflected Shock Tunnel mode, to develop and test both qualitative and quantitative image processing techniques for boundary layer analysis, requiring experiments to be conducted in the Oxford High Density Tunnel for validation and finally, to perform the first exploratory experiments on boundary layer instabilities at flight representative enthalpies in the Oxford T6 Stalker Tunnel, making use of the test conditions and applicable image processing techniques developed. These aims are towards the greater goal of understanding the aerothermodynamic effects of hypersonic flow conditions, particularly the harsh conditions generated by impulse facilities, on boundary layer transition mechanisms over axisymmetric bodies at low angles of attack and the experiments conducted

open a host of new research avenues.

The T6 Stalker Tunnel, which is a multi-modal facility able to operate in three main modes of operation, was developed and commissioned in the Reflected Shock Tunnel for this work and this process is described in detail in Chapter 4. A low fidelity model was developed to provide initial fill conditions based on the required stagnation pressure, stagnation enthalpy and freestream Mach number. This required tailoring, which is the process of ensuring that sufficient test time is achieved through the selection of appropriate driver gas conditions in order to limit the disturbances generated when the reflected shock interacts with the boundary between the driver and driven gases. For a free piston facility such as T6, the problem of tuning could then be investigated. This refers to the process of selecting the appropriate reservoir and driver gas conditions such that both the loss in driver gas pressure during diaphragm rupture is compensated for and the piston reaches the end of the compression tube with a speed within safe margins so as not to cause damage to the facility. Once the initial conditions fulfilling the requirements of tailoring and tuning were computed, a more complete facility simulation was performed in the quasi-one-dimensional Lagrangian code, L1D. Here, minor adjustments were done to the conditions based on the results of the simulation to reach the optimal test conditions. It was found that a nominally 90 kg piston would provide better results than the existing 36 kg piston, so this was refurbished and installed into the tunnel. For the piston dynamics to be properly incorporated into the computational model, the friction and launcher loss parameters of the piston required investigation and this was done through blank-off testing. Blank-off tests involved replacing the normal diaphragm with a blanking plate that had a pressure transducer installed to record what would normally be the rupture pressure. This pressure trace could be compared with that from L1D and the parameters adjusted until a good match was achieved. It was found that the 90 kg piston had a significantly higher levels of friction (68%) and launcher losses (8%) when compared to the 36 kg piston. Next, the choice of diaphragm material thickness

and score depth was investigated to determine what would rupture at the required pressure. This was done in a different mode of testing, Shock Tube Mode, without the nozzle and stagnation regions. Various diaphragm score depths were tested and their shock speeds recorded and compared to the ideal value to obtain a spread of score depths versus rupture pressures from which diaphragms could be chosen. Finally, the first reflected shock tests were conducted with a nominally Mach 7 nozzle and pitot rate installed to characterise the nozzle exit conditions. The results were compared to the computational model and small adjustments were made to bring the condition within 1% of the nozzle supply enthalpy and 2.6% of the nozzle supply pressure. The test time for this first condition was 0.5 ms and the core flow diameter was found to be at least 160 mm, with the Mach 7 nozzle producing a freestream Mach number of 6.6. The decrease in freestream Mach number from the nominal condition is due to a combination of non-ideal gas effects and a reduction of the effective nozzle exit area due to the build up of the boundary layer on the nozzle. With the success of this initial test (named "Condition A"), further conditions were developed, including a nitrogen driver condition ("Condition D") which increased the available test time at lower enthalpies and a nominally Mach 8 nozzle condition which was ultimately used for the some of the final T6 experiments.

Secondly, high speed schlieren image processing techniques were developed in order to extract boundary layer instability information from the flowfield. As a result of the high frequency nature of the instabilities expected in T6, pressure transducers were not a reliable measurement technique. High speed schlieren imaging was thus the primary means of flow diagnostics and associated image processing techniques were developed to be used to characterise the instabilities in T6, outlined in detail in Chapter 5. The schlieren imaging techniques are used for detection of the frequencies and convection speed of second mode instabilities (grouped under "Frequency Detection Methods"), for camera frame rates above and below the frequency of the second modes. The simplest of methods makes use of the fluctuating pixel intensity in the schlieren images caused by the acoustic nature of

the second modes in the boundary layer and this can be extracted from the image series at locations within the boundary layer and axially along the surface. The main disadvantage of this is that the method is only useful at frame rates above the second mode frequency. By extracting a row of pixel intensity and plotting this over time, the gradient of the wavepackets convecting downstream can be used to obtain the group velocity and with the wavelength, calculate frequency. A cross-correlation algorithm can be applied to track the wavepackets over time and building on this method these can be stitched together into a continuous image from which the frequency can extracted. Semi-global matching can also be applied, provided the wavepackets do not significantly deform over time. These methods can be applied to images captured at frame rates less than the second mode frequency which is useful for conditions under which instability frequencies are high. Techniques which allowed for the analysis of other features of the flow were explored (grouped under "Feature Detection Methods"). Wavelet scalograms indicated the presence of turbulent spots and possibly a weak indication of self-coupling. Bispectral analysis was used to indicate self-coupling and harmonics of the second modes. Spectral Proper Orthogonal Decomposition (SPOD) indicated the presence of coherent structures in the flowfield. The techniques developed were first applied to experiments conducted on another tunnel at Oxford, a cold flow facility called the High Density Tunnel (HDT). The model used here was a 7^o cone model with a nose tip radius of 1.25 mm, instrumented with pressure transducers. The second mode instabilities are between 208-216 kHz from pressure transducer measurements which enabled the methodology to be proven in a less challenging environment where regular pressure transducers could be relied upon as a means of validation allowing a direct comparison to be made for each of the processing techniques. An additional smaller investigation was conducted on the effect of varying parameters such as frame rate and resolution on the information extracted, with the purpose of informing future experimental setups. The application of the processing techniques and results from the campaign in HDT are included in

Chapter 6.

Finally, the work done on the condition development and schlieren image processing development culminates in the final testing campaign in T6, which is described in Chapter 7. A database of boundary layer experiments in the T6 tunnel was gathered for both second mode and non-modal instability dominated flows using a 7^o cone model, 407 mm in length with interchangeable nose tips of varying radii. Selected image processing techniques were demonstrated in this challenging testing environment in order to gain an understanding of the boundary layer transition processes occurring and establish a solid foundation for future instability work to be carried out in T6. Second mode instabilities were analysed at Mach 6.6 and 7.6 using two different high speed cameras at frame rates of 1-2 million frames per second. The images were enhanced through subtraction of the background flow-off images as well as an averaged flow-on image. This was essential to improving the visibility of the wavepackets, particularly as the boundary layer was extremely thin. The results from the Mach 6.6 condition were included but the findings should be taken with caution as the images were captured towards the end of the flow establishment period. The image quality was not adequate to provide clearly identifiable second mode wave packets, however coherent structures of high intensity could be detected convecting downstream at approximately 0.79 times the edge velocity, corresponding to a frequency of 1.3-1.35 MHz, approximately 4-7% off the theoretical prediction of 1.4 MHz. For the Mach 7.6 condition, cross-correlation proved successful in extracting the wavepacket frequencies and it agreed well with the results from the image stitching and gradient convection speed methods. These both provided a frequency which was between 1-4% off the theoretical prediction of 0.855 MHz. This was over four times the second mode frequencies obtained in HDT at similar unit Reynolds numbers but significantly lower wall to total temperature ratios. For the same model with a nose tip over three times blunter, the entropy swallowing distance extended well past the edge of the cone and second mode dominated transition was no longer the

case. Instead, the dominant mechanism of transition appeared to be non-modal instabilities, which formed structures characterised by their elongated length above the boundary layer and angle to the surface. With the use of modified image processing techniques developed earlier in the thesis, these structures could be tracked and their convection speed and tangential angle could be extracted. The instabilities were swept along at just under the edge velocity (0.93-0.94U_e). They tended to flatten as they progressed downstream, ranging in maximum angle from 30^o at the upstream region in the field of view, to 8^o further downstream before collapsing. In terms of spectral content, no one frequency was dominant, but rather short bursts of high intensity was found when examining the power spectral density plot, consistent with the results from other researchers.

In summary, significant progress has been made in the development and study of hypersonic boundary layers in the Oxford T6 tunnel facility. There remain improvements to be made as the range of conditions under which observable boundary layers form in T6 required significant effort to determine, leading to a smaller than desired number of cases of high quality. This is due to factors such as high freestream noise levels, particulates in the flow and short duration test times. The effect of the Covid-19 global pandemic also resulted in a lab shutdown and a number of delays to the tunnel testing schedule and manufacturing. However, the work done in this thesis has laid a solid groundwork for the further study of instabilities in T6 and opens up a host of possibilities for future research.

8.2 Future Work

Some avenues for future research are proposed here:

- The effect of freestream noise levels on non-modal instabilities would be a key finding for future work. To do this, the freestream noise of the T6 tunnel should be characterised, potentially with the use of focused laser differential interferometry (FLDI) as some promising studies have demonstrated ([58], [186]).

- A useful comparison to the results presented here would be FLDI measurements of the second mode frequencies in T6. At the time of this thesis preliminary FLDI tests have been performed in HDT but not yet been implemented in T6.

- Now that the conditions under which instabilities can be established in T6 have been demonstrated, a useful future study should aim at comparing non-modal instabilities between the High Density Tunnel and T6 Tunnel. One key challenge is establishing conditions conducive to non-modal instability formation, as preliminary experiments were conducted with nose tips as blunt as 9.5 mm in HDT with little success. HDT has been shown to have a very low noise environment and this may be preventing strong non-modal instabilities from forming.

- Characterisation of the surface roughness - the model roughness was specified to be the same as for previous tests in HDT, and while this may have worked for the conditions in HDT, in the noisier environment of T6 may amplify the effect of surface roughness. A study properly characterising the roughness of the model or testing models with different surface finishes in T6 and comparing the effects on non-modal instability growth would inform this problem. Studies have shown even micro-roughness could be important to transient growth [27].

- A method of calibrating the schlieren measurements to relate pixel intensities to density gradients in both T6 and HDT tunnels (currently under development but not yet implemented).

- Investigating the effects of implementing a more stringent cleaning procedure in the T6 tunnel versus not on the development of second mode and non-modal instabilities.

References

[1] H. Tsien. "Similarity Laws of Hypersonic Flows". In: *Journal of Mathematics and Physics* 25.3 (1946).

[2] J. M. Seitzman. *AE6050 Gas Dynamics Lecture Notes*. 2016.

[3] S. McDonald. "Defense spending act makes hypersonics a top priority, calling for billions in investment". In: *CNBC Defense* (Dec. 2021). URL: https://www.cnbc.com/2021/12/29/defense-act-makes-hypersonic-top-priority-calls-for-investing-billions.html.

[4] UK Ministry of Defence, Defence Science, and UK Technology Laboratory. *Press Release: Science & Technology drive to deliver UK space launch*. 2022. URL: https://www.gov.uk/government/news/science-technology-drive-to-deliver-uk-space-launch?utm_medium=email&utm_campaign=govuk-notifications-topic&utm_source=99a91d94-5ecf-440d-8b3b-b1e41eaa11c4&utm_content=daily.

[5] J. Prisco. *Why a Mach 5 passenger plane is a crazy idea that might just work*. 2021. URL: https://edition.cnn.com/travel/article/hypersonic-airplane-hermeus/index.html.

[6] C. Fox. *United plans supersonic passenger flights by 2029*. 2021. URL: https://www.bbc.co.uk/news/technology-57361193.

[7] United States Air Force. *X-51A Waverider*. URL: https://www.af.mil/About-Us/Fact-Sheets/Display/Article/104467/x-51a-waverider/.

[8] Y. A. Cengel and A. J. Ghajar. *Heat and Mass Transfer: Fundamentals & Applications*. 5th. McGraw-Hill, 2015, p. 387.

[9] S. R. Pate. *AEDC-TR-77-107 Dominance of radiated aerodynamic noise on boundary layer transition in supersonic-hypersonic wind tunnels*. Tech. rep. Arnold Engineering Development Center, 1978.

[10] E. R. van Driest. "The Problem of Aerodynamic Heating". In: *Aerodynamic Heating: Aerodynamic Aspects Session, National Summer Meeting, IAS*. 1956, pp. 26–41.

[11] O. Reynolds. "An experimental investigation of the circumstances which determine whether the motion of water shall be direct or sinuous, and of the law of resistance in parallel channels". In: *Philosophical Transactions of the Royal Society of London* 174 (1883), pp. 935–982.

[12] G. Grossir. "Longshot Hypersonic Wind Tunnel Flow Characterization and Boundary Layer Stability Investigations". PhD thesis. Universite Libre de Bruxelles, 2015.

[13] L. M. Mack. "Computations of the stability of the laminar compressible boundary layer". In: *Methods in Computational Physics*. Ed. by B. Alder, S. Fernback, and M. Rotenberg. New York: Academic Press, 1965, pp. 247–299.

[14] L. M. Mack. *Doc. No. 900-277 Rev. A. Boundary-Layer Stability Theory*. Tech. rep. Pasadena: Jet Propulsion Laboratory, 1969.

[15] L. M. Mack. "Linear stability theory and the problem of supersonic boundary-layer transition". In: *AIAA Journal* 13.3 (1975), pp. 278–289.

[16] A. V. Fedorov. "Transition and Stability of High-Speed Boundary Layers". In: *Annual Review of Fluid Mechanics* 43.1 (2011), pp. 79–95.

[17] K. F. Stetson, E. R. Thompson, J. C. Donaldson, and L. G. Siler. "Laminar boundary layer stability experiments on a cone at Mach 8, Part I: Sharp Cone". In: *AIAA 16th Fluid and Plasma Dynamics Conference*. Danvers: AIAA, 1983.

[18] P. Paredes, M. M. Choudhari, and F. Li. "Laminar-turbulent transition upstream of the entropy-layer swallowing location in hypersonic boundary layers". In: *AIAA Aviation 2019 Forum* (2019), pp. 1–13.

[19] P. Paredes, M. M. Choudhari, F. Li, J. S. Jewell, and R. L. Kimmel. "Nonmodal Growth of Traveling Waves on Blunt Cones at Hypersonic Speeds". In: *AIAA Journal* 57.11 (2019), pp. 4738–4749.

[20] G. Grossir, F. Pinna, G. Bonuccif, T. Regert, P. Rambaud, and O. Chazot. "Hypersonic boundary layer transition on a 7 degree Half-Angle cone at Mach 10". In: *AIAA AVIATION 2014 -7th AIAA Theoretical Fluid Mechanics Conference* June (2014).

[21] H. Olivier and S. Gu. "Operation, Capabilities and Limitations of Existing Hypersonic Facilities". In: *VKI Lecture Series: Flow Characterization and Modeling of Hypersonic Wind Tunnels, von Karman Inst. for Fluid Dynamics STO-EN AVT-325-01*. Sint-Genesius-Rode, Belgium, 2018.

[22] E. H. Hirschel. *Basics of aerothermodynamics*. Springer, AIAA, 2005, pp. 1–413.

[23] L. Prandtl. "Uber Flussigkeitsbewegung bei sehr kleiner Reibung". In: *Verhandlungen des dritten internationalen mathematiker-kongresses*. Ed. by A. Krazer. Heidelberg, 1904.

[24] J. D. Anderson Jr. "Ludwig Prandtl's Boundary Layer". In: *Physics Today* 58.12 (2005), pp. 42–48.

[25] G. B. Schubauer and H. K. Skramstad. "Laminar Boundary-Layer Oscillations and Stability of Laminar Flow". In: *Journal of the Aeronautical Sciences* 14.2 (1947), pp. 69–78.

[26] E. Reshotko. *AGARD-R-709 Special Course on Stability and Transition of Laminar Flow: Environment and Stability*. Tech. rep. March. Belgium: von Karman Institute, 1984.

[27] E. Reshotko. "Transient growth: A factor in bypass transition". In: *Physics of Fluids* 13.5 (2001), pp. 1067–1075.

[28] P. J. Schmid and D. S. Henningson. *Stability and Transition in Shear Flows*. New York: Springer-Verlag, 2001.

[29] K. L. Suder and J. E. O'Brien. *Technical Memorandum 100913: Experimental study of bypass transition in a boundary layer*. Tech. rep. NASA, 1988.

[30] H. Werle. "Transition and separation: Visualizations in the ONERA water tunnel". In: *La Recherche Aerospatiale: Bull. Bimestriel de l'Office National d'Etudes et de Recherches Aerospatial* (1980).

[31] F. M. White. *Viscous Fluid Flow*. 3rd. McGraw-Hill, 2006.

[32] A. Wagner. "Passive hypersonic boundary layer transition control using ultrasonically absorptive carbon-carbon ceramic with random microstructure". PhD thesis. Katholieke Universiteit Leuven, 2014, pp. 1–146.

[33] M. V. Morkovin. *ICASE Interim Report 1: Transition at Hypersonic Speeds*. Tech. rep. Virginia: Institute for Computer Applications in Science and Engineering, NASA Langley Research Center, 1987.

[34] L. Benjamin. "Investigation of instability growth in a hypersonic boundary layer using schlieren visualization". PhD thesis. Delft University of Technology, 2017.

[35] R. L. Kimmel and J. M. Kendall. "Nonlinear disturbances in a hypersonic laminar boundary layer". In: *29th Aerospace Sciences Meeting*. Reno, Nevada: AIAA, 1991.

[36] L. M. Mack. "Stability of Axisymmetric Boundary Layers on Sharp Cones at Hypersonic Mach Numbers". In: *AIAA 19th Fluid Dynamics, Plasma Dynamics and Lasers Conference*. Honolulu: AIAA, 1987.

[37] K. F. Stetson. "On Nonlinear Aspects of Hypersonic Boundary-Layer Stability". In: *AIAA Journal* 26.7 (1988).

[38] S. Unnikrishnan and D. V. Gaitonde. "Linear, nonlinear and transitional regimes of second-mode instability". In: *Journal of Fluid Mechanics* (2020).

[39] J. M. Kendall. "Wind Tunnel Experiments Relating to Supersonic and Hypersonic Boundary-Layer Transition". In: *AIAA Journal* 13.3 (1975).

[40] J. M. Kendall. "Wind Tunnel Experiments Relating to Supersonic and Hypersonic Boundary Layer Transition". In: *AIAA 12th Aerospace Sciences Meeting*. 74-133. Washington: AIAA, 1974.

[41] R. L. Kimmel, A. Demetriades, and J. C. Donaldson. "Space-time correlation measurements in a hypersonic transitional boundary layer". In: *AIAA Journal* 12.12 (1996), pp. 2484–2489.

[42] A. Demetriades. "Hypersonic viscous flow over a slender cone, part III: Laminar instability and transition". In: *AIAA 7th Fluid and Plasma Dynamics Conference*. Palo Alto: AIAA, 1974.

[43] K. M. Casper, S. J. Beresh, R. M. Wagnild, J. F. Henfling, R. W. Spillers, and B. Pruett. "Simultaneous pressure measurements and high-speed schlieren imaging of disturbances in a transitional hypersonic boundary layer". In: *43rd Fluid Dynamics Conference*. San Diego: AIAA, 2013.

[44] M. Estorf, R. Radespiel, S. P. Schneider, H. B. Johnson, and S. Hein. "Surface-pressure measurements of second-mode instability in quet hypersonic flow". In: *46th AIAA Aerospace Sciences Meeting and Exhibit*. Reno, 2008.

[45] T. Roediger, H. Knauss, E. Kramer, M. Estorf, S. P. Schneider, and B. Smorodsky. "Hypersonic instability waves measured using fast-response heat-flux gauges". In: *46th AIAA Aerospace Sciences Meeting and Exhibit*. Reno: AIAA, 2008.

[46] K. M. Casper, S. J. Beresh, J. F. Henfling, and R. W. Spillers. "Toward transition statistics measured on a 7-Degree hypersonic cone for turbulent spot modeling". In: *52nd Aerospace Sciences Meeting* (2014), pp. 1–14.

[47] J. Lachowicz, N. Chokani, and S. Wilkinson. "Boundary-layer stability measurements in a hypersonic quiet tunnel". In: *AIAA Journal* 34.12 (1996), pp. 2496–2500.

[48] K. F. Stetson and R. L. Kimmel. "On the breakdown of a hypersonic laminar boundary layer". In: *Aerospace Sciences Meeting*. AIAA, 1993.

[49] PCB Piezotronics. *Model 132A31 Micro ICP pressure sensor, 140 mV/psi, pigtail conn. (for high frequency): Installation and Operating Manual*. Tech. rep. New York: PCB Piezotronics, 2015. URL: `www.pcb.com`.

[50] D. J. Ort and J. J. Dosch. "Influence of mounting on the accuracy of piezoelectric pressure measurements for hypersonic boundary layer transition". In: *AIAA Scitech 2019 Forum*. January. 2019, pp. 1–13.

[51] D. C. Berridge and S. P. Schneider. "Calibration of PCB-132 Sensors in a Shock Tube". In: *Rto-Avt-200-25* (2012), pp. 1–14.

[52] M. Wason. "Calibration of High-Frequency Pressure Sensors Using Low-Pressure Shock Waves". PhD thesis. Purdue University, 2019, pp. 1–9.

[53] T. Regert, G. Grossir, S. Paris, and L. Blay Esteban. "Schlieren visualization for high-speed flows based on laser-induced fluorescence". In: *Experiments in Fluids* 55.1668 (2014).

[54] S. J. Laurence, A. Wagner, and K. Hannemann. "Schlieren-based techniques for investigating instability development and transition in a hypersonic boundary layer". In: *Experiments in Fluids* 55.8 (2014).

[55] C. Vandercreek, M. Smith, and K. Yu. "Focused Schlieren and Deflectometry at AEDC Hypervelocity Wind Tunnel No. 9". In: *27th AIAA Aerodynamic Measurement Technology and Ground Testing Conference*. Chicago: American Institute of Aeronautics and Astronautics, 2010.

[56] J. Hofferth, R. Humble, D. Floryan, and W. Saric. "High-Bandwidth Optical Measurements of the Second-Mode Instability in a Mach 6 Quiet Tunnel". In: *51st AIAA Aerospace Sciences Meeting including the New Horizons Forum and Aerospace Exposition*. Grapevine: American Institute of Aeronautics and Astronautics, 2013.

[57] N. J. Parziale, J. E. Shepherd, and H. G. Hornung. "Differential Interferometric Measurement of Instability in a Hypervelocity Boundary Layer". In: *AIAA Journal* 51.3 (2012), pp. 750–753.

[58] N. J. Parziale. "Slender-Body Hypervelocity Boundary-Layer Instability". PhD thesis. California Institute of Technology, 2013.

[59] N. J. Parziale, J. E. Shepherd, and H. G. Hornung. "Free-stream density perturbations in a reflected-shock tunnel". In: *Experiments in Fluids* 55.2 (2014).

[60] N. J. Parziale, J. E. Shepherd, and H. G. Hornung. "Observations of hypervelocity boundary-layer instability". In: *Journal of Fluid Mechanics* 781 (2015), pp. 87–112.

[61] A. Demetriades. *Hydrodynamic Stability and Transition to Turbulence in the Hypersonic Boundary Layer over a Sharp Cone*. Tech. rep. July. Air Force Office of Scientific Research, 1975.

[62] G. S. Settles. *Schlieren and Shadowgraph Techniques: Visualizing Phenomena in Transparent Media*. Berlin: Springer-Verlag, 2001.

[63] P. Krehl and S. Engemann. "August Toepler - The first who visualized shock waves". In: *Shock Waves* 5.1-2 (1995), pp. 1–18.

[64] G. S. Settles and M. J. Hargather. "A review of recent developments in schlieren and shadowgraph techniques". In: *Measurement Science and Technology* 28.4 (2017).

[65] J. L. Potter and J. D. Whitfield. "Boundary-layer transition under hypersonic conditions". In: *AGARDograph* 97.Part III (1965).

[66] M. C. Fischer and R. D. Wagner. "Transition and hot-wire measurements in hypersonic helium flow". In: *AIAA Journal* 10.10 (1972), pp. 1326–1332.

[67] L. G. Smith. "Pulsed-Laser Schlieren Visualization of Hypersonic Boundary-Layer Instability Waves". In: *18th AIAA Aerospace Ground Testing Conference*. Colorado Springs: American Institute of Aeronautics and Astronautics, 1994.

[68] S. J. Laurence, A. Wagner, K. Hannemann, V. Wartemann, H. Lüdeke, H. Tanno, and K. Itoh. "Time-resolved visualization of instability waves in a hypersonic boundary layer". In: *AIAA Journal* 50.1 (2012), pp. 243–246.

[69] S. J. Laurence, A. Wagner, and K. Hannemann. "Experimental study of second-mode instability growth and breakdown in a hypersonic boundary layer using high-speed schlieren visualization". In: *Journal of Fluid Mechanics* 797 (2016), pp. 471–503.

[70] C. S. Butler and S. J. Laurence. "Interaction of second-mode disturbances with an incipiently separated compression-corner flow". In: *Journal of Fluid Mechanics* 913 (2021), pp. 1–13.

[71] C. S. Butler and S. J. Laurence. "Interaction of second-mode wave packets with an axisymmetric expansion corner". In: *Experiments in Fluids* 62.7 (2021), pp. 1–17. URL: `https://doi.org/10.1007/s00348-021-03235-2`.

[72] A. Towne, O. T. Schmidt, and T. Colonius. "Spectral proper orthogonal decomposition and its relationship to dynamic mode decomposition and resolvent analysis". In: *Journal of Fluid Mechanics* 847 (2018), pp. 821–867.

[73] L. Crocco. "Eine neue Stromfunktion fur die Erforschung der Bewegung der Gase mit Rotation". In: *Zeitschrift fur Angewandte Mathematik und Mechanik* 17.1 (1937), pp. 1–7.

[74] N. R. Rotta. *Effects of Nose Bluntness on the Boundary Layer Characteristics of Conical Bodies at Hypersonic Speeds*. Tech. rep. New York: New York University, 1966.

[75] P. Paredes, M. M. Choudhari, and F. Li. "Blunt-body paradox and improved application of transient-growth framework". In: *AIAA Journal* 56.7 (2018), pp. 2604–2614.

[76] R. E. Kennedy, J. S. Jewell, P. Paredes, and S. J. Laurence. "Characterization of instability mechanisms on sharp and blunt slender cones at Mach 6". In: *Journal of Fluid Mechanics* 936 (2022), pp. 1–24.

[77] K. F. Stetson. "Nosetip bluntness effects on cone frustum boundary layer transition in hypersonic flow". In: *AIAA 16th Fluid and Plasma Dynamics Conference*. Ed. by AIAA. Danvers, Massachusetts: AIAA, 1983.

[78] J. S. Jewell and R. L. Kimmel. "Boundary-layer stability analysis for stetson's Mach 6 blunt-cone experiments". In: *Journal of Spacecraft and Rockets* 54.1 (2017), pp. 258–265.

[79] E. C. Marineau, C. G. Moraru, D. R. Lewis, J. D. Norris, J. F. Lafferty, R. M. Wagnild, and J. A. Smith. "Mach 10 boundary-layer transition experiments on sharp and blunted cones". In: *AIAA AVIATION 2014 -19th AIAA International Space Planes and Hypersonic Systems and Technologies Conference* June (2014), pp. 1–24.

[80] A. A. Maslov, A. N. Shiplyuk, D. A. Bountin, and A. A. Sidorenko. "Mach 6 boundary-layer stability experiments on sharp and blunted cones". In: *Journal of Spacecraft and Rockets* 43.1 (2006), pp. 71–76.

[81] K. F. Stetson, E. R. Thompson, J. C. Donaldson, and L. G. Siler. "Laminar Boundary Layer Stability Experiments on a Cone at Mach 8, Part II: Blunt Cone". In: *AIAA 22nd Aerospace Sciences Meeting*. Ed. by AIAA. Reno, Nevada: AIAA, 1984.

[82] D. Baals and W. Corliss. *Wind Tunnels of NASA*. National Aeronautics and Space Administration, 1981.

[83] A. L. Braslow. *Monographs in Aerospace History: A History of Suction-Type Laminar-Flow Control with Emphasis on Flight Research*. Tech. rep. NASA History Division: Office of Policy and Plans, 1999.

[84] O. Chazot and F. Panerai. "Hypersonic Nonequilibrium Flows: Fundamentals and Recent Advances". In: ed. by Eswar (Unites States Air Force Research Laboratory) Josyula. American Institute of Aeronautics and Astronautics, Inc., 2015.

[85] G. de Crombrugghe, O. Chazot, T. J. McIntyre, and R. G. Morgan. "Experimental evidence of the impact of radiation coupling on binary scaling applied to shock layer flows". In: *International Journal of Heat and Mass Transfer* 120 (2018), pp. 568–574. URL: https://doi.org/10.1016/j.ijheatmasstransfer.2017.12.071.

[86] G. de Crombrugghe, R. G. Morgan, and O. Chazot. "Theoretical approach and experimental verification of the role of diffusive transport under binary scaling conditions". In: *International Journal of Heat and Mass Transfer* 97 (2016), pp. 675–682. URL: http://dx.doi.org/10.1016/j.ijheatmasstransfer.2016.02.018.

[87] R. J. Stalker. "Isentropic Compression of Shock Tube Driver Gas". In: *ARS Journal* 30.6 (1960), p. 564.

[88] R. J. Stalker. "Area Change with a Free-Piston Shock Tube". In: *AIAA Journal* 2 (1963), p. 396.

[89] R. J. Stalker. "Use of Argon in a Free Piston Shock Tunnel". In: *AIAA Plasmadynamics Conference*. Monterey, California: American Institute of Aeronautics and Astronautics (AIAA), 1966.

[90] C. Mundt, P. A. Jacobs, R. R. Boyce, and K. Hannemann. "A Comparative Study of Piston-Driven Shock-Tunnels". In: *Deutscher Luft-und Raumfahrtkongress*. Munich, 2003.

[91] S. D. Subiah, P. L. Collen, L. J. Doherty, R. T. Penty Geraets, A. Hyslop, and M. McGilvray. "Condition Development and Commissioning of the Oxford T6 Stalker Tunnel in Reflected Shock Tunnel Mode". In: *International Conference on Flight Vehicles, Aerothermodynamics and Re-entry Missions & Engineering*. Monopoli, Italy, 2019.

[92] P. L. Collen, L. J. Doherty, S. D. Subiah, T. Sopek, I. Jahn, D. E. Gildfind, R. T. Penty Geraets, C. Hambidge, R. G. Morgan, and M. McGilvray. "Development and Commissioning of the T6 Stalker Tunnel". In: *Experiments in Fluids* (2021).

[93] H. G. Hornung, B. Sturtevant, J. Belanger, S. Sanderson, M. Brouilette, and M. Jenkins. "Performance data of the new free-piston shock tunnel at GALCIT". In: *Proceedings of the 18th International Symposium of Shock Waves*. Sendai, 1991.

[94] R. J. Stalker and R. G. Morgan. "The University of Queensland free piston shock tunnel T4 - initial operation and preliminary calibration". In: *Proceedings of the 4th National Aerospace Engineering Symposium*. Australia, 1988.

[95] S. J. Stennett, D. E. Gildfind, P. A. Jacobs, R. G. Morgan, C. M. James, and P. Toniato. "The X3R free-piston reflected shock tunnel: Australias's new large-scale, long-duration hypersonic testing capability". In: *23rd AIAA International Space Planes and Hypersonic Systems and Technologies Conference*. American Institute of Aeronautics and Astronautics, 2020.

[96] C. Mundt and P. Altenhofer. "Results of HELM in initial operation as a shock tube". In: *10th International Workshop on Shock Tube Technology*. Brisbane, 2011.

[97] C. Mundt. "Development of a new piston-driven shock-tunnel HELM". In: *Experimental Methods of Shock Wave Research*. 2016, pp. 265–283.

[98] K. Hannemann, J. M. Schramm, A. Wagner, and G. P. Camillo. "The High Enthalpy Shock Tunnel Gottingen of the German Aerospace Center (DLR)". In: *Journal of large-scale research facilities* 4.A133 (2018).

[99] K. Itoh, S. Ueda, T. Komuro, K. Sato, M. Takahashi, H. Miyajima, H. Tanno, and H. Muramoto. "Improvement of a free piston driver for a high-enthalpy shock tunnel". In: *Shock Waves* 8.4 (Aug. 1998), pp. 215–233. URL: https://doi.org/10.1007/s001930050115.

[100] K. Hannemann, K. Itoh, D. J. Mee, and H. G. Hornung. "Free Piston Shock Tunnels HEG, HIEST, T4 and T5". In: *Experimental Methods of Shock Wave Research*. Springer, 2016, pp. 181–264.

[101] T. V. Jones, P. Street, and M. Westby. "Recent Enhancements to the DRA shock tunnel". In: *The European Forum on Wind Tunnels*. Southampton, United Kingdom, 1992.

[102] M. McGilvray, L. J. Doherty, A. J. Neely, R. Pearce, and P. Ireland. "The Oxford High Density Tunnel". In: *20th AIAA International Space Planes and Hypersonic Systems and Technologies Conference*. Glasgow, Scotland, 2015, pp. 1–7.

[103] S. Wylie, L. J. Doherty, and M. McGilvray. "Commissioning of the Oxford High Density Tunnel (HDT) for Boundary Layer Instability Measurements at Mach 7". In: *Fluid Dynamics Conference*. AIAA AVIATION Forum. American Institute of Aeronautics and Astronautics, June 2018. URL: https://doi.org/10.2514/6.2018-3074.

[104] Z. Hong, D. F. Davidson, and R. K. Hanson. "Contact surface tailoring condition for shock tubes with different driver and driven section diameters". In: *Shock Waves* 19.4 (2009), pp. 331–336.

[105] R. K. Hanson. "Quantitative Laser Diagnostics for Combustion Chemistry and Propulsion: Lecture 11 - Shock Tube Tecnhiques/Applications". In: *Lecture Notes* (2013), pp. 1–38. URL: https://cefrc.princeton.edu/combustion-summer-school/archived-programs/2013-session/lecture-notes.

[106] R. J. Stalker. *The Free-Piston Shock Tube*. 1966.

[107] H. G. Hornung. *The Piston Motion in a Free-Piston Driver for Shock Tubes and Tunnels*. Tech. rep. Pasadena: California Institute of Technology, 1988.

[108] H. Tanno, K. Itoh, T. Komuro, and K. Sato. "Experimental study on the tuned operation of a free piston driver". In: *Shock Waves* 10.1 (2000), pp. 1–7.

[109] S. A. Stanfield, R. L. Kimmel, D. Adamczak, and T. J. Juliano. "Boundary-layer Transition Experiment During Reentry of HIFiRE-1". In: *Journal of Spacecraft and Rockets* 52.3 (2015), pp. 637–649.

[110] H. B. Yates, E. H. Matlis, T. J. Juliano, and M. W. Tufts. "Plasma-actuated flow control of hypersonic crossflow-induced boundary-layer transition". In: *AIAA Journal* 58.5 (2020), pp. 2093–2108.

[111] P. L. Collen, L. J. Doherty, M. McGilvray, I. Naved, R. T. Penty Geraets, T. A. Hermann, R. G. Morgan, and D. E. Gildfind. "Commissioning of the T6 Stalker Tunnel". In: American Institute of Aeronautics and Astronautics (AIAA), Jan. 2019, pp. 1–14.

[112] R. T. Penty Geraets, M. McGilvray, L. J. Doherty, R. G. Morgan, C. M. James, T. Vanyai, and D. R. Buttsworth. "Development of a fast-response calorimeter gauge for hypersonic ground testing". In: *33rd AIAA Aerodynamic Measurement Technology and Ground Testing Conference*. 2017, p. 3238.

[113] Kulite Semiconductor Products. *Kulite High Temperature Ultraminiature Pressure Transducer XCE-062 Series*. Tech. rep. New Jersey: Kulite Semiconductor Products, 2014. URL: www.kulite.com.

[114] D. J. Wise and M. K. Smart. "Roughness-induced transition of hypervelocity boundary layers". In: *Journal of Spacecraft and Rockets* 51.3 (2014), pp. 847–854.

[115] M. Hayne. *Research Report 2003/20: The Manufacture and Mounting of Thin Film Gauges for Heat Transfer*. Tech. rep. University of Queensland, 2003.

[116] D. L. Schultz and T. V. Jones. *AGARD-AG-165: Heat-transfer measurements in short-duration hypersonic facilities*. Tech. rep. Neuilly sur Seine: AGARD, 1973.

[117] M. McGilvray, L. J. Doherty, R. G. Morgan, and D. E. Gildfind. "T6 : The Oxford University Stalker Tunnel". In: *20th AIAA International Space Planes and Hypersonic Systems and Technologies Conference*. Glasgow, Scotland: American Institute of Aeronautics and Astronautics, 2015, pp. 1–11.

[118] M. K. Smart, R. J. Stalker, R. G. Morgan, and A. Paull. "Hypersonics Research in Australia". In: *Advances on Propulsion Technology for High-Speed Aircraft* (2008), pp. 11–1. URL: http://www.rto.nato.int/Pubs/rdp.asp?RDP=RTO-EN-AVT-150.

[119] J. D. Anderson Jr. *Hypersonic and High-Temperature Gas Dynamics, Second Edition*. eng. 2nd. AIAA education series. Reston, Va.: American Institute of Aeronautics and Astronautics, 2006.

[120] C. A. Snyder. *NASA Chemical Equilibrium with Applications*. 2016. URL: https://www.grc.nasa.gov/WWW/CEAWeb/.

[121] D. E. Gildfind, C. M. James, and R. G. Morgan. "Free-piston driver performance characterisation using experimental shock speeds through helium". In: *Shock Waves* 25.2 (2015), pp. 169–176.

[122] J. D. Anderson. *Modern Compressible Flow: With Historical Perspective*. 4th. McGraw-Hill, 2021.

[123] D. E. Gildfind, P. A. Jacobs, and R. G. Morgan. "Vibration isolation in a free-piston driven expansion tube facility". In: *Shock Waves* 23 (2013), pp. 431–438.

[124] A. Wagner. "High frequency pressure measurements in shock tunnels using piezoelectric transducers". In: *12th International Workshop on Shock Tube Technology*. Kakuda, 2018.

[125] Wolfram MathWorld. *Full Width at Half Maximum*. 2019. URL: http://mathworld.wolfram.com/FullWidthatHalfMaximum.html.

[126] C. M. James, D. E. Gildfind, R. G. Morgan, P. A. Jacobs, and F. Zander. "Designing and simulating high enthalpy expansion tube conditions". In: *Proceedings of the 2013 Asia-Pacific International Symposium on Aerospace Technology*. Takamatsu, Japan, 2013.

[127] R. J. Goozee, P. A. Jacobs, and D. R. Buttsworth. "Simulation of a complete reflected shock tunnel showing a vortex mechanism for flow contamination". In: *Shock Waves* 15.3-4 (2006), pp. 165–176.

[128] R. J. Goozee. "Simulation of a complete shock tunnel with parallel computer codes". PhD thesis. University of Queensland, 2003.

[129] P. A. Jacobs, R. J. Gollan, D. F. Potter, F. Zander, D. E. Gildfind, P. Blyton, W. Y. K. Chan, and L. J. Doherty. *Estimation of high-enthalpy flow conditions for simple shock and expansion processes using the ESTCj program and library*. Tech. rep. University of Queensland, 2011.

[130] J. A. Fay and F. R. Riddell. "Theory of Stagnation Point Heat Transfer in Dissociated Air". In: *Journal of the Aerospace Sciences* 25.2 (1958), pp. 73–85.

[131] E. V. Zoby and E. M. Sullivan. "Effects of corner radius on stagnation-point velocity gradients on blunt axisymmetric bodies". In: *Journal of Spacecraft and Rockets* 3.10 (1966), p. 1567.

[132] E. W. K. Chang, W. Y. K. Chan, K. J. Hopkins, T. J. McIntyre, and A. Veeraragavan. "Electrically-heated flat plate testing in a free-piston driven shock tunnel". In: *Aerospace Science and Technology* 103 (2020).

[133] P. A. Jacobs and R. J. Gollan. "Implementation of a Compressible-Flow Simulation Code in the D Programming Language". In: *Applied Mechanics and Materials* 846 (2016), pp. 54–60.

[134] T. Sopek, P. A. Jacobs, S. D. Subiah, Peter L. Collen, and M. McGilvray. "Effect of non-equilibrium thermochemistry on Pitot pressure measurements in shock tunnels". In: *AIAA (Submitted)* (2022), pp. 1–13.

[135] W. Y. K. Chan, P. A. Jacobs, M. K. Smart, S. Grieve, C. S. Craddock, and L. J. Doherty. "Aerodynamic design of nozzles with uniform outflow for hypervelocity ground-test facilities". In: *Journal of Propulsion and Power* 34.6 (2018), pp. 1467–1478.

[136] D. C. Wilcox. *Turbulence Modeling for CFD*. Third. DCW Industries, 2006.

[137] R. H. Nichols and C. Nelson. "Wall function boundary conditions including heat transfer and compressibility". In: *AIAA Journal* 42.6 (2004).

[138] S. Gordon and B. McBride. *Computer program for calculation of complex chemical equilibrium compositions and applications. Part 1: Analysis*. Tech. rep. Cleveland: NASA Lewis Research Center, 1994.

[139] R. N. Gupta and R. A. Thompson. *NASA TN: A review of reaction rates and thermodynamic and transport properties for the 11-species air model for chemical and thermal non-eqiulibrium calculations to 30000 K*. Tech. rep. NASA, 1989.

[140] C. Park. "Assessment of two-temperature kinetic model for ionizing air". In: *Journal of Thermophysics and Heat Transfer* 3.3 (1989), pp. 233–244.

[141] W. Y. K. Chan, R. W. Whitside, M. K. Smart, D. E. Gildfind, P. A. Jacobs, and T. Sopek. "Nitrogen driver for low-enthalpy testing in free-piston-driven shock tunnels". In: *Shock Waves* 31.6 (2021), pp. 541–550. URL: https://doi.org/10.1007/s00193-021-01002-0.

[142] I. Lavery. "A nitrogen driver for the T4 shock tunnel". PhD thesis. University of Queensland, 1993.

[143] S. Hess. "A low enthalpy test condition for the T4 shock tunnel". PhD thesis. University of Queensland, 2009.

[144] E. C. Smith. "The Starting Process in a Hypersonic Nozzle". In: *Journal of Fluid Mechanics* 24.4 (1966), pp. 625–640.

[145] M. McGilvray. "Scramjet testing at high enthalpies in expansion tube facilities". PhD thesis. University of Queensland, 2008. URL: https://espace.library.uq.edu.au/view/UQ:155369.

[146] L. J. Doherty. "An Experimental Investigation of an Airframe Integrated Three-Dimensional Scramjet Engine at a Mach 10 Flight Condition". PhD thesis. University of Queensland, 2014.

[147] P. A. Jacobs, R. C. Rogers, E. H. Weidner, and R. D. Bittner. "Flow Establishment in a Generic Scramjet Combustor". In: *Journal of Propulsion and Power* 8.4 (1992), pp. 890–899.

[148] R. A. East, R. J. Stalker, and J. P. Baird. "Measurements of heat transfer to a flat plate in a dissociated high enthalpy laminar airflow". In: *Journal of Fluid Mechanics* 97.4 (1980), pp. 673–699.

[149] W. R. Davies and L. Bernstein. "Heat Transfer and Transition to Turbulence in the Shock-Induced Boundary Layer on a Semi-Infinite Flat Plate". In: *Journal of Fluid Mechanics* 36.1 (1969), pp. 87–112.

[150] P. L. Collen, L. J. Doherty, S. D. Subiah, A. Hyslop, and M. McGilvray. "Performance Capability Experiments in T6: A Hypervelocity, Transient and Multi-Mode Ground Test Facility for High-Enthalpy Aerothermodynamics Research". In: *International Conference on Flight Vehicles, Aerothermodynamics and Re-entry Missions & Engineering*. Monopoli, Italy: ESA, 2019.

[151] P. L. Collen. "Development of a High-Enthalpy Ground Test Facility for Shock-Layer Radiation". PhD thesis. University of Oxford, 2021.

[152] N. M. Shumway and S. J. Laurence. "Methods for identifying key features in schlieren images from hypersonic boundary-layer stability experiments". In: *53rd AIAA Aerospace Sciences Meeting* January (2015), pp. 1–22.

[153] G. P. Camillo, A. Wagner, C. Dittert, L. Benjamin, V. Wartemann, J. Neumann, and R. Hink. "Experimental investigation of the effect of transpiration cooling on second mode instabilities in a hypersonic boundary layer". In: *Experiments in Fluids* 61.7 (2020), pp. 1–19. URL: https://doi.org/10.1007/s00348-020-02994-8.

[154] J. S. Jewell, R. E. Kennedy, S. J. Laurence, and R. L. Kimmel. "Transition on a Variable Bluntness 7-Degree Cone at High Reynolds Number". In: *AIAA Aerospace Sciences Meeting, 2018*. 210059. 2018, pp. 1–14.

[155] B. Russell and J. Han. *CREWES Research Report: Jean Morlet and the Continuous Wavelet Transform*. Tech. rep. Alberta: CGG GeoSoftware Company, 2016, pp. 1–15.

[156] J. P. Antoine. "The continuous wavelet transform in image processing". In: *CWI Quarterly* 11.4 (1998), pp. 323–345.

[157] J. Morlet, G. Arens, E. Fourgeau, and D. Giard. "Wave propagation and sampling theory - Part II: Sampling theory and complex waves". In: *Geophysics* 47.2 (1982), pp. 222–236.

[158] J. Morlet, G. Arens, E. Fourgeau, and D. Giard. "Wave propagation and sampling theory - Part I: Complex signal and scattering in multilayered media". In: *Geophysics* 47.2 (1982), pp. 203–221.

[159] P. Welch. "The use of fast Fourier transform for the estimation of power spectra: a method based on time averaging over short, modified periodograms". In: *IEEE Transactions on audio and electroacoustics* 15.2 (1967), pp. 70–73.

[160] R. E. Kennedy, S. J. Laurence, M. S. Smith, and E. C. Marineau. "Hypersonic boundary-layer transition features from high-speed schlieren images". In: *AIAA SciTech Forum - 55th AIAA Aerospace Sciences Meeting* January (2017).

[161] MathWorks. *Two-Dimensional Cross-Correlation of Arbitrary Complex Matrices*. 2021. URL: https://uk.mathworks.com/help/signal/ref/xcorr2.html.

[162] MathWorks. *Stereo Disparity Using Semi-Global Block Matching*. 2021. URL: https://uk.mathworks.com/help/visionhdl/ug/stereoscopic-disparity.html.

[163] H. Hirschmuller. "Accurate and Efficient Stereo Processing by Semi-Global Matching and Mutual Information". In: *International Conference on Computer Vision and Pattern Recognition*. 2005.

[164] R. Spangenberg, T. Langner, and R. Rojas. "Weighted Semi-Global Matching and Center-Symmetric Census Transform for Robust Driver Assistance". In: *International Conference on Computer Analysis of Images and Patterns*. 2013.

[165] S. Gehrig, F. Eberli, and T. Meyer. "A Real-Time Low-Power Stereo Vision Engine Using Semi-Global Matching". In: *International Conference on Computer Vision Systems*. 2009.

[166] A. Swami, J. Mendel, and C. Nikias. *Higher-Order Spectral Analysis Toolbox For Use with MATLAB*. Tech. rep. United Signals & Systems Inc., 2001.

[167] D. Brillinger. "An Introduction to Polyspectra". In: *The Annals of Mathematical Statistics* 36.5 (1965), pp. 1351–1374.

[168] O. T. Schmidt and T. Colonius. "Guide to spectral proper orthogonal decomposition". In: *AIAA Journal* 58.3 (2020), pp. 1023–1033.

[169] W. K. George. *Lectures in Turbulence for the 21st Century*. Tech. rep. January. Imperial College of London, UK, and Chalmers University of Technology, Gothenburg, 2013, p. 351. URL: http://www.turbulence-online.com/Publications/Lecture_Notes/Turbulence_Lille/TB_Lille_24Oct2010.pdf.

[170] X. Zhao. "Spectral Proper Orthogonal Decomposition-based Bispectral Analysis of Nonlinear Flows". PhD thesis. University of California San Diego, 2021.

[171] A. Nekkanti and O. T. Schmidt. "Frequency-time analysis, low-rank reconstruction and denoising of turbulent flows using SPOD". In: *Journal of Fluid Mechanics* 926 (2021), pp. 1–35.

[172] M. Sieber, C. O. Paschereit, and K. Oberleithner. "Spectral proper orthogonal decomposition". In: *Journal of Fluid Mechanics* 792 (2016), pp. 798–828.

[173] J. L. Lumley. *The structure of inhomogeneous turbulent flows*. Ed. by A. L. Yaglom and V. I. Tatarski. Nauka, 1967, pp. 166–178.

[174] J. L. Lumley. *Stochastic Tools in Turbulence*. Academic Press, 1970.

[175] Thorlabs. *Mounted Achromatic Doublets, AR Coated: 400 - 700 nm*. 2022. URL: https://www.thorlabs.com/newgrouppage9.cfm?objectgroup_id=2696.

[176] Vision Research Inc. *Phantom TMX 7510*. 2021. URL: https://www.phantomhighspeed.com/products/cameras/tmx/7510.

[177] Specialised Imaging Limited. *Kirana5M*. 2020. URL: https://www.specialised-imaging.com/products/video-cameras/kirana.

[178] Photron. *Fastcam Mini AX50/AX100/AX200*. 2021. URL: https://photron.com/fastcam-mini-ax/.

[179] F. G. Keyes. "A summary of viscosity and heat-conduction data for He, A, H2, O2, CO, CO2, H2O, and air". In: *Transactions of the ASME 73* (1951), pp. 589–596.

[180] C. Roy and F. Blottner. "Review and Assessment of Turbulence Models for Hypersonic Flows: 2D/Asymmetric Cases". In: *Aerospace Sciences Meeting*. American Institute of Aeronautics and Astronautics, 2006.

[181] G. I. Taylor and J. W. Maccoll. "The air pressure on a cone moving at high speeds.-II". In: *Proceedings of the Royal Society of London Series A, Containing Papers of a Mathematical and Physical Character* 139.838 (1933), pp. 298–311.

[182] V. J. Bolos and R. Benitez. "The Wavelet Scalogram in the Study of Time Series". In: *Advances in Differential Equations and Applications*. Ed. by F. Casas and V. Martinez. Castellon: Springer International Publishing, 2014, pp. 147–154.

[183] D. A. Bountin, A. Shiplyuk, and A. A. Maslov. "Evolution of nonlinear processes in a hypersonic boundary layer on a sharp cone". In: *Journal of Fluid Mechanics* 611 (2008), pp. 427–442.

[184] G. Grossir, F. Pinna, and O. Chazot. "Influence of nose-tip bluntness on conical boundary-layer instabilities at Mach 10". In: *AIAA Journal* 57.9 (2019), pp. 3859–3873.

[185] J. D'Errico. *SLM - Shape Language Modeling*. 2022. URL: `https://uk.mathworks.com/matlabcentral/fileexchange/24443-slm-shape-language-modeling`.

[186] J. S. Jewell, A. Hameed, N. J. Parziale, and S. Gogineni. "Disturbance speed measurements in a circular jet via double focused laser differential interferometry". In: *AIAA Scitech 2019 Forum* January (2019).

Appendices

A

Cross-Correlation Results

Complete results for the cross-correlation method applied to the HDT results obtained with different cameras and frame rates is included here.

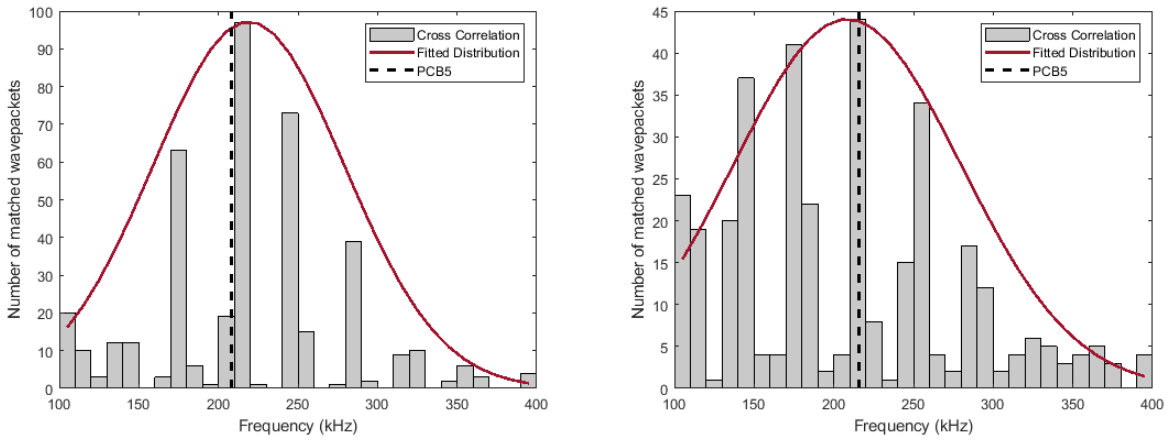


Figure A.1: Histogram showing number of matched wavepackets at frequencies for frame rates of 30 kfps for shots 1928 (left) and 1932 (right)

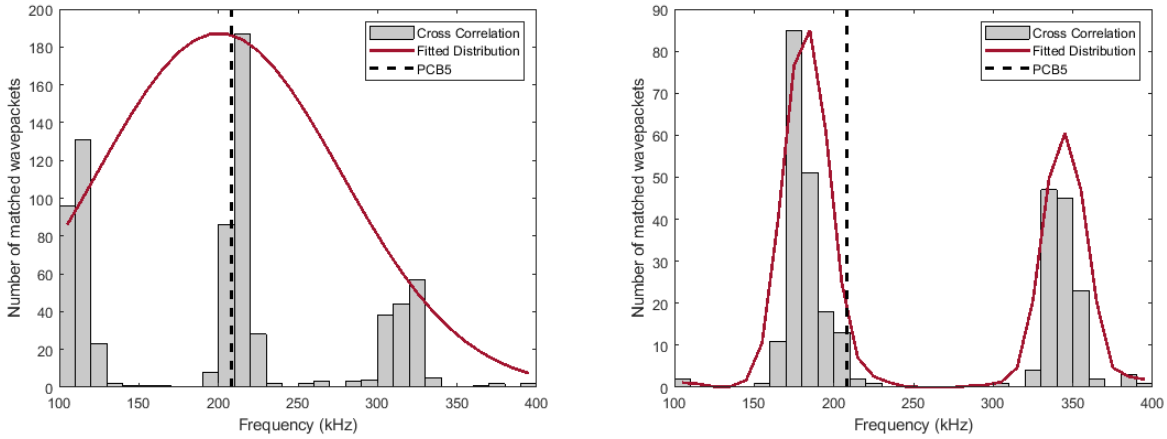


Figure A.2: Histogram showing number of matched wavepackets at frequencies for frame rates of 100 kfps for shots 1926 (left) and 1930 (right)

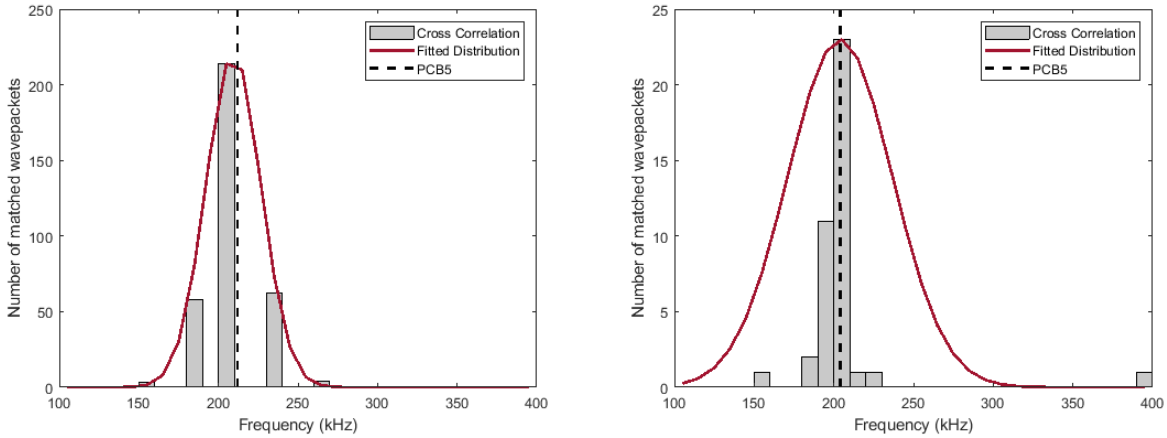


Figure A.3: Histogram showing number of matched wavepackets at frequencies for frame rates of 500 kfps for shots 1924 (left) and 1937 (right)

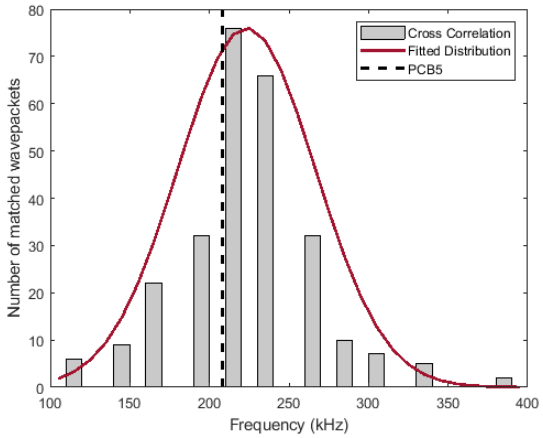


Figure A.4: Histogram showing number of matched wavepackets at frequencies for frame rates of 540 kfps for shot 1931

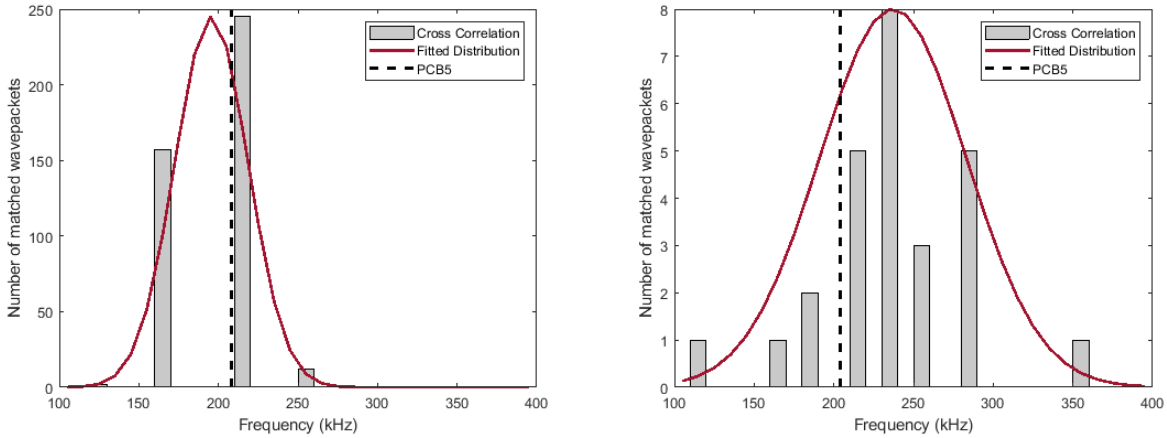


Figure A.5: Histogram showing number of matched wavepackets at frequencies for frame rates of 870 kfps for shots 1922 (left) and 1936 (right)

B

Image Stitching Results

Complete results for the image stitching method applied to the HDT results obtained with different cameras and frame rates is included here.

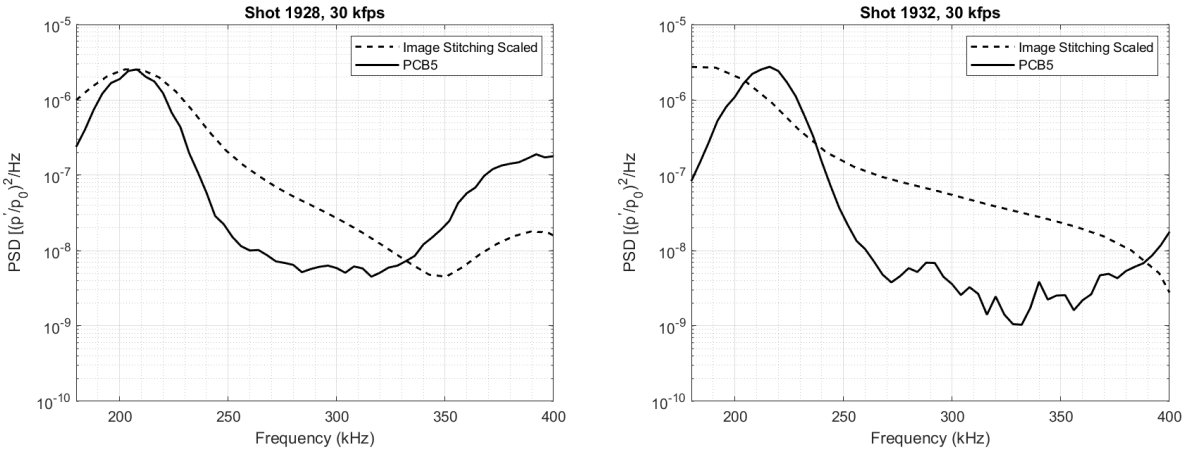


Figure B.1: Image stitching results for frame rates of 30 kfps for shot 1928 (left) and 1932 (right)

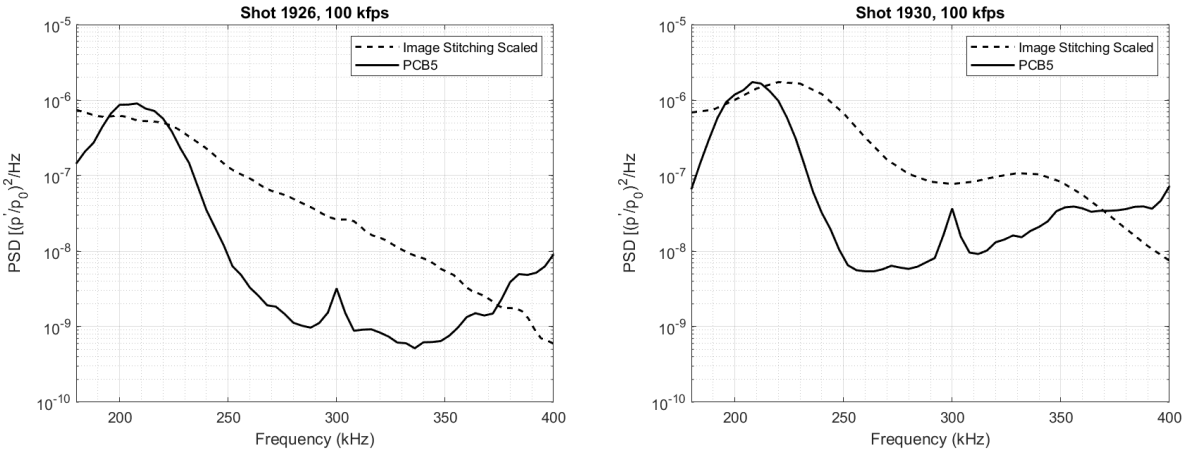


Figure B.2: Image stitching results for frame rates of 100 kfps for shot 1926 (left) and 1930 (right)

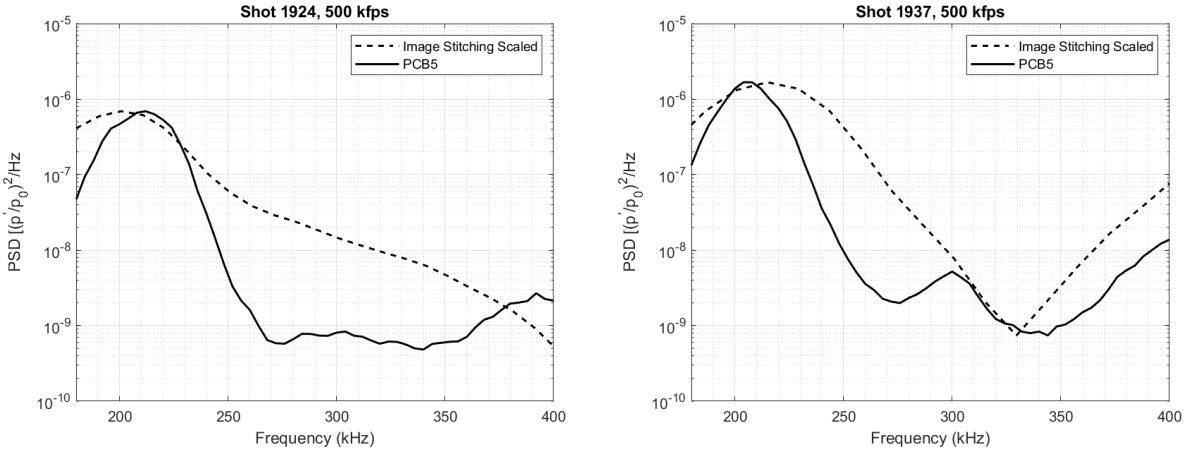


Figure B.3: Image stitching results for frame rates of 500 kfps for shot 1924 (left) and 1937 (right)

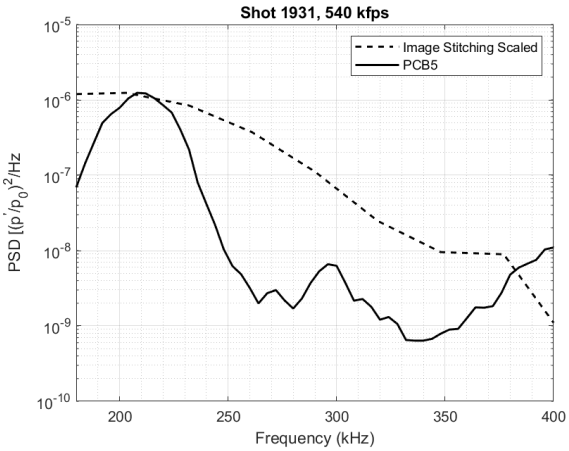


Figure B.4: Image stitching results for frame rates of 540 kfps for shot 1931

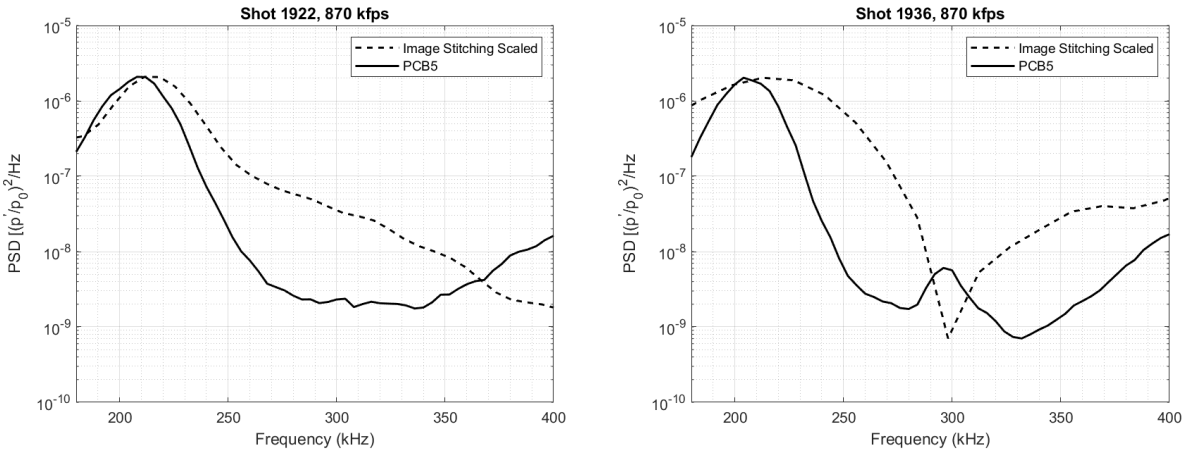


Figure B.5: Image stitching results for frame rates of 870 kfps for shot 1922 (left) and 1936 (right)

C

Wavelet Scalogram Results

Scalograms from images captured with different cameras and frame rates obtained from selected HDT experimenters are included here.

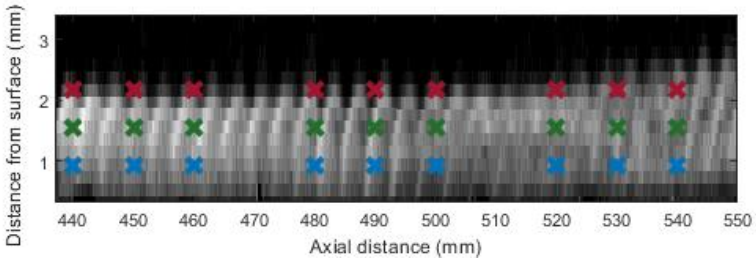


Figure C.1: Locations of wavelet scalograms for shot 1922

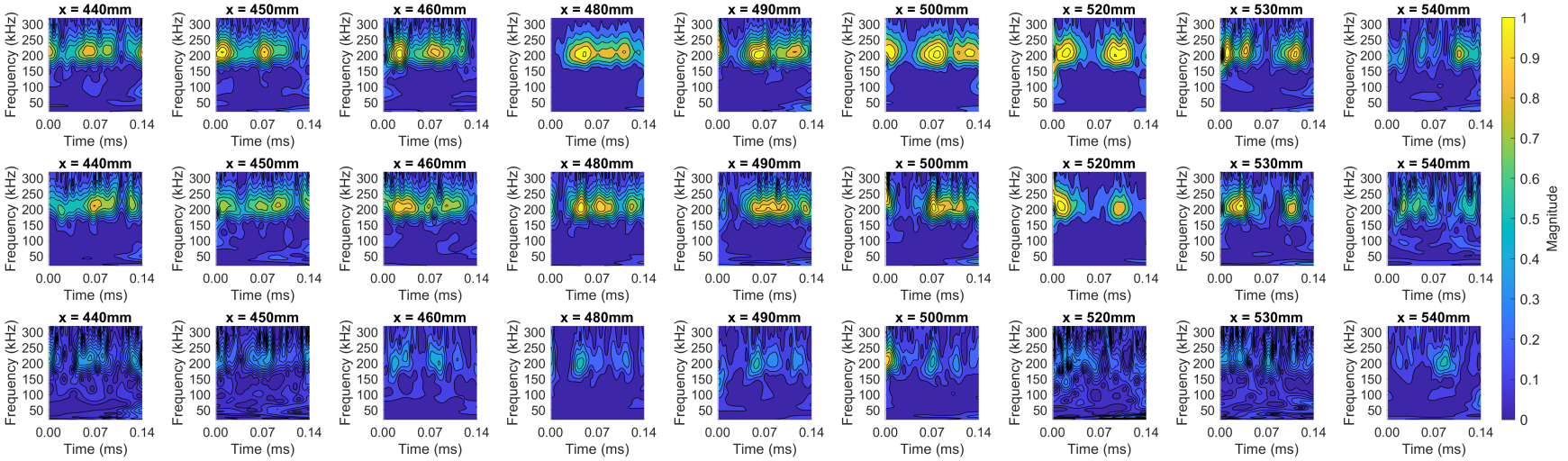


Figure C.2: Shot 1922 wavelet scalograms at locations downstream of a theoretically sharp nosetip and above the cone surface

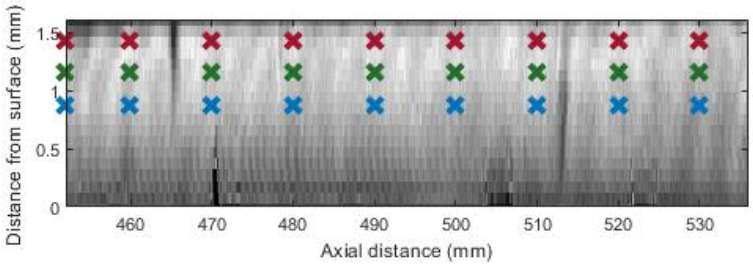


Figure C.3: Locations of wavelet scalograms for shot 1936

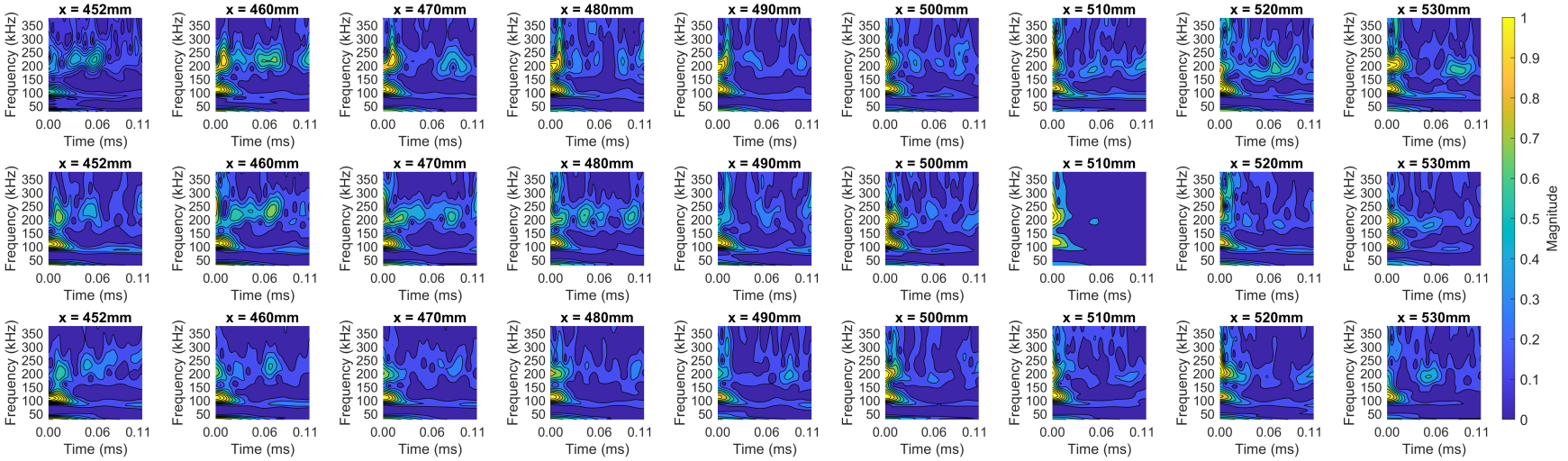


Figure C.4: Shot 1936 wavelet scalograms at locations downstream of a theoretically sharp nosetip and above the cone surface

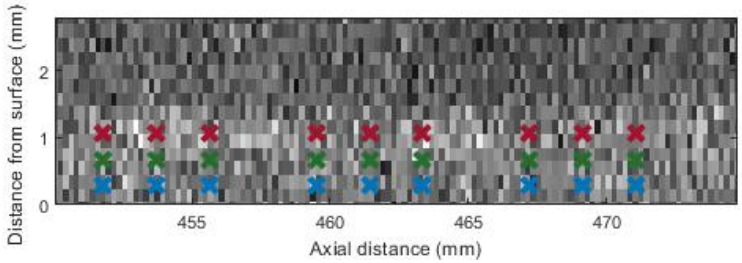


Figure C.5: Locations of wavelet scalograms for shot 1931

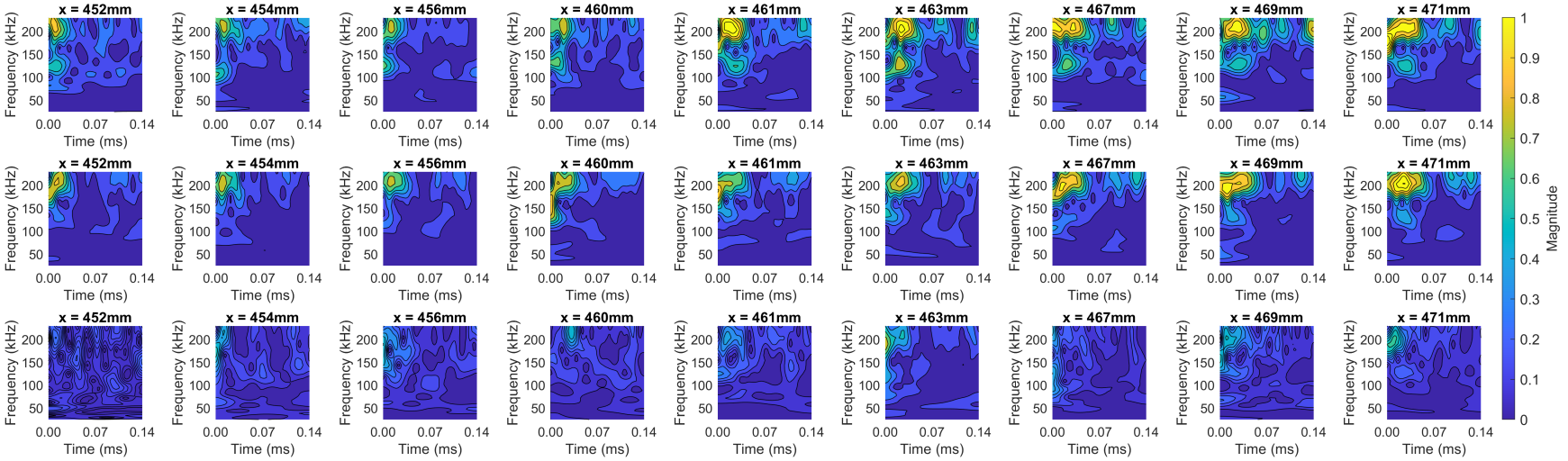


Figure C.6: Shot 1931 wavelet scalograms at locations downstream of a theoretically sharp nosetip and above the cone surface

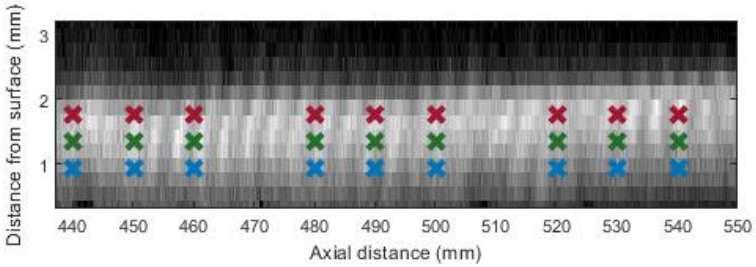


Figure C.7: Locations of wavelet scalograms for shot 1924

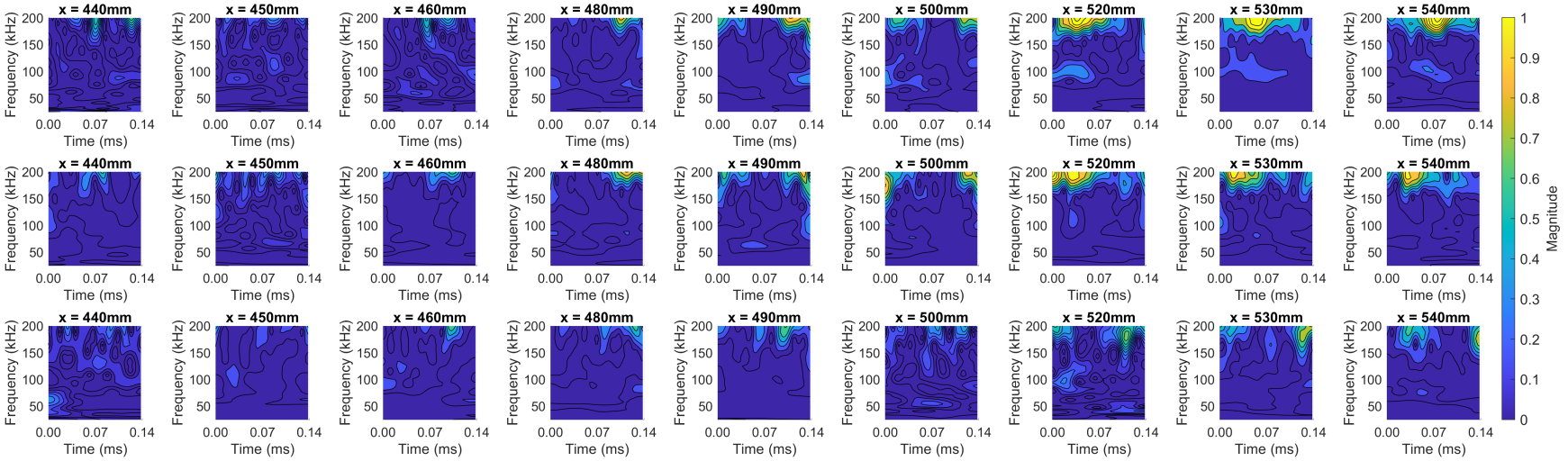


Figure C.8: Shot 1924 wavelet scalograms at locations downstream of a theoretically sharp nosetip and above the cone surface

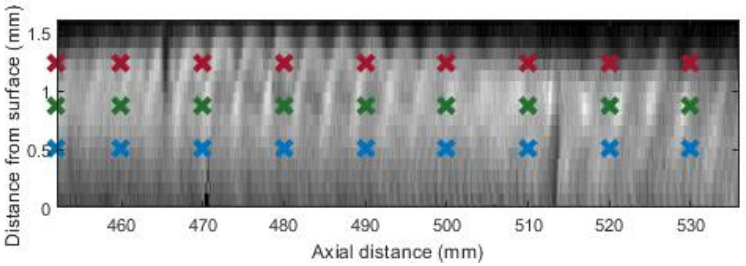


Figure C.9: Locations of wavelet scalograms for shot 1937

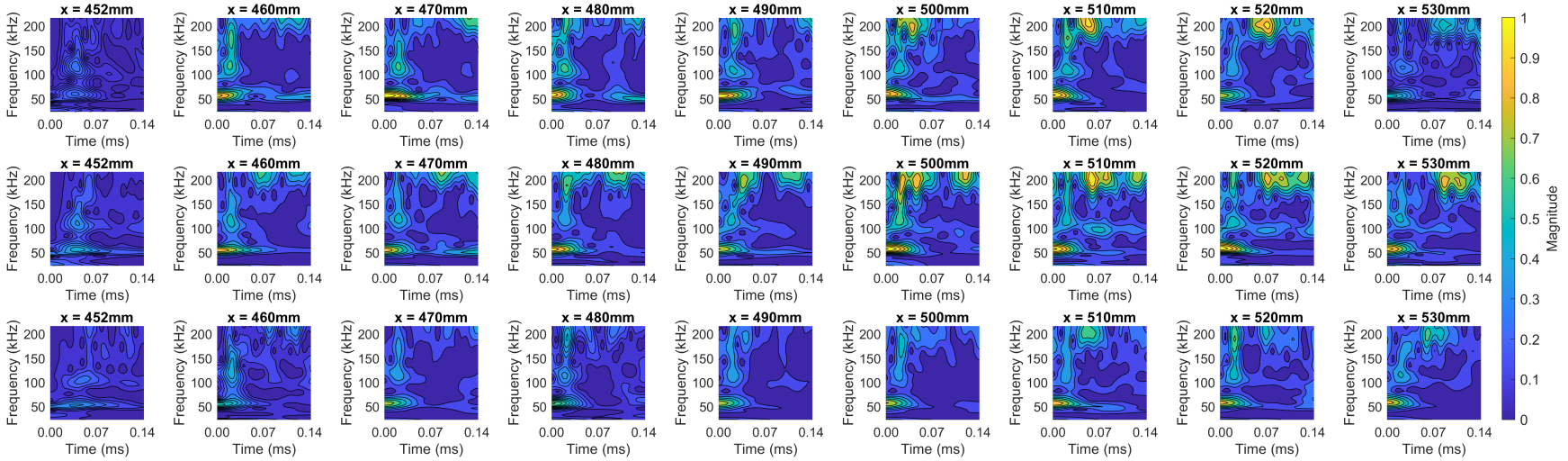


Figure C.10: Shot 1937 wavelet scalograms at locations downstream of a theoretically sharp nosetip and above the cone surface

D

Bispectral Analysis Results

Results from the bispectral analysis applied to selected images from the HDT campaign are included here.

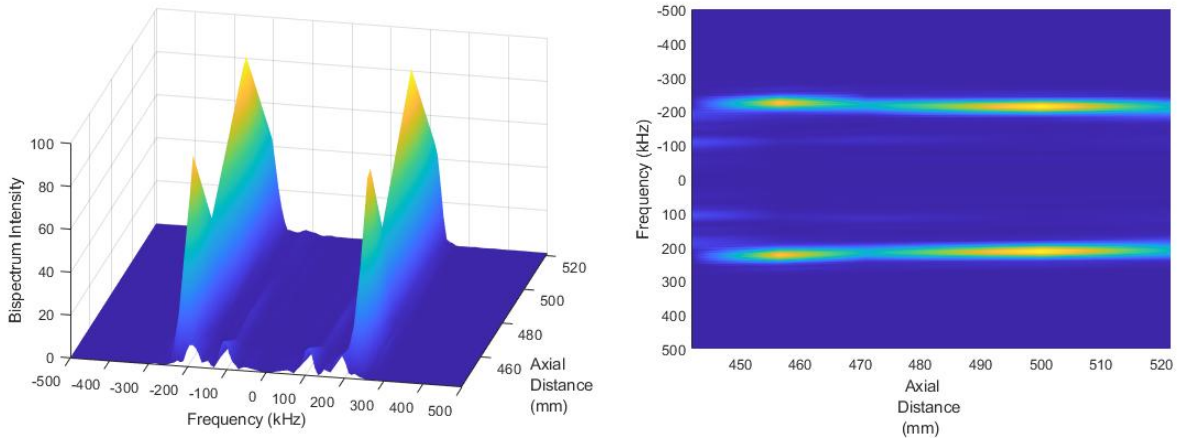


Figure D.1: Bispectrum for shot 1922 from PCB data at sensor locations from theoretically sharp nose tip

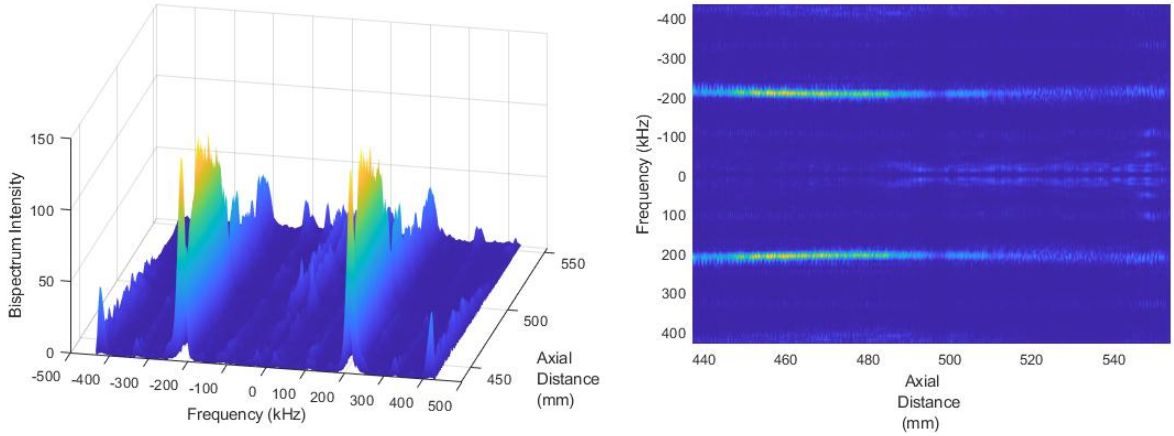


Figure D.2: Bispectrum for shot 1922 at axial locations from theoretically sharp nose tip

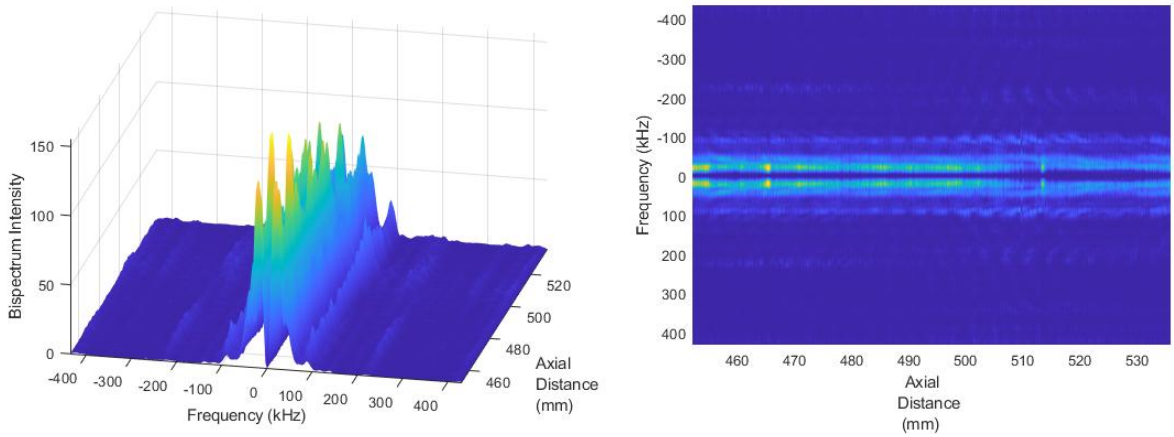


Figure D.3: Bispectrum for shot 1936 at axial locations from theoretically sharp nose tip

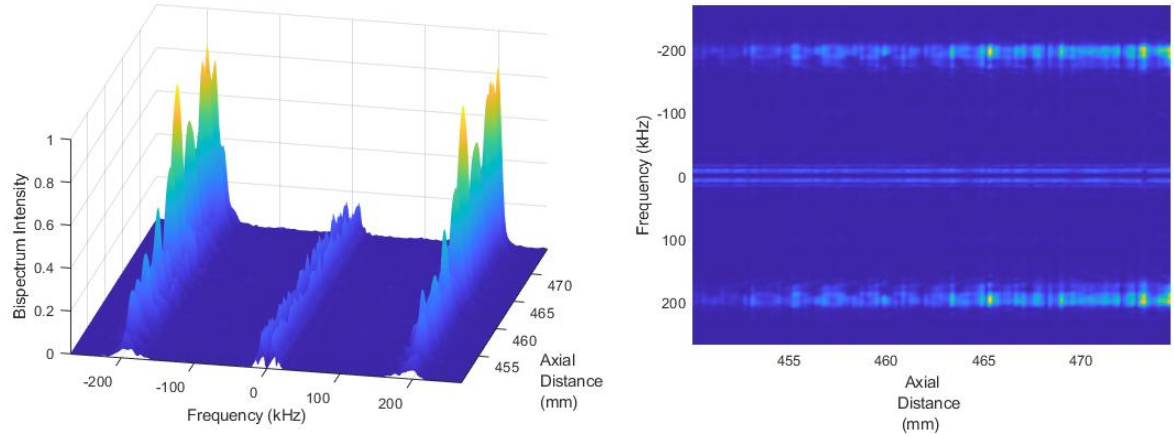


Figure D.4: Bispectrum for shot 1931 at axial locations from theoretically sharp nose tip

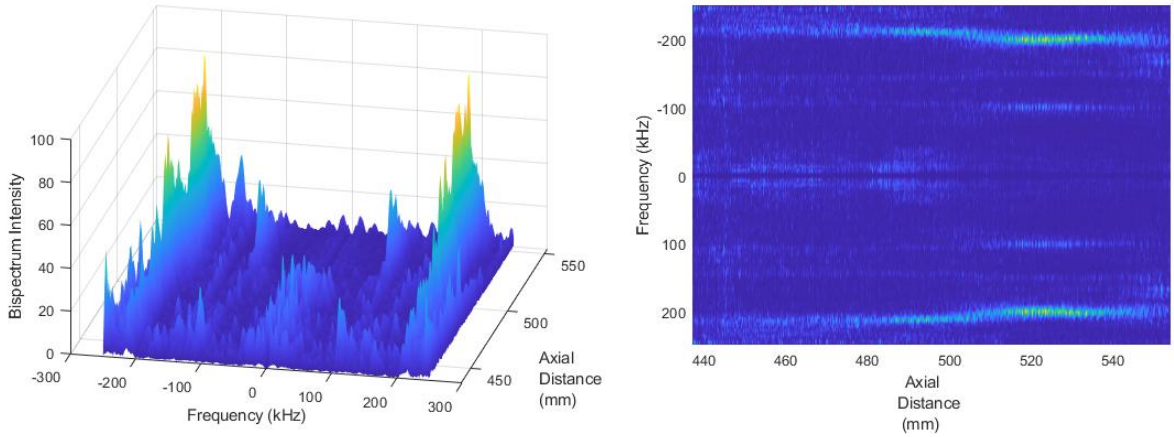


Figure D.5: Bispectrum for shot 1924 at axial locations from theoretically sharp nose tip

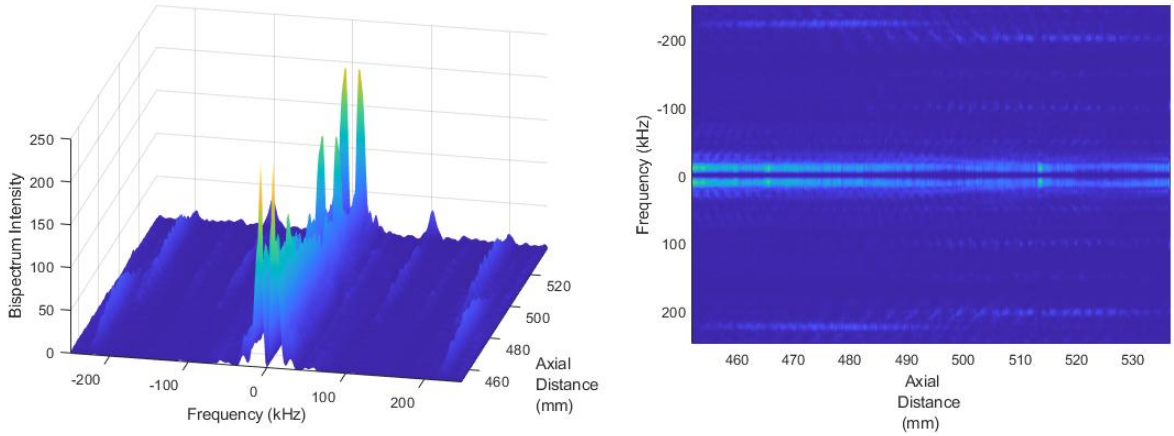


Figure D.6: Bispectrum for shot 1937 at axial locations from theoretically sharp nose tip

E
SPOD Results

Selected SPOD results from the HDT experiments are included here.

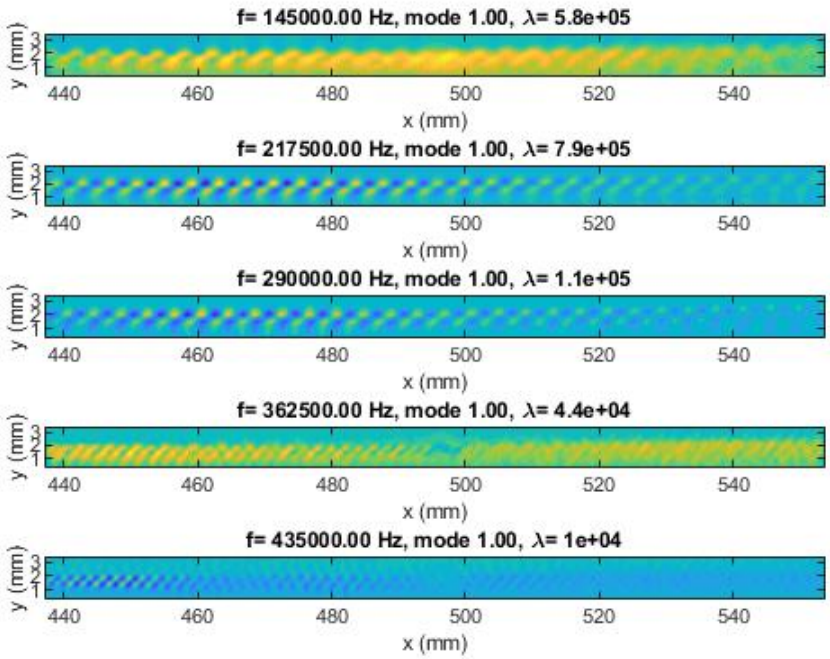


Figure E.1: SPOD analysis for shot 1922 at 870kfps

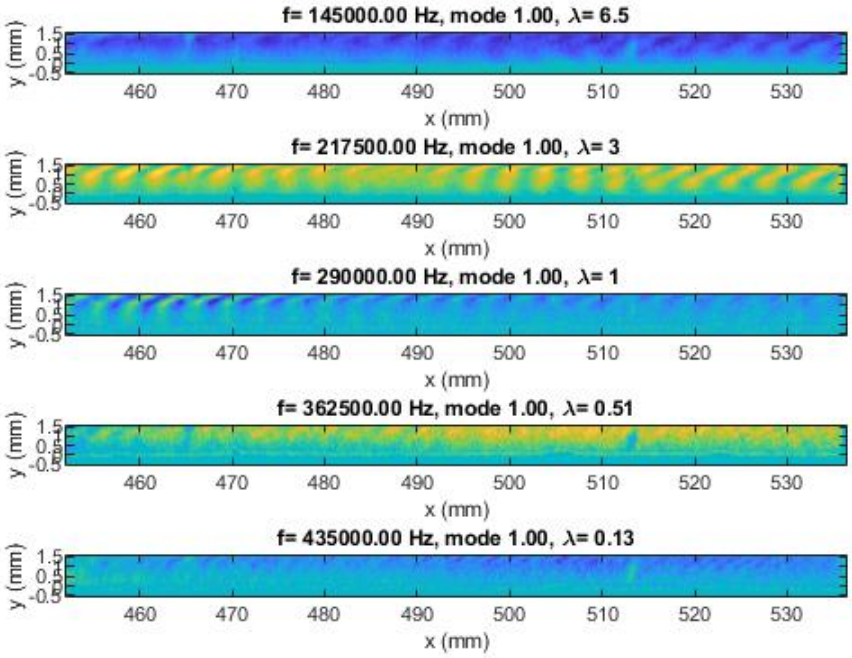


Figure E.2: SPOD analysis for shot 1936 at 870kfps

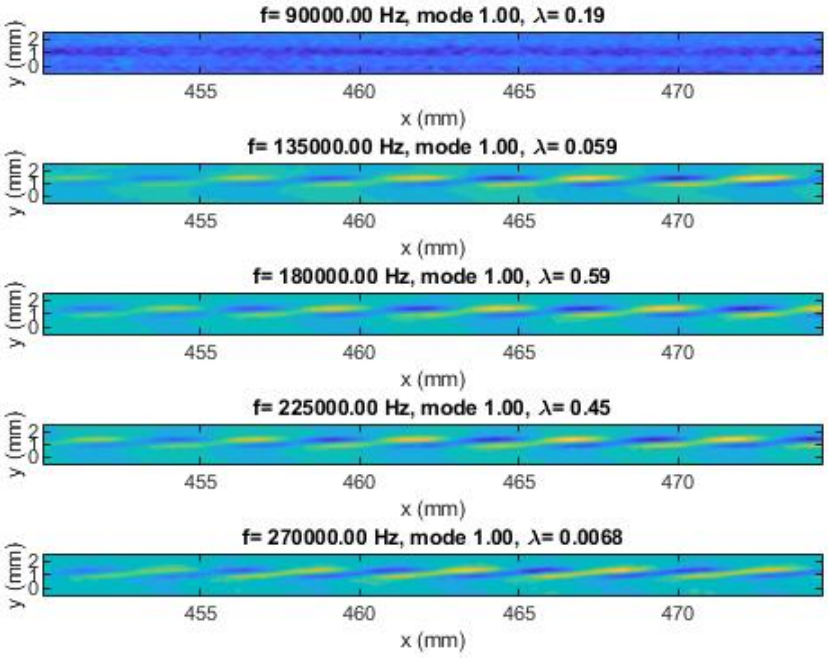


Figure E.3: SPOD analysis of shot 1931 at 540kfps

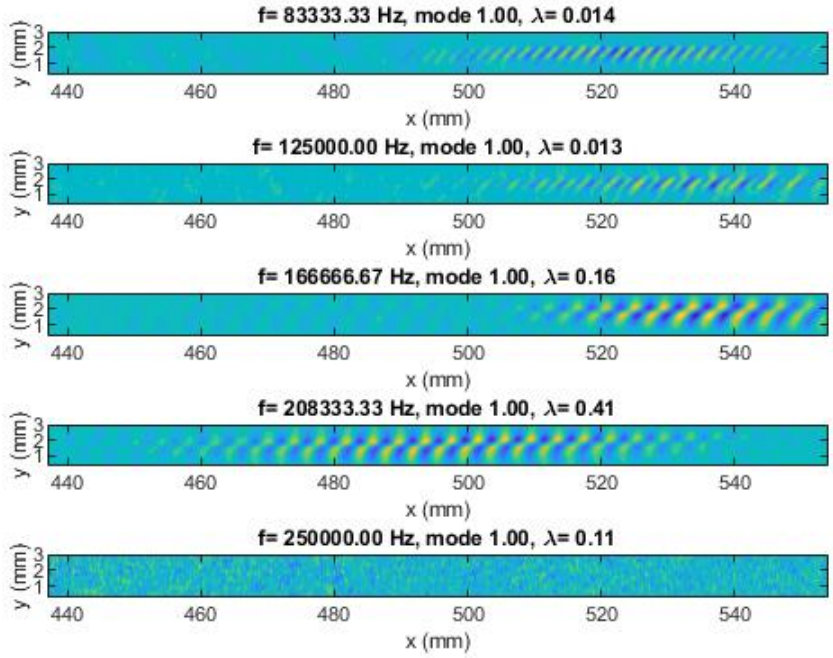


Figure E.4: SPOD analysis for shot 1924 at 500kfps

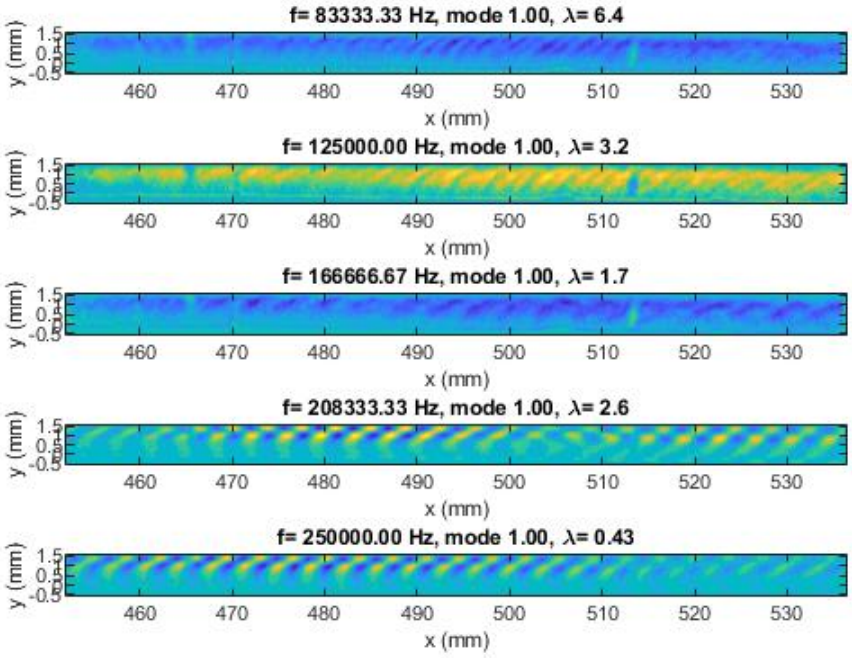


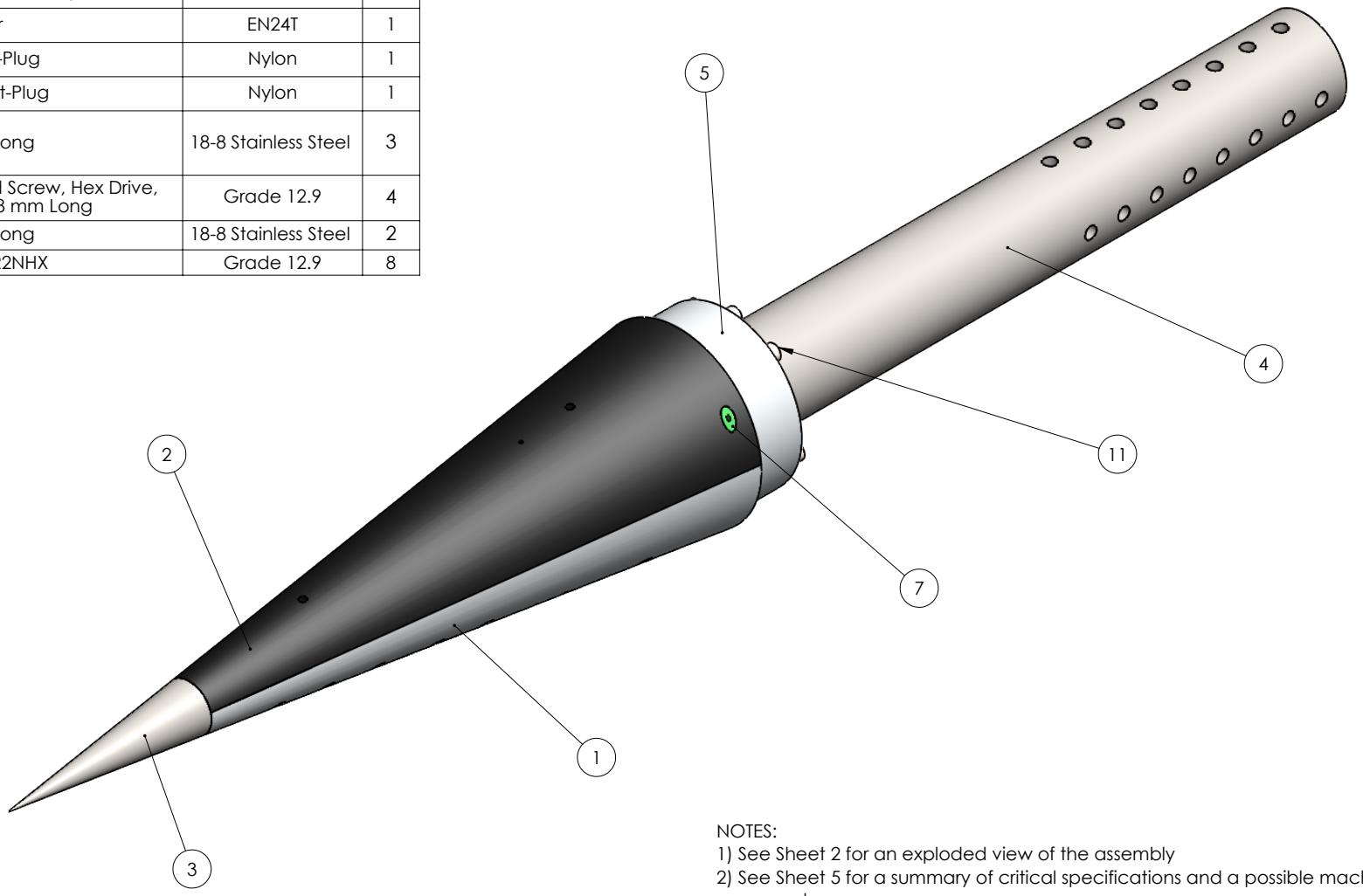
Figure E.5: SPOD analysis for shot 1937 at 500kfps

F

T6 and HDT Cone Model CAD

ITEM NO.	DESCRIPTION	MATERIAL	QTY.
1	BLC7-000-7-Degree-Cone-01-Main-Body	Al 6068-T6 or Equivalent	1
2	BLC7-000-7-Degree-Cone-02-PEEK-Lid	PEEK	1
3	BLC7-000-7-Degree-Cone-03A-Nose-Tip	EN36B	3
4	BLC7-000-7-Degree-Cone-04-Modified-Sting	EN24T	1
5	BLC7-000-7-Degree-Cone-05-Collar	EN24T	1
6	BLC7-000-7-Degree-Cone-06A-Left-Plug	Nylon	1
7	BLC7-000-7-Degree-Cone-06B-Right-Plug	Nylon	1
8	Dowel Pin, 2 mm Diameter, 5 mm Long	18-8 Stainless Steel	3
9	Alloy Steel Low-Profile Socket Head Screw, Hex Drive, Black Oxide, M3 x 0.5 mm Thread, 8 mm Long	Grade 12.9	4
10	Dowel Pin, 5 mm Diameter, 8 mm Long	18-8 Stainless Steel	2
11	B18.3.1M - 5 x 0.8 x 40 Hex SHCS -- 22NHX	Grade 12.9	8

REV.	MODIFICATION	BY	DATE
0	NEW	JS	25/06/2020
1	TOLERANCES UPDATED	SS	12/08/2020



NOTES:
1) See Sheet 2 for an exploded view of the assembly
2) See Sheet 5 for a summary of critical specifications and a possible machining procedure

This is a CAD produced drawing - no manual modifications are to be made.
This drawing is the property of the University of Oxford. It must not be copied, or the contents thereof or any information received in conjunction therewith be imparted to any third party. It must not be used for any other contract and the receipt of this drawing implies that these conditions as stated are accepted.

TOLERANCES UNLESS OTHERWISE STATED			
—	≤ 100 mm	= ± 0.1 mm	
> 100 mm	≤ 1000 mm	= ± 0.2 mm	
> 1000 mm	—	= ± 0.5 mm	
	Angular	= ± 1.0 °	

DESIGNED BY	JS	SCALE	1:2
DRAWN BY	SS	DATE	12/08/20
APPROVED BY	SW	DATE	17/08/20

MATERIAL: As specified in BOM table

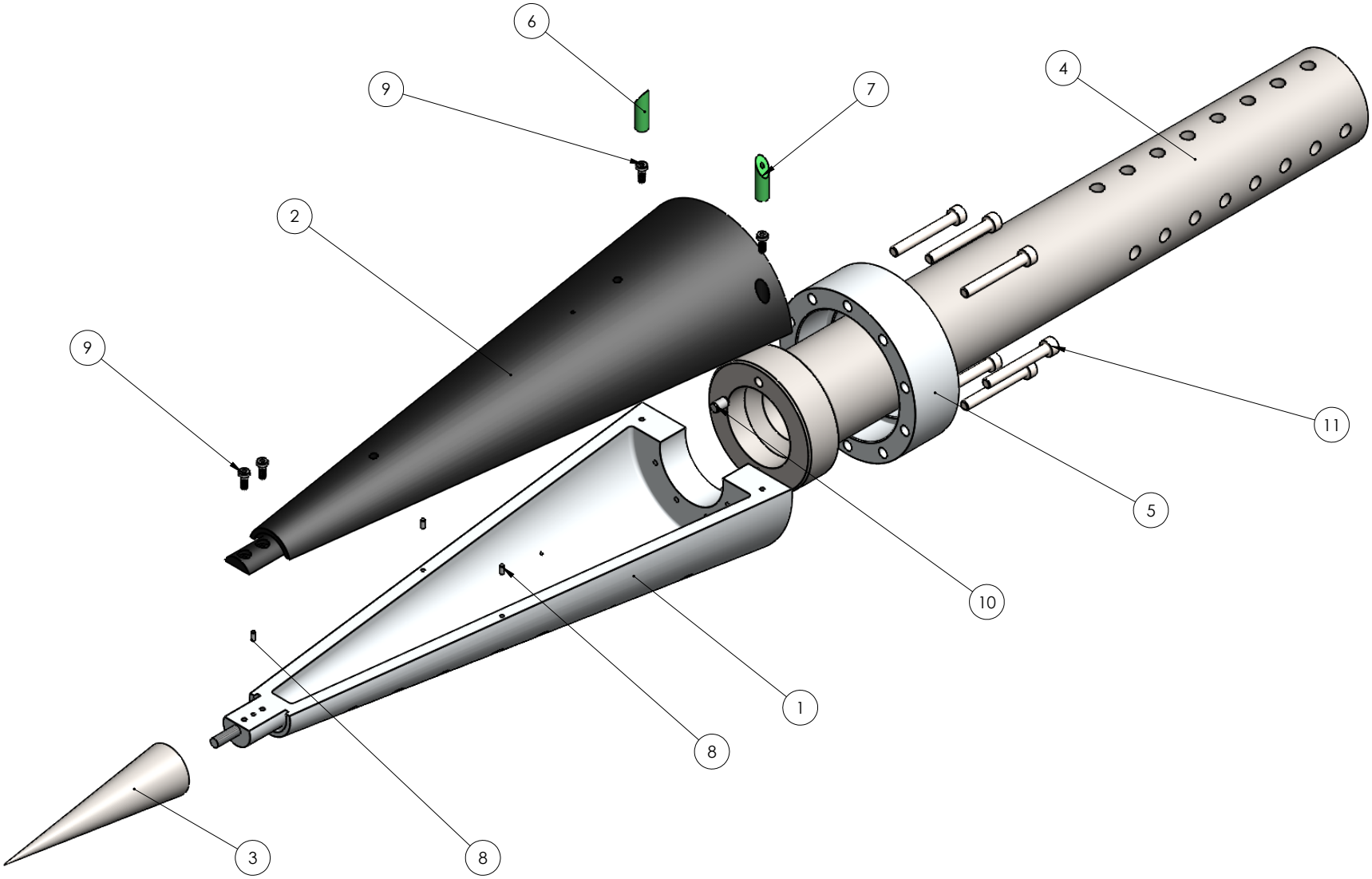
DO NOT SCALE - IF IN DOUBT ASK
DIMENSIONS IN mm
REMOVE ALL BURRS AND SHARP EDGES

Oxford Hypersonics
Oxford Thermofluids Insititute
Southwell Building
Osney Mead
Oxford OX2 0ES
Tel: 01865 288723

DESCRIPTION: 7-Degree-Cone-Assembly

PART NUMBER	SHEET	ISSUE	
BLC7-000-00	1/5	1.2	A3

REV.	MODIFICATION	BY	DATE
0	NEW	JS	25/06/2020
1	TOLERANCES UPDATED	SS	12/08/2020



This is a CAD produced drawing - no manual modifications are to be made.
This drawing is the property of the University of Oxford. It must not be copied, or the contents thereof or any information received in conjunction therewith be imparted to any third party. It must not be used for any other contract and the receipt of this drawing implies that these conditions as stated are accepted.

TOLERANCES UNLESS OTHERWISE STATED			
—	≤ 100 mm	= ± 0.1 mm	
> 100 mm	≤ 1000 mm	= ± 0.2 mm	
> 1000 mm	—	= ± 0.5 mm	
	Angular	= ± 1.0 °	

DESIGNED BY	JS	SCALE	1:2
DRAWN BY	SS	DATE	12/08/20
APPROVED BY	SW	DATE	17/08/20

MATERIAL
As specified in BOM table

DO NOT SCALE - IF IN DOUBT ASK
DIMENSIONS IN mm
REMOVE ALL BURRS AND SHARP EDGES

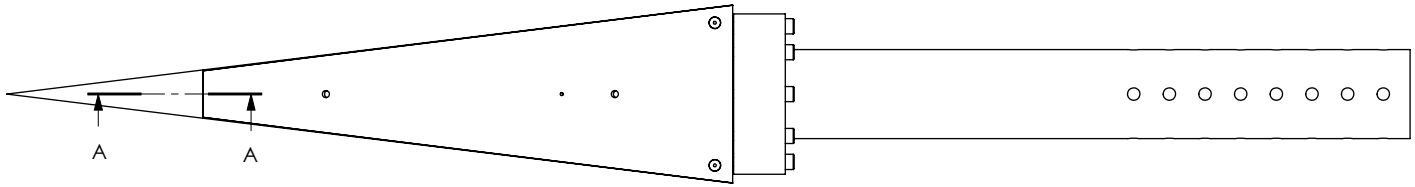
Oxford Hypersonics
Oxford Thermofluids Insititute
Southwell Building
Osney Mead
Oxford OX2 0ES
Tel: 01865 288723

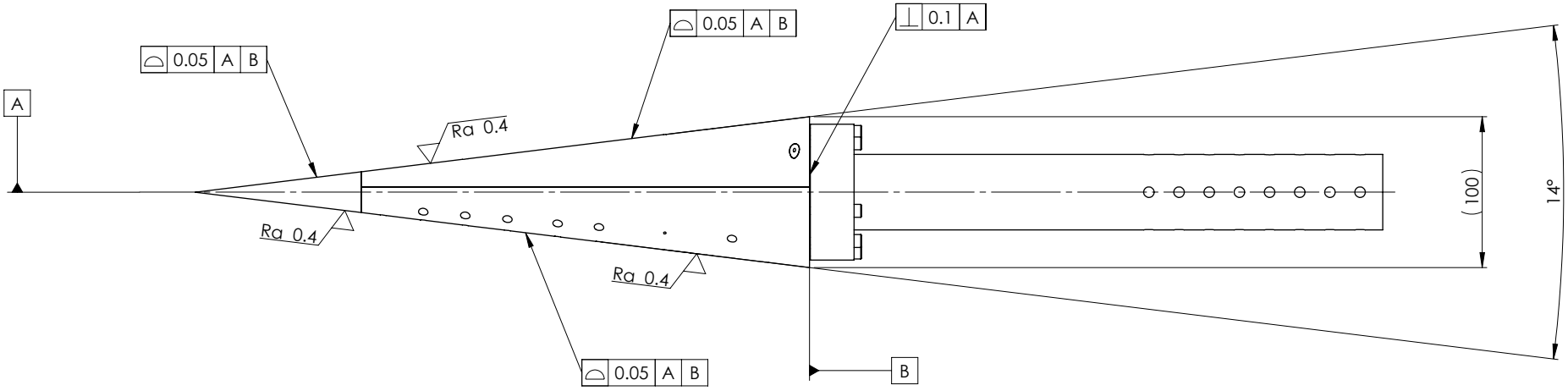
DESCRIPTION
7-Degree-Cone-Assembly

PART NUMBER	SHEET	ISSUE	
BLC7-000-00	2/5	1.2	A3

REV.	MODIFICATION	BY	DATE
0	NEW	JS	25/06/2020
1	TOLERANCES UPDATED	SS	12/08/2020

NOTES:
1) See Sheet 4 for Section A-A





This is a CAD produced drawing - no manual modifications are to be made.
This drawing is the property of the University of Oxford. It must not be copied, or the contents thereof or any information received in conjunction therewith be imparted to any third party. It must not be used for any other contract and the receipt of this drawing implies that these conditions as stated are accepted.

TOLERANCES UNLESS OTHERWISE STATED			
—	≤ 100 mm	= ± 0.1 mm	
> 100 mm	≤ 1000 mm	= ± 0.2 mm	
> 1000 mm	—	= ± 0.5 mm	
	Angular	= ± 1.0 °	

DESIGNED BY	JS	SCALE	1:2
DRAWN BY	SS	DATE	12/08/20
APPROVED BY	SW	DATE	17/08/20

MATERIAL: As specified in BOM table

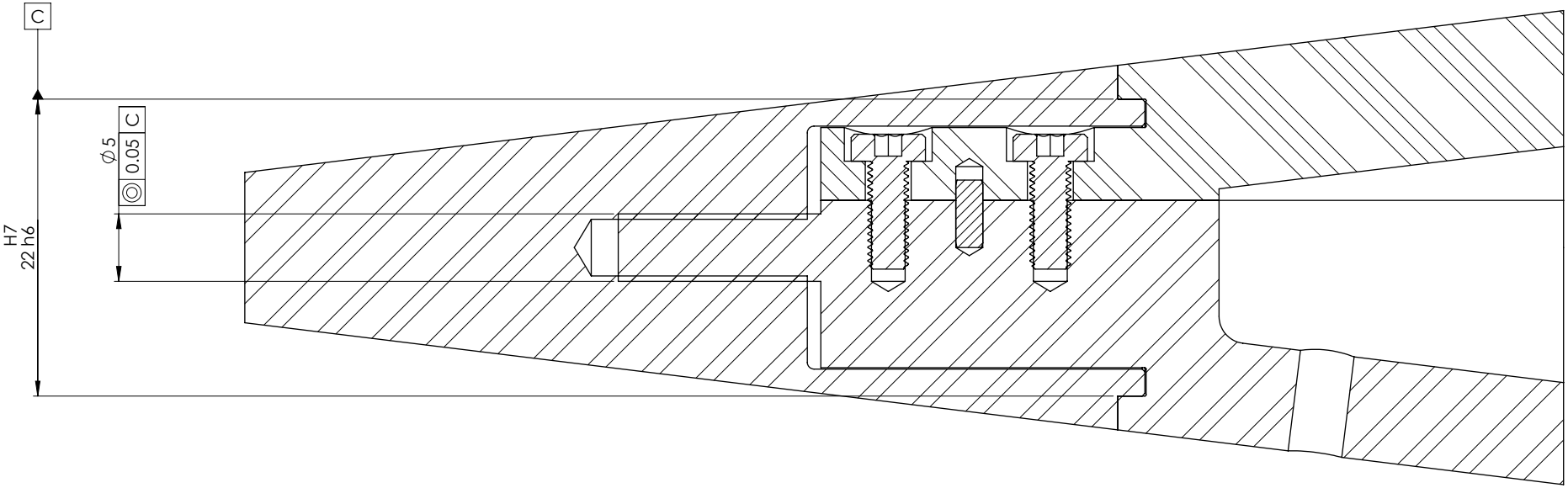
DO NOT SCALE - IF IN DOUBT ASK
DIMENSIONS IN mm
REMOVE ALL BURRS AND SHARP EDGES

Oxford Hypersonics
Oxford Thermofluids Insititute
Southwell Building
Osney Mead
Oxford OX2 0ES
Tel: 01865 288723

DESCRIPTION: 7-Degree-Cone-Assembly

PART NUMBER	SHEET	ISSUE	
BLC7-000-00	3/5	1.2	A3

REV.	MODIFICATION	BY	DATE
0	NEW	JS	25/06/2020
1	TOLERANCES UPDATED	SS	12/08/2020



SECTION A-A
SCALE 3 : 1

This is a CAD produced drawing - no manual modifications are to be made.
This drawing is the property of the University of Oxford. It must not be copied, or the contents thereof or any information received in conjunction therewith be imparted to any third party. It must not be used for any other contract and the receipt of this drawing implies that these conditions as stated are accepted.

TOLERANCES UNLESS OTHERWISE STATED			
—	≤ 100 mm	= ± 0.1 mm	
> 100 mm	≤ 1000 mm	= ± 0.2 mm	
> 1000 mm	—	= ± 0.5 mm	
	Angular	= ± 1.0 °	

DESIGNED BY	JS	SCALE	1:2
DRAWN BY	SS	DATE	12/08/20
APPROVED BY	SW	DATE	17/08/20

MATERIAL
As specified in BOM table

DO NOT SCALE - IF IN DOUBT ASK
DIMENSIONS IN mm
REMOVE ALL BURRS AND SHARP EDGES

Oxford Hypersonics
Oxford Thermofluids Insititute
Southwell Building
Osney Mead
Oxford OX2 0ES
Tel: 01865 288723

DESCRIPTION
7-Degree-Cone-Assembly

PART NUMBER	SHEET	ISSUE	
BLC7-000-00	4/5	1.2	A3

REV.	MODIFICATION	BY	DATE
0	NEW	JS	25/06/2020
1	TOLERANCES UPDATED	SS	12/08/2020

Preamble:

The machining procedure detailed below need not be strictly adhered to as long as the following critical aspects (specified in drawings) of the design can be achieved:

1. Assembly outer surface finish and achieving < 0.04 mm joint step/gap including repeatability when removing and reinstalling 'T6-Cone-PEEK-Lid', 'T6-Cone-Nose-Tip-A', and 'T6-Cone-Nose-Tip-B'
2. An external surface of $\sqrt{}$ Ra 0.4 must be achieved on the following components:
   - T6-Cone-Nose-Tip-A
   - T6-Cone-Nose-Tip-B
   - T6-Cone-PEEK-Lid
   - T6-Cone-Main-Body
3. Assembly outer surface angularity tolerance
4. Instrumentation hole locational tolerance

Possible Machining Procedure:

1. Machine components 'T6-Cone-PEEK-Lid', 'T6-Cone-Main-Body', and 'T6-Cone-Nose-Tip' separately on a lathe. Do not machine the H7 locating groove at this stage
2. Cut components 'T6-Cone-PEEK-Lid' and 'T6-Cone-Main-Body' at 5 mm from the lathe axis as specified in drawings
3. Mill the internal surface profile on components 'T6-Cone-PEEK-Lid' and 'T6-Cone-Main-Body' as specified in drawings
4. Bolt and dowel components 'T6-Cone-PEEK-Lid' and 'T6-Cone-Main-Body' together. Machine the H7 locating groove
5. Attach component 'T6-Cone-Nose-Tip' and machine the assembly to the final outer surface angularity, profile, and smoothness tolerances
6. Remaining components are machined separately

This is a CAD produced drawing - no manual modifications are to be made.
This drawing is the property of the University of Oxford. It must not be copied, or the contents thereof or any information received in conjunction therewith be imparted to any third party. It must not be used for any other contract and the receipt of this drawing implies that these conditions as stated are accepted.

TOLERANCES UNLESS OTHERWISE STATED			
—	≤ 100 mm	= ± 0.1 mm	
> 100 mm	≤ 1000 mm	= ± 0.2 mm	
> 1000 mm	—	= ± 0.5 mm	
	Angular	= ± 1.0 °	

DESIGNED BY	JS	SCALE	1:2
DRAWN BY	SS	DATE	12/08/20
APPROVED BY	SW	DATE	17/08/20

MATERIAL: As specified in BOM table

DO NOT SCALE - IF IN DOUBT ASK
DIMENSIONS IN mm
REMOVE ALL BURRS AND SHARP EDGES

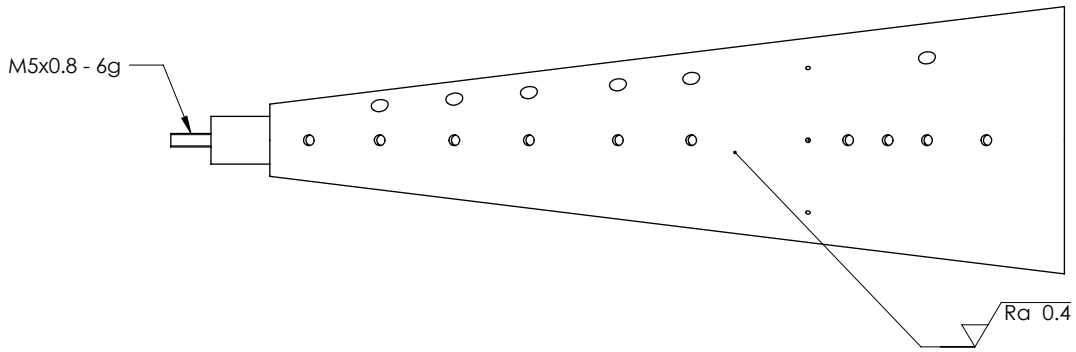
Oxford Hypersonics
Oxford Thermofluids Insititute
Southwell Building
Osney Mead
Oxford OX2 0ES
Tel: 01865 288723

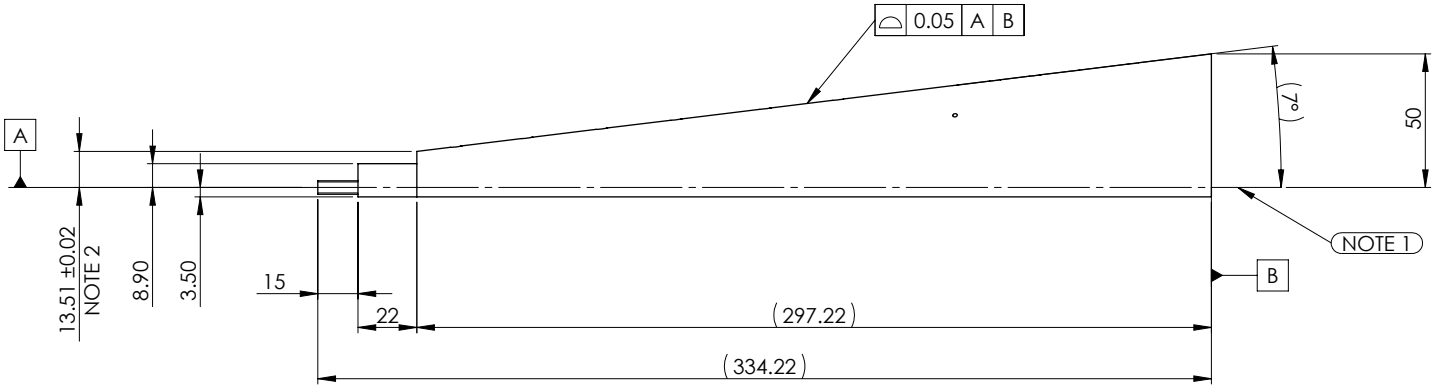
DESCRIPTION: 7-Degree-Cone-Assembly

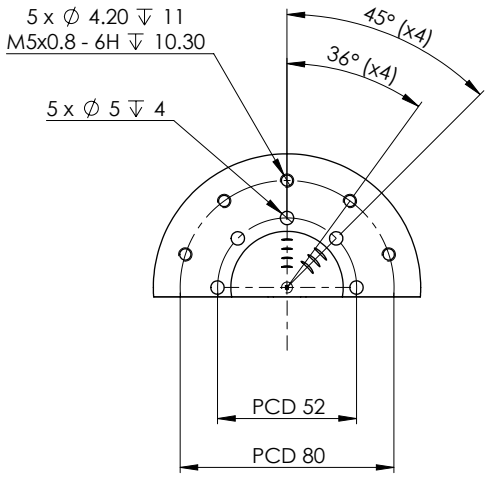
PART NUMBER	SHEET	ISSUE	
BLC7-000-00	5/5	1.2	A3

REV.	MODIFICATION	BY	DATE
0	NEW	JS	25/06/2020
1	DRAWING TOLERANCES AND MATERIAL UPDATED	SS	12/08/2020

NOTES:
1) Lathe axis of rotation
2) Final machining on assembly with 'T6-Cone-PEEK-Lid', 'T6-Cone-Nose-Tip-A', and 'T6-Cone-Nose-Tip-B' to achieve < 0.04 mm joint step/gap







This is a CAD produced drawing - no manual modifications are to be made.
This drawing is the property of the University of Oxford. It must not be copied, or the contents thereof or any information received in conjunction therewith be imparted to any third party. It must not be used for any other contract and the receipt of this drawing implies that these conditions as stated are accepted.

TOLERANCES UNLESS OTHERWISE STATED			
—	≤ 100 mm	= ± 0.1 mm	
> 100 mm	≤ 1000 mm	= ± 0.2 mm	
> 1000 mm	—	= ± 0.5 mm	
	Angular	= ± 1.0 °	

DESIGNED BY	JS	SCALE	1:2
DRAWN BY	SS	DATE	12/08/20
APPROVED BY	SW	DATE	17/08/20

MATERIAL: Al 6068-T6 or Equivalent

DO NOT SCALE - IF IN DOUBT ASK
DIMENSIONS IN mm
REMOVE ALL BURRS AND SHARP EDGES

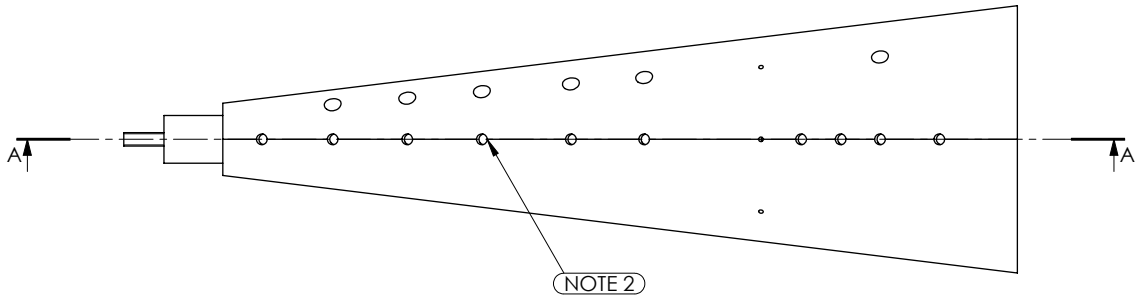
Oxford Hypersonics
Oxford Thermofluids Insititute
Southwell Building
Osney Mead
Oxford OX2 0ES
Tel: 01865 288723

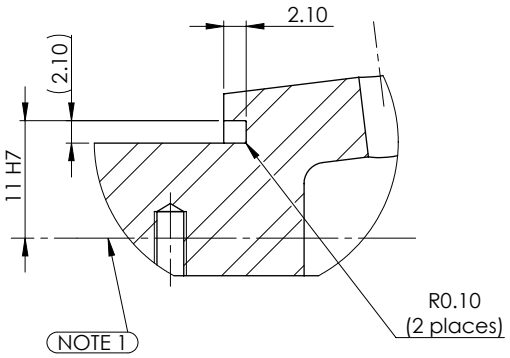
DESCRIPTION: 7-Degree-Cone-Main-Body

PART NUMBER	SHEET	ISSUE	
BLC7-000-01	1/7	1.2	A3

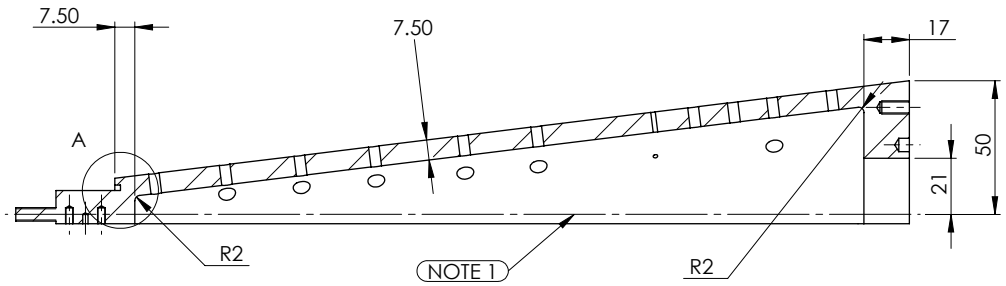
REV.	MODIFICATION	BY	DATE
0	NEW	JS	25/06/2020
1	DRAWING TOLERANCES AND MATERIAL UPDATED	SS	12/08/2020

NOTES:
1) Lathe axis of rotation
2) See Sheet 4 for '0 degree ray' hole dimensions





DETAIL A
SCALE 2 : 1



This is a CAD produced drawing - no manual modifications are to be made.
This drawing is the property of the University of Oxford. It must not be copied, or the contents thereof or any information received in conjunction therewith be imparted to any third party. It must not be used for any other contract and the receipt of this drawing implies that these conditions as stated are accepted.

TOLERANCES UNLESS OTHERWISE STATED			
—	≤ 100 mm	= ± 0.1 mm	
> 100 mm	≤ 1000 mm	= ± 0.2 mm	
> 1000 mm	—	= ± 0.5 mm	
	Angular	= ± 1.0 °	

DESIGNED BY	JS	SCALE	1:2
DRAWN BY	SS	DATE	12/08/20
APPROVED BY	SW	DATE	17/08/20

MATERIAL
Al 6068-T6 or Equivalent

DO NOT SCALE - IF IN DOUBT ASK
DIMENSIONS IN mm
REMOVE ALL BURRS AND SHARP EDGES

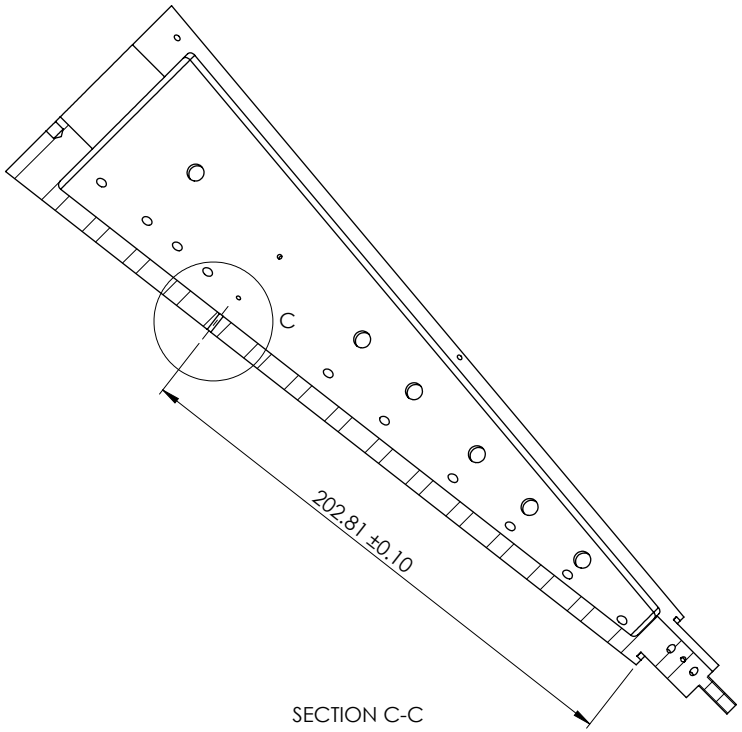
Oxford Hypersonics
Oxford Thermofluids Insititute
Southwell Building
Osney Mead
Oxford OX2 0ES
Tel: 01865 288723

DESCRIPTION
7-Degree-Cone-Main-Body

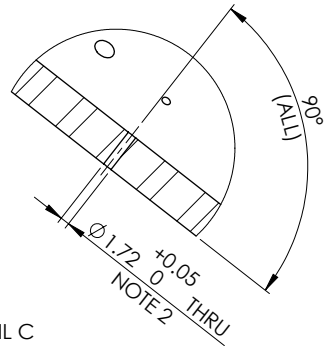
PART NUMBER	SHEET	ISSUE	
BLC7-000-01	2/7	1.2	A3

NOTES:
1) This sheet concerns holes on the '315 degree ray'
2) All holes are normal to the exterior surface

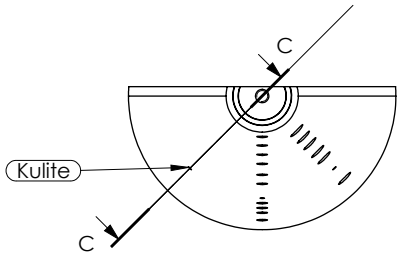
REV.	MODIFICATION	BY	DATE
0	NEW	JS	25/06/2020
1	DRAWING TOLERANCES AND MATERIAL UPDATED	SS	12/08/2020



SECTION C-C



DETAIL C
SCALE 1 : 1



This is a CAD produced drawing - no manual modifications are to be made.
This drawing is the property of the University of Oxford. It must not be copied, or the contents thereof or any information received in conjunction therewith be imparted to any third party. It must not be used for any other contract and the receipt of this drawing implies that these conditions as stated are accepted.

TOLERANCES UNLESS OTHERWISE STATED			
—	≤ 100 mm	= ± 0.1 mm	
> 100 mm	≤ 1000 mm	= ± 0.2 mm	
> 1000 mm	—	= ± 0.5 mm	
	Angular	= ± 1.0 °	

DESIGNED BY	JS	SCALE	1:2
DRAWN BY	SS	DATE	12/08/20
APPROVED BY	SW	DATE	17/08/20

MATERIAL: Al 6068-T6 or Equivalent

DO NOT SCALE - IF IN DOUBT ASK
DIMENSIONS IN mm
REMOVE ALL BURRS AND SHARP EDGES

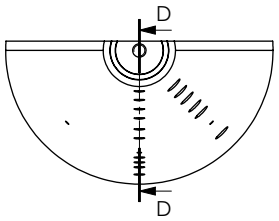
UNIVERSITY OF OXFORD
Oxford Hypersonics
Oxford Thermofluids Insititute
Southwell Building
Osney Mead
Oxford OX2 0ES
Tel: 01865 288723

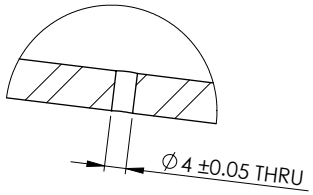
DESCRIPTION: 7-Degree-Cone-Main-Body

PART NUMBER	SHEET	ISSUE	
BLC7-000-01	3/7	1.2	A3

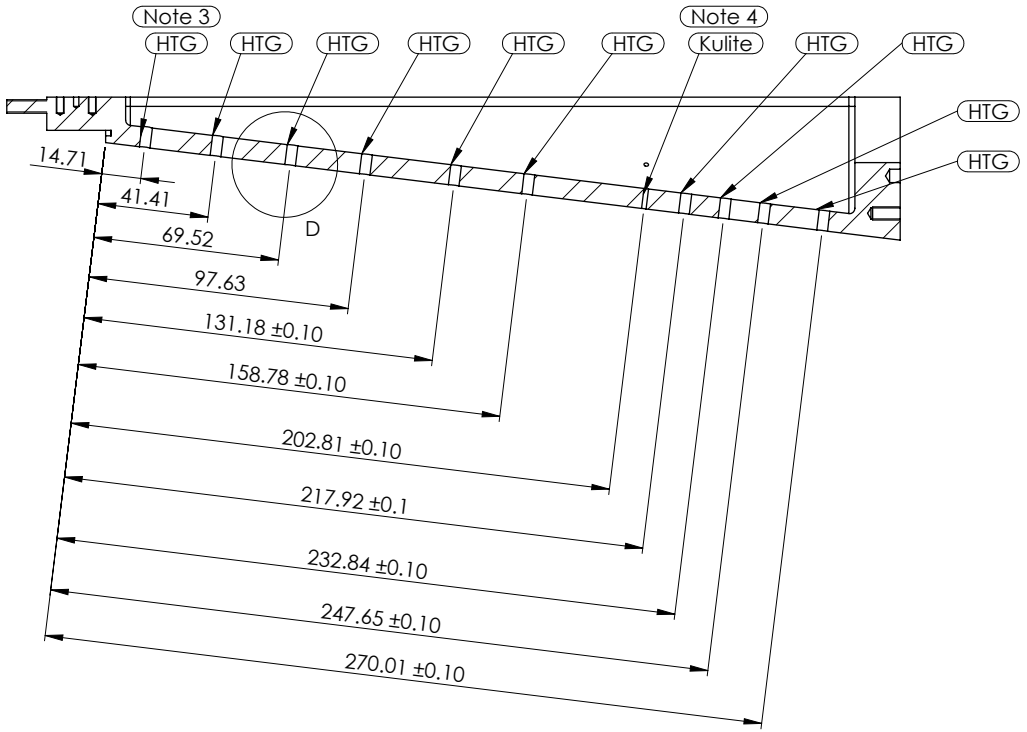
NOTES:
1) This sheet concerns holes on the '0 degree ray'
2) All holes are normal to the exterior surface
3) 'HTG' holes as specified in Detail D
4) 'Kulite' holes as specified in Detail C on Sheet 3

REV.	MODIFICATION	BY	DATE
0	NEW	JS	25/06/2020
1	DRAWING TOLERANCES AND MATERIAL UPDATED	SS	12/08/2020





DETAIL D
SCALE 1:1



SECTION D-D
SCALE 1 : 2

This is a CAD produced drawing - no manual modifications are to be made.
This drawing is the property of the University of Oxford. It must not be copied, or the contents thereof or any information received in conjunction therewith be imparted to any third party. It must not be used for any other contract and the receipt of this drawing implies that these conditions as stated are accepted.

TOLERANCES UNLESS OTHERWISE STATED
— ≤ 100 mm = ± 0.1 mm
> 100 mm ≤ 1000 mm = ± 0.2 mm
> 1000 mm — = ± 0.5 mm
Angular = ± 1.0 °

DESIGNED BY	JS	SCALE	1:2
DRAWN BY	SS	DATE	12/08/20
APPROVED BY	SW	DATE	17/08/20

MATERIAL
Al 6068-T6 or Equivalent

DO NOT SCALE - IF IN DOUBT ASK
DIMENSIONS IN mm
REMOVE ALL BURRS AND SHARP EDGES

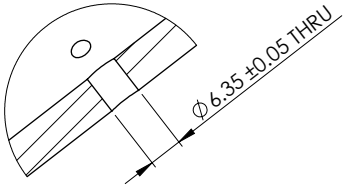
Oxford Hypersonics
Oxford Thermofluids Insititute
Southwell Building
Osney Mead
Oxford OX2 0ES
Tel: 01865 288723

DESCRIPTION
7-Degree-Cone-Main-Body

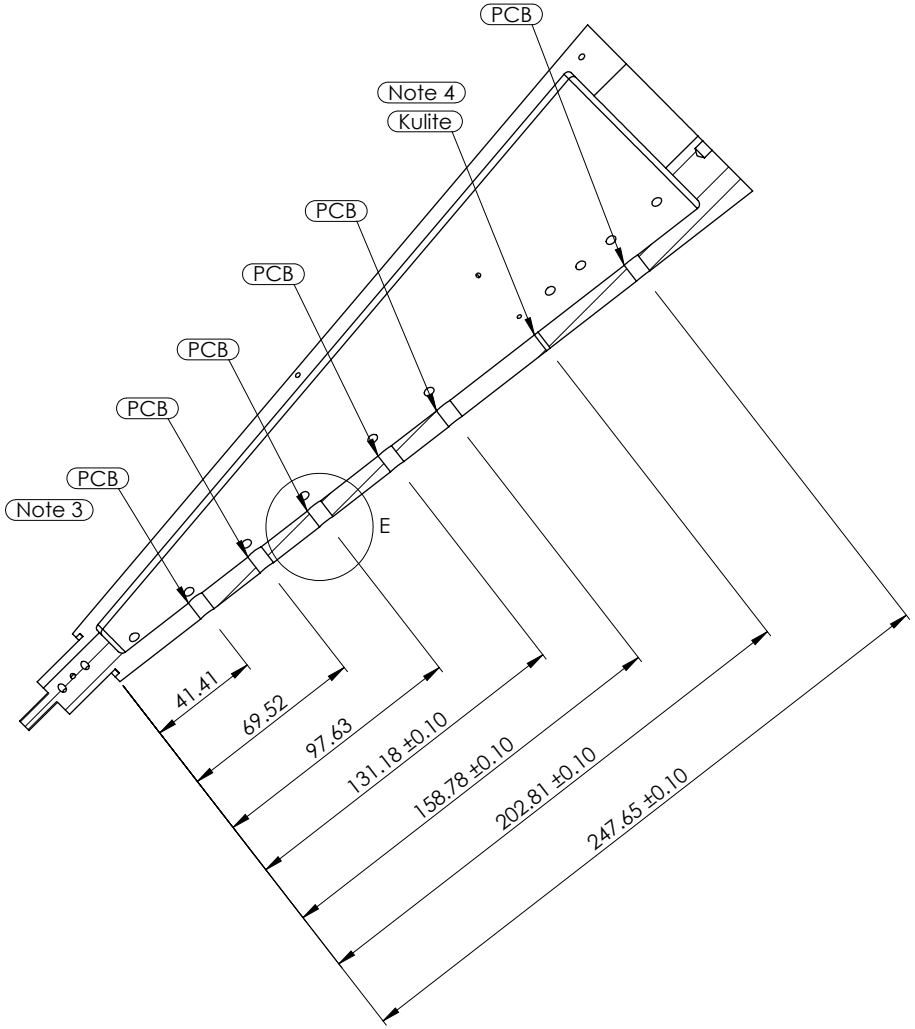
PART NUMBER	SHEET	ISSUE	
BLC7-000-01	4/7	1.2	A3

NOTES:
1) This sheet concerns holes on the '45 degree ray'
2) All holes are normal to the exterior surface
3) 'PCB' holes as specified in Detail E
4) 'Kulite' holes as specified in Detail C on Sheet 3

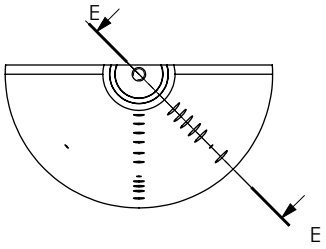
REV.	MODIFICATION	BY	DATE
0	NEW	JS	25/06/2020
1	DRAWING TOLERANCES AND MATERIAL UPDATED	SS	12/08/2020



DETAIL E
SCALE 1 : 1



SECTION E-E



This is a CAD produced drawing - no manual modifications are to be made.
This drawing is the property of the University of Oxford. It must not be copied, or the contents thereof or any information received in conjunction therewith be imparted to any third party. It must not be used for any other contract and the receipt of this drawing implies that these conditions as stated are accepted.

TOLERANCES UNLESS OTHERWISE STATED
— ≤ 100 mm = ± 0.1 mm
> 100 mm ≤ 1000 mm = ± 0.2 mm
> 1000 mm — = ± 0.5 mm
Angular = ± 1.0 °

DESIGNED BY	JS	SCALE	1:2
DRAWN BY	SS	DATE	12/08/20
APPROVED BY	SW	DATE	17/08/20

MATERIAL
Al 6068-T6 or Equivalent

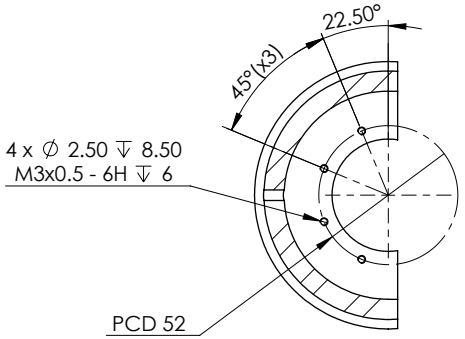
DO NOT SCALE - IF IN DOUBT ASK
DIMENSIONS IN mm
REMOVE ALL BURRS AND SHARP EDGES

UNIVERSITY OF OXFORD
Oxford Hypersonics
Oxford Thermofluids Insititute
Southwell Building
Osney Mead
Oxford OX2 0ES
Tel: 01865 288723

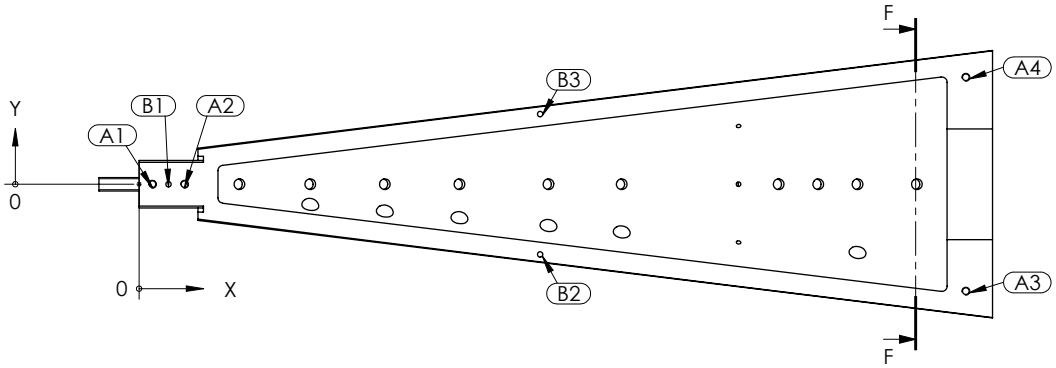
DESCRIPTION
7-Degree-Cone-Main-Body

PART NUMBER	SHEET	ISSUE	
BLC7-000-01	5/7	1.2	A3

REV.	MODIFICATION	BY	DATE
0	NEW	JS	25/06/2020
1	DRAWING TOLERANCES AND MATERIAL UPDATED	SS	12/08/2020



SECTION F-F



TAG	X LOC	Y LOC	SIZE
A1	5	0	∅ 2.50 ↧ 6 M3x0.5 - 6H ↧ 6
A2	17	0	
A3	309.22	-40	
A4	309.22	40	
B1	11	0	∅ 2 ↧ 3.50
B2	150	-26.25	
B3	150	26.25	

This is a CAD produced drawing - no manual modifications are to be made.
This drawing is the property of the University of Oxford. It must not be copied, or the contents thereof or any information received in conjunction therewith be imparted to any third party. It must not be used for any other contract and the receipt of this drawing implies that these conditions as stated are accepted.

TOLERANCES UNLESS OTHERWISE STATED
— ≤ 100 mm = ± 0.1 mm
> 100 mm ≤ 1000 mm = ± 0.2 mm
> 1000 mm — = ± 0.5 mm
Angular = ± 1.0 °

DESIGNED BY	JS	SCALE	1:2
DRAWN BY	SS	DATE	12/08/20
APPROVED BY	SW	DATE	17/08/20

MATERIAL
Al 6068-T6 or Equivalent

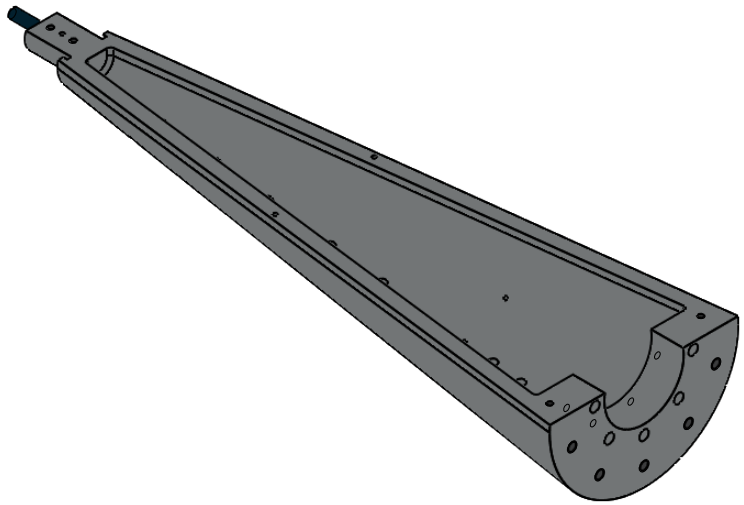
DO NOT SCALE - IF IN DOUBT ASK
DIMENSIONS IN mm
REMOVE ALL BURRS AND SHARP EDGES

Oxford Hypersonics
Oxford Thermofluids Insititute
Southwell Building
Osney Mead
Oxford OX2 0ES
Tel: 01865 288723

DESCRIPTION
7-Degree-Cone-Main-Body

PART NUMBER	SHEET	ISSUE	
BLC7-000-01	6/7	1.2	A3

REV.	MODIFICATION	BY	DATE
0	NEW	JS	25/06/2020
1	DRAWING TOLERANCES AND MATERIAL UPDATED	SS	12/08/2020



ISOMETRIC VIEW

This is a CAD produced drawing - no manual modifications are to be made.
This drawing is the property of the University of Oxford. It must not be copied, or the contents thereof or any information received in conjunction therewith be imparted to any third party. It must not be used for any other contract and the receipt of this drawing implies that these conditions as stated are accepted.

TOLERANCES UNLESS OTHERWISE STATED
— ≤ 100 mm = ± 0.1 mm
> 100 mm ≤ 1000 mm = ± 0.2 mm
> 1000 mm — = ± 0.5 mm
Angular = ± 1.0 °

DESIGNED BY	JS	SCALE	1:2
DRAWN BY	SS	DATE	12/08/20
APPROVED BY	SW	DATE	17/08/20

MATERIAL
Al 6068-T6 or Equivalent

DO NOT SCALE - IF IN DOUBT ASK
DIMENSIONS IN mm
REMOVE ALL BURRS AND SHARP EDGES

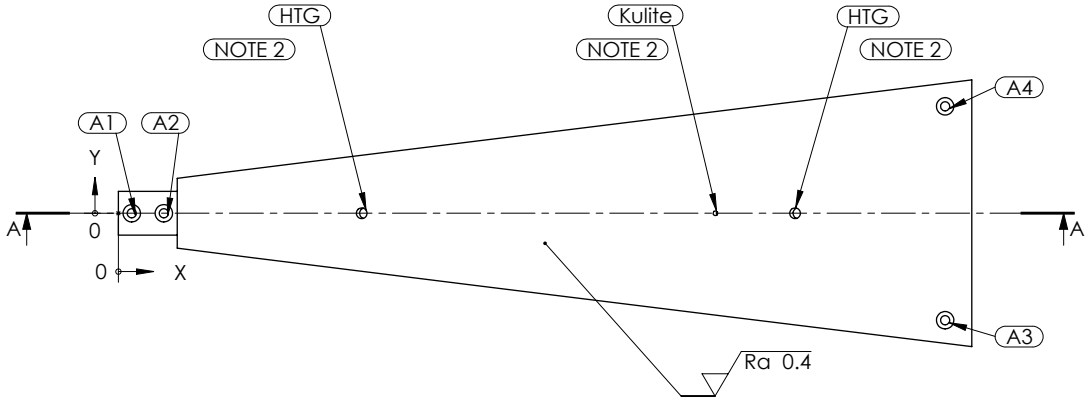
Oxford Hypersonics
Oxford Thermofluids Insititute
Southwell Building
Osney Mead
Oxford OX2 0ES
Tel: 01865 288723

DESCRIPTION
7-Degree-Cone-Main-Body

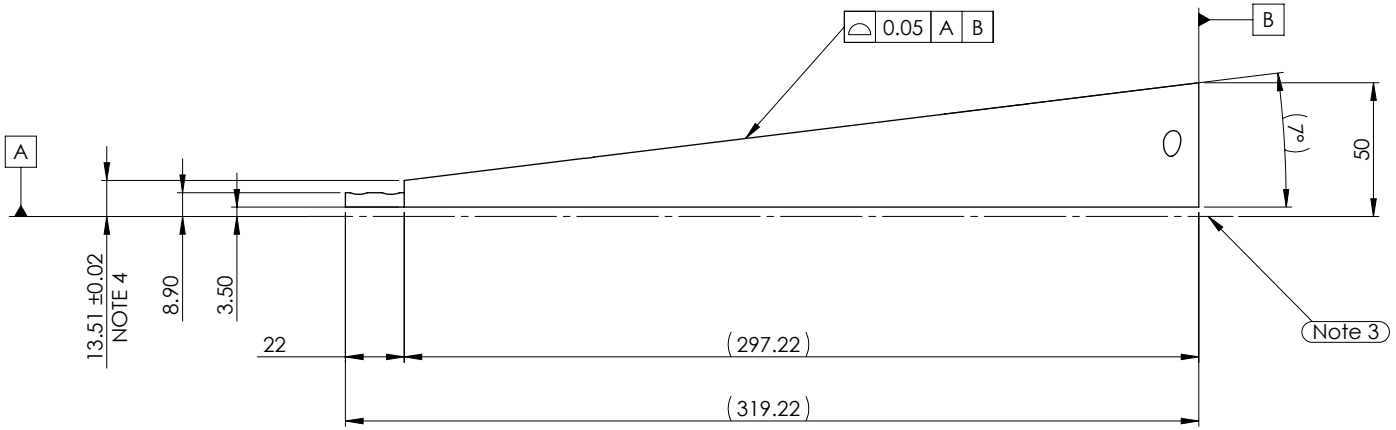
PART NUMBER	SHEET	ISSUE	
BLC7-000-01	7/7	1.2	A3

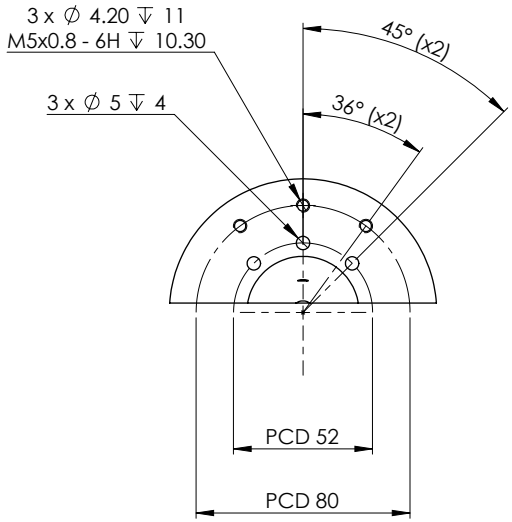
NOTES:
1) See Sheet 2 for Section A-A
2) Refer to Sheet 3 for details of 'HTG' and 'Kulite' thru holes
3) Lathe axis of rotation
4) Final machining on assembly with 'T6-Cone-Main-Body', 'T6-Cone-Nose-Tip-A', and 'T6-Cone-Nose-Tip-B' to achieve < 0.04 mm joint step/gap

REV.	MODIFICATION	BY	DATE
0	NEW	JS	25/06/2020
1	DRAWING TOLERANCES UPDATED	SS	12/08/2020



TAG	X LOC	Y LOC	SIZE
A1	5	0	⌀ 3.40 THRU ALL ⌴ ⌀ 6.50 ↧ 3
A2	17	0	
A3	309.22	-40	
A4	309.22	40	





This is a CAD produced drawing - no manual modifications are to be made.
This drawing is the property of the University of Oxford. It must not be copied, or the contents thereof or any information received in conjunction therewith be imparted to any third party. It must not be used for any other contract and the receipt of this drawing implies that these conditions as stated are accepted.

TOLERANCES UNLESS OTHERWISE STATED
— ≤ 100 mm = ± 0.1 mm
> 100 mm ≤ 1000 mm = ± 0.2 mm
> 1000 mm — = ± 0.5 mm
Angular = ± 1.0 °

DESIGNED BY	JS	SCALE	1:2
DRAWN BY	SS	DATE	12/08/20
APPROVED BY	SW	DATE	17/08/20

MATERIAL: PEEK

DO NOT SCALE - IF IN DOUBT ASK
DIMENSIONS IN mm
REMOVE ALL BURRS AND SHARP EDGES

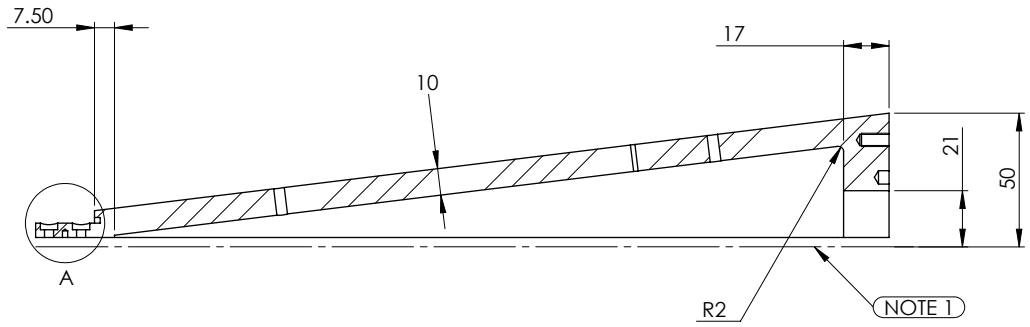
UNIVERSITY OF OXFORD
Oxford Hypersonics
Oxford Thermofluids Insititute
Southwell Building
Osney Mead
Oxford OX2 0ES
Tel: 01865 288723

DESCRIPTION: 7-Degree-Cone-PEEK-Lid

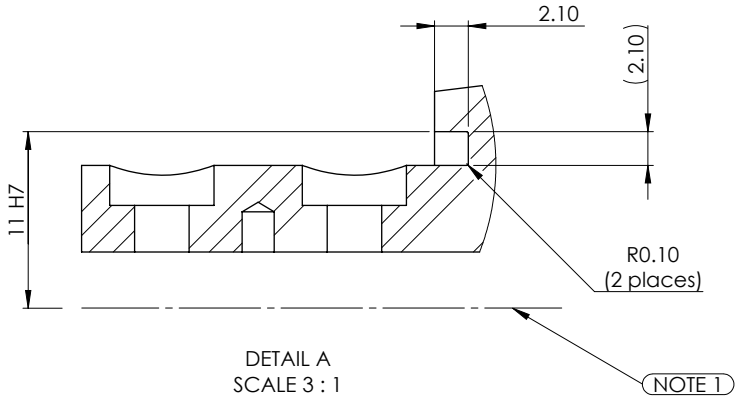
PART NUMBER	SHEET	ISSUE	
BLC7-000-02	1/4	1.2	A3

NOTES:
1) Lathe axis of rotation

REV.	MODIFICATION	BY	DATE
0	NEW	JS	25/06/2020
1	DRAWING TOLERANCES UPDATED	SS	12/08/2020



SECTION A-A



DETAIL A
SCALE 3 : 1

This is a CAD produced drawing - no manual modifications are to be made.
This drawing is the property of the University of Oxford. It must not be copied, or the contents thereof or any information received in conjunction therewith be imparted to any third party. It must not be used for any other contract and the receipt of this drawing implies that these conditions as stated are accepted.

TOLERANCES UNLESS OTHERWISE STATED			
—	≤ 100 mm	= ± 0.1 mm	
> 100 mm	≤ 1000 mm	= ± 0.2 mm	
> 1000 mm	—	= ± 0.5 mm	
	Angular	= ± 1.0 °	

DESIGNED BY	JS	SCALE	1:2
DRAWN BY	SS	DATE	12/08/20
APPROVED BY	SW	DATE	17/08/20

MATERIAL: PEEK

DO NOT SCALE - IF IN DOUBT ASK
DIMENSIONS IN mm
REMOVE ALL BURRS AND SHARP EDGES

Oxford Hypersonics
Oxford Thermofluids Insititute
Southwell Building
Osney Mead
Oxford OX2 0ES
Tel: 01865 288723

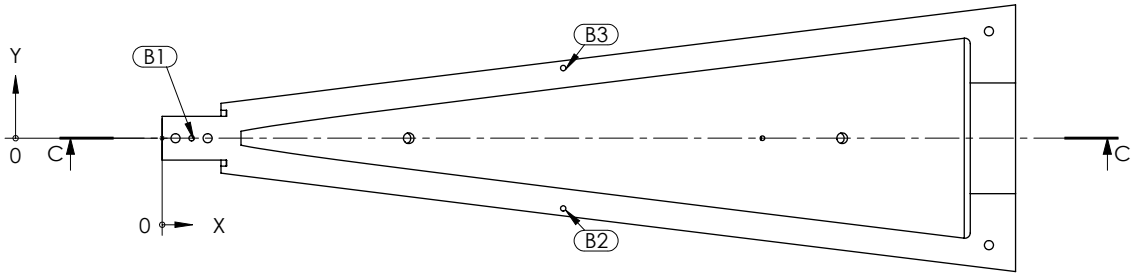
DESCRIPTION: 7-Degree-Cone-PEEK-Lid

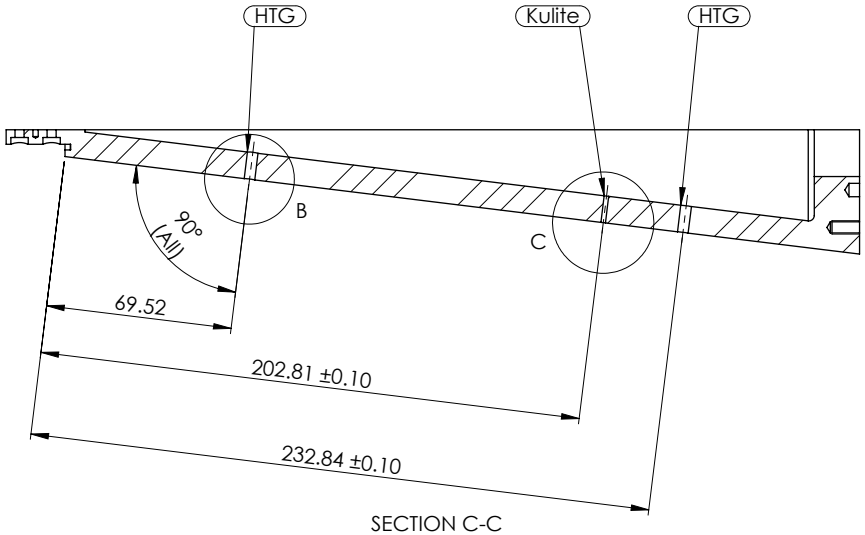
PART NUMBER	SHEET	ISSUE	
BLC7-000-02	2/4	1.2	A3

NOTES:
1) Both 'HTG' and 'Kulite' holes are normal to the exterior surface
2) 'HTG' holes as specified in Detail B
3) 'Kulite' holes as specified in Detail C

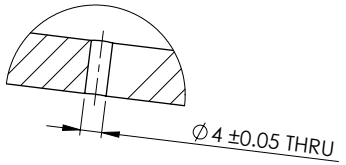
REV.	MODIFICATION	BY	DATE
0	NEW	JS	25/06/2020
1	DRAWING TOLERANCES UPDATED	SS	12/08/2020

TAG	X LOC	Y LOC	SIZE
B1	11	0	⌀ 2 ↧ 2.50
B2	150	-26.25	
B3	150	26.25	

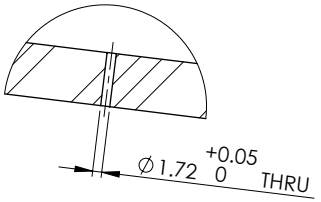




SECTION C-C



DETAIL B
SCALE 1 : 1



DETAIL C
SCALE 1 : 1

This is a CAD produced drawing - no manual modifications are to be made.
This drawing is the property of the University of Oxford. It must not be copied, or the contents thereof or any information received in conjunction therewith be imparted to any third party. It must not be used for any other contract and the receipt of this drawing implies that these conditions as stated are accepted.

TOLERANCES UNLESS OTHERWISE STATED
— ≤ 100 mm = ± 0.1 mm
> 100 mm ≤ 1000 mm = ± 0.2 mm
> 1000 mm — = ± 0.5 mm
Angular = ± 1.0 °

DESIGNED BY	JS	SCALE	1:2
DRAWN BY	SS	DATE	12/08/20
APPROVED BY	SW	DATE	17/08/20

MATERIAL: PEEK

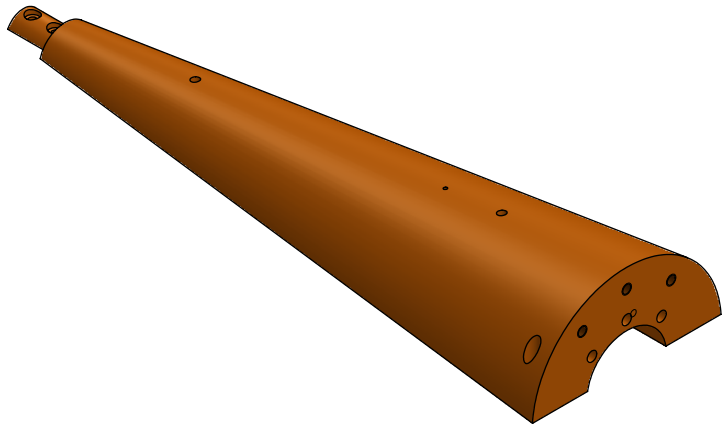
DO NOT SCALE - IF IN DOUBT ASK
DIMENSIONS IN mm
REMOVE ALL BURRS AND SHARP EDGES

Oxford Hypersonics
Oxford Thermofluids Insititute
Southwell Building
Osney Mead
Oxford OX2 0ES
Tel: 01865 288723

DESCRIPTION: 7-Degree-Cone-PEEK-Lid

PART NUMBER	SHEET	ISSUE	
BLC7-000-02	3/4	1.2	A3

REV.	MODIFICATION	BY	DATE
0	NEW	JS	25/06/2020
1	DRAWING TOLERANCES UPDATED	SS	12/08/2020



ISOMETRIC VIEW

This is a CAD produced drawing - no manual modifications are to be made.
This drawing is the property of the University of Oxford. It must not be copied, or the contents thereof or any information received in conjunction therewith be imparted to any third party. It must not be used for any other contract and the receipt of this drawing implies that these conditions as stated are accepted.

TOLERANCES UNLESS OTHERWISE STATED
— ≤ 100 mm = ± 0.1 mm
> 100 mm ≤ 1000 mm = ± 0.2 mm
> 1000 mm — = ± 0.5 mm
Angular = ± 1.0 °

DESIGNED BY	JS	SCALE	1:2
DRAWN BY	SS	DATE	12/08/20
APPROVED BY	SW	DATE	17/08/20

MATERIAL: PEEK

DO NOT SCALE - IF IN DOUBT ASK
DIMENSIONS IN mm
REMOVE ALL BURRS AND SHARP EDGES

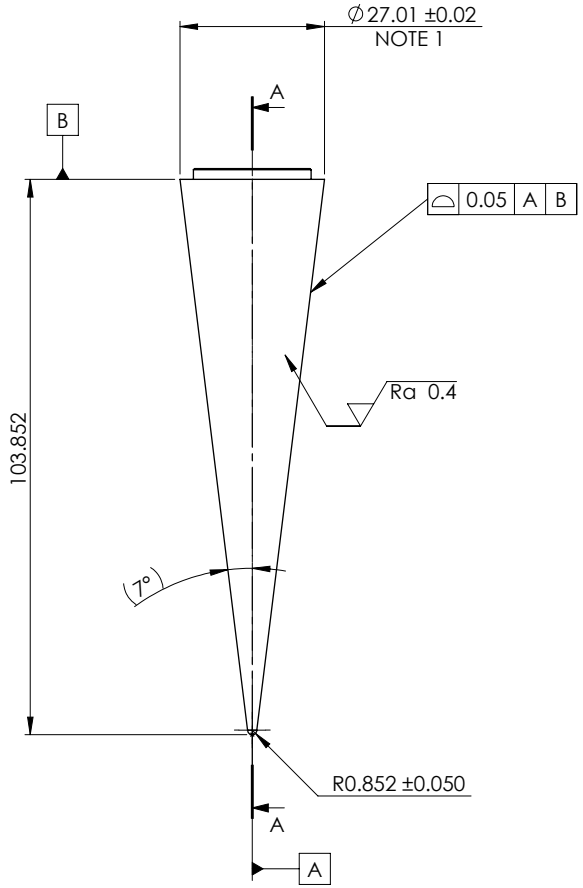
Oxford Hypersonics
Oxford Thermofluids Insititute
Southwell Building
Osney Mead
Oxford OX2 0ES
Tel: 01865 288723

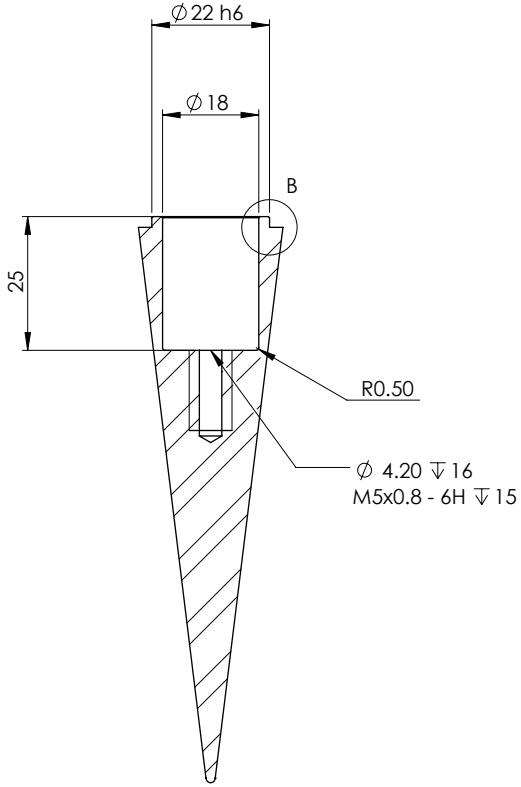
DESCRIPTION: 7-Degree-Cone-PEEK-Lid

PART NUMBER	SHEET	ISSUE	
BLC7-000-02	4/4	1.2	A3

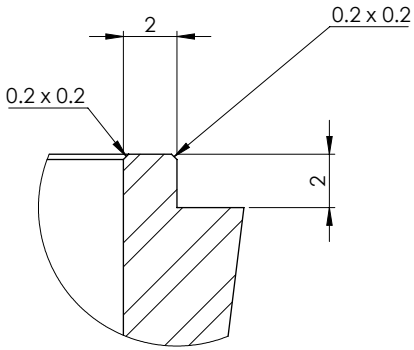
NOTE:
1) Final machining on assembly with 'T6-Main-Body' and 'T6-Cone-PEEK-Lid' to achieve < 0.04 mm joint step/gap.

REV.	MODIFICATION	BY	DATE
0	NEW	JS	25/06/2020
1	DRAWING TOLERANCES UPDATED	SS	12/08/2020
	MATERIAL SPECIFICATION UPDATED	SS	01/09/2020





SECTION A-A



DETAIL B
SCALE 5 : 1

This is a CAD produced drawing - no manual modifications are to be made.
This drawing is the property of the University of Oxford. It must not be copied, or the contents thereof or any information received in conjunction therewith be imparted to any third party. It must not be used for any other contract and the receipt of this drawing implies that these conditions as stated are accepted.

TOLERANCES UNLESS OTHERWISE STATED
— ≤ 100 mm = ± 0.1 mm
> 100 mm ≤ 1000 mm = ± 0.2 mm
> 1000 mm — = ± 0.5 mm
Angular = ± 1.0 °

DESIGNED BY	JS	SCALE	1:1
DRAWN BY	SS	DATE	12/08/20
APPROVED BY	SW	DATE	01/09/20

MATERIAL
EN36B case hardened to min 58 HRC, 0.02" depth

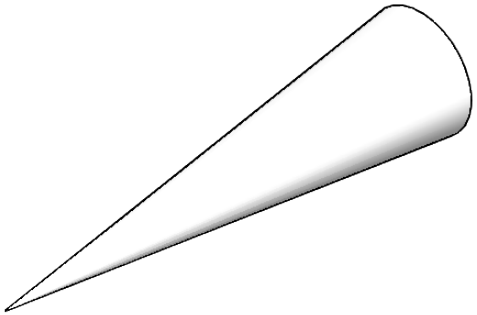
DO NOT SCALE - IF IN DOUBT ASK
DIMENSIONS IN mm
REMOVE ALL BURRS AND SHARP EDGES

Oxford Hypersonics
Oxford Thermofluids Insititute
Southwell Building
Osney Mead
Oxford OX2 0ES
Tel: 01865 288723

DESCRIPTION
7-Degree-Cone-Nose-Tip-B

PART NUMBER	SHEET	ISSUE	
BLC7-000-03B	1/2	1.3	A3

REV.	MODIFICATION	BY	DATE
0	NEW	JS	25/06/2020
1	DRAWING TOLERANCES UPDATED	SS	12/08/2020
	MATERIAL SPECIFICATION UPDATED	SS	01/09/2020



ISOMETRIC VIEW

This is a CAD produced drawing - no manual modifications are to be made.
This drawing is the property of the University of Oxford. It must not be copied, or the contents thereof or any information received in conjunction therewith be imparted to any third party. It must not be used for any other contract and the receipt of this drawing implies that these conditions as stated are accepted.

TOLERANCES UNLESS OTHERWISE STATED

—	≤ 100 mm	= ± 0.1 mm
> 100 mm	≤ 1000 mm	= ± 0.2 mm
> 1000 mm	—	= ± 0.5 mm
	Angular	= ± 1.0 °

DESIGNED BY	JS	SCALE	1:1
DRAWN BY	SS	DATE	12/08/20
APPROVED BY	SW	DATE	01/09/20

MATERIAL
EN36B case hardened to min 58 HRC, 0.02" depth

DO NOT SCALE - IF IN DOUBT ASK
DIMENSIONS IN mm
REMOVE ALL BURRS AND SHARP EDGES

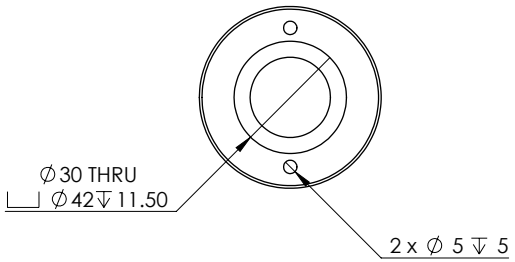
UNIVERSITY OF OXFORD
Oxford Hypersonics
Oxford Thermofluids Insititute
Southwell Building
Osney Mead
Oxford OX2 0ES
Tel: 01865 288723

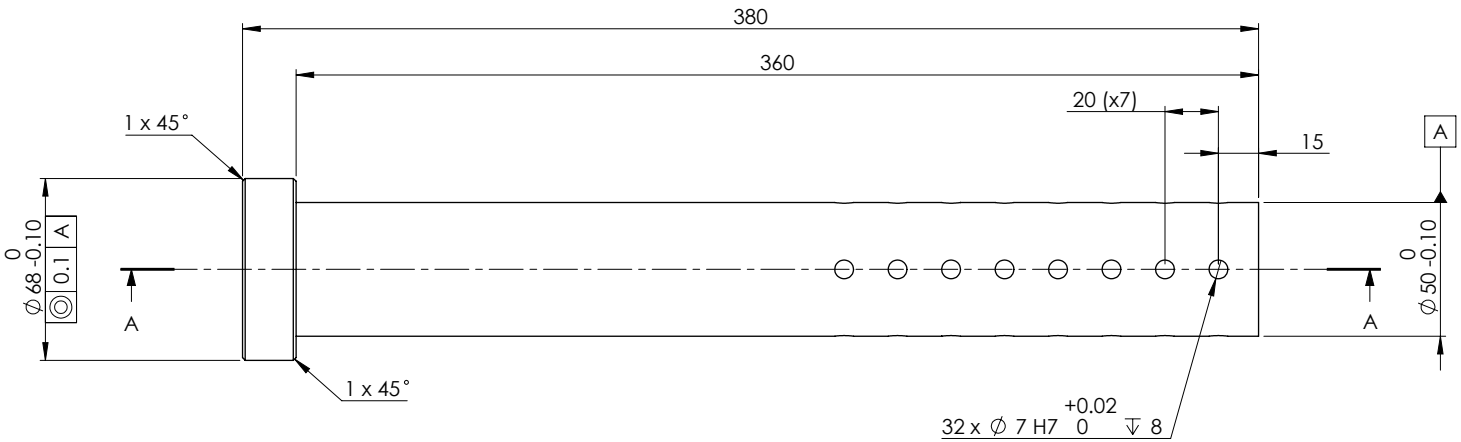
DESCRIPTION
7-Degree-Cone-Nose-Tip-B

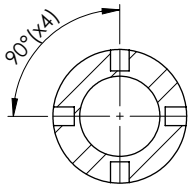
PART NUMBER	SHEET	ISSUE	
BLC7-000-03B	2/2	1.3	A3

NOTES:
1) Each row of holes is located at 90° intervals relative to the axis of revolution. Each row should have 8 holes, see Section B-B.

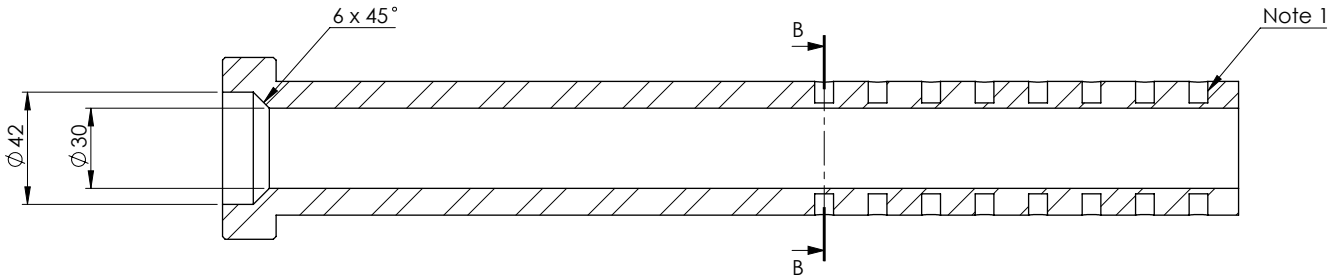
REV.	MODIFICATION	BY	DATE
0	NEW	JS	25/06/2020
1	DRAWING TOLERANCES UPDATED	SS	12/08/2020







SECTION B-B



SECTION A-A

This is a CAD produced drawing - no manual modifications are to be made.
This drawing is the property of the University of Oxford. It must not be copied, or the contents thereof or any information received in conjunction therewith be imparted to any third party. It must not be used for any other contract and the receipt of this drawing implies that these conditions as stated are accepted.

TOLERANCES UNLESS OTHERWISE STATED			
—	≤ 100 mm	= ± 0.1 mm	
> 100 mm	≤ 1000 mm	= ± 0.2 mm	
> 1000 mm	—	= ± 0.5 mm	
	Angular	= ± 1.0 °	

DESIGNED BY	JS	SCALE	1:2
DRAWN BY	SS	DATE	12/08/20
APPROVED BY	SW	DATE	17/08/20

MATERIAL: EN24T or Equivalent

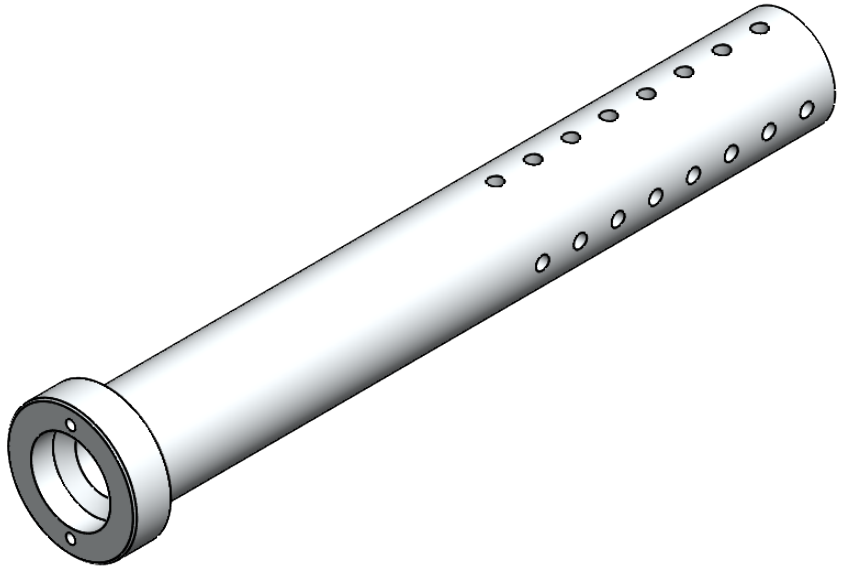
DO NOT SCALE - IF IN DOUBT ASK
DIMENSIONS IN mm
REMOVE ALL BURRS AND SHARP EDGES

Oxford Hypersonics
Oxford Thermofluids Insititute
Southwell Building
Osney Mead
Oxford OX2 0ES
Tel: 01865 288723

DESCRIPTION: 7-Degree-Cone-Modified-Sting

PART NUMBER	SHEET	ISSUE	
BLC7-000-04	1/2	1.2	A3

REV.	MODIFICATION	BY	DATE
0	NEW	JS	25/06/2020
1	DRAWING TOLERANCES UPDATED	SS	12/08/2020



ISOMETRIC VIEW

This is a CAD produced drawing - no manual modifications are to be made.
This drawing is the property of the University of Oxford. It must not be copied, or the contents thereof or any information received in conjunction therewith be imparted to any third party. It must not be used for any other contract and the receipt of this drawing implies that these conditions as stated are accepted.

TOLERANCES UNLESS OTHERWISE STATED			
—	≤ 100 mm	= ± 0.1 mm	
> 100 mm	≤ 1000 mm	= ± 0.2 mm	
> 1000 mm	—	= ± 0.5 mm	
	Angular	= ± 1.0 °	
DESIGNED BY	JS	SCALE	1:2
DRAWN BY	SS	DATE	12/08/20
APPROVED BY	SW	DATE	17/08/20

MATERIAL
EN24T or Equivalent

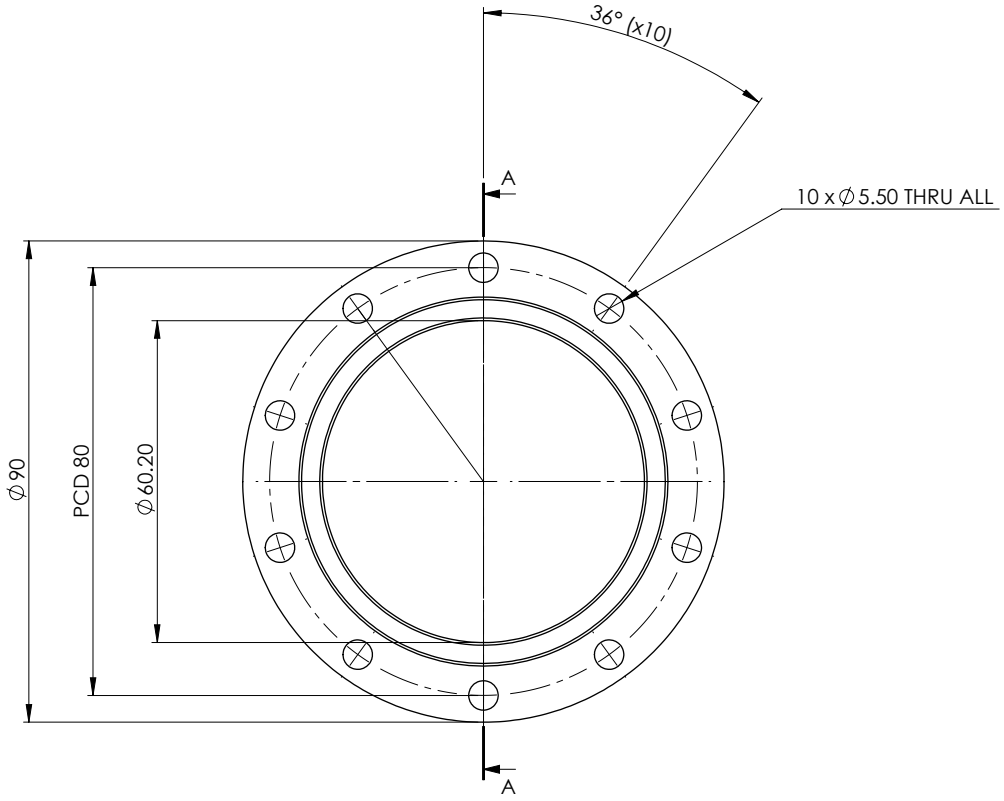
DO NOT SCALE - IF IN DOUBT ASK
DIMENSIONS IN mm
REMOVE ALL BURRS AND SHARP EDGES

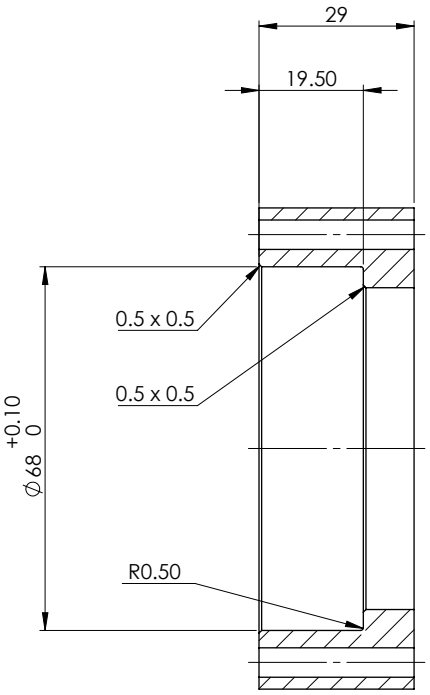
Oxford Hypersonics
Oxford Thermofluids Insititute
Southwell Building
Osney Mead
Oxford OX2 0ES
Tel: 01865 288723

DESCRIPTION
7-Degree-Cone-Modified-Sting

PART NUMBER	SHEET	ISSUE	
BLC7-000-04	2/2	1.2	A3

REV.	MODIFICATION	BY	DATE
0	NEW	JS	25/06/2020
1	DRAWING TOLERANCES UPDATED	SS	12/08/2020





SECTION A-A

This is a CAD produced drawing - no manual modifications are to be made.
This drawing is the property of the University of Oxford. It must not be copied, or the contents thereof or any information received in conjunction therewith be imparted to any third party. It must not be used for any other contract and the receipt of this drawing implies that these conditions as stated are accepted.

TOLERANCES UNLESS OTHERWISE STATED			
—	≤ 100 mm	= ± 0.1 mm	
> 100 mm	≤ 1000 mm	= ± 0.2 mm	
> 1000 mm	—	= ± 0.5 mm	
	Angular	= ± 1.0 °	

DESIGNED BY	JS	SCALE	1:1
DRAWN BY	SS	DATE	12/08/20
APPROVED BY	SW	DATE	17/08/20

MATERIAL: EN24T or Equivalent

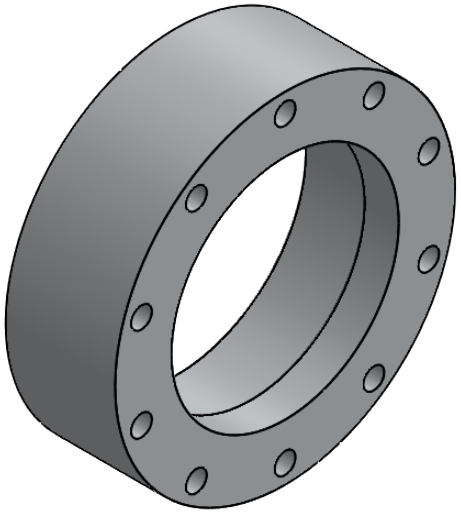
DO NOT SCALE - IF IN DOUBT ASK
DIMENSIONS IN mm
REMOVE ALL BURRS AND SHARP EDGES

Oxford Hypersonics
Oxford Thermofluids Insititute
Southwell Building
Osney Mead
Oxford OX2 0ES
Tel: 01865 288723

DESCRIPTION: 7-Degree-Cone-Collar

PART NUMBER	SHEET	ISSUE	
BLC7-000-05	1/2	1.2	A3

REV.	MODIFICATION	BY	DATE
0	NEW	JS	25/06/2020
1	DRAWING TOLERANCES UPDATED	SS	12/08/2020



ISOMETRIC VIEW

This is a CAD produced drawing - no manual modifications are to be made.
This drawing is the property of the University of Oxford. It must not be copied, or the contents thereof or any information received in conjunction therewith be imparted to any third party. It must not be used for any other contract and the receipt of this drawing implies that these conditions as stated are accepted.

TOLERANCES UNLESS OTHERWISE STATED			
—	≤ 100 mm	= ± 0.1 mm	
> 100 mm	≤ 1000 mm	= ± 0.2 mm	
> 1000 mm	—	= ± 0.5 mm	
	Angular	= ± 1.0 °	

DESIGNED BY	JS	SCALE	1:1
DRAWN BY	SS	DATE	12/08/20
APPROVED BY	SW	DATE	17/08/20

MATERIAL: EN24T

DO NOT SCALE - IF IN DOUBT ASK
DIMENSIONS IN mm
REMOVE ALL BURRS AND SHARP EDGES

Oxford Hypersonics
Oxford Thermofluids Insititute
Southwell Building
Osney Mead
Oxford OX2 0ES
Tel: 01865 288723

DESCRIPTION: 7-Degree-Cone-Collar

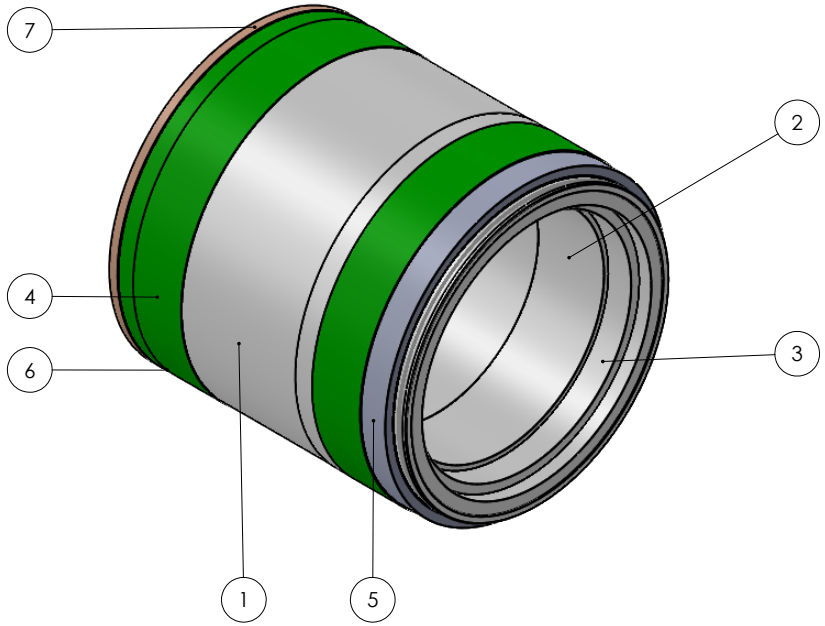
PART NUMBER	SHEET	ISSUE	
BLC7-000-05	2/2	1.2	A3

G

90kg Piston Refurbishment CAD

REV	MODIFICATION	MOD.	CHKD.	APPD.	DATE
0	NEW DRAWING				02/04/2020
1	REPLACEMENT REAR RING MODIFICATION ADDED	SS			03/04/2020

Item No.	Description	Part Number	Revision	Material	Qty.
1	Body Part 1	T6-004-A-01-01	0.1	Comsteel 410	1
2	Body Part 2	T6-004-A-01-02	0.1	Comsteel 410	1
3	Replacement Rear Ring	T6-004-A-01-4B	0.1	Al 7075-T6	1
4	Main Lusint Ring	T6-004-A-02	0.1	Lusint 600	2
5	Rear Split Ring	T6-004-A-03	0.1	Delrin	1
6	Chevron Seal	T6-004-A-04	0.1	Nylatron GSM (Extruded)	1
7	Bronze Ring	T6-004-A-05	0.1	Bronze	1



This is a CAD produced drawing - no manual modifications are to be made.
This drawing is the property of the University of Oxford. It must not be copied, or the contents thereof or any information received in conjunction therewith be imparted to any third party. It must not be used for any other contract and the receipt of this drawing implies that these conditions as stated are accepted.

TOLERANCES UNLESS OTHERWISE STATED
— ≤ 100 mm = ± 0.1 mm
> 100 mm ≤ 1000 mm = ± 0.2 mm
> 1000 mm — = ± 0.5 mm

DESIGNED BY	DG/LD	SCALE	1:4
DRAWN BY	LD/SS	DATE	2/4/20
CHECKED BY		DATE	
APPROVED BY		DATE	

MATERIAL: As per Parts Table

DO NOT SCALE - IF IN DOUBT ASK
DIMENSIONS IN mm
REMOVE ALL BURRS AND SHARP EDGES

UNIVERSITY OF OXFORD
Osney Thermo-Fluids Laboratory
Southwell Building
Osney Mead
Oxford OX2 0ES
Tel: 01865 288768

DESCRIPTION: Modified Piston A - Assembly

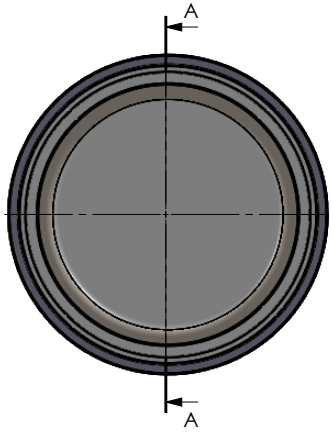
PART NUMBER	SHEET	ISSUE	
T6-004-A-0B	1/2	1.2	A3

NOTES:
1) Item No. 3 and 4 of Existing Assembly to be removed and replaced with Item No. 3 of Modified Assembly

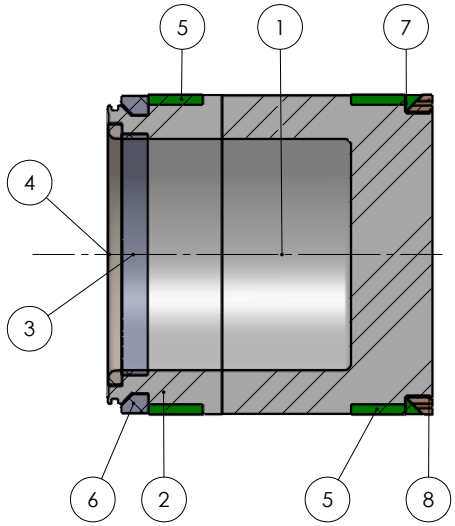
REV	MODIFICATION	MOD.	CHKD.	APPD.	DATE
0	NEW DRAWING				02/04/2020
1	REPLACEMENT REAR RING MODIFICATION ADDED	SS			03/04/2020

Item No.	Description	Part Number	Qty.
1	Body Part 1	T6-004-A-01-01	1
2	Body Part 2	T6-004-A-01-02	1
3	Inner Delrin Ring	T6-004-A-01-03	1
4	Inner Aluminium Ring	T6-004-A-01-04	1
5	Main Lusint Ring	T6-004-A-02	2
6	Rear Split Ring	T6-004-A-03	1
7	Chevron Seal	T6-004-A-04	1
8	Bronze Ring	T6-004-A-05	1

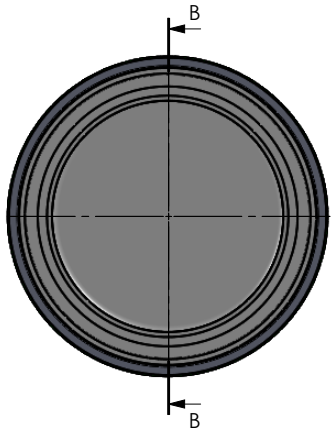
Item No.	Description	Part Number	Qty.
1	Body Part 1	T6-004-A-01-01	1
2	Body Part 2	T6-004-A-01-02	1
3	Replacement Rear Ring	T6-004-A-01-4B	1
4	Main Lusint Ring	T6-004-A-02	2
5	Rear Split Ring	T6-004-A-03	1
6	Chevron Seal	T6-004-A-04	1
7	Bronze Ring	T6-004-A-05	1



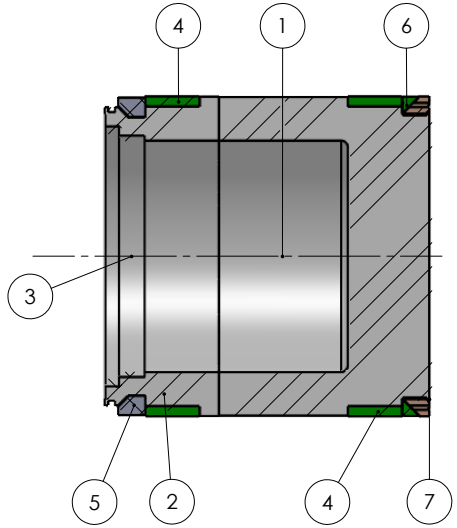
EXISTING ASSEMBLY



SECTION A-A
EXISTING ASSEMBLY
NOTE 1



MODIFIED ASSEMBLY



SECTION B-B
MODIFIED ASSEMBLY

This is a CAD produced drawing - no manual modifications are to be made.
This drawing is the property of the University of Oxford. It must not be copied, or the contents thereof or any information received in conjunction therewith be imparted to any third party. It must not be used for any other contract and the receipt of this drawing implies that these conditions as stated are accepted.

TOLERANCES UNLESS OTHERWISE STATED
— ≤ 100 mm = ± 0.1 mm
> 100 mm ≤ 1000 mm = ± 0.2 mm
> 1000 mm — = ± 0.5 mm

DESIGNED BY	DG/LD	SCALE	1:4
DRAWN BY	LD/SS	DATE	2/4/20
CHECKED BY		DATE	
APPROVED BY		DATE	

MATERIAL: As per Parts Table

DO NOT SCALE - IF IN DOUBT ASK
DIMENSIONS IN mm
REMOVE ALL BURRS AND SHARP EDGES

Osney Thermo-Fluids Laboratory
Southwell Building
Osney Mead
Oxford OX2 0ES
Tel: 01865 288768

DESCRIPTION: Piston A - Assembly

PART NUMBER	SHEET	ISSUE	
T6-004-A-0B	2/2	1.2	A3